MODELING, IMAGE PROCESSING AND ATTITUDE ESTIMATION OF HIGH SPEED STAR SENSORS

A Dissertation

by

ANUP BHARAT KATAKE

Submitted to the Office of Graduate Studies of
Texas A&M University
in partial fulfillment of the requirements for the degree of

DOCTOR OF PHILOSOPHY

August 2006

Major Subject: Aerospace Engineering

MODELING, IMAGE PROCESSING AND ATTITUDE ESTIMATION OF HIGH SPEED STAR SENSORS

A Dissertation

by

ANUP BHARAT KATAKE

Submitted to the Office of Graduate Studies of
Texas A&M University
in partial fulfillment of the requirements for the degree of

DOCTOR OF PHILOSOPHY

Approved by:

Chair of Committee,	John L. Junkins
Committee Members,	Daniele Mortari
	Thomas Pollock
	Rabi Mahapatra
Head of Department,	Helen Reed

August 2006

Major Subject: Aerospace Engineering

ABSTRACT

Modeling, Image Processing and Attitude Estimation of
High Speed Star Sensors. (August 2006)
Anup Bharat Katake, B.Tech., Indian Institute of Technology, Bombay, India;
M.S., Texas A&M University
Chair of Advisory Committee: Dr. John L. Junkins

Attitude estimation and angular velocity estimation are the most critical components of a spacecraft's guidance, navigation and control. Usually, an array of tightly-coupled sensors (star trackers, gyroscopes, sun sensors, magnetometers) is used to estimate these quantities. The cost (financial, mass, power, time, human resources) for the integration of these separate sub-systems is a major deterrent towards realizing the goal of smaller, cheaper and faster to launch spacecrafts/satellites. In this work, we present a novel stellar imaging system that is capable of estimating attitude and angular velocities at true update rates of greater than 100Hz, thereby eliminating the need for a separate star tracker and gyroscope sub-systems.

High image acquisition rates necessitate short integration times and large optical apertures, thereby adding mass and volume to the sensor. The proposed high speed sensor overcomes these difficulties by employing light amplification technologies coupled with fiber optics. To better understand the performance of the sensor, an electro-optical model of the sensor system is developed which is then used to design a high-fidelity night sky image simulator. Novel star position estimation algorithms based on a two-dimensional Gaussian fitting to the star pixel intensity profiles are then presented. These algorithms are non-iterative, perform local background estimation in the vicinity of the star and lead to significant improvements in the star centroid determination. Further, a new attitude determination algorithm is devel-

oped that uses the inter-star angles of the identified stars as constraints to recompute the body measured vectors and provide a higher accuracy estimate of the attitude as compared to existing methods. The spectral response of the sensor is then used to develop a star catalog generation method that results in a compact on-board star catalog. Finally, the use of a fiber optic faceplate is proposed as an additional means of stray light mitigation for the system. This dissertation serves to validate the conceptual design of the high update rate star sensor through analysis, hardware design, algorithm development and experimental testing.

To the stars that shine bright and bring light into my life

ACKNOWLEDGMENTS

Long journeys usually have small and unexpected beginnings. What begins as a simple thought to pursue higher education, ends up changing your life and people around forever. As foreigners like me who leave their sheltered home, country and embark on this adventure, we seek a guru who will help us reach our goals, adapt to strange surroundings, and absorb new ideas and thoughts. To me this person has been my advisor Dr. John L. Junkins. He has provided me with invaluable guidance and support throughout my graduate studies and helped me navigate this journey with the right "attitude". He has been a constant source of inspiration, always motivating me to do better, see the bigger picture and I am deeply grateful to him.

Dr. Daniele Mortari's infectious enthusiasm and expert guidance on attitude determination have helped "point" this dissertation more accurately and my heartfelt thanks to him. Dr. Thomas Pollock introduced me to the wonderful world of optics and I would sincerely like to thank him for his advice and for "showing me the light". A big thanks to Dr. Rabi Mahapatra for sharing his knowledge of embedded systems. Members of the faculty of aerospace engineering gave me their time, knowledge and advice during my graduate studies and I would like to express my gratitude and thanks to them. An important member of the aerospace family I would like to thank is Ms. Lisa Willingham, who has helped me with many administrative and organizational tasks.

During my graduate studies I had the fortune to work on several high profile projects, one of which was the StarNav-I experiment on the STS107 Columbia. I would like to thank Mr. Michael Jacox of StarVision Technologies Inc. for providing me with the opportunity to be a part of the successful mission. I would also like to thank all my colleagues at StarVision Technologies Inc. for their help and for making

the workplace a fun-filled learning environment.

My close friends Sesha Sai Vaddi, Raghavendran Mani and Sangeeta Bokadia helped make College Station a home away from home. Living room cricket sessions, long chats over late night cups of coffee will always remain fond memories. I would like to thank Puneet Singla and Christian Bruccoleri for their help in academics and for being great friends.

My parents have had to undergo a lot of hardships and sacrifices to make me what I am today. I would like to thank my family for all the support and love they have given me. This dissertation would not have been possible without their love, encouragement and belief in me.

The first time I met my wife, Prabha, was when I received her at the airport when she came here for her graduate studies. Little did I know then, that I would be receiving her in my life as well. Together we have been down several roads - some smooth and some rough, but never have I felt alone or lost. They say that behind every successful man there is a successful woman and I am no exception. Words cannot express how much your love and support (and cooking!) mean to me. Thank you!

TABLE OF CONTENTS

CHAPTER Page

I INTRODUCTION 1

II SPEEDSTAR: A LIGHT INTENSIFIED STAR SENSOR 6

A. System Architecture 6
B. Image Intensification 8
1. Basic Operation 9
a. Input Window 9
b. Photocathode 10
c. Micro-channel Plate (MCP) 13
d. Phosphor Anode 14
e. Gated Operation 16
2. Image Intensifiers Types - Historical Development . . 18
C. Imaging Sensors 19
1. CCD 21
2. CMOS Active Pixel Sensor 22
3. CCD - CMOS Comparisons 22
D. Intensifier to Imager Coupling 26
1. Relay Lens 28
2. Fiber Optic Coupling 29
E. Concluding Remarks 30

III ELECTRO-OPTICAL MODELING AND IMAGE SIMULATOR DESIGN 32

A. Noise Characterization 33
1. Sources of Noise 34
a. Shot Noise 34
b. Dark Current 36
c. Reset Noise 36
d. Pattern Noise 37
e. Other Sources of Noise 37
2. Image Intensifier Noise 39
3. Image Intensifier Signal 40
4. Image Intensified Camera SNR 41

CHAPTER Page

5. Gain Model of the Image Intensifier 42
B. Linear System Theory Applied to Imaging Systems 43
C. Optical Response of the Intensified Camera System 46
1. Lens Assembly 47
a. Aberrations 49
b. Defocused Optics 55
2. Image Intensifier 56
3. Fiber Optic Taper 60
4. Imaging Sensor 63
a. Fill Factor 64
5. The Net System MTF 64
D. The Star Image Simulator 69
1. Star Irradiance Estimation 71
2. The Real Lens System 73
3. Sensor Geometry and Sampling 76
a. Pixel Phase 77
4. The Designed Simulator 80
E. Concluding Remarks 88

IV STAR POSITION ESTIMATION IMPROVEMENTS 89

A. Introduction and Existing Centroiding Methods 89
1. Center of Mass 90
2. Non-Linear 2-D Gaussian Fitting 91
B. Linear Least Squares Log of Gaussian Estimation (LOG-LSQ) 93
1. Algorithm Development 94
2. Performance on Simulated Stars 97
3. Weighted Estimation 98
C. Background Estimation 103
1. Need for Automatic Thresholding 104
2. Least Squares Bias Estimation 105
3. Performance Improvement 108
D. Centroiding Accuracy - Simulated Images 111
E. Concluding Remarks 117

V NIGHT SKY EXPERIMENTATION 118

A. Hardware Setup 118
1. Image Intensifier 119

CHAPTER Page

2. Power Supply 119
3. Intensifier to Sensor Coupler 119
4. Imaging Sensor 121
5. Component Integration 122
B. Night Sky Testing 125
1. Photometric Analysis 127
a. Variable Gain at Fixed Aperture 129
2. Centroiding Performance 130
C. Concluding Remarks 138

VI CONSTRAINED STAR RE-CENTROIDING AND ATTITUDE ESTIMATION 139

A. Introduction and Wahba's Problem 139
B. Classical Solution to the Wahba Problem 140
C. Constrained Centroiding - A Mechanical Equilibrium of a Rigid Body Analogy 143
1. Development of the Algorithm 144
2. Coplanarity of Torques 146
3. Energy Approach Using Forces 147
4. Torque Balance Approach 149
5. Solution to the Flexible Body System 151
a. Solution by Singular Value Decomposition 152
b. Singularity Avoidance for the Case of Two Body Observations 153
D. Numerical Tests and Results 154
1. Input Conditions 154
2. Measurement of Attitude Error 154
3. Attitude Error v/s Number of Observations 156
E. Concluding Remarks 159

VII SPECTRAL MATCHING OF STAR CATALOGS 164

A. Introduction 164
B. Background on Stellar Photometry and Radiometry 167
1. Stellar Magnitudes 167
a. Visual and Apparent Magnitudes 168
2. Spectral Classification of Stars 169
3. Stars as Blackbody Radiators 170
C. Generation of On-board Star Catalogs 172

CHAPTER Page

1. Fixed Magnitude Cutoff Star Catalog 173
2. Quasi-uniform Star Catalog 174
D. A Methodology for Building a Spectrally Matched Catalog 176
1. Optical Train Spectral Response 179
a. Transmittance of a Radiation Hardened Lens . . . 181
2. Image Intensified Sensor Spectral Response 182
3. Loss in Apparent Magnitudes 187
4. Accounting for Atmospheric Transmission 192
E. Catalog Extraction Results 197
F. Concluding Remarks 201

VIII STRAY LIGHT MITIGATION 203

A. Origins of Stray Light 203
1. Effect on Imaging Performance 203
2. Mitigation Techniques - Light Shades 205
B. Fiber Optics Technology 208
1. Theory of Ray Propagation 209
2. Meridional Model 210
3. Skew Rays 211
4. Fiber Optic Faceplate 214
a. Construction 215
5. FOP as a Stray Light Mitigation Device 216
C. Modeling Using Non-sequential Ray Tracing 216
1. Setup 217
2. Simulation Results 221
D. Experimental Testing 224
1. Results 225
E. Concluding Remarks 229

IX CONCLUSIONS 231

REFERENCES 235

VITA 242

LIST OF TABLES

TABLE		Page
I	Comparison of star tracker and gyroscope suites	2
II	Input window materials and transmittance	10
III	Characteristics of various phosphor screens	15
IV	Qualitative comparison between the CCD and CMOS-APS sensors	27
V	MTF for the ITT FS9910 as specified by the manufacturer	58
VI	Star data for one of the simulated images for a random attitude	88
VII	Absolute mean and standard deviations (pixels) in the error in centroiding using weighted and un-weighted measurements	103
VIII	Specifications for the configured image intensifier	120
IX	Specifications of the power supply	121
X	Performance comparison in the inter-star angle errors obtained by using center of mass and LOG-LSQ methods on the night-sky images	135
XI	Parameters of the star simulator	155
XII	Statistics - root mean square error(rmse) and standard deviation(std) in the attitude estimate error using the classical ESOQ2 and flexible body constrained recentroiding approaches	158
XIII	Spectral classes of the Yerkes System, luminosity compared with Sun	170
XIV	Example of stray light specifications for a star tracker	206
XV	Parameters of the modeled FOP and lens system	218

LIST OF FIGURES

FIGURE		Page
1	The SpeedStar system	7
2	Cut-away view of the intensified CCD electro-optics and focal plane	8
3	A simple first-generation image intensifier	10
4	Spectral sensitivity and the quantum efficiencies versus wavelength for various photo-emitters	11
5	A cut away view of the MCP and generation of secondary electrons along the channel	14
6	Spectral emission characteristics of available phosphor screens and quantum efficiency of the most commonly used phosphor - P43	17
7	Luminescence decay profiles for P20 and P43 phosphor screens	18
8	Schematics of the gate operation	19
9	Examples of various generations of image intensifiers	20
10	CCD architecture and readout	21
11	CMOS architecture and readout	23
12	Losses in photon absorption	24
13	Intensifier to imager coupling mechanisms	29
14	An fiber optic taper bundle attached to an imager	30
15	Various sources of noise for an imaging system	35
16	Photon transfer curve for dark current dominated shot noise	38
17	Airy pattern: Irradiance distribution by a circular aperture	48

FIGURE Page

18 A 3 element aspheric lens system with focal length of $25mm$ and $F_{\#}$ of 0.73 with five fields 52

19 Spot diagram for the 3-element lens system 53

20 MTF of the aberrated 3-element lens system 54

21 MTF of the aberrated and defocused 3-element lens system 57

22 1-D MTF of the image intensifier 59

23 The 2-D and 3-D MTFs of the image intensifier 61

24 The MTFs for the fiber optic taper 62

25 MTF of the imaging sensor for square pixels of dimensions $5\mu m$ . . . 65

26 MTF of the imaging sensor for rectangular pixels of dimensions $5\mu \times 7.5\mu mm$ 66

27 MTF curves with a 100% fillfactor and a fillfactor of 75% 67

28 MTF of the complete image intensified camera system 68

29 Star point spread profiles from a simplified image simulator and from actual night sky test 70

30 Wavelength dependant efficiency of the photocathode for the image intensifier 73

31 Point spread functions for the defocused 3-element lens across the field of view 74

32 Interpolated point spread functions using the regional psfs 75

33 Pixel phase errors in centroiding using a Gaussian fitting procedure . 78

34 Illustration of the frames associated with pixel phase. Crosses are the pixel centers and the circle indicates the centroid of the star . . . 79

35 Star image simulator 82

FIGURE Page

36 Magnitude of the OTF for the interpolated star psf (star1) and the pixel response 83

37 Integrated continuous psfs for the stars in the image 84

38 Pixel phase corrected sampling grids for the stars in the image 85

39 Sampled stars 86

40 Simulated night sky image for a random attitude 87

41 2D Gaussian distribution for noise magnitude= 1% 98

42 Centroiding error using the LOG-LSQ and COM approaches for noise magnitude= 1% 99

43 2D Gaussian distribution for noise magnitude= 10% 100

44 Centroiding error using the LOG-LSQ and COM approaches for noise magnitude= 10% of signal amplitude 100

45 Effect of noise on the measurements used in the LOG-LSQ approach 101

46 Weighting function for the LOG-LSQ scheme 102

47 A bias added star intensity distribution and incorrect extraction of pixels 105

48 Increase in the error in centroiding due to incorrect threshold 106

49 Illustration of border regions used for background estimation 107

50 Simulated star intensity distributions, recovered surface and weighting function for local background estimation 109

51 Errors in the centroiding without using local background estimation and with background estimation 110

52 Flowchart of the centroiding methodology 113

53 Simulated star image. Note the variation in the background across the image 115

FIGURE Page

54 Inter-star angle error for 500 tests for centroiding using LOG-LSQ and center of mass approaches 116

55 18mm input and 1/3" imager compatible fiber optic taper used intensifier to CCD coupling 122

56 Spreading of light at the output of fiber when surfaces are not in perfect contact 124

57 An inside view of the integrated prototype 125

58 Night sky images of various parts of the sky. Taken at f4.0 and gain control voltage of 3.7V 126

59 Star intensity distribution surfaces on the imaging sensor 128

60 Half-width half-maximum for stars of different visual magnitudes . . 129

61 Acquired images at various gain voltages at f2.0 131

62 Statistics of the background noise levels for different gain settings . . 132

63 Detected star centroids in the night sky image of the Orion's belt . . 134

64 Inter-star angle statistics for star number 4 using COM and LOG-LSQ methods 136

65 Mean of the deviations in the inter-star angles for all star pairs across all image sets 137

66 Body measured vectors to the pixel centers and centroid 144

67 Attitude errors: around boresight, orthogonal to boresight and net error for 3 stars in the field of view 160

68 Attitude errors: around boresight, orthogonal to boresight and net error for 4 stars in the field of view 161

69 Attitude errors: around boresight, orthogonal to boresight and net error for 5 stars in the field of view 162

FIGURE Page

70 Attitude errors: around boresight, orthogonal to boresight and net error for 6 stars in the field of view 163

71 Number of stars at and below a given magnitude extracted from the Hipparcos catalog 166

72 Blackbody radiation for different temperatures 171

73 Spectral radiance curves for spectral classes of the stars 172

74 Steps involved in creating a mission star catalog based on a fixed magnitude cutoff approach 174

75 Outline of the steps involved in obtaining spectral response dependant cutoff magnitudes 177

76 Transmissivity of a commonly used glass material - Schott N-BK7 . . 180

77 Transmittance of BK7 before and after exposure to radiation 181

78 Layout of a possible radiation hardened lens design for a star tracker 182

79 Transmittance versus wavelength curves for the glass types used in the rad-hard lens design 183

80 QE of the GenIII image intesifier GaAsP photocathode 184

81 Emission characteristics of the P43 phosphor 185

82 QEFF of a typical CMOS image sensor 186

83 Spectral radiance curves for spectral classes of the stars 187

84 Spectral Profiles of the region of interest 188

85 Normalized equal apparent brightness in space 190

86 Apparent brightness profiles at the output of the image intensified star sensor system 191

87 Apparent magnitude loss in space with respect to Class M star for various spectral classes 193

FIGURE Page

88 Path traversed by stellar radiation at zenith angle z 195

89 Atmospheric transparency v/s wavelength for various zenith angles . 196

90 Loss in apparent magnitudes with observer at sea level and zenith angles 0° and 60° 197

91 Number of stars extracted per spectral class from the Hipparchos catalog using fixed cutoff and spectral matching for a instrument located above the Earth's atmosphere 199

92 Difference in the number of stars extracted per spectral class between the fixed cutoff and spectral matching approaches 200

93 Stray light decreases signal-to-noise ratio and post processing of the image reveals the presence of faint stars 204

94 Stray light rays hitting the detectors as patterns and streaks. 205

95 Schematic of the double baffle 207

96 Baffle length v/s Sun rejection angle and Earth rejection angle 208

97 Ray incident at a plane interface with $n_1 > n_2$. Ray is refracted into n_2 if $\phi_1 < \phi_c$ 210

98 Illustration of meridional ray propagation along the fiber 210

99 Acceptance angle for varying NA using the meridional model 212

100 Propagation of a skew ray along the fiber in a helical path 212

101 Increase in the effective numerical aperture due to the presence of skew rays 214

102 The modeled fiber optic bundle in ZEMAX. Complete system layout - side view 219

103 Close-up and side view of the setup in ZEMAX. Blue rays are stray light and green rays are star light 220

FIGURE Page

104 Detector output after non-sequential ray trace for stray light incident at various angles 222

105 Helical paths taken by highly oblique angle of incidence skew rays (shown in blue). Notice how the rays never intersect the fiber axis . . 223

106 The procured FOP as viewed in different angles. The black appearance is due to the EMA 224

107 The experimental setup for the stray light measurements 225

108 A montage of the acquired images at increasing angles of incidence of the laser 227

109 Stray light energy attenuation curves obtained for various integration times 228

CHAPTER I

INTRODUCTION

Star sensors or star trackers are among the most widely used attitude estimation sensors aboard a spacecraft. Spacecrafts frequently use a star tracker in conjunction with some subset of other sensors such as sun sensors, magnetometers, accelerometers and gyroscopes to form an Inertial Measurement System (IMS) for guidance, navigation and control (GNC). Of all the above mentioned sensors, star trackers offer by far the most accurate attitude estimate with 2arcsec to 5arcsec being a top of the line pointing error. In order to obtain an attitude estimate from star sensors, we rely on acquiring a high quality image of the stars, and identifying them by performing in essence a pattern recognition using an on-board catalog. The high accuracy however, comes at a price - usually a slow update rate. Imaging faint sources of light is inherently a time consuming process since a large signal to noise ratio between the star pixel response and the combination of background light and noise is desired for reliable detection. The accumulated star energy in the imaging sensor pixel is directly proportional to the integration time of the image to be acquired and to the aperture (area) of the optical system. A fundamental tradeoff in traditional designs is between the integration time and mass of the optics. Fast integration dictates massive, large aperture optics for traditional designs. Increasing the integration time leads to a slower attitude output rate and image degradation due to motion-induced smear, while increasing the aperture implies addition of weight - a critical parameter for spacecraft systems engineers.

In order to measure angular accelerations and velocities the spacecraft employs

---

The journal model is *IEEE Transactions on Automatic Control*.

Table I. Comparison of star tracker and gyroscope suites

Parameter	**Ball + MIMU**	**Ball + BAE MEMS**	**Draper LoPASS**
Mass	7.2kg	2.7kg	2kg
Power	30W	9W	3.5W
Accuracy (with filter)	2.7arcsec	8arcsec	360arcsec
Update Rate	10Hz	10Hz	5Hz

gyroscopes. All gyroscopes, owing to their measurement methodology, drift over time and accumulate bias. On-board algorithms periodically correct for the drift by using the star tracker attitude estimates. Thus, it is not possible to design an accurate spacecraft guidance and navigation system with using just one of the two sensors. The star tracker and gyroscope system suite can constitute a significant fraction of the spacecraft total cost and the subsequent integration requirements multiplies that cost by the associated complications with the avionics and structural interfaces. Dual sensors also imply an approximately doubled power consumption. Although efforts are being made to reduce the power consumed by the star trackers [1] by using advanced imaging arrays such as the CMOS Active Pixel Sensor, the decrease in the power consumption has not been drastic. Table I shows some of the available sensor combinations.

The Ball Aerospace star tracker and the Honeywell MIMU are the state of the art sensing systems and present a very high power, weight and cost factor. Recent advances in micro-electrical mechanical systems (MEMS) have led to the fabrication of very compact accelerometers that are very light weight and consume very little

power. However, these are very susceptible to drift and have large measurement errors. The Draper LoPASS system [2] uses MEMS gyroscopes as the primary means of attitude estimation by integrating the angular rates. The star tracker attitude estimates are used to correct for the large gyroscope drift. None of these systems offer the desired combination of high update rates, small attitude estimation errors, small mass and low power.

Our aim in this dissertation is to document the research on the design, development and testing the validity of a revolutionary sensing system which achieves a very high update rate (> 100Hz). This star tracker concept seeks to eliminate the need for a separate angular rate measurement unit thereby reducing mass, power and the net cost of the attitude sensor suite. The dissertation encompasses several aspects of star tracker instrument design such as imaging hardware, image processing, modeling, optical system design and star catalog generation. The main objectives of the research leading to this dissertation are:

- To study the theory of light amplification by high performance image intensifiers, analyze the effects of the introduction of the intensifier on the optical and electro-optical performance of the imaging system

- To design and implement a new methodology to provide improved accuracy in star position estimation and consequently in attitude and in rate estimation.

- To construct a prototype of the image intensified star sensor in order to validate the concept and verify the performance of the new centroiding scheme via night sky testing

- To develop a star catalog building technique that is matched with the spectral response of the electro-optical system

- To introduce new means for reducing stray radiation in the optical train by the use of fiber optics technology and to demonstrate the effectiveness through experimentation

This dissertation documents the results of this research organized as follows:

In Chapter II, some background on the development of the image intensification technology is given. The components making up an intensified camera system are discussed and parameters governing their selection and performance are studied. A technology background on the available imaging sensors is provided. Techniques for coupling the amplified light to the focal plane array are presented.

In Chapter III, the noise characteristics of the electro-optical system are derived. It is shown that the signal to noise ratio (SNR) is dependent on the gain of the intensifier and that the gain dictates which noise sources (intensifier or image sensor) decide the overall SNR of the system. The optical response of the imaging system under study derived by applying concepts from linear systems theory. In order to obtain input test data in the absence of hardware, a high-fidelity night sky image simulator is designed. This simulator takes into account the performance of the optical train under consideration including aberrations and non-uniform point spread functions, sensor geometries, and star irradiance.

Chapter IV discusses current methods used for star centroiding and introduces a novel star position estimation and background estimation technique. This technique is based upon a 2D Gaussian fitting to the star intensity distributions on the focal plane. Simulated image data is used to estimate the improvement in the centroiding accuracy.

In Chapter V, a prototype model of the image intensified star sensor is constructed. The prototype is used to obtain night sky images of various star fields.

Results from the night sky testing of the designed system are presented. Data obtained in the imaging tests is also used to analyze the performance of the proposed centroiding scheme.

Chapter VI introduces a novel attitude estimation technique in which the body vectors to the identified stars are updated using the inter-star angle constraints. This "recentroiding" process is shown to lead to an increased accuracy in the attitude estimates when compared to currently used algorithms as such as ESOQ2. The combination of this idea and the results of Chapter IV, lead to a factor of 3 in the accuracy improvement.

In Chapter VII the attention is focussed on the generation of a star catalog that accounts for the spectral class of the star and the spectral response of the system. It is shown that a significant difference in the number of stars per class is obtained if spectral matching is done. The case of terrestrial star identification applications is also discussed and atmospheric extinction is addressed.

Finally, Chapter VIII is concerned with the mitigation of stray light in the optical train and proposes the use of fiber optics technology to provide a virtual baffle as an additional means of suppressing stray light with reduced mass and volume penalties. Simulation using ray tracing software packages and laboratory experimentation is performed to validate the concept.

CHAPTER II

SPEEDSTAR: A LIGHT INTENSIFIED STAR SENSOR

A. System Architecture

In the previous chapter we emphasized the need for a sensor to enable both high speed stellar attitude and angular velocity estimation. Several efforts have been made [3], [4], [5] towards analyzing the update rate requirements and the attainable accuracy for the derived rate estimates. However, all of these works assume that a high frame rate imaging system capable of acquiring images of sufficiently dense star fields is available or possible in the near future. Thus, they do not address the key issues: feasibility and design of hardware for implementation of such a system. The ability to detect the star against the background noise is primarily dictated by the light gathering capacity of the imaging system. This in turn mainly depends on the clear aperture of the optical train, the integration time of the frame and the photon conversion efficiency of the focal plane sensor. A fast update rate translates to a small integration time and given a sensor technology, the only available control variable in existing designs to affect energy flux on the focal plane is the aperture. Increasing the aperture while keeping the field of view constant causes a growth in the aberrations of the optical train (decreased f-number) and makes the lens design task more challenging. Moreover, the larger aperture implies much more mass and a bigger sensor footprint, both of which are highly undesirable for instrument integration with the spacecraft.

The recently invented light intensified star sensor, called here SpeedStar, represents a paradigm shift that overcomes the limitations of the traditional imaging techniques by employing state of the art image intensification technology coupled with fiber optics. Fig. 1 shows the overall architecture of the SpeedStar system. A

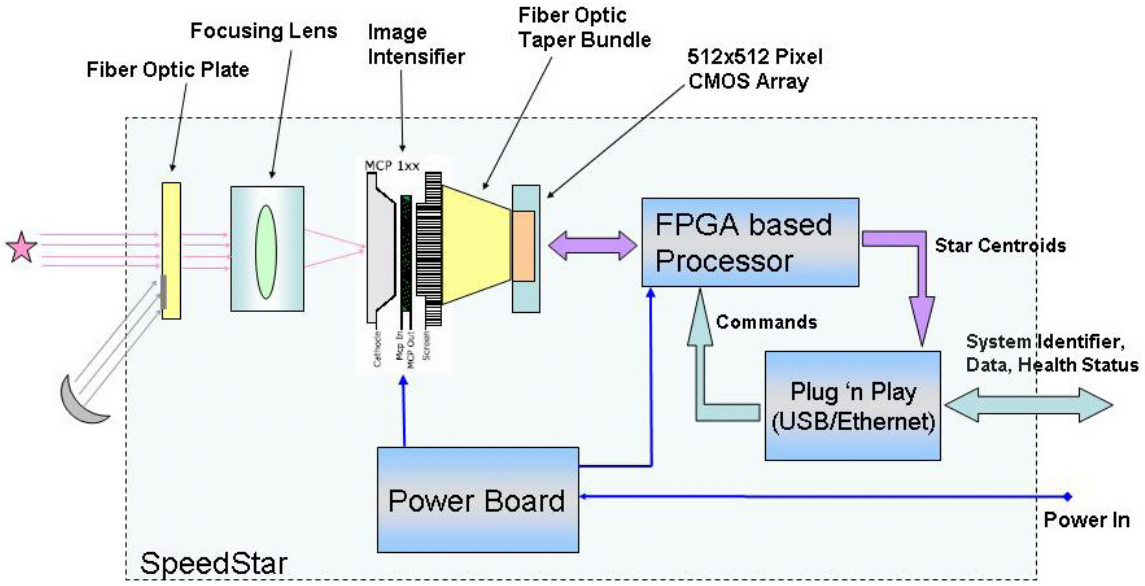

Fig. 1. The SpeedStar system

fiber optic plate(FOP) acts as the clear aperture upon which the light radiation is incident. The primary objective of the FOP is to provide selective transmission of the starlight and provide an additional means of stray light control. A focussing lens system forms the image of the stars visible on the input window of the image intensifier. An image intensifier (Fig. 2 [6]), as the name suggests, is an electro-optical device that amplifies the incident light by using the photo-electric and avalanche effects for electron multiplication. The output of the intensifier (photons) is then optimally coupled to the imaging sensor using a fiber optic taper bundle. A field programmable gate array (FPGA) is used for imager control, image processing and interfacing. A serial link or a plug 'n play (PNP) bus such as ethernet forms the interface with the outside world for command and data handling. In the following sections, we shall provide some background on the development and the current status of the image intensification as well as focal plane sensor technologies. We also discuss a number of

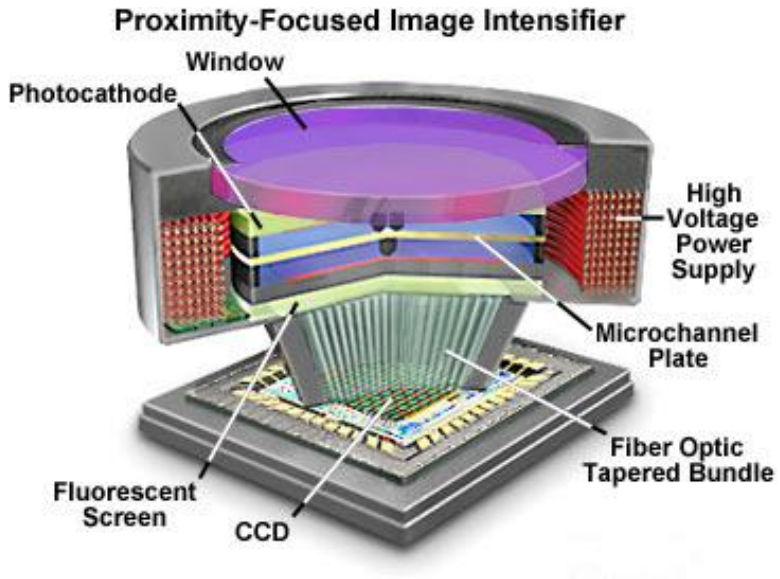

Fig. 2. Cut-away view of the intensified CCD electro-optics and focal plane

challenges implicit in this approach, and report means to address these in the designs studied.

B. Image Intensification

The basic goal of the image intensifier is to amplify the light contained in the scene of interest. Image intensifiers fall into the broad category of electro-optical technologies that operate on the principle of photo-electric effect. A photon incident on an electrically biased photo-sensitive material transfers its energy into the material, thereby giving rise to an electron called "photo-electron" that is emitted from the substrate. This effect was discovered and rigorously explained by Albert Einstein in 1905 for which he won the Nobel Prize. However, it was not until the 1960's that the practical electronic devices based on this effect began appearing in the market. Since then, the technology has progressed in leaps and bounds and has evolved into today's image intensifiers that are highly sensitive and distortion free. Qualitatively we will

see that each incident photon causes an electron "avalanche" near where the photon impinged; the number of electrons in the "avalanche" are controlled by an applied voltage across the intensifier. Another point to note is that the input radiation can belong to any spectral band from the ultra-violet to the far infra-red. The generated photo-electrons, after suitable processing, can be converted back to photons whose wavelength lie in the visible range. Thus, the image intensifiers are also known as "image convertors".

1. Basic Operation

The radiation from the scene of interest is captured by an optical aperture and the image of the scene is formed on the input window of the image intensifier (Fig. 3). The input window can be made up of glass of various types or can be a fiber optic faceplate. The other side of the window forms the photocathode. The photocathode absorbs the incident radiation and converts it to photoelectrons. The number of photoelectrons generated depends on the spectral response and the efficiency of the photocathode. A phosphor screen is located at the rear of the intensifier. A potential difference is applied between the photocathode and the phosphor screen which causes the photo-electrons to be accelerated towards the phosphor. Upon impact with the screen, the high energy electrons are converted back to multiple photons. This leads to an overall gain in the number of photons thereby causing image intensification [7].

a. Input Window

Several options are available for the choice of the input window size and materials. The most commonly available window diameters are 18mm, 25mm and 40mm and the selection is primarily dictated by compatibility in form factor with the imaging

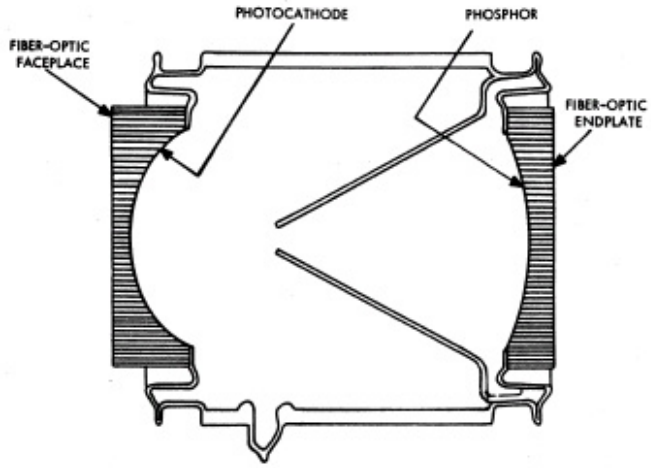

Fig. 3. A simple first-generation image intensifier

Table II. Input window materials and transmittance

Window Type	Transmitting Wavelength
Synthetic Silica	160nm or longer
Fiber Optic Plate	350nm or longer
MgF_2	115nm or longer
Borosilicate Glass	300nm or longer

detector. The transmittance of the material is also dependent on the wavelength of the incident radiation. Table II lists some of the available materials and their spectral operating range. The borosilicate glass window is most commonly used for imaging in the visible and near IR regions.

b. Photocathode

The spectral response and efficiency of the image intensifier is primarily dependent on the materials used in the photocathode. The desired sensitivity at various wavelengths

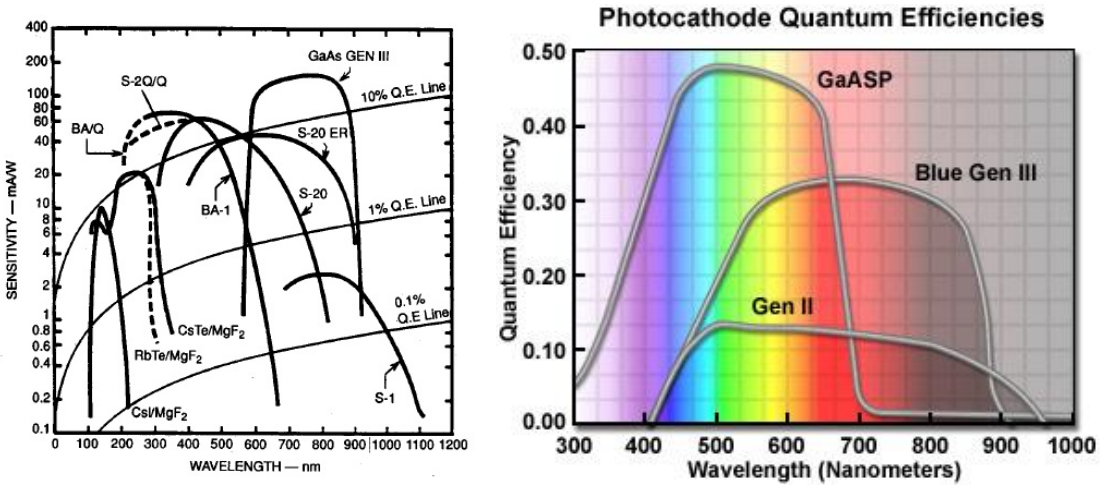

(a) Spectral Sensitivity (b) Quantum Efficiency

Fig. 4. Spectral sensitivity and the quantum efficiencies versus wavelength for various photo-emitters

is obtained by selective doping of the photocathode materials. Fig. 4(a) [7, 8] shows the spectral sensitivities of various photo-emitters. Traditional cathodes were made of alkali materials and exhibited sensitivity ranging from the UV to the near-IR regions of the spectrum. The photocathodes of today are based on gallium arsenide (GaAS) or gallium arsenide phosphor (GaAsP) materials and show very high sensitivities in the visible range. Special material cathodes also exist, such as the Cs-Te cathode often called the "solar-blind" photocathode since it has a high sensitivity only in the UV and near zero in the visible. Such cathodes can be used to effectively block out the visible solar radiation and are operable even in broad daylight.

The photon to electron conversion ratio or the quantum efficiency of the photocathode is dependent on the sensitivity of the material. The relationship between the spectral sensitivity and the quantum efficiency is given by [9]

$$QE = \frac{123.950 \times RadiantSensitivity(mA/W)}{\lambda} \tag{2.1}$$

where λ is the wavelength in nanometers. Fig. 4(b) shows the quantum efficiencies of some of the photocathodes. As can be seen the GaAsP cathodes are highly sensitive and are able to achieve a quantum efficiency of about 50% at 500nm.

An important factor in determining the image quality of the intensifier is the blurring induced by the photocathode. The velocity with which the photons are emitted from the photocathode depends on the difference between the energy threshold of the photoelectric emission for the material and the actual energy of the absorbed photon. Moreover, the electrons are emitted in random directions. Consequently, the velocity of the electrons contains an axial as well as a transverse component. The emitted electrons are then accelerated towards the phosphor screen by a large potential difference. However since the electric field is applied along the axial direction, this field has no effect on the transverse component of the electron velocity, thus causing divergence and blurring.

The spread of the electrons is directly proportional to the transverse velocity and inversely proportional to the time of flight from the photocathode to the phosphor screen. Since the transverse velocity component is decided by the energy of the incoming radiation, the only variable that can be controlled is the time of flight. The time of flight can be reduced in two ways - by increasing the acceleration potential, and by minimizing the distance between the photocathode and the anode. Decreasing the cathode-anode separation leads to a class of intensifiers called proximity focussed intensifiers. However, there is a limit to what the minimum spacing and the maximum acceleration potential can be. The smaller the distance the higher the electric field is and one runs the risk of high-voltage breakdown. Typically, the electric field should not exceed 5kV/mm.

In addition to proximity focussing, electrostatically focused and magnetically focused intensifiers are also available. The electrostatically focused systems use electric

fields to actively control the path taken by the emitted electron, while magnetically focused systems use a combination of electric and magnetic fields to achieve the same result. The magnetic systems offer the highest resolutions but the need for large focusing magnets or solenoid coils is a major drawback of these systems.

c. Micro-channel Plate (MCP)

A micro-channel plate (MCP) as the name suggests is an electrical device made up of millions of very thin glass channels bundled in parallel and sliced in form of a disk. Typical channel diameters are 6μm - 10μm and have a length to diameter ratio between 40 and 100. Fig. 5 illustrates the construction and the working of the MCP. Each of the channel acts as an independent electron multiplier. The channel matrix is constructed from semi-conducting glass and treated in a way so as to optimize secondary electron emission and to allow charge replenishment from an external voltage source. Parallel electrical contact to each channel is provided by deposition of metallic coating on the front and the rear surfaces of the MCP, which then serve as the electrodes. When an electron, emitted by the photocathode, enters the MCP and hits the channel wall, secondary electrons are produced. These secondary electrons are then accelerated by the voltage applied across the MCP along their parabolic trajectories to strike the opposite wall where additional electrons are generated. This process is repeated many times along the channel walls and as a result, a large number of electrons are output from the MCP leading to an increased gain.

The gain of a single MCP stage can be as high as 10^4 and multiple MCPs can be stacked to provide gains up to 10^7. When the MCP is used in high gain scenarios, the electrons striking the channel walls towards the end of the channel can cause the generation of positive ions. This leads to a phenomenon called ion feedback, wherein the positive ions are attracted to the front end of the MCP. If the ions strike

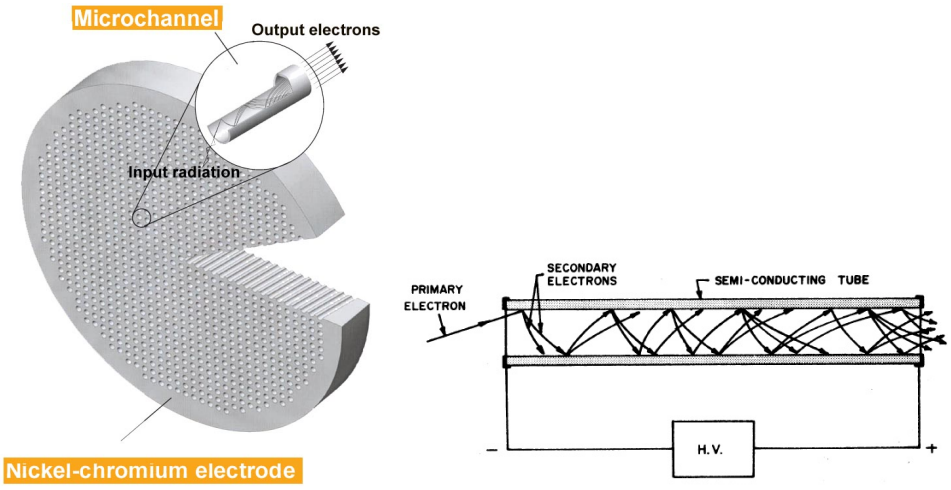

(a) MCP (b) Operation of the MCP

Fig. 5. A cut away view of the MCP and generation of secondary electrons along the channel

the front end of the MCP, secondary electrons will be released again which appear as noise in the output of the MCP. To prevent the ion travel, the channels in the MCP are biased by giving a slight tilt (about 8°) with the horizontal. Curved MCPs are also constructed to alleviate this problem. The curved shape prevents the heavy positive ions from traveling up the channel while still allowing the lighter electrons to flow down the channel. Curved MCPs can be used at gains as high as 10^7 without significant ion-feedback problems.

d. Phosphor Anode

An image intensifier uses a phosphor screen at the output window to covert the multiplied photoelectrons back to photons. Typically the phosphor is coated directly on the surface of the output window by using a sedimentation process, to yield a homogenous layer structure 3-4 grains thick. Several types of phosphor screens (Table III) are available and there are three criteria that determine the selection of the

Table III. Characteristics of various phosphor screens

Type	Light Emission				Decay Time	
	Range		Maximum	Color	Decay of light intensity	
	from	to	Typically at		from 90% to 10%	from 10% to 1%
P43	360 nm	680 nm	545 nm	green	1 ms	1.6 ms
P46	490 nm	620 nm	530 nm	yellow green	300 ns	90μs
P47	370 nm	480 nm	400 nm	blue white	100 ns	2.9μs
P20	470 nm	670 nm	550 nm	yellow green	4 ms	55 ms
P11	400 nm	550 nm	450 nm	blue	3 ms	37 ms

phosphor for a particular application

- **Efficiency**: The efficiency of the screen is defined as the ratio of the optical power emitted by the screen to the input electrical power of the accelerated electrons. Efficiency depends not only on the type of the material used for the screen construction but also on parameters like grain size, layer thickness, presence of aluminum layer and the thermal processing involved.

- **Emission Spectrum**: Depending upon the material used, the photons emitted from the screen lie within a spectral range. The selection of the emission wavelength is dictated by the sensitivity of the imaging detector at that wavelength. For example, in the case of the hand-held night-vision device with the detector being the human eye, the best suited wavelength is 530nm i.e. green wavelength. This is because the sensitivity of the eye peaks in the green wavelength region. Fig. 6 shows the spectral emission characteristics of the available

phosphor screen materials [10].

- **Luminescence Decay Time**: The activated phosphor screen continues to emit photons even when there are no more electrons impinging its surface. The time taken by the phosphor screen output to reduce to 1% of its fully activated output is termed as the decay time. When the phosphor screen is used with an imaging sensor (CCD or CMOS), a phosphor screen with a short decay time is recommended so that no residual energy is captured in the next image. For night-time visual observation, a phosphor with large decay time is recommended so as to reduce the screen flicker. Fig. 7 shows the decay time of the available phosphor screen materials [11].

e. Gated Operation

With the development of the MCP, it is possible to use the intensifier as an optical shutter by varying the potential between the photocathode and the MCP. When the photocathode potential is lower than the MCP potential, the electrons emitted from the photocathode are attracted by this potential difference towards the MCP and multiplication takes place. Usually, in the gated mode, the intensifier is normally OFF and is switched ON by the application of a negative pulse, of about 200V, that is generated by a pulse generator (Fig. 8). When the gate is OFF however, the photocathode is at a higher potential (reverse-biased) than the MCP, so the electrons emitted by the cathode are forced to return back to the cathode and do not reach the MCP.

The width (time) of the pulse determines the time for which the gate is turned ON. The gate function is very useful when capturing high-speed optical phenomenon while excluding extraneous signals. Moreover, the gate can also function as a shut-off

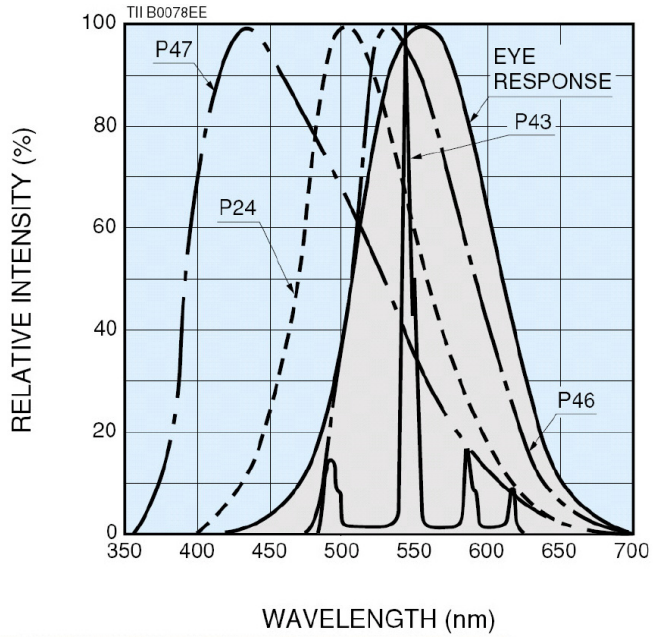

(a) Spectral Emission Profiles

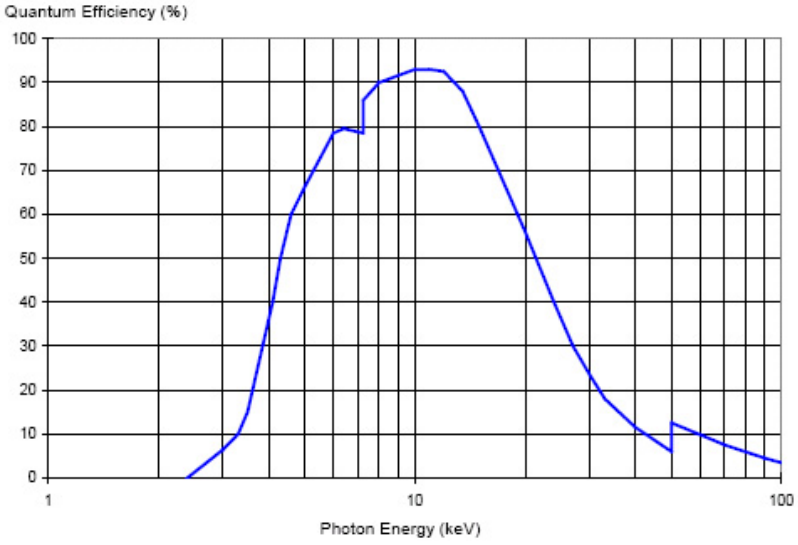

(b) P43 Phosphor Quantum Efficiency

Fig. 6. Spectral emission characteristics of available phosphor screens and quantum efficiency of the most commonly used phosphor - P43

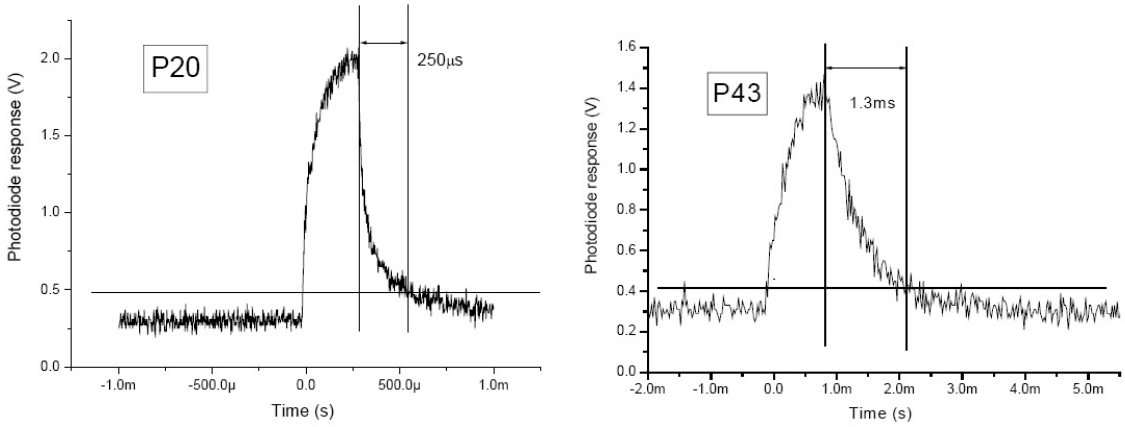

(a) P20 Phosphor (b) P43 Phosphor

Fig. 7. Luminescence decay profiles for P20 and P43 phosphor screens

mechanism when very high energy radiation is detected, for example: the moon or the sun in the field of view.

2. Image Intensifiers Types - Historical Development

Image intensifiers are classified based on their level of maturity in design and resolution. The earliest intensifier, called Generation Zero, was an infra-red image converter. An electromagnetically focused device, now known as Generation 1/2 device, was developed for night-vision, aerial and high-speed photography. A high light level resolution of 45line-pairs per millimeter(lp/mm) and a luminous gain of about 10^5 was achievable using such a device.

Fig. 9(a) shows a Generation I intensifier that was developed for the military for light-weight passive night vision telescopes. The Gen.I device was electrostatically focused and the photocathode was usually an alkali resulting in a 400nm - 500nm spectral response. These devices had a typical gain of 20 to 100 and a resolution of about 36 lp/mm [12]. Further developments in the late 1960s through the mid 1970s resulted in the development of the Generation II intensifier (Fig. 9(b)) that

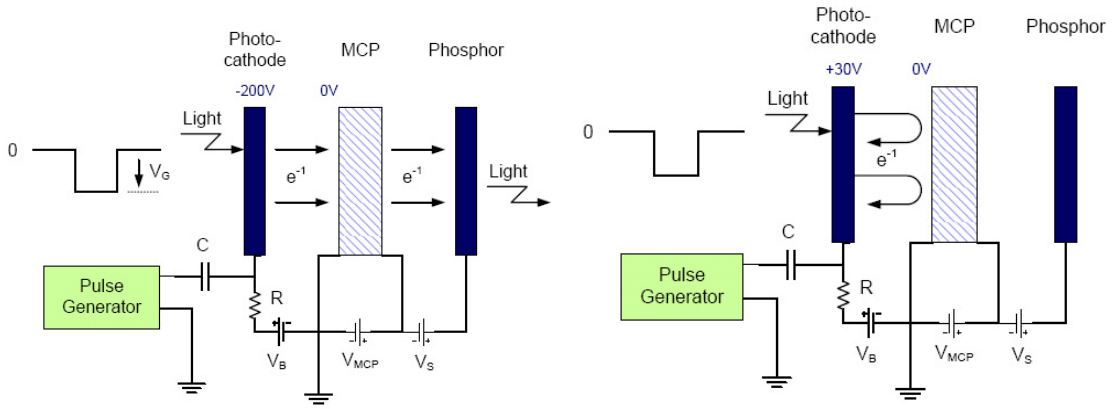

(a) Gate ON (b) Gate OFF

Fig. 8. Schematics of the gate operation

utilized a multi-alkali photocathode and a micro-channel plate for secondary electron generation.

The late 1970s and 1980s led to the development of the Generation III image intensifiers. The Gen.III (Fig. 9(c)) is very similar to the Gen.II but for the highly sensitive GaAs/GaAsP photocathode and a ion-barrier coated MCP. Using the new photocathode material, the spectral response can now be extended into the infra-red region. Several versions of the Gen.III are currently available that have been tailored for spectral wavelengths of interest. For example, the Gen.III extended blue has a Cs-Te photocathode that enables imaging in the VUV band and blocking of all visible light.

C. Imaging Sensors

The photons emitted by the intensifiers are captured by interfacing solid state imaging sensors in the focal plane. Charge coupled devices (CCDs) and complementary metal oxide semi-conductors actie pixel sensor(CMOS-APS) detectors are the two main technologies in use today. CCDs have been in use since 1970s while the CMOS

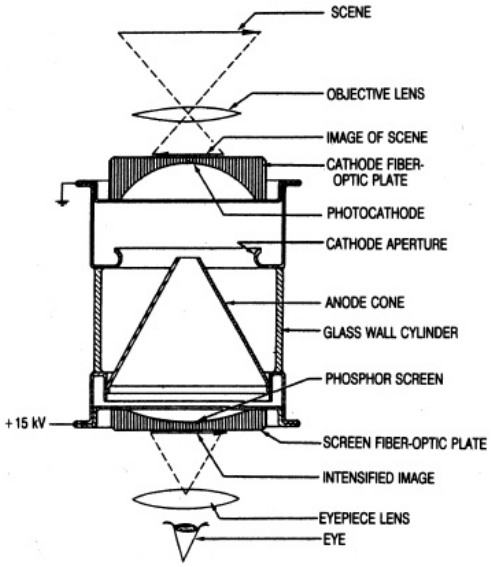

(a) Gen.I

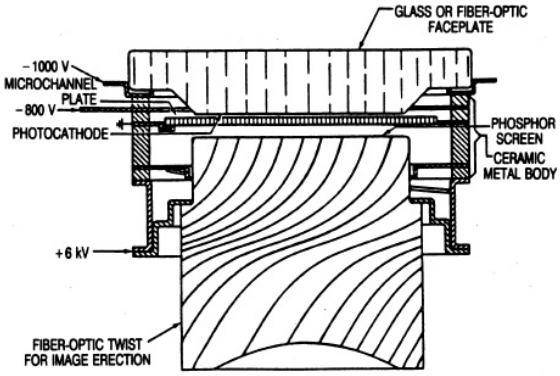

(b) Gen.II

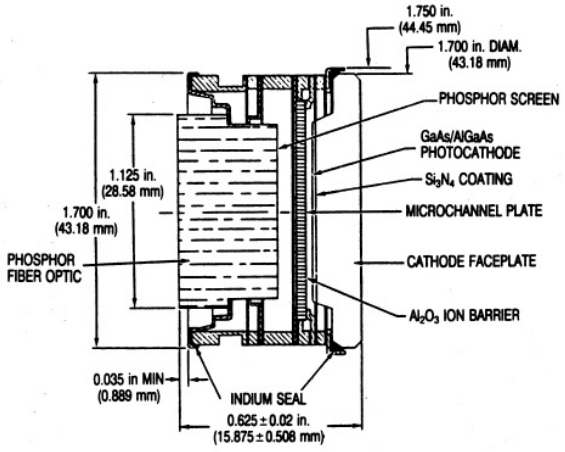

(c) Gen.III

Fig. 9. Examples of various generations of image intensifiers

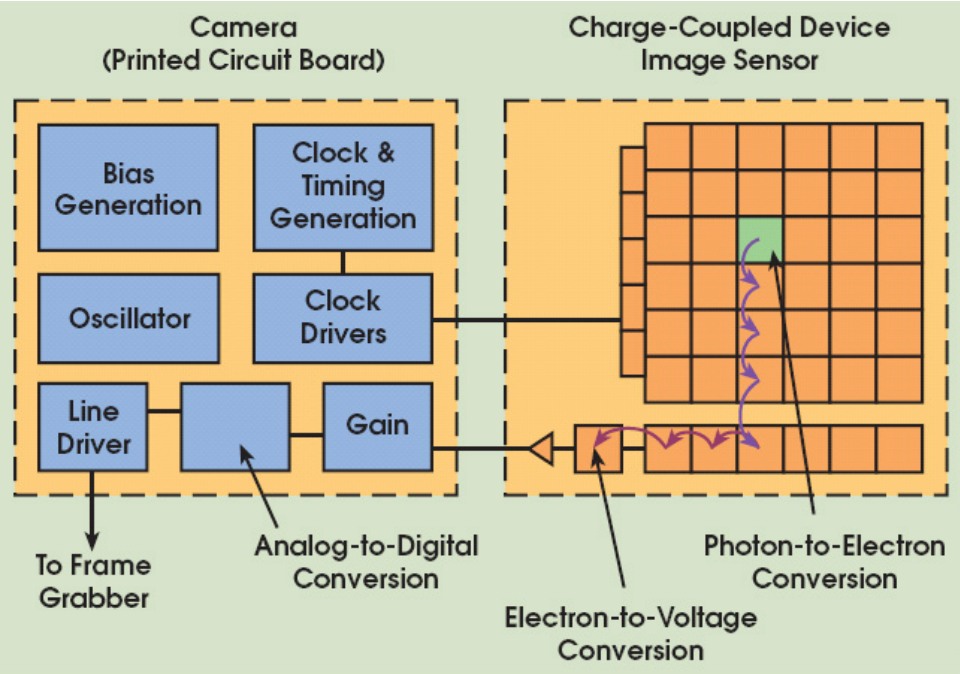

Fig. 10. CCD architecture and readout

sensors are only about a decade old and are trying to take over the imaging market. Each of the devices works on the same principle of charge generation due to incident radiation on a silicon substrate. Each technology has its own unique strength and weakness and thus its use is dependent on the application.

1. CCD

The charge generated in each pixel is transported to the readout node by the application of multiple clock pulses to the horizontal (serial) and vertical (parallel) shift registers (Fig. 10). At the node, the charge is converted to a voltage level, buffered and sent to an off-chip location for analog-to-digital conversion (ADC). Special bias generation and clock driver circuits are used to the generated the multitude of clock pulses and voltage levels required to drive the CCD.

In order to reduce smear due to serial transfer of the charge, additional storage

area is provided on-chip. In the interline CCDs, the optically active rows are interlaced with optically in-active charge storage regions. At the end of the integration time, with the application of single vertical transfer pulse, all the contents of the active regions are simultaneously transferred to the storage region and read out serially. In the frame transfer CCD, the storage area is identical to the active 2D array and the entire frame (all rows and all columns) are transferred instantaneously to this region, where they are readout serially. The presence of optically dead regions adjacent to the pixel leads to a decrease in the light gathering capability of the pixel. To overcome this problem, micro-lenses are fabricated directly on the surface of the pixel to increase the effective area for light collection [13].

2. CMOS Active Pixel Sensor

As compared to the CCDs that require serial transfer of collected charge by application of several phases of clock levels, the CMOS pixel contains a local amplifier and read-out circuitry at each pixel (Fig. 11). This gives the CMOS sensor a memory-like readout addressability i.e. each pixel can be individually activated and imaged. Moreover, the CMOS sensor is like a "system-on-chip" and contains an on-board analog to digital converter, thus providing a digital interface to the outside world. This drastically reduces the overall system complexity. Also, the sensor operates on a single low level (+5V) voltage supply and on a single clock leading to a tremendous decrease in the power consumption.

3. CCD - CMOS Comparisons

The performance of the two imaging technologies can be characterized with the use of several indices such as

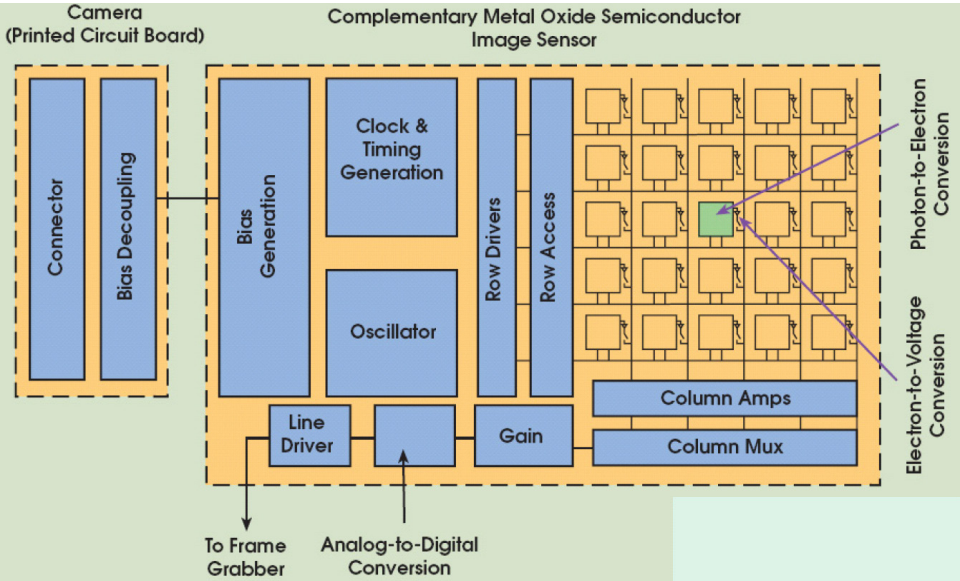

Fig. 11. CMOS architecture and readout

- **Charge Generation**: Charge generation refers to the ability of the sensor to intercept incoming photos and generate signal electrons through the photoelectric effect. This can be characterized by a parameter called Quantum Efficiency (QE). Mathematically, it is defined as the ratio of the number of photo-generated electrons captured by a pixel to the number of photons incident upon the pixel. An ideal sensor would have a QE of 100%. However, losses due to reflection, transmission and absorption cause the QE to fall. Fig. 12 shows the typical losses that occur during charge generation. The absorption loss is caused due to the presence of regions located above and within the pixel that are insensitive to light. CMOS arrays suffer from higher absorption losses than their CCD counterparts because the transistors implemented in each pixel for readout are optically inactive. Each pixel requires three other transistors for readout and thus the light sensitive area is only about 25% of the entire pixel. Also, the memory-like arrangement of the CMOS pixels requires several metal

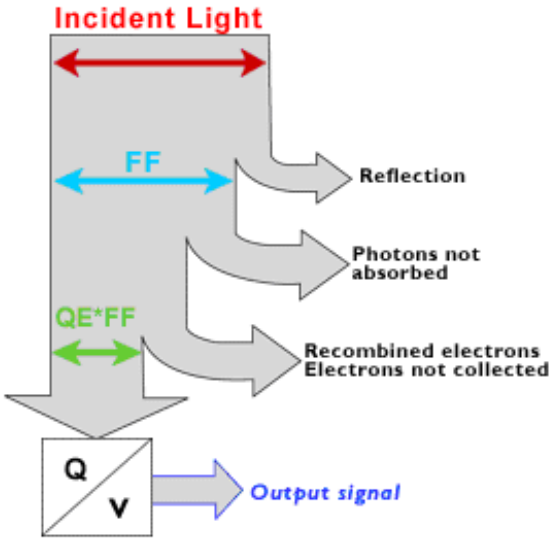

Fig. 12. Losses in photon absorption

interconnect layers that are stacked and interleaved above the pixel. Thus the incoming photons have to pass through a narrow optical tunnel. This problem is somewhat mitigated by the fabrication of micro-lenses above the pixel that help direct light into the sensitive region of the pixel. The wavelength dependence of these losses causes the QE to be non-uniform on the sensor spectral range.

An incoming photon can be converted to an ehp (electron-hole pair) if its diffusion length is smaller than the depletion region depth of the pixel. Since CCDs work at higher voltage levels, the depletion region extends for a larger distance than the region in CMOS. Thus, the CCDs are able to generate more ehp's for a given photon flux than the CMOS devices. All these factors result in the CCD devices having a higher QE than CMOS sensors. Some CCDs have a QE $> 70\%$, but virtually no CMOS detectors have a QE $> 45\%$. A sensor with a higher QE will be more sensitive to incident radiation and thus ideal for low light imaging. However, a low detector QE can be compensated by an increase

in the aperture of the image intensified system.

- **Dark Current**: The background signal present in the sensor when no light is incident on the device is termed as the dark signal. This is the result of thermally generated electrons in the depletion region, bulk region and Si/SiO2 interface. The magnitude of the dark signal depends on the sensor architecture and increases exponentially with increase in the operating temperature of the device. Localized effects in the silicon cause the dark signal to vary from pixel to pixel. The average current associated with the readout of an entire dark image is called the dark current. A CMOS pixel contains onboard readout transistors that contribute in increasing the dark current of the device. In contrast, CCD devices such as the Sony SuperHAD sensors have extremely low dark current. The dark current can be reduced by cooling the detectors to a low temperature. Peltier coolers, TEC devices are thus commonly used with scientific CCDs.

- **Dynamic Range**: Dynamic range is the ratio of the maximum output signal, or the saturation level, of an image sensor to the dark noise level of the imager. The dynamic range is directly related to the full well capacity of the pixel. A larger well capacity implies a larger dynamic range at the same dark noise level. This means that the sensor will be able to capture very bright and very dark objects in the same frame with greater clarity. Although, the full well capacity of the CMOS sensors is only slightly less than a typical CCD, CCDs offer a much higher dynamic range due to the much lower dark noise levels.

- **Charge Collection**: Charge collection refers to the ability of the sensor to accurately reproduce an image after the electrons are generated. The parameters that govern this process are - number of pixels, full well capacity of the pixel, variation in sensitivity from pixel to pixel and charge collection efficiency

(crosstalk). A larger number of pixels implies larger resolution and both CMOS and CCD sensors fair equally well in this aspect. CCD devices have larger full well capacities as compared to CMOS since they are driven by larger voltage levels. Pixel-to-pixel sensitivity non-uniformity or fixed pattern noise (FPN) is almost identical in both the cases since it is decided by the fabrication precision.

Ideally, all the photo-generated electrons in a single pixel should remain in the same pixel. However, due to weak electric fields, thermal diffusion can cause the electrons to wander into the neighboring pixels. This causes a "crosstalk" between neighboring pixels and leads to the image to appear out of focus. The amount of crosstalk is inversely proportional to the pixel size and thus is more pronounced in sensors with smaller pixel areas. CCD manufacturers use high resistivity silicon and high voltage clocking in order to increase the depth to which the electric field exists inside a pixel. On the other hand, CMOS arrays perform more poorly in this regard.

Table IV shows a qualitative comparison of the CCDs and CMOS sensors [14, 15]. Further, points to note are that since the CMOS detectors are based on the metal-oxide semiconductor technology, they are therefore more inexpensive to manufacture and are inherently more radiation tolerant as compared to the CCDs, further strengthening their advantage for space applications.

D. Intensifier to Imager Coupling

The photons emitted by the phosphor screen have to be captured and transferred to the CCD/CMOS sensor for imaging. Two most commonly used devices used for doing so are - relay lens and fiber optic tapers. The most important metric for choosing between the two methods is the coupling efficiency - which can be defined

Table IV. Qualitative comparison between the CCD and CMOS-APS sensors

	CCD	CMOS
Signal out of pixel	electron packet	voltage
Signal out of chip	voltage (analog)	digital bits
Fill factor	high	moderate to low
Amplifier mismatch	n/a	moderate
System complexity	high	low
Sensor complexity	low	high
Manufacturing cost	moderate to high	low
Dark current	low	moderate to high
Responsivity	moderate	slightly better
Dynamic range	high	moderate
Radiation tolerance	poor	moderate to high
Uniformity	high	low to moderate
Speed	moderate	high
Windowing	limited	extensive
Anti-blooming	required	in-built
Biasing and clocking	multiple, high voltages	single, low voltage
Power Consumption	high	low

as the ratio of the optical power relayed to the detector to the net power emitted by the source. The coupling efficiency is dependent on the solid angle over which the emission occurs and the acceptance solid angle of the transmitting optic. In order to achieve maximum coupling efficiency, the acceptance solid angle must be at-least equal to the emission solid angle. It is a well known fact that the emission of photons from the phosphor screen is Lambertian in nature i.e. intensity of the emitted light is equal in all directions. This implies that the emission solid angle is approximately πradians.

1. Relay Lens

A relay lens is a compound lens consisting of two lenses with opposed infinite conjugates. The first lens (called the collimator) is used to collimate the divergent beam of light emitted from the source into a parallel beam. For this purpose, the lens is placed so that the phosphor screen is at the focal point of the collimator. The second lens (camera lens) focuses the parallel beam onto the detector placed at its focus.

One of the main advantages of using a relay lens is that the camera system can be used both as an intensified camera and a regular camera by simply removing the intensifier and the relay lens. However, the Lambertian nature of the emitted light results in losses of the emitted radiation since not all the light is captured by the lens (Fig. 13(a)). Although the loss in light can be overcome by increasing the gain of the MCP, operating the MCP at a higher gain setting implies a significantly reduced image intensifier life span. Moreover, using a lens coupling increases the stray light in the system and can pose serious problems to imaging of faint light sources. The maximum coupling efficiency that can be achieved by using a relay lens is only about $5\% - 10\%$.

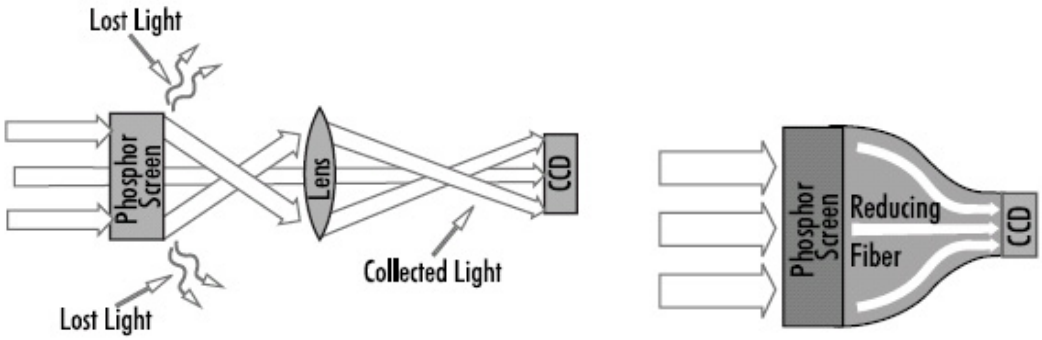

(a) Relay lens losses (b) Fiber-optic coupling

Fig. 13. Intensifier to imager coupling mechanisms

2. Fiber Optic Coupling

A fiber optic taper is made up of millions of fibers, each of which is around 6μm in diameter, fused together to create an image transfer tube. A non-unity magnification ratio is also possible by using fiber optic bundles with different input and output diameters. The numerical aperture (NA) of the fiber indicates the acceptance angle of the fiber. Light that is incident within this angle will be guided through the fiber by the process of total internal reflection. The numerical aperture of the fiber is dependent only on the refractive indices of the materials used in its construction. A fiber with an NA of 1.0 can accept light whose incidence angle is less than or equal to $\pm 90°$. Thus, it is a perfect match for capturing the Lambertian distribution of the phosphor emitted photons. Furthermore, the flat surfaces of its ends allow for easy attachment to the intensifier output window and the imager (Fig. 14).

Several factors determine the coupling efficiency of a fiber optic taper bundle - numerical aperture of the fiber, angular distribution of the incident light, bulk absorption coefficients of the fiber materials, imperfections in the fiber core, and the quality of the taper to imager interface to name a few. In a properly fabricated fiber-optic coupled intensifier, the coupling efficiency can be as high as 70% [16]. With the

Fig. 14. An fiber optic taper bundle attached to an imager

increased coupling efficiency, it is not possible to operate the intensifier at much lower gains, thus prolonging its life. However, the assembly process can be cumbersome and requires a sophisticated setup. Since the fiber taper is held in contact with the output window of the intensifier and the imaging sensor, any tilt at the interface will result in a gap which contributes heavily to interface losses. Additionally, the gap also causes the propagated light to spread (increased blur). In order to account for the surface roughness at the microscopic levels, a polymer based gel or glue with a matching refractive index is applied at the interfaces and cured using a UV curing station at the specified power setting.

In summary, although the fiber optic coupled intensifiers are harder to assemble and are not reconfigurable, they deliver the highest sensitivity at low light levels while reducing noise and increasing the life expectancy for the expensive intensifier tubes. They are thus, highly preferred over the known designs for relay lens mechanisms.

E. Concluding Remarks

In this chapter we discussed the design of a very high update rate star tracker. This was made possible by optimizing the use of state-of-the-art image intensification tech-

nology and fiber optics for high efficiency coupling. The components making up the intensifier - photocathode, MCP and phosphor screen were discussed in detail. The photocathode material can be selected in such a way so as to tune its spectral response to the spectral content of the radiation to be detected. The gain of the intensifier can be varied by changing the voltage applied to the secondary electron multiplier (MCP). Moreover, high speed phenomenon can be easily captured while keeping the noise level small by gating the MCP. Two techniques for coupling the phosphor emission to the image sensor were discussed. The fiber optic taper was selected owing to its high coupling efficiency and compactness. These elements have been integrated into a novel intensified camera design that represents a significant advance in the sensors available for attitude determination. In essence, this dissertation presents the features of this design, develops models to analyze and predict its performance, develops algorithms for processing the output optimally and finally, presents results from night-sky experiments with the first prototype.

In the next chapter we shall concentrate on the developing the optical model of the intensified camera system. This will help us better understand the optical response and characterize performance of the system when imaging point sources such as stars.

CHAPTER III

ELECTRO-OPTICAL MODELING AND IMAGE SIMULATOR DESIGN

The performance of an electro-optical imaging system, such as the intensified camera system, can be mainly characterized by two metrics - signal to noise ratio (SNR) and the optical resolving power of the system. The SNR provides the most important measure of the quality of the numerical response values that are output from the camera. The optical resolution indicates the fine feature resolving capability of the sensor i.e. the smallest feature in the scene that be faithfully reproduced by the system. In order to estimate these metrics however, it is essential to develop a mathematical and/or empirical model that represents the actual behavior of the system. For a complex system, such as the one considered here, it is wise to apply a "divide and conquer" policy, in which the system is broken down into its constituent sub-systems. Standard modeling techniques can then be easily applied to many of these sub-systems, and these sub-system models can be coupled to model the overall system.

The objective of this chapter is to develop the sub-system models that permit the evaluation of the system's performance. These models will be generic and useful for performance prediction and system design studies. We begin by a noise analysis of the system. Several sources of noise, internal and external to the system are considered. The SNR of the overall system is then estimated and comparisons are made against the non-intensified system. Next the optical model of the complete system is generated by determining the point spread functions of each of the components. Using linear system theory, the component transfer functions of the sub-systems are combined to yield a system transfer function. Based upon the findings, a high fidelity image simulator is then designed which given any pointing direction of the star sensor can

re-create the scene visible to the imaging system. The simulator is vital to the design, development and validation of the entire hardware-software system since it provides a mechanism to generate almost realistic images that can be used as inputs to the image processing algorithms. End-to-end design iterations can be accomplished, and results from experiments with the prototype can be evaluated more confidently.

A. Noise Characterization

Noise is defined as any unwanted disturbance that corrupts a signal. It can get added to the signal at any stage of its existence - at the signal generator, while it's transmission through the channel or during its detection at the receiver. The sources of the noise could be internal(system electronics, transducers, detectors etc) or external(ambient). Noise can be mainly classified into two types: systematic and random. Systematic noise adds an effective bias to the ideal signal levels and can be removed if the bias is known or can be estimated. Random noise, on the other hand, cannot be deterministically compensated since only statistical information such as mean, variance, power spectral density can be estimated. Additionally, the random noise can be spatially and temporally variable. Henceforth, in all our discussions, the term noise will imply the random noise component only.

The ability of an electro-optical system to detect and distinguish a valid signal is primarily dependent on the signal to noise ratio(SNR). Obviously, higher the SNR, the higher the probability of a valid detection. Needless to say, all measurement systems try to achieve as high a SNR as possible through optimized hardware design and/or by employing external noise reduction techniques. Mathematically, the SNR is defined as the ratio of the signal power to the noise power i.e.

$$\text{SNR} = \frac{P_{sig}}{P_{noise}} = \left(\frac{A_{sig}}{A_{noise}}\right)^2 \tag{3.1}$$

where P is the average power and A is the root-mean-square(rms) amplitude. Noise in an imaging system can arise from many sources. Irrespective of its source, the end result of the addition of noise is a variation in the image intensity. In electro-optical imaging systems, the SNR is usually calculated as the ratio of the mean of the pixel values to the standard deviation of the pixel value.

1. Sources of Noise

In an imaging system, the incident photons are converted by the detector into photoelectrons which are then collected in a potential well. These collected charges are then converted to voltage levels, amplified, readout and converted to a digital signal. Each stage of conversion and processing adds noise to the detected signal as shown in Fig. 15 [6].

a. Shot Noise

Shot noise arises due to the statistical fluctuations in the arrival time of the discrete photons. This noise is inherent to the measurement and cannot be removed by any means possible. The noise is proportional to the intensity of the signal itself. Shot noise being a Poisson process ideally follows Poisson statistics - the variance is equal to the mean. Thus, the contribution to the overall noise is given by

$$\langle n_{shot}^2 \rangle = \langle n_{PE}^2 \rangle = n_{PE} \tag{3.2}$$

where $\langle n_{\cdot}^2 \rangle$ denotes the variance i.e. the second statistical moment about the mean and n_{PE} is the number of photoelectrons generated in the pixel. In CCD's the number of photoelectrons generated should be multiplied by a factor indicating the charge transfer efficiency during the readout. But since the charge transfer efficiency is usually very close to 1, this factor has been ignored in the above equation.

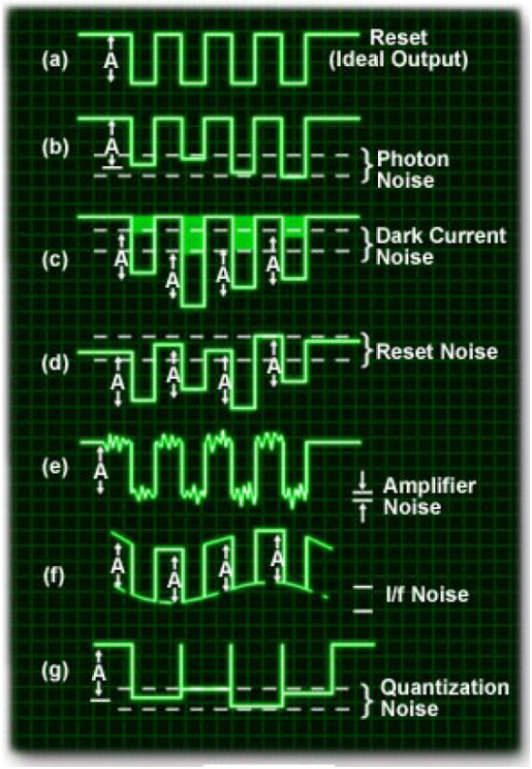

Fig. 15. Various sources of noise for an imaging system

b. Dark Current

When a photon impacts the semi-conductor pixel, it dissipates energy which leads to the formation of photoelectron-hole pairs(ehp's). In an ideal situation, the ehp's would be generated only due to the incoming photon. Unfortunately however, ehp's are also generated due to the thermal effects in the depletion regions, bulk material and the surface states. The number of thermally generated ehp's depends on the operating temperature, integration time, the area of the pixel and is modeled as [17]

$$n_{dark} = \frac{J_D A_D t_{int}}{q} \tag{3.3}$$

where A_D is the area of the pixel detector, t_{int} is the integration time of the frame, q is the charge of an electron ($1.6 \times 10^{-19} coloumb$) and J_D is the dark current density and is subject to the proportionality

$$J_D \propto T^2 e^{-\frac{\alpha}{k_B T}} \tag{3.4}$$

where T is the absolute temperature, α is constant that depends on the semiconductor energy bandgaps and k_B is the Boltzmann constant. The dark current density approximately doubles for every $8 - 9°C$ rise in temperature. Thus in order to reduce the dark current noise, the detector is usually cooled to around $-20°C$ by using Peltier devices such thermo-electric coolers or by using liquid nitrogen.

c. Reset Noise

The charge collected at each pixel is converted to a voltage level by a sensing node capacitor circuit. The noise associated with the resetting of this capacitor is termed as the reset noise. The reset noise can be significantly reduced by using correlated double sampling [17].

d. Pattern Noise

Pattern noise arises due to the variations in the pixels in the imaging array since each pixel has a slightly different construction geometry and responsivity. The variation in the dark current across the pixels when no light is incident on the imager is termed fixed pattern noise (FPN). The FPN is input signal independent and is additive to the other noise powers. Photo-response non-uniformity (PRNU), on the other hand, occurs due to the variation in the responsivity of the pixels and is illumination dependent. Thus, it is usually characterized by a multiplicative factor of the generated photoelectrons [17].

Since the dark current can be drastically reduced by cooling of the array, FPN is usually negligible and PRNU dominates the pattern noise. If U is the factor expressing non-uniformity of the pixels then,

$$\langle n_{pattern} \rangle \approx \langle n_{PRNU} \rangle = U n_{PE} \tag{3.5}$$

e. Other Sources of Noise

The voltage corresponding to the pixel charge is amplified by a series of on-chip (and off-chip for CCDs) amplifiers. The amplifier noise is usually specified by the manufacturer as readout noise, noise equivalent electrons or noise floor. Digitization of the analog signal by an analog to digital convertor adds quantization noise due to the discrete output levels.

For a majority of applications, it is sufficient to consider only a subset of all the sources of noise - shot noise, dark noise, noise floor and PRNU. The total system

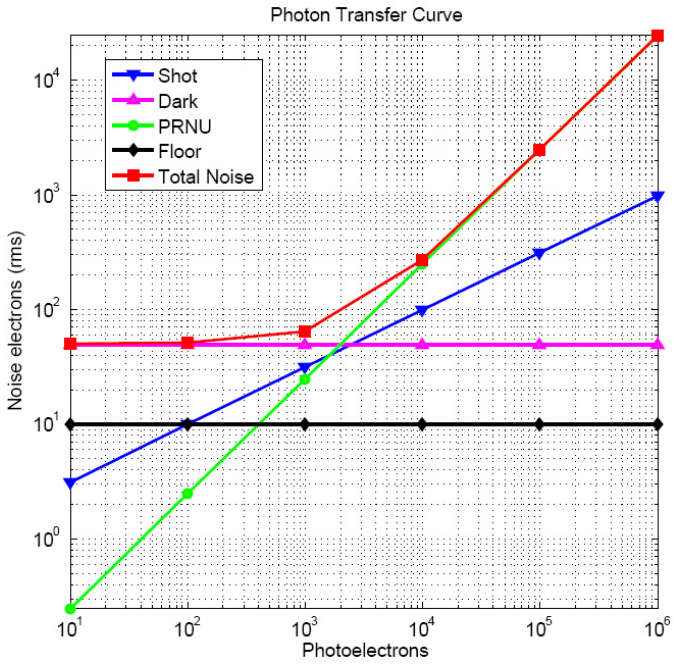

Fig. 16. Photon transfer curve for dark current dominated shot noise

noise is

$$\langle n_{sys} \rangle = \sqrt{\langle n_{shot}^2 \rangle + \langle n_{dark}^2 \rangle + \langle n_{floor}^2 \rangle + \langle n_{PRNU}^2 \rangle} \tag{3.6}$$

$$= \sqrt{\langle n_{PE} \rangle + \langle n_{dark}^2 \rangle + \langle n_{floor}^2 \rangle + (U\langle n_{PE} \rangle)^2} \tag{3.7}$$

Fig. 16 shows the plot of the noise as a function of the signal levels. In this analysis, U was set to 2.5%, the dark noise was 50electrons and the noise floor was 10 electrons. As can be seen, for very low photon fluxes, the dark noise along with the noise floor dominates. As the signal strength is increased, the photon shot noise and PRNU begin to dominate while at very high illumination levels, the PRNU dominates.

Having determined expressions for the various noise sources, the SNR for the imaging system is given by

$$\text{SNR} = \frac{n_{PE}}{\sqrt{\langle n_{PE} \rangle + \langle n_{dark}^2 \rangle + \langle n_{floor}^2 \rangle + (U\langle n_{PE} \rangle)^2}} \tag{3.8}$$

2. Image Intensifier Noise

The inclusion of an image intensifier in the electro-optical train, further adds noise to the system. The photocathode converts the incident photons into photoelectrons and thus has a photon shot noise as well as a dark current component. As in the case of CCD/CMOS sensors, the photocathode can be cooled to reduce the dark current. The noise due to the cathode is given by [17]

$$\langle n^2_{PC-shot} \rangle = \langle n^2_{cathode} \rangle + \langle n^2_{PC-dark} \rangle \tag{3.9}$$

The photoelectrons are multiplied by the MCP channels which provide a gain G_{MCP}. Consequently, the noise is also amplified as

$$\langle n^2_{MCP} \rangle = k_{MCP} G^2_{MCP} \langle n^2_{PC-shot} \rangle \tag{3.10}$$

where the constant k_{MCP} is called as the SNR degradation due to the MCP and is usually taken as 1.8. The amplified electrons are then converted back to photons by the phosphor screen with an efficiency of η_{screen}. The transformed noise is thus

$$\langle n^2_{screen} \rangle = \eta^2_{screen} \langle n^2_{MCP} \rangle \tag{3.11}$$

The emitted photons are transmitted through the fiber optic taper bundle. If T_{fot} represents a factor that represents the transmissivity of the fiber taper along with the coupling efficiency, then noise is attenuated as

$$\langle n^2_{fot-out} \rangle = T^2_{fo} \langle n^2_{screen} \rangle \tag{3.12}$$

The photons are then incident on the imaging sensor (CCD or CMOS) which converts them to photoelectrons and adds noise corresponding to the sensor design. If η_{sen} represents the mean quantum efficiency of the imaging sensor, then the sensor noise

is given by

$$\langle n_{sen}^2 \rangle = \eta_{sen}^2 \langle n_{fot-out}^2 \rangle + \langle n_{sen-dark}^2 \rangle + \langle n_{floor}^2 \rangle + \langle n_{PRNU}^2 \rangle \tag{3.13}$$

Using Eq.3.12 in the above equation, the total noise of the intensified camera system is given by

$$\langle n_{sen}^2 \rangle = \eta_{sen}^2 T_{fo}^2 \eta_{screen}^2 k_{MCP} G_{MCP}^2 \langle n_{PC-shot}^2 \rangle + \langle n_{sen-dark}^2 \rangle + \langle n_{floor}^2 \rangle + \langle n_{PRNU}^2 \rangle \tag{3.14}$$

3. Image Intensifier Signal

The number of photoelectrons generated by the photocathode is given by the application of the camera formula [17]

$$n_{cathode} = \frac{\eta_{cathode} M_q(\lambda_0) \Delta\lambda}{4F^2} t_{int} T_{optics} A_{pixel} \tag{3.15}$$

where $\eta_{cathode}$ is the mean quantum efficiency of the cathode, λ_0 is the center wavelength of the cathode spectral responsivity, $\Delta\lambda$ is the spectral bandwidth of the cathode, $M_q(\lambda_0)$ is the spectral photon radiance due to the source given in $\frac{\text{photons}}{s - \mu m - m^2}$. The optics are assumed to have a transmissivity of T_{optics}, F is the f-number of the lens system and A_{pixel} is the projected area of the pixel onto the photocathode. After passing through the MCP, phosphor screen and the fiber taper, the number of emitted photons is given by

$$n_{photon-sen} = T_{fo} \eta_{screen} G_{MCP} n_{cathode} \tag{3.16}$$

The number of electrons generated by the imaging sensor is then given by

$$\begin{aligned} n_{sen} &= \eta_{sen} n_{photon-sen} \\ \text{i.e.} \quad n_{sen} &= \eta_{sen} T_{fo} \eta_{screen} G_{MCP} \frac{\eta_{cathode} M_q(\lambda_0) \Delta\lambda}{4F^2} t_{int} T_{optics} A_{pixel} \end{aligned} \tag{3.17}$$

4. Image Intensified Camera SNR

The SNR of the image intensified camera system is given by the ratio

$$\text{SNR} = \frac{\eta_{sen} T_{fo} \eta_{screen} G_{MCP} n_{cathode}}{\sqrt{\eta_{sen}^2 T_{fo}^2 \eta_{screen}^2 k_{MCP} G_{MCP}^2 \langle n_{PC-shot}^2 \rangle + \langle n_{sen-dark}^2 \rangle + \langle n_{floor}^2 \rangle + \langle n_{PRNU}^2 \rangle}} \tag{3.18}$$

High Gain: High gain ($> 10,000$) is used for photon counting applications. Under such conditions the intensifier noise is a lot greater than the sensor noise. Eq.3.18 then reduces to

$$\text{SNR} = \frac{n_{cathode}}{\sqrt{k_{MCP} \left[\langle n_{cathode}^2 \rangle + \langle n_{PC-dark}^2 \rangle \right]}} \tag{3.19}$$

From the above equation it can be seen that the SNR is independent of gain and sensor characteristics. If the photocathode is cooled, then the dark current is almost negligible. The SNR then becomes

$$\text{SNR} = \sqrt{\frac{n_{cathode}}{k_{MCP}}} \tag{3.20}$$

In order to get a high SNR in this case, a high photocathode quantum efficiency, large integration times and large pixel geometries are required.

Moderate Gain: In this scenario, the image intensifier noise is less than that of the sensor noise. The SNR then becomes

$$\text{SNR} = \frac{\eta_{sen} T_{fo} \eta_{screen} G_{MCP} n_{cathode}}{\sqrt{\langle n_{sen-dark}^2 \rangle + \langle n_{floor}^2 \rangle + \langle n_{PRNU}^2 \rangle}} \tag{3.21}$$

For a non-intensified camera system, $n_{cathode} = n_{PE}$ and the SNR is given by

$$\text{SNR} = \frac{n_{PE}}{\sqrt{\langle n_{sen-dark}^2 \rangle + \langle n_{floor}^2 \rangle + \langle n_{PRNU}^2 \rangle}} \tag{3.22}$$

Comparing this with the above equation and noting that all other factors except

the gain are less than unity, the SNR of the intensified camera system is lower than that of the non-intensified camera. Using the above two equations, the ratio of the SNR of the intensified system SNR_{IIC} to that of the non-intensified SNR_C can be written as

$$\frac{SNR_{IIC}}{SNR_C} = T_{fo}\eta_{screen}G_{MCP}\eta_{cathode} \tag{3.23}$$

A Gen3 image intensifier with GaAs photocathode has a peak quantum efficiency of about 0.45 at $575nm$ [10]. The efficiency of a P43 phosphor screen is about 0.5 (conservative) at the primary emission wavelength of $550nm$ and the fiber optic taper has a transmissivity of 0.3 for a lambertian light source. Combining all these factors, the minimum gain of the MCP required so that the ratio of SNR's is equal to one, is 14.8. The P43 phosphor however, has a large decay time of $1ms$. Using a faster phosphor such as the P24 which has a decay time of $40\mu s$ and an efficiency of about 0.2, causes the gain to increase to 37.1. Thus, if the intensified camera is operated at above this gain, the SNR of the intensified system will be higher than that of the non-intensified system. Additionally, a major advantage of using the intensifier at moderate gains is the ability to gate the incoming photons temporally without the need for a mechanical shutter.

5. Gain Model of the Image Intensifier

The micro-channel plate in the intensifier is the primary module responsible for amplification in the number of photo-electrons. The multiplication of photo-electrons occurs due to an avalanche effect as they strike the walls of the channel. The application of the MCP voltage V_{MCP} and the electron generation leads to a small bias current in the MCP which sets an upper limit to the dynamic range of the MCP.

A single stage MCP usually has bias current densities on the order of $1\mu A/cm^2$ and gains ranging up to 10^4. It has been found, using theory and experimentation [18], that the gain of the MCP G_{MCP} is related to the operating voltage of the MCP by

$$G_{MCP} = \left(\frac{V_{MCP}}{V_c}\right)^g \tag{3.24}$$

where, g is an exponential gain factor that is typically $8.5 - 13$ and V_c is the crossover voltage for the channel i.e. the applied MCP voltage at which the gain is exactly unity (typically $350 - 530V$).

B. Linear System Theory Applied to Imaging Systems

Let $f(x, y, z)$ represent an object in the spatial domain. If the resolution of the imaging system is independent of the distance to the object, as is in the case of imaging objects at infinite conjugates, then the object can be treated as a planar i.e. 2D distribution. Note that the function $f(x, y)$ could represent the object as a wave field or intensity or irradiance distribution.

An imaging system provides a single valued mapping of the object to the $2 - D$ output $g(x, y)$. For incoherent light, the imaging system is linear in intensity of the incident light [17]. An ideal imaging system thus possesses two properties:

1. **Linearity:** If the input object $f_1(x, y)$ results in the output object $g_1(x, y)$ and an input object $f_2(x, y)$ results in output $g_2(x, y)$, then the linear combination of the two inputs $af_1(x, y) + bf_2(x, y)$ when passed through the linear imaging system results in the output $ag_1(x, y) + bg_2(x, y)$

2. **Shift Invariance:** A system is shift invariant if a shift in the position of the input causes a proportional shift in the position of the output i.e. if $f(x, y)$ yields the output image $g(x, y)$, then the shifted input image $f(x - x_0, y - y_0)$

results in a shifted output image $g(x - m_x x_0, y - m_y y_0)$, where $m_x\, m_y$ account for the magnification.

Note that the above properties are valid for an ideal imaging system only - i.e. a system with no defects or aberrations. Although, an imaging system can never be free of aberrations, for the purpose of the development of the main features of imaging theory, the aberrations can be neglected.

All linear shift invariant (LSIV) systems can be characterized by transfer functions [19]. Let $f(x, y) = \delta(x, y)$ be a Dirac delta function provided as the input to the LSIV system. Then the output of the system $g(x, y)$ is called the impulse response function or the point source function of the LSIV system. Let g_0 be the volume covered by the point source function i.e.

$$g_0 = \int\int g(x, y)dxdy \tag{3.25}$$

Then the point spread function (psf) is defined as

$$\text{psf} = \frac{g(x, y)}{g_0} \tag{3.26}$$

The input image can be decomposed into a collection of point sources at each spatial location. If $f(x, y)$ represents an array of such sources, then the output can be obtained by summing the contributions of the resulting point source response functions i.e.

$$\begin{aligned} g(x, y) &= \int\int f(x', y')\, a(x - x', y - y')\, dx'dy' \\ &= g_0 \int\int f(x', y')\, psf(x - x', y - y')\, dx'dy' \\ &= g_0 \left[f(x, y) \otimes psf(x, y)\right] \end{aligned} \tag{3.27}$$

where $\otimes$ represents the 2D convolution operator. Let $\mathcal{F}$ represent the 2D Fourier

transform operator. The 2D Fourier transform of a 2D function $f(x, y)$ is given by

$$\begin{aligned} F(u, v) &\equiv \mathcal{F}[f(x, y)] \\ &= \int\int f(x, y) \exp(-j2\pi(ux + vy))dxdy \end{aligned} \tag{3.28}$$

where (u, v) represent the spatial frequencies in the frequency domain.

Taking the 2D Fourier transform of Eq.3.27 and using the property that convolution in spatial domain is equivalent to multiplication in the frequency domain, we get

$$G(u, v) = PSF(u, v)F(u, v) \tag{3.29}$$

The Fourier transform of the point spread function is called as the Optical Transfer Function (OTF) of the system i.e.

$$OTF(u, v) = \int\int psf(x, y) \exp(-j2\pi(ux + vy))dxdy \tag{3.30}$$

The OTF of the system plays a key role in the design and optimization of the optical system. The OTF is in general a complex valued function and can thus be decomposed into its magnitude and phase. The modulation transfer function (MTF) represents the magnitude of the OTF while the phase transfer function represents the phase of the complex valued OTF. In the absence of aberrations, the OTF is real-valued and positive so that the OTF and MTF are equal. In general,

$$OTF(u, v) = MTF(u, v)e^{jPTF(u,v)} \tag{3.31}$$

The OTF i.e. MTF and PTF alter the signal content as it passes through the system. The phase information is primarily responsible for the relative spatial positioning within the image. Thus, for LSIV systems, the PTF simply indicates a spatial shift with respect to arbitrary origin. The MTF is a measure of how well the system

can reproduce the input signal and thus indicates the highest resolvable frequency of the imaging system. If the input signal is above the cutoff frequency, then the output will be proportional to the inputs average signal value and the frequency content will be lost. An image with significant MTF degradation will still be recognizable, however, if the phase information is degraded, then the image will be destroyed.

For an imaging system composed of several components, each of the component is characterized by its own transfer function. The OTF of the entire system is then described by the product of the individual transfer functions i.e.

$$OTF_{sys} = \prod_{i}^{N} OTF_i(u, v) \tag{3.32}$$

C. Optical Response of the Intensified Camera System

The image intensified camera system (IIC) consists of a lens system, image intensifier, fiber optic taper and finally the image sensor. At each stage, the optical resolution is degraded by the MTF of the specific component. The net resolution or MTF of the IIC is given by

$$MTF_{sys}(u, v) = MTF_{lens}(u, v)MTF_{ii}(u, v)MTF_{fot}(u, v)MTF_{sen}(u, v) \tag{3.33}$$

where,

$\text{MTF}_{lens}(u, v)$: MTF of the lens assembly
$\text{MTF}_{ii}(u, v)$: MTF of the image intensifier
$\text{MTF}_{fot}(u, v)$: MTF of the fiber optic taper
$\text{MTF}_{sen}(u, v)$: MTF of the image sensor

In order to estimate the optical response of the entire assembly, it is essential to determine the component MTFs.

1. Lens Assembly

The lens assembly forms a circular aperture to the scene. The primary objective of the lens is to gather light from the sources in its field of view and form their image on the focal plane. The ideal lens can be simply modeled by a circular aperture of diameter D [19]. For a point source located at infinity, the lens would form a point image at its focus. However, diffraction effects cause the irradiance distribution to spread over a finite area.

Let $t(r)$ represent the aperture function, where r is the radial distance. Note that the system exhibits cylindrical symmetry.

$$t(r) = \text{cyl}\left(\frac{r}{D}\right) \tag{3.34}$$

where $cyl(\cdot)$ is the cylinder function given by

$$\text{cyl}\left(\frac{r}{D}\right) = \begin{cases} 1 & \text{if } r \leq D \\ 0 & \text{if } r > D \end{cases} \tag{3.35}$$

The point spread function $psf(r')$ on the focal plane obtained by far-field diffraction analysis is given by,

$$psf(r') = \left[2\frac{J_1(r')}{(r')}\right]^2 \tag{3.36}$$

where, J_1 is the order one Bessel function of the first kind and r' is the dimensionless distance from the optical axis measured in the focal plane given by

$$r' = \frac{\pi r}{\lambda F_{\#}} \tag{3.37}$$

where, $F_{\#} = f/D$ is the F-number of the optical system, λ is the mean wavelength of the light in the visible band. Fig. 17 shows the resultant distribution called Airy pattern.

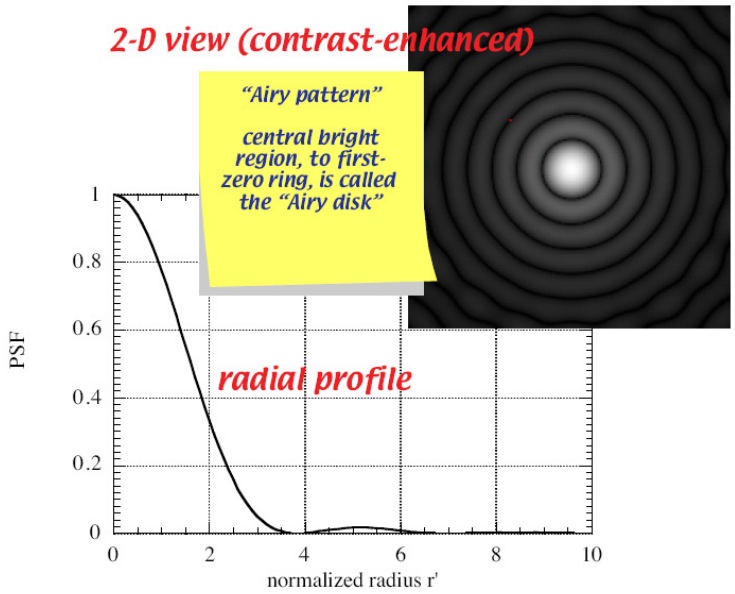

Fig. 17. Airy pattern: Irradiance distribution by a circular aperture

The central bright region is called the Airy disk which has a radius Δ given by the position of the first null as

$$\Delta = 1.22\lambda F_{\#} \tag{3.38}$$

The ideal diffraction limited lens OTF OTF_{diff} is then given by the 2D Fourier transform of the PSF as:

$$OTF_{diff} = \frac{2}{\pi}\left[\cos^{-}1\left(\frac{f_x}{f_{oco}}\right) - \left(\frac{f_x}{f_{oco}}\right)\sqrt{1-\left(\frac{f_x}{f_{oco}}\right)^2}\right] \qquad \text{when} f_x \leq f_{oco} \tag{3.39}$$

where, f_x/f_{oco} is the normalized spatial frequency and f_{oco} is the optical cutoff given by

$$f_{oco} = \frac{D}{\lambda} \tag{3.40}$$

The above equation is valid only for monochromatic light. Using the concept of average wavelength (Holst[20]), the polychromatic MTF can be obtained from the

above equations. Over a small interval of wavelength $[\lambda_1\, \lambda_2]$, the average wavelength λ_{ave} can be written approximately as

$$\lambda_{ave} = \frac{\lambda_1 + \lambda_2}{2} \tag{3.41}$$

At zero spatial frequency, the slope of the MTF_{diff} is $4/\pi$ and a straight line approximation to the MTF_{diff} can be written as

$$MTF_{diff}(f_x) \approx 1 - \frac{4}{\pi}\frac{f_x}{f_{oco}} \tag{3.42}$$

where, the optical cutoff has been calculated using the average wavelength.

a. Aberrations

In an ideal lens, all the rays striking the surface of the lens, converge at the same point in the image plane. Additionally, all wavelengths corresponding to the same point object also focus at the same point. In practice however, this is never the case. The index of refraction of the glass material is dependent on the wavelength. The amount of refraction a ray undergoes also depends on the position i.e. the distance from the optical axis, at which the ray strikes the lens [21]. The departure from the ideal lens behavior is termed as lens aberrations. Usually, design of an optical system, including star cameras, must take care to model and optimize lens aberrations over the wavelength of interest.

Aberrations can be classified as chromatic aberrations - which depend on the wavelength of the light and monochromatic; these exist even for a single wavelength of light. Monochromatic aberrations are the consequence of paraxial assumptions i.e. all the rays are lie very close to the optical axis and make a very small angle with it. For an aperture of finite size and especially large apertures that are used in low-light imaging systems, the cone of rays from the object make large angles with the optical

axis and thus never converge to the same point on the image. This type of aberration is called spherical aberration. The refracted rays converge within a circle of minimum radius, called circle of confusion and diverge again. If the rays are off-axis rays, then the image produced may resemble that of a comet-shaped figure and this aberration is termed as coma.

Astigmatism is another aberration that arises due to the asymmetric distribution of the light rays around the optical axis. In this aberration, objects that emanate rays which strike along the radial direction of lens appear sharper at some distance behind the lens, while at the same distance objects whose rays strike along the tangential direction appear blurred. The situation is reversed at some distance further along the optical axis. The paraxial imaging assumptions also lead to the departure of the image surface from the planar surface. The surface of best focus is thus a curved surface called Petzval surface and the aberration arising because of the flat image plane is termed as Petzval field curvature. Since the image is usually formed on a planar surface such as the film, CCD/CMOS imager, this aberration presents a significant amount of blur and field flatteners are usually employed in the design.

Chromatic aberrations arise due to dispersion i.e. variation of index of refraction with wavelength. Dispersion causes the focal length to be different for different wavelengths, thus polychromatic rays are focussed at different points. Chromatic aberration can be lateral i.e. along the image image or axial i.e along the optical axis. A combination of high and low dispersion is usually used to create an achromatic system.

Thus, in order to overcome these various aberrations, multiple elements of lenses of different materials, dispersion and shape are used. Ray tracing software packages such as ZEMAX, OSLO, CODEV are used to calculate the aberrations and perform optimization with respect to several indices such as MTFs and aberrations. The

aberrations themselves can be characterized by using the wavefront error i.e. the an error indicating the departure of the output wavefront from the aberration free wavefront. Several mathematical formulations such as Seidel coefficients and Zernike polynomials are used to represent the aberrations. Shannon[22] developed an empirical relationship for the OTF in the presence of most common aberrations in terms of the rms wavefront error W_{rms} as

$$OTF_{aberr} \approx 1 - \left(\frac{W_{rms}}{0.18}\right)^2 \left[1 - 4\left(\frac{f_x}{f_{oco}} - \frac{1}{2}\right)^2\right] \qquad \text{when} f_x \leq f_{oco} \tag{3.43}$$

The OTF of the optical system then is given by the combination of the ideal OTF and the OTF due to the aberrations

$$OTF_{lens} \approx OTF_{diff}\, OTF_{aberr} \tag{3.44}$$

A closed form of the expression for the OTF or the MTF of a real lens system with multiple order aberrations is however, very complicated and difficult to obtain. In this discussion, we use the simulation capabilities of the ZEMAX package to arrive at the optical response of a real lens system.

Fig. 18 shows a 2D layout of 3-element aspheric lens design made in ZEMAX. The lens has an effective focal length of $25mm$ and an aperture of $33mm$, thus giving it a $F_{\#}$ of 0.7. This lens is similar to large aperture lenses that are used on low-light imaging devices and which require a large field-of-view.

Fig. 19 and Fig. 20 show the spot diagram and the MTF of the 3-element lens system for rays located at five fields $(0 - 5^{\circ})$. Due to the aberrations present in system, the spot size has increased from the Airy disk size to about $2.9\mu m$ in radius. The MTF plot also shows the aberration free diffraction MTF limit MTF_{diff}. As can be seen clearly, the MTF has been reduced due to the presence of aberrations in the system.

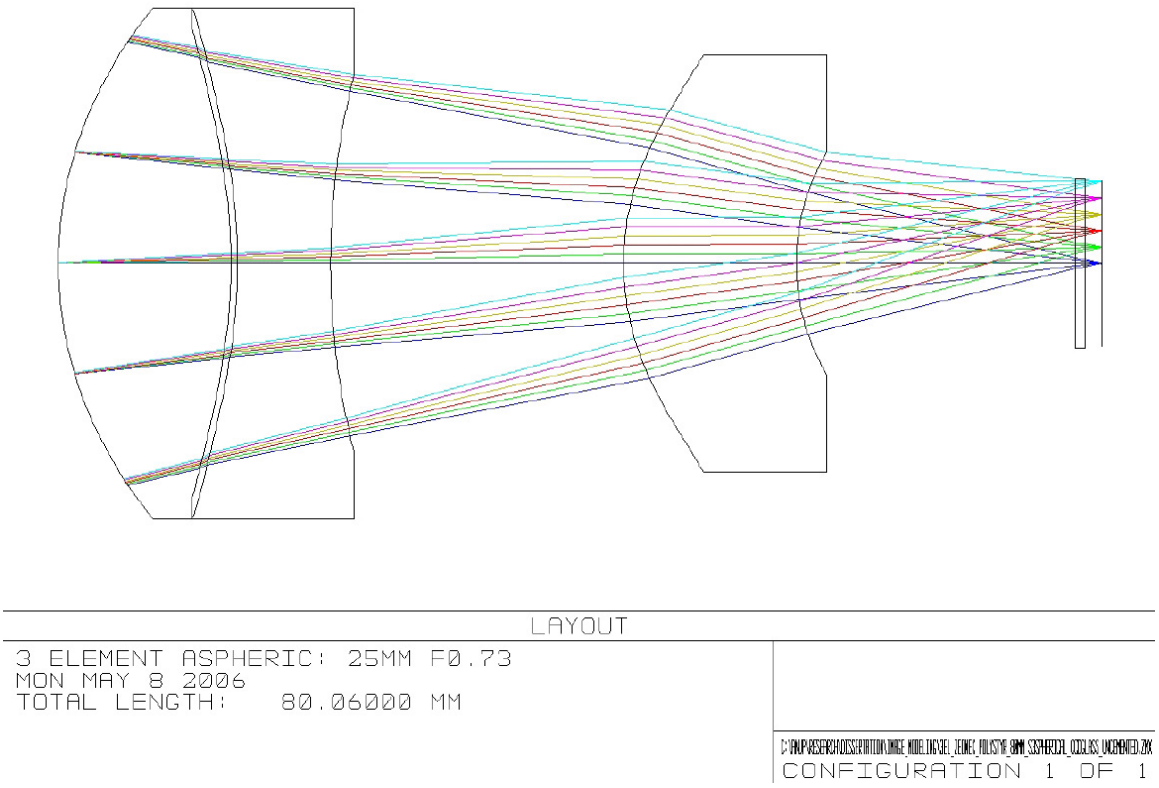

Fig. 18. A 3 element aspheric lens system with focal length of $25mm$ and $F_{\#}$ of 0.73 with five fields

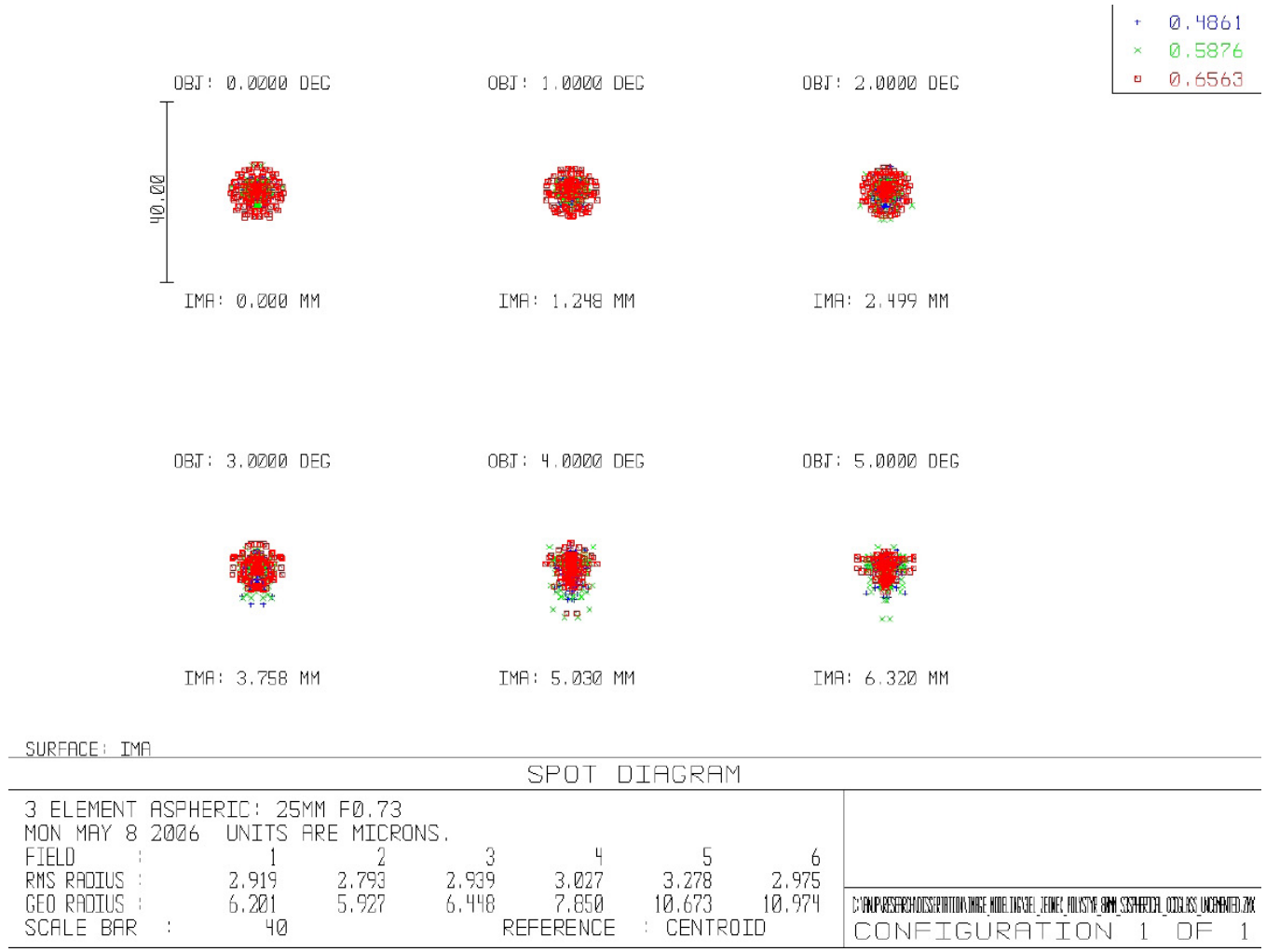

Fig. 19. Spot diagram for the 3-element lens system

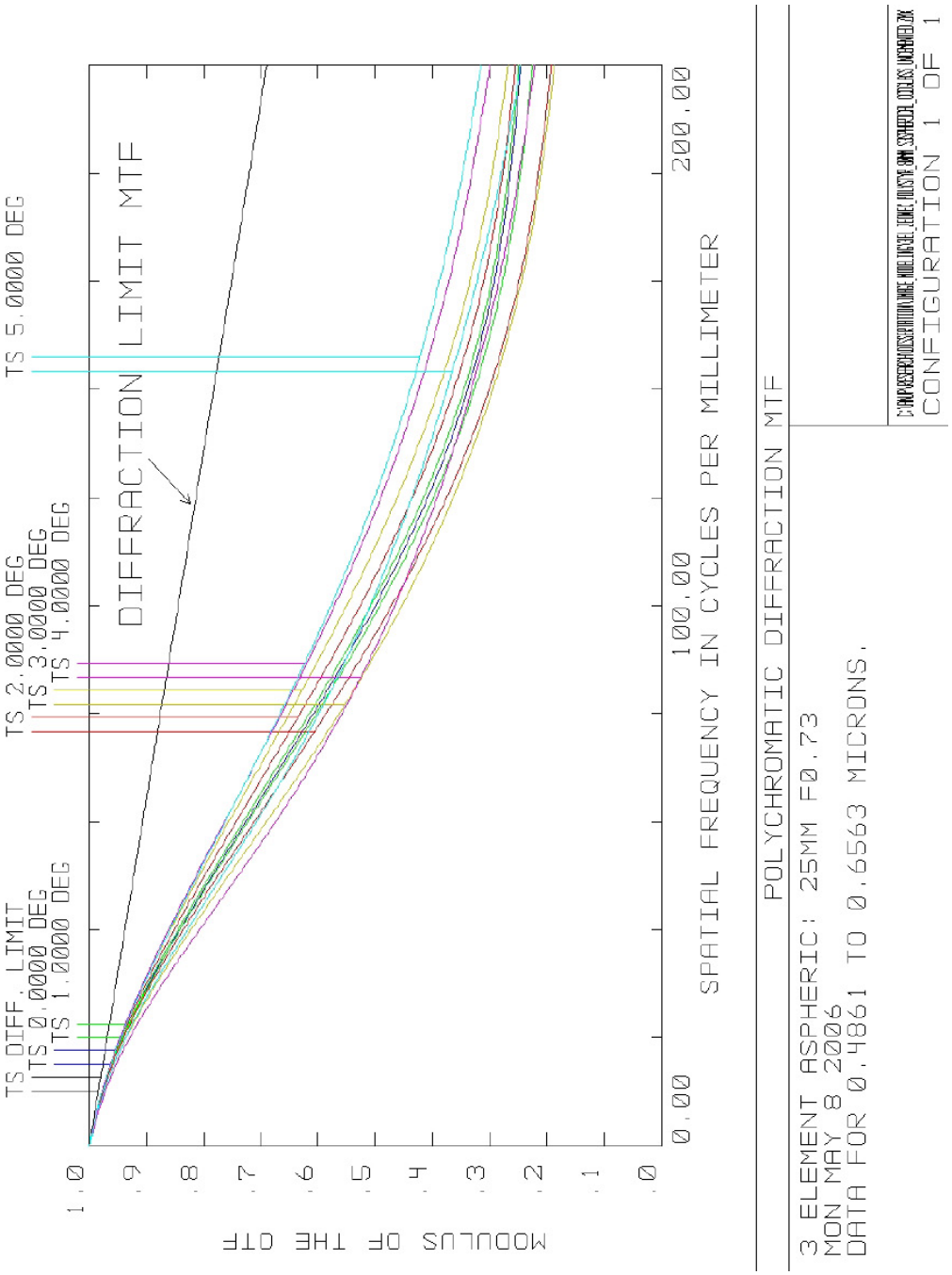

Fig. 20. MTF of the aberrated 3-element lens system

b. Defocused Optics

For a lens with a $F_{\#}$ of 1.0 and mean wavelength of $550nm$, the Airy disk given by Eq.3.38 is only $1.3\mu m$ large which is in the order of 1/10 of a pixel. For imaging point sources such as stars, it is essential to spread the irradiance over multiple pixels so as to estimate the centroid with a higher accuracy. A large spot size can be obtained by increasing the $F_{\#}$ in the above equation. However, an increased $F_{\#}$ implies a reduced aperture and thus diminished light gathering capacity of the optics. Thus, the more efficient way of increasing the spot size is by defocusing. Shifting the focal plane away from the point of best focus, causes the Airy disk to increase in size and ultimately become a uniform circular blur. If δz is the small displacement from the ideal image plane, then the blur diameter of the circle of confusion, is given by

$$C = \frac{\delta z}{F_{\#}} \tag{3.45}$$

The OTF of the defocused optics is then given by

$$OTF_{defocus}(f_x) = \frac{4}{\pi}\int_{f_x/f_{oco}}^{1} \sqrt{1-x^2}\cos\left(a\left[x - \frac{f_x}{f_{oco}}\right]\right)\, dx \tag{3.46}$$

where,

$$a = \frac{\pi f_x}{f_{oco}}\frac{1}{F_{\#}^2\lambda}\delta z \tag{3.47}$$

The lens system OTF can then be approximated by

$$OTF_{lens} \approx OTF_{diff}\, OTF_{aberr}\, OTF_{defocus} \tag{3.48}$$

A simulated ray-trace in the ZEMAX software package on the 3-element lens design can be performed which includes the effect of defocus. In this set of simulations, the image plane was shifted from the paraxial position by $0.3mm$. Doing so resulted in spot sizes being around $10\mu m$ in radius. Fig. 21 shows the MTF of the defocused

and aberrated system. As can be observed from the plots, the MTF has decreased drastically and in-fact phase reversal is evident.

2. Image Intensifier

The image intensifier consists of a glass window with the photo-cathode deposit, the micro-channel plate and the fiber optic output window. The resolution of the intensifier is thus a combination of the MTF's of each of its components. When light rays strike the photocathode, photo-electrons are emitted in a Lambertian distribution and the voltage potential accelerates these electrons towards the MCP. Since the velocity profile of the emitted electrons contains an axial as well as a transverse component which cannot be controlled, spreading of the electron emission is inevitable. In order to reduce the blur, the MCP is placed in close proximity to the photocathode. Thus, the photocathode to MCP separation is a very important parameter which decides the resolution of the image intensifier. Additionally, the MCP pore size and the phosphor screen resolution (fiber size) also affect the intensifier MTF.

Csorba [23] has developed an analytical expression of the point spread function for the proximity focused image intensifier. The derivation is based on photocathode energy emission and current density considerations and is given by

$$psf_{ii}(r) = \frac{1}{\pi\rho^2} \exp\left[-\left(\frac{r}{\rho}\right)^2\right] \tag{3.49}$$

where, ρ is the focussing error coefficient given by

$$\rho = 2L\sqrt{\frac{\epsilon}{V_s}} \tag{3.50}$$

where, L is the phosphor screen to photocathode separation, V_s is the screen voltage and ϵ is the voltage equivalent of the most probable emission energy of the photocathode emission. The MTF of the intensifier is the magnitude of the Fourier transform

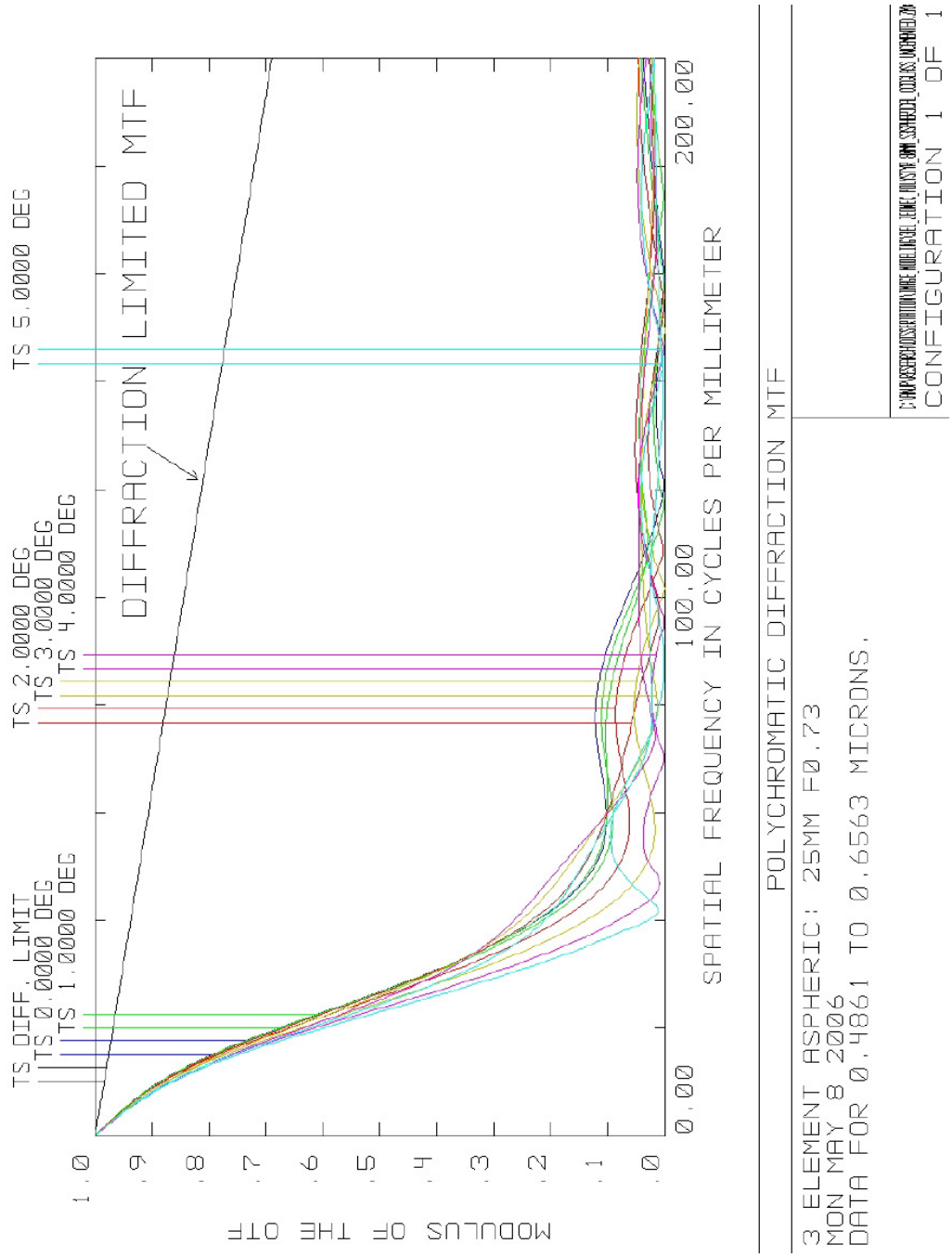

Fig. 21. MTF of the aberrated and defocused 3-element lens system

Table V. MTF for the ITT FS9910 as specified by the manufacturer

Spatial Frequency (lp/mm)	MTF
0	1
2.5	0.83
7.5	0.60
15	0.38
25	0.18
45	0.1

of the psf and is given by

$$MTF_{ii} = \mathcal{F}\left[psf_{ii}(r)\right] = \exp\left(-4\pi^2 \frac{\epsilon}{V_s} L^2 f^2\right) = \exp\left[-\left(\pi\rho f\right)^2\right] \tag{3.51}$$

where, f is the spatial frequency in line-pairs per millimeter (lp/mm). The MTF associated with intensifiers can also be described using another empirical mathematical function derived by Johnson[24]

$$MTF_{ii} = \exp\left[-\left(\frac{f}{f_c}\right)^n\right] \tag{3.52}$$

where, f_c is the frequency constant and n is the MTF index. The MTF index describes the overall shape of the curve and large values of the index are associated with a rapid decrease in the MTF at the frequency constant f_c. The MTF as specified by the manufacturer for the ITT9910 intensifier used in shown in Table V.

Using the specified values, the parameters f_c and n of Eq.3.52 can be estimated by curve fitting. The resultant frequency constant has a value of 15 and 1.01 for the MTF index. Fig. 22 shows the one dimensional curve fitted MTF for the image

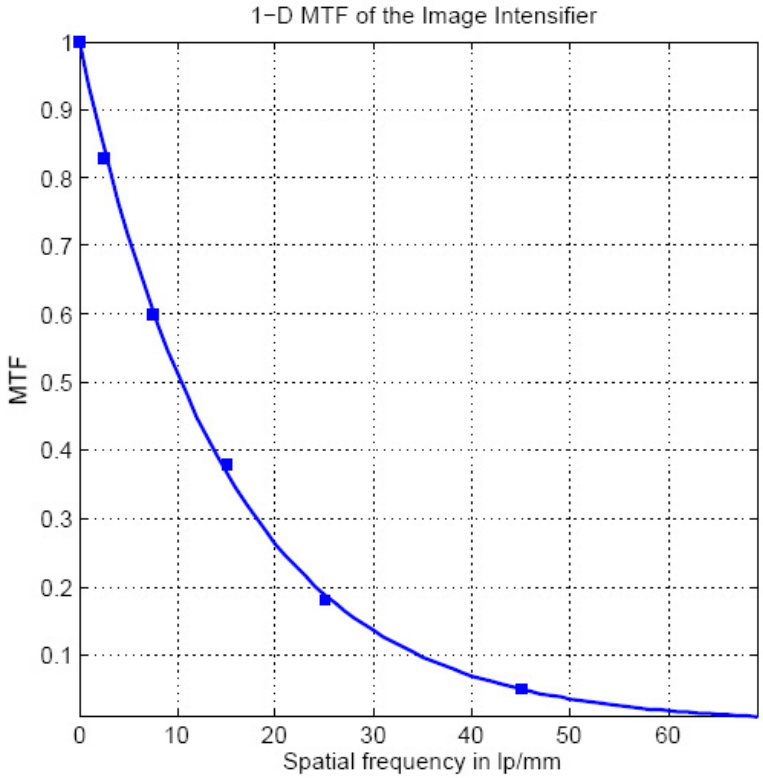

Fig. 22. 1-D MTF of the image intensifier

intensifier.

The 2-D versions of the MTF can be obtained by appropriately sampling the 1D function according to Nyquist limit and then converting the sampled function to polar co-ordinates and rotating it about the z-axis. If N is the number of imaging elements along each direction x and y, and Δx is the spacing between the image elements, then the Nyquist sampling frequency f_{Ny} is equal to $1/2\Delta x$. The sampling interval is assumed to be equal along both the dimensions. The MTF in the polar

co-ordinates r is thus given by following equations:

$$\begin{aligned} R_{scale} &= \frac{N/2}{f_{Ny}} \\ r &= \sqrt{(f_x - N/2)^2 + (f_y - N/2)^2} \\ MTF_{II}(r) &= \exp\left[-\left(\frac{r/R_{scale}}{f_c}\right)\right] \end{aligned} \tag{3.53}$$

Fig. 23 shows the 2D and the 3D MTF obtained from performing the above calculations.

3. Fiber Optic Taper

The fiber optic taper is primarily responsible coupling the intensifier output to the imaging sensor. Since the photon emission from the phosphor screen is Lambertian in nature, high numerical aperture fibers are required on the input side of the taper. The fiber size usually ranges from $6\mu m$ on the input side to about $3\mu m$ at the output. Consequently, the resolution of the taper is decided by the largest fiber size and thus the fiber pitch. The fiber can be mathematically described as a cylinder function, much similar to the lens aperture. The MTF is then given by the Fourier transform of the cylinder function as

$$MTF_{fot}(f) = \mathcal{F}\left[\text{cyl}\left(\frac{r}{d}\right)\right] = 2\left|\frac{J_1(2\pi df)}{2\pi df}\right| \tag{3.54}$$

where d is the fiber pitch and f is the spatial frequency in lp/mm. The fiber optic taper used in this analysis was a $18mm$ input window and $1/3in$ imager compatible taper with fiber size of $6\mu m$ at the input and $3\mu m$ at the output side. Using the above equation, the MTF was calculated and is shown in Fig. 24. The 3-D MTF can also be generated using the same sampling and polar co-ordinate transform as discussed before.

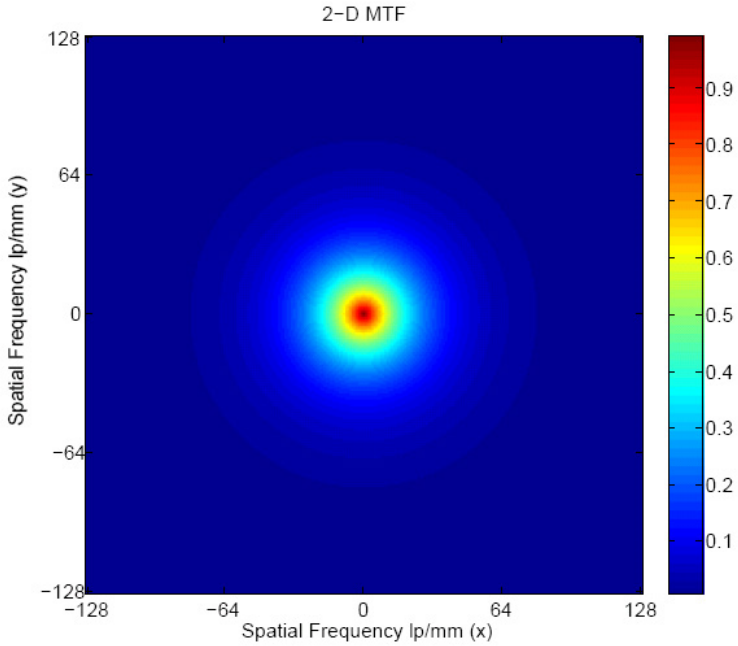

(a) 2D MTF

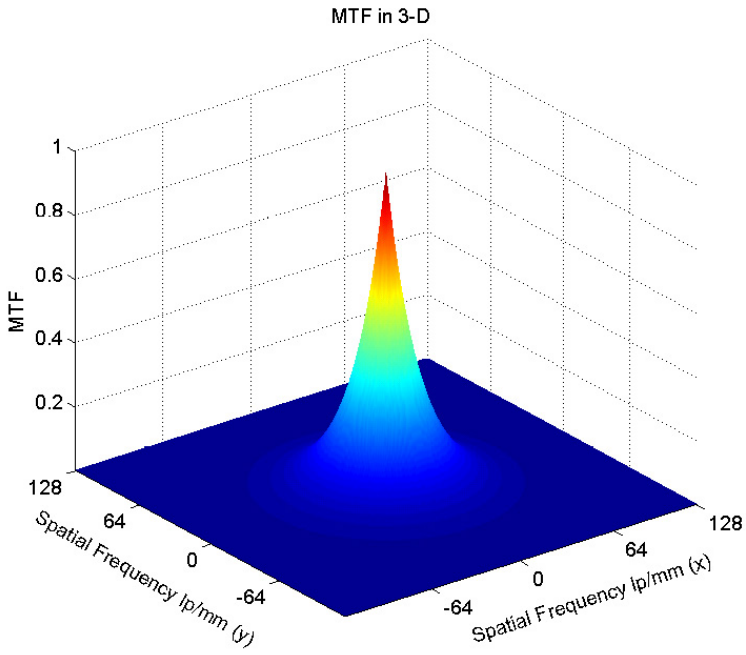

(b) 3D MTF

Fig. 23. The 2-D and 3-D MTFs of the image intensifier

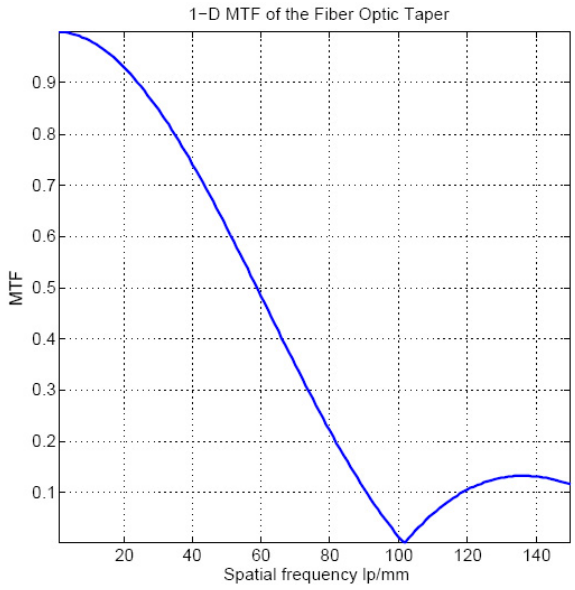

(a) 1D MTF

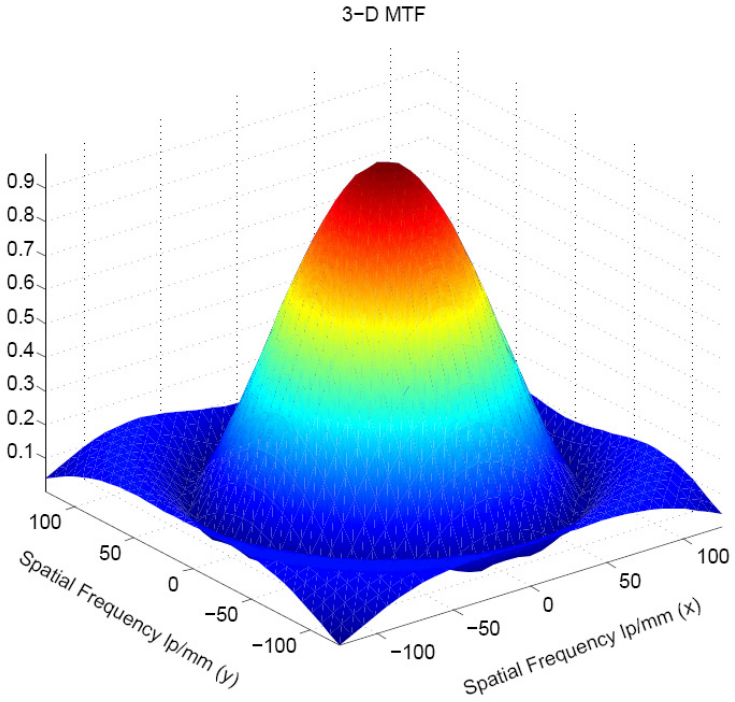

(b) 3D MTF

Fig. 24. The MTFs for the fiber optic taper

4. Imaging Sensor

The imaging sensor is made up of thousands or even millions of two-dimensional imaging elements called pixels arranged in a regular grid. The size of the pixel determines the finest feature detail that can be resolved by the imager i.e. a smaller pixel size implies higher MTF. However, dark current noise, substrate effects and other small electronic noise effects increase with decreasing pixel size thereby causing a drop in the SNR of the sensor. Thus, a compromise between the resolution and SNR is usually sought.

If b, d represent the size of the pixel in the spatial domain along the two directions x and y, then the point spread function of the single pixel is give by the rectangle function

$$\text{rect2D}\left(\frac{x}{b}, \frac{y}{d}\right) = \begin{cases} 1 & \text{if } x \leq b \text{ and } y \leq d \\ 0 & \text{if } x > b \text{ or } y > d \end{cases} \tag{3.55}$$

The image formation process by the sensor involves spatio-temporal integration of the scene viewed by each pixel followed by 2D sampling of this averaged scene. When developing the optical response i.e. resolution of the sensor, it is however, not necessary to be worried about the number, arrangement or integration by the pixel elements. The resolution can be completely determined by analyzing a single pixel. The OTF of the pixel is given by the Fourier transform of the psf i.e.

$$OTF_{sen} = \mathcal{F}\left[\text{rect}\left(\frac{x}{b}, \frac{y}{d}\right)\right] \tag{3.56}$$

and the magnitude of the OTF gives the MTF of the imaging sensor in terms of the 2D sinc function

$$MTF_{sen} = |OTF_{sen}| = \text{sinc}\left(bf_x, df_y\right) = \frac{\sin(\pi f_x b)}{\pi f_x b}\frac{\sin(\pi f_y d)}{\pi f_y d} \tag{3.57}$$

Given the dimensions of the pixels, the maximum spatial frequency that can be

reproduced faithfully by the sensor without aliasing as given by the Nyquist sampling theorem is $1/2b$ in the x-direction and $1/2d$ in the y-direction. Fig. 25 shows the MTF along the two directions for a sensor with pixel size of $5\mu m \times 5\mu m$. If the pixels are of equal dimensions i.e. $b = d$, then the two MTFs are equal. If $b \neq d$, then the MTF along the smaller dimension is greater, implying a higher feature resolving capability along that direction. Fig. 26 illustrates this case. The 3D MTF appears to be stretched along the direction of higher resolution.

a. Fill Factor

Not all of the available area on the sensor die is used actively for imaging. The CMOS imaging sensors contain additional circuits located at each pixel for independent control, analog-to-digital conversion and readout. CCD sensors may contain interlined rows for charge transfer and readout as well. The extra circuitry adds optically dead area to the neighborhood of each pixel, thus increasing the separation or pitch between adjacent pixels. This causes a reduction in the modulation at each spatial frequency by a factor of $\mathrm{sinc}(b/2D)$ along each dimension, where b is the size of the active pixel area along one direction and D is the pixel pitch along the same direction. Fig. 27 shows the decrease in the MTF due to a fillfactor of 75% i.e. a pixel size of $5\mu m$ and a pixel pitch of $6.67\mu m$.

5. The Net System MTF

The net MTF of the intensified camera system can be estimated by the combination of the component MTFs as given by Eq.3.33. Fig. 28 shows the MTF of the complete system. As can be seen clearly, the MTF is limited by the resolution of the intensifier tube. In this case, the modulation is essentially zero for frequencies greater than 40lp/mm.

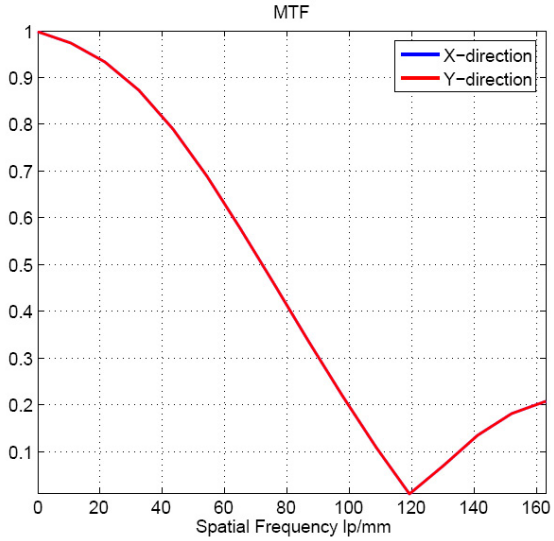

(a) 1D MTFs

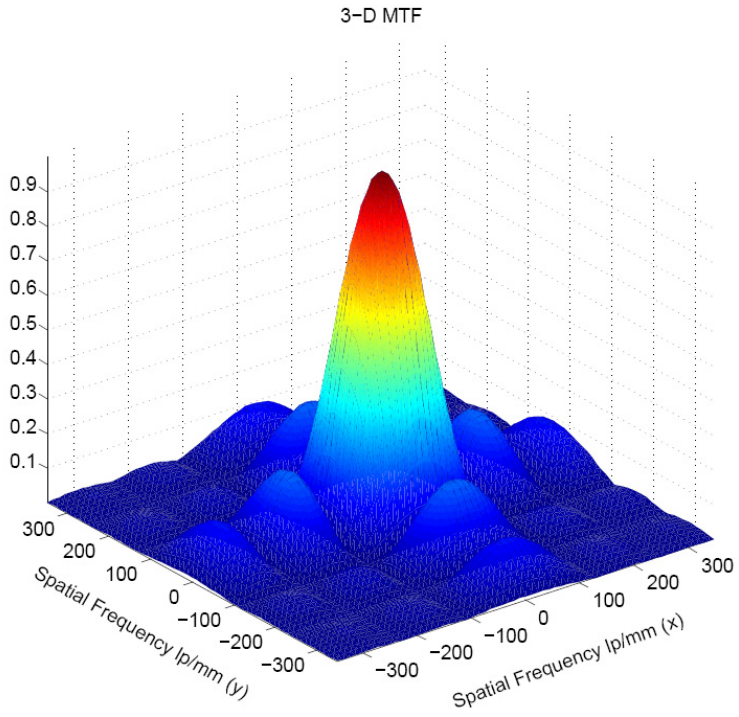

(b) 3D MTF

Fig. 25. MTF of the imaging sensor for square pixels of dimensions $5\mu m$

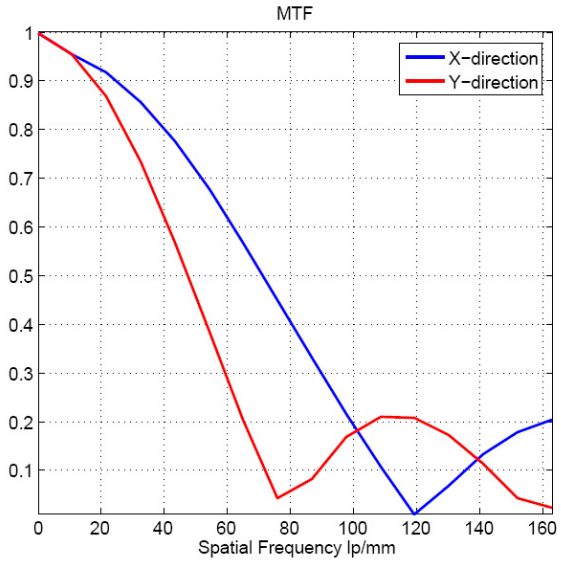

(a) 1D MTFs

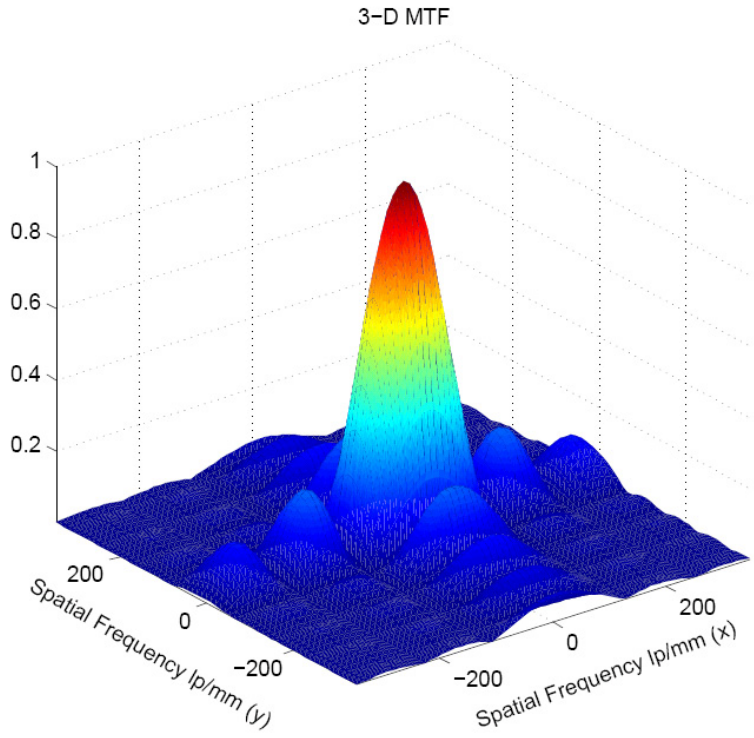

(b) 3D MTF

Fig. 26. MTF of the imaging sensor for rectangular pixels of dimensions $5\mu \times 7.5\mu mm$

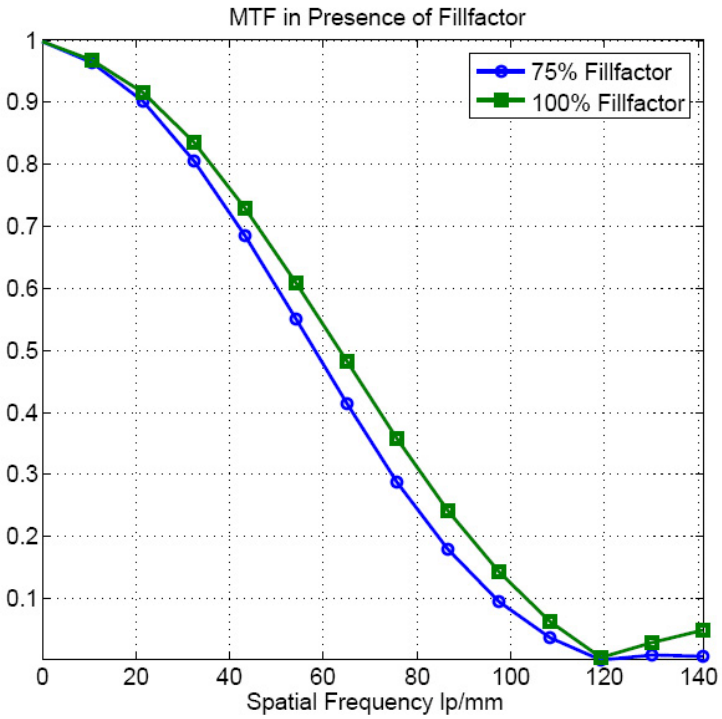

Fig. 27. MTF curves with a 100% fillfactor and a fillfactor of 75%

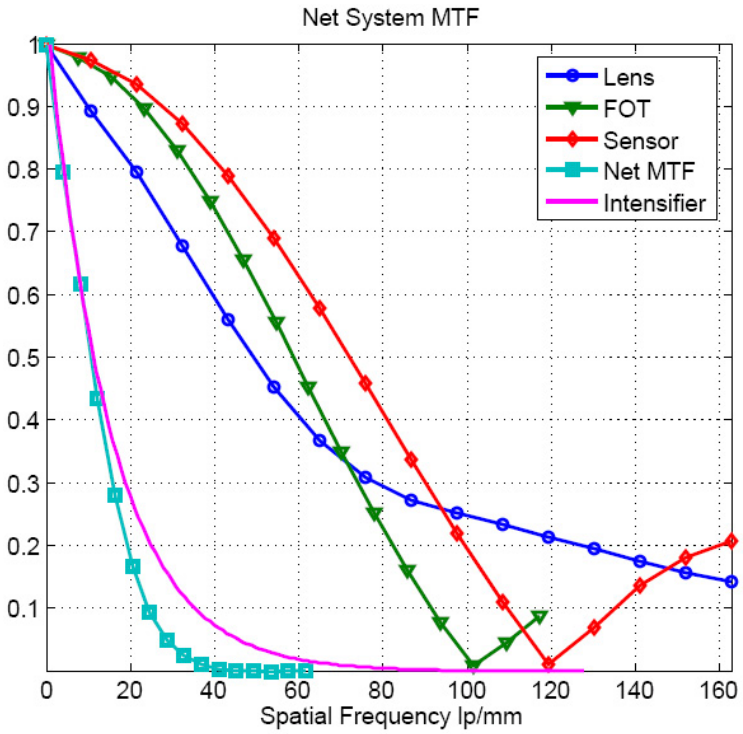

Fig. 28. MTF of the complete image intensified camera system

D. The Star Image Simulator

During product design and development it is highly beneficial to have simulated input data in order to test the performance of the entire system. For star sensors, the input data takes the form of night sky images which are used to test the image processing, calibration and attitude estimation algorithms. Night sky testing however, implies the existence of the sensor hardware. More often than not, the integrated hardware is usually not available, since sub-systems of the hardware itself are undergoing concurrent design. Thus, there is a strong need to have a night sky image simulator that can emulate the electrical and optical performance of the sub-systems as well as the integrated system under design. Although several simulators for terrestrial imaging and rendering exist, hardly any night sky simulators exist. Mortari et.al.[25] have designed a night sky simulator that can take as input the sensor specifics such as field-of-view, pixel counts, attitude and use these to generate an image of the visible stars. Their simulator however, does not account for sensor system specific characteristics of the optical train such as the psf, aberrations, as well as sensor properties such as quantum efficiency, optical response, spatio-temporal integration and sampling to name a few. A Gaussian star psf is assumed in their simulator design. As is well known, the presence of aberrations and discrete sampling leads to star psf's that are distorted and no longer Gaussian. Fig. 29 shows a star psf generated using the Gaussian approximation as well as a psf obtained from hardware. The difference is clearly evident.

The objective of this work is to design a high-fidelity simulator that is capable of generating realistic night sky images which are consistent with the electro-optical performance of the system hardware. By analyzing the stars visible in the field-of-view at the given attitude, the location and the magnitudes of these stars can

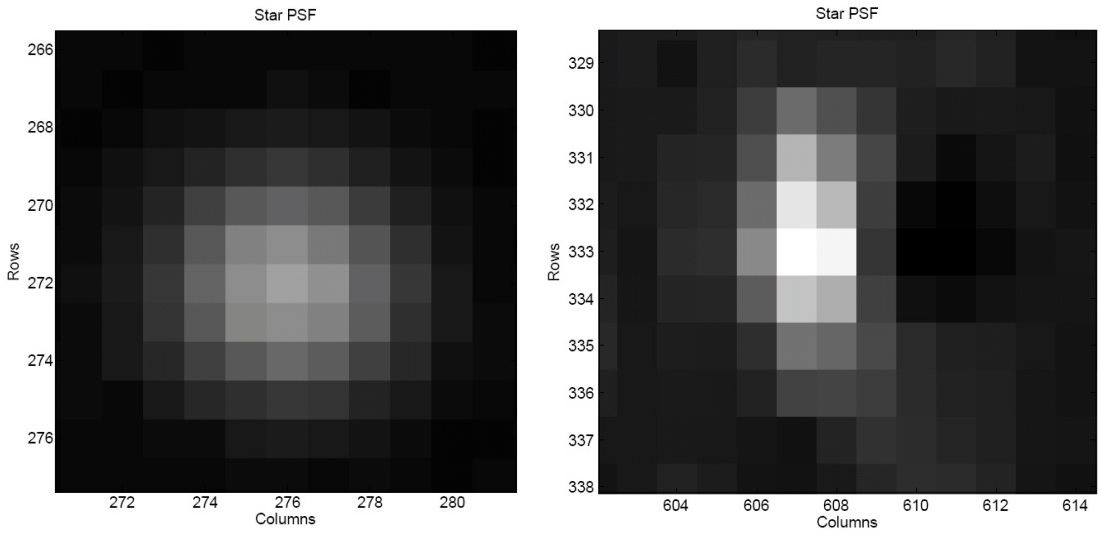

(a) Gaussian PSF from Simplified Simulator

(b) PSF from Night Sky Test

Fig. 29. Star point spread profiles from a simplified image simulator and from actual night sky test

be determined to form an irradiance map which acts as the input to the imaging system. The optics, i.e. the lens assembly, focusses the point objects (stars) onto the image intensifier with a psf that depends on the aberrations and the defocus of the system. The lens psf then gets modified by the OTF of the image intensifier and is incident on the fiber taper which further modifies it according to its own OTF. An imaging sensor located at the backplane then performs a spatio-temporal averaging of the psf to give an integrated psf. The integrated psf is then sampled according to the sensor geometry and the photons converted to electrons based on the sensor efficiency. Finally, the electrons are converted to a digital pixel reading given the full-well capacity and conversion ratio of the sensor.

Mathematically, the image formation process can be written as convolutions of the point spread functions of each component, followed by a sampling by 2D sampling

grid i.e.

$$\begin{aligned} p_{cont}(x,y) &= irrad_{star}(x,y) \otimes psf_{lens}(x,y) \otimes psf_{ii}(x,y) \\ &\quad \otimes psf_{fot}(x,y) \otimes psf_{sen}(x,y) \\ p_{samp}(m\Delta x, n\Delta y) &= p_{cont}(x,y) \times \gamma\left(\frac{x}{\Delta x}, \frac{y}{\Delta y}\right) \end{aligned} \tag{3.58}$$

where, $\otimes$ denotes the 2D convolution operator, $\gamma(\cdot,\cdot)$ denotes the 2D sampling grid formed by Dirac delta functions, $[\Delta x,\ \Delta y]$ denote the sampling interval in the x and y directions, $p_{cont}(\cdot,\cdot)$ and $p_{samp}(\cdot,\cdot)$ denote the continuous and the sampled versions of the net psf respectively. Taking a 2D Fourier transform of the above equation,

$$\begin{aligned} P_{cont}(u,v) &= IRRAD_{star}(u,v) \times OTF_{lens}(u,v) \times OTF_{ii}(u,v) \\ &\quad \times OTF_{fot}(u,v) \times OTF_{sen}(u,v) \\ P_{samp} &= P_{cont}(u,v) \otimes \Gamma(u,v) \end{aligned} \tag{3.59}$$

where (u,v) represent the spatial frequencies and the uppercase letters indicate that the quantity corresponds to the Fourier transform of its lowercase equivalent. The OTF for each component were developed in the previous section and can be readily applied in the above equations.

1. Star Irradiance Estimation

Using the Hipparachos and TychoII star catalogs [26, 27] and a star visual magnitude cut-off of 7.0, an on-board star catalog containing 4990 stars was derived. Given the sensor attitude and the field-of-view of the system, the stars that are visible to the sensor were obtained using the procedure outlined in Mortari[25]. The visual magnitude associated with each star was also obtained from the catalog. The irradiance

due to a star of visual magnitude mv is given by

$$E_{star} = 10^{0.4(-mv-19)} \mathrm{W/m^2} \tag{3.60}$$

Note that in the above equation, E_{star} represents the total flux from the star across all wavelengths. If the spectral class of the star is known, then it is possible to obtain the spectral radiation profile as a function of the wavelength. In our discussions below however, we will assume an average wavelength λ_0 at which this irradiance is obtained.

If $\{\lambda_1 \leq \lambda \leq \lambda_2\}$ represent the spectral range of radiation that is visible to the sensor, the number of photo-electrons generated in the pixel of the imager is given by

$$n_{PE} = \int_{\lambda_1}^{\lambda_2} \eta_{cathode}(\lambda)\eta_{screen}(\lambda)\eta_{sen}(\lambda)G_{MCP}\frac{E_{star}}{\hbar c/\lambda_0}t_{int}A_{optics}T_{optics}T_{fot}d\lambda \tag{3.61}$$

In the above expression $\eta_{sensor}(\lambda)$ represents the product of the quantum efficiency and the fill factor (QEFF) of the sensor. The QEFF of the sensor is a function of the wavelength of the incident light. However, the phosphor emission profile is concentrated over a very small band of about $20nm$. Over this spectral region, the QEFF of the sensor, transmissivity of the fiber optic taper and efficiency of the screen can be considered to be constant. For implementation purposes, the above integration can be discretized as a summation as

$$n_{PE} = \sum_{\lambda_1}^{\lambda_2} \eta_{cathode}(\lambda)\eta_{screen}\eta_{sen}G_{MCP}\frac{E_{star}}{\hbar c/\lambda_0}t_{int}A_{optics}T_{optics}T_{fot}\Delta\lambda \tag{3.62}$$

where, $\Delta\lambda$ is a small wavelength interval. The photocathode efficiency was obtained from the datasheets for the image intensifier [28] and was fitted with a polynomial based function and is shown in Fig. 30

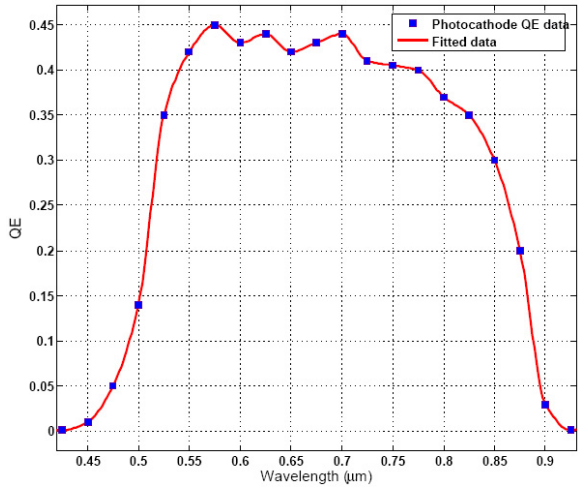

Fig. 30. Wavelength dependant efficiency of the photocathode for the image intensifier

2. The Real Lens System

In the previous discussions of the imaging system using linear system theory, it was assumed that the optical system is shift invariant. In reality however, the wavefront error and consequently the aberration, is not constant across the field of view. Thus, the point spread function is different for different parts of the focal plane. In other words, the system is not isoplanatic [21]. Fig. 31 shows the psf of the defocused 3-element lens system used at various angles. It is immediately evident that the psf shapes and values are drastically different from each other.

Since the isoplanatic condition is violated, given a star located at some angular position in the image, the psf at that position has to be estimated. For this purpose, the image plane can be divided into several small sections. Over each section it can then be assumed, to some degree of approximation, that the system is isoplanatic. Since the system is rotationally symmetric, the image plane is divided into annular regions with each region associated with its unique psf. For an image point located in-between the annular regions, the psf at that location is then obtained by a linear interpolation of the psf's of its closest annular regions. If psf_i and psf_j are the psf's

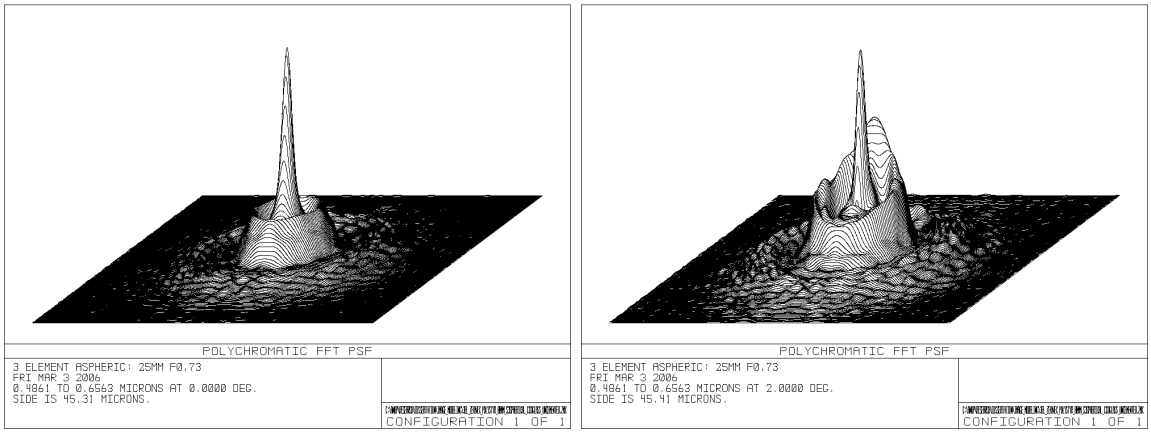

(a) 0°(on-axis) (b) 2°

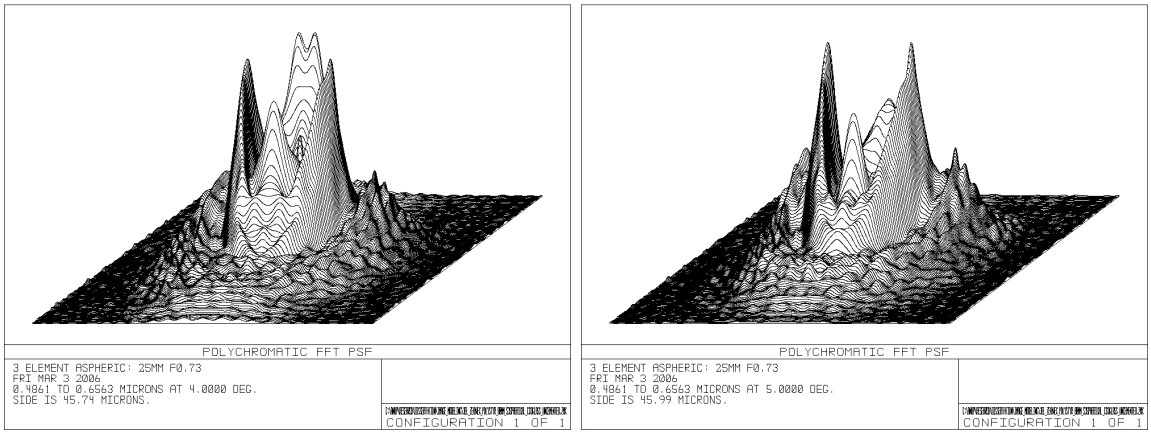

(c) 4° (d) 5°

Fig. 31. Point spread functions for the defocused 3-element lens across the field of view

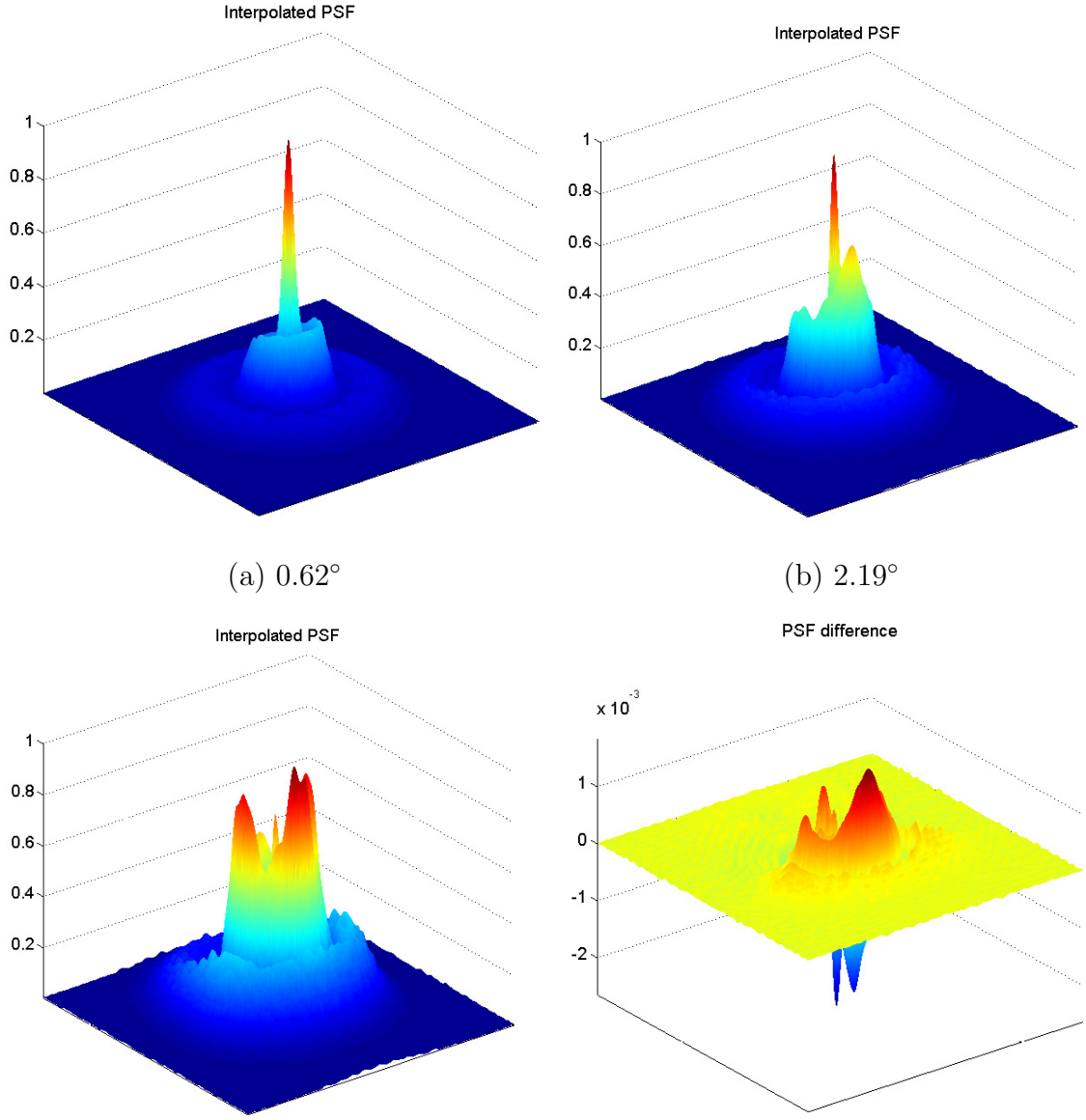

(a) 0.62°

(b) 2.19°

(c) 3.31°

(d) Difference in the local and interpolated psf for the star at 3.31°

Fig. 32. Interpolated point spread functions using the regional psfs

for the regions i, j separated by angle α, then for a point located at angle β from psf_i, the interpolated psf is obtained as $(\alpha - \beta)psf_i + \beta psf_j$. Ideally, the number of regions should be as high as possible, but for simulation purposes with regards to processing power and storage requirements, 10 zones - each covering about 0.5° were used. Fig. 32(a)-Fig. 32(c) show three interpolated psf's that were obtained using this procedure and Fig. 32(d) shows the difference in the interpolated psf and the regional psf located at 3.0°. The difference in the psf is on the order of 10^{-3}, which when given that the magnitude of the un-normalized regional psf is of the same order, represents a significant variation.

3. Sensor Geometry and Sampling

As discussed previously, the point spread function of a pixel of dimension $b \times d$ is given by a 2D rectangle function and the corresponding OTF is given by Eq.3.57. The PSF of the electro-optical train prior to the imaging sensor is usually termed as the instrument PSF or iPSF [29]. The pixel then performs a 2D averaging of the iPSF to give the integrated iPSF. Given the discrete nature of the pixels, the integrated iPSF is then sampled as per the sensor pixel geometry. This entire process can be written mathematically as

$$psf_{samp}(m\Delta x, n\Delta y) = \left[ipsf(x,y) \otimes rect\left(\frac{x}{b}, \frac{y}{d}\right)\right] \times \gamma\left(\frac{x}{\Delta x}, \frac{y}{\Delta y}\right) \tag{3.63}$$

If the fillfactor of the sensor is unity then the sampling interval $[\Delta x, \Delta y]$ is equal to the pixel dimensions $[b, d]$. However, if optically inactive regions are present causing the fillfactor to be less than one, then, the pixel pitch increases. Conversely, the sampling interval also increases to $[b', d'] = [b/FF, d/FF]$. If the sampling interval is such that $\Delta x \leq 1/2u_{max}$ and $\Delta y \leq 1/2v_{max}$, where u_{max} and v_{max} are the highest spatial frequencies in the input signal, then the sampled signal will be free of aliasing.

The highest spatial frequencies in the input are governed by the pixel pitch i.e. $u_{max} = 1/2b'$ and $v_{max} = 1/2d'$

Thus there are two ways to obtain the sampled psf. The sampling can be considered as a convolution in the frequency domain and the convolved signal can be filtered using a low-pass filter to obtain the band-limited sampled version. An inverse Fourier transform can then be taken to yield the psf in the spatial domain. Conversely, after the multiplication of the input ipsf has been performed in the Fourier domain, an inverse Fourier transform can be taken to give a continuous integrated psf in the spatial domain. Multiplication by the 2D sampling grid can then be performed to give sampled signal. In our work, the second method is employed since the sampling is easier to visualize and comprehend in the spatial domain. Additionally, it is much easier to shift the sampling locations in space than it is in the frequency domain. This grid shifting is required to account for a phenomenon discussed below.

a. Pixel Phase

Let us now conduct an experiment to estimate the centroid of an ideal 2D Gaussian distribution. One of the most commonly used centroiding techniques that tries to fit a psf to the pixel data is the 2D Gaussian fitting method (Stone[30]). Fig. 33 shows the error obtained in centroiding as the true centroid is translated along the x-direction. In addition to indicating a random error, an underlying sinusoidal variation in the centroid estimation can be observed. The period of the sinusoid is exactly one pixel width. This error is termed as the pixel phase and is given by

$$\phi \equiv x - \text{int}(x + 0.5) \tag{3.64}$$

This error arises because the intensity distribution over the pixels is dependent upon where in the pixel, the centroid lies. If the centroid lies at the center of the pixel,

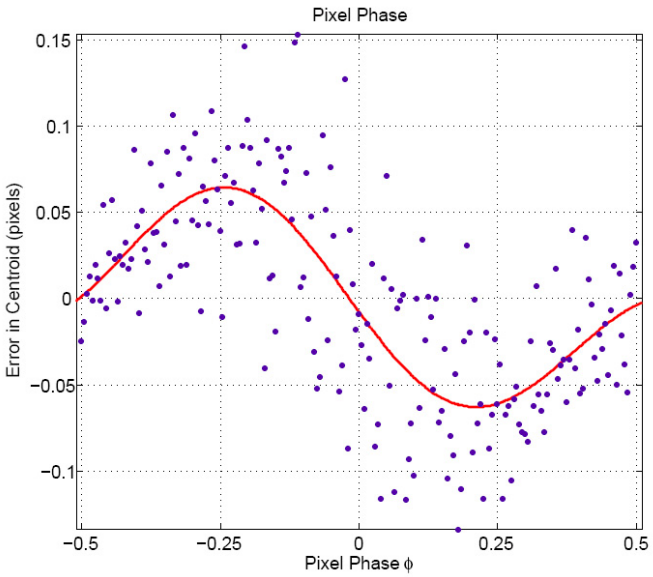

Fig. 33. Pixel phase errors in centroiding using a Gaussian fitting procedure

then that pixel will contain the maximum intensity value. The pixel phase error will thus be zero. If, for example, the centroid lies towards the edge of the pixel, then the intensity will be split between the adjacent pixels. The ratio with which the intensity will be distributed will be decided by how close the centroid is to the boundary of the pixel.

In order to create a realistic simulator, it is thus required to replicate this phenomenon during the generation of the image. This is accomplished by shifting the sampling grid for each star by an amount corresponding to it's pixel phase. Fig. 34 shows the basic principle behind this operation. The centers of the pixels have been indicated with crosses while the circle indicates the centroid of the star. As can be seen in a frame attached to the pixel center, the centroid is offset from the center by an amount given by the pixel phase ϕ. When the convolution with the sensor OTF is performed and the inverse Fourier transform taken, the continuous psf in the spatial

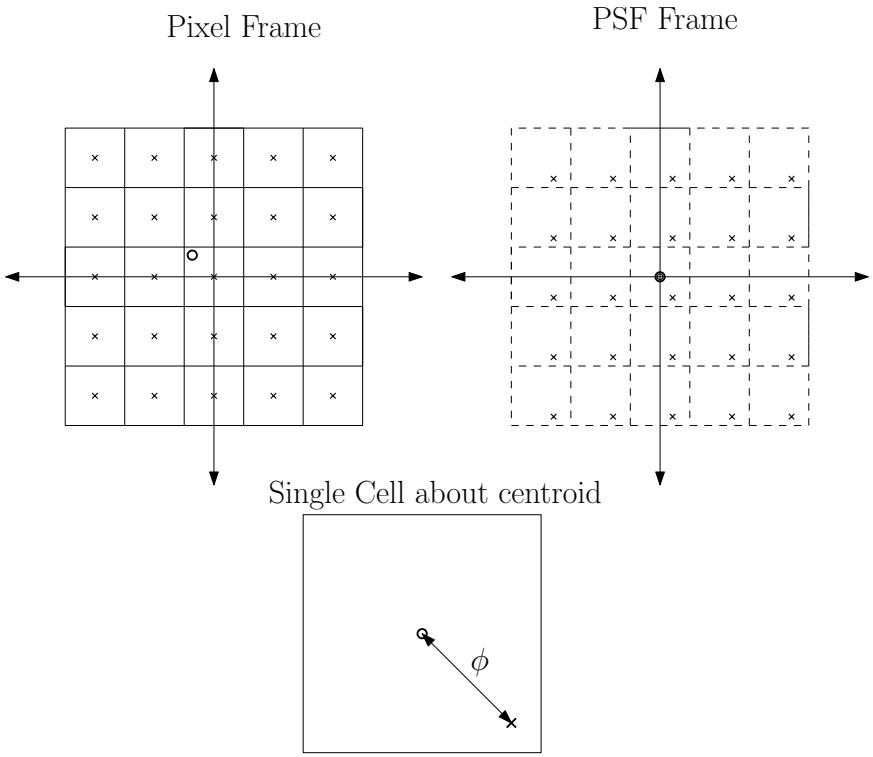

Fig. 34. Illustration of the frames associated with pixel phase. Crosses are the pixel centers and the circle indicates the centroid of the star

domain is centered about the true centroid. The discrete version must be obtained by sampling this continuous signal by a 2D sampling. Ideally, in the case of no pixel phase error, the center of the sampling grid would align exactly with the center of continuous psf i.e. the pixel frame and the psf frame coincide perfectly. In the presence of pixel phase however, the PSF frame and the pixel frame are not coincident. The center of the pixels are shifted by the pixel phase. Thus, if the sampling points are located at the co-ordinates of the shifted pixel centers, the phase effect will be accounted for.

4. The Designed Simulator

Using the theory and procedures discussed in the previous sections, a star image simulator was developed in the MATLAB simulation environment. The user controllable inputs include:

- Optics: focal length, aperture, glass transmissivity, psf over various fields
- Image Intensifier: Gain
- Fiber Optic Taper: fiber pitch, transmissivity
- Imaging Sensor: number of pixels, pixel size, fillfactor, full-well capacity, number of bits for digitization, integration time
- Star Catalog: maximum visual magnitude cutoff threshold
- Attitude: random or specified

Fig. 35 shows the outline of the process involved in simulating the night sky image. Using the attitude information (prescribed or random), the stars visible to the sensor are extracted from the star catalog and mapped onto the focal plane using

the system specifics such as field of view and sensor dimensions. The angular position of each star is then fed into the PSF interpolation block, which estimates the psf of the optics at the particular location. The star visual magnitudes are provided as input to the star irradiance estimation function. This function takes into account the system aperture, gain, quantum efficiencies, and glass transmissivities to estimate the number of photo-electrons that will be generated due to each star.

The pixel response is calculated as a function of pixel size and the fillfactor. 2D Fourier transforms of the pixel psf, along with the interpolated psf, intensifier psf and irradiance are then computed and multiplied in the Fourier domain to give the system OTF. Inverse Fourier transform of this leads to the continuous psf in the spatial domain. Using the centroid information, the pixel phase is calculated and the 2D sampling grid is then shifted by this amount. The continuous signal is then sampled by this grid and a discrete star signal is obtained. With the knowledge of the full-well capacity of the pixel and the number of bits in the analog to digital convertor, the photo-electrons on each pixel are converted to a binary digital pixel intensity value. This procedure is repeated for each star in the image and a final output image of the visible night sky is obtained.

Table VI shows the star locations in pixels, angular position in the image and the visual magnitudes for stars for one image generation run. The sensor was assumed to be a 512×512 pixel sensor with $5\mu m \times 5\mu m$ pixels with 100% fill factor. The focal length was $25mm$ and diameter of the lens was $25mm$ as well. A star magnitude cutoff of $m.v.7.0$ was used and the integration time was set to $25ms$. The full-well capacity was $100,000$ electrons and a 8bit ADC was assumed.

Fig. 36-Fig. 39 show the output at each step for the simulator. From the spot profiles it can be seen easily that the intensity distribution is not a Gaussian. Fig. 40 shows the final digitized star simulator image.

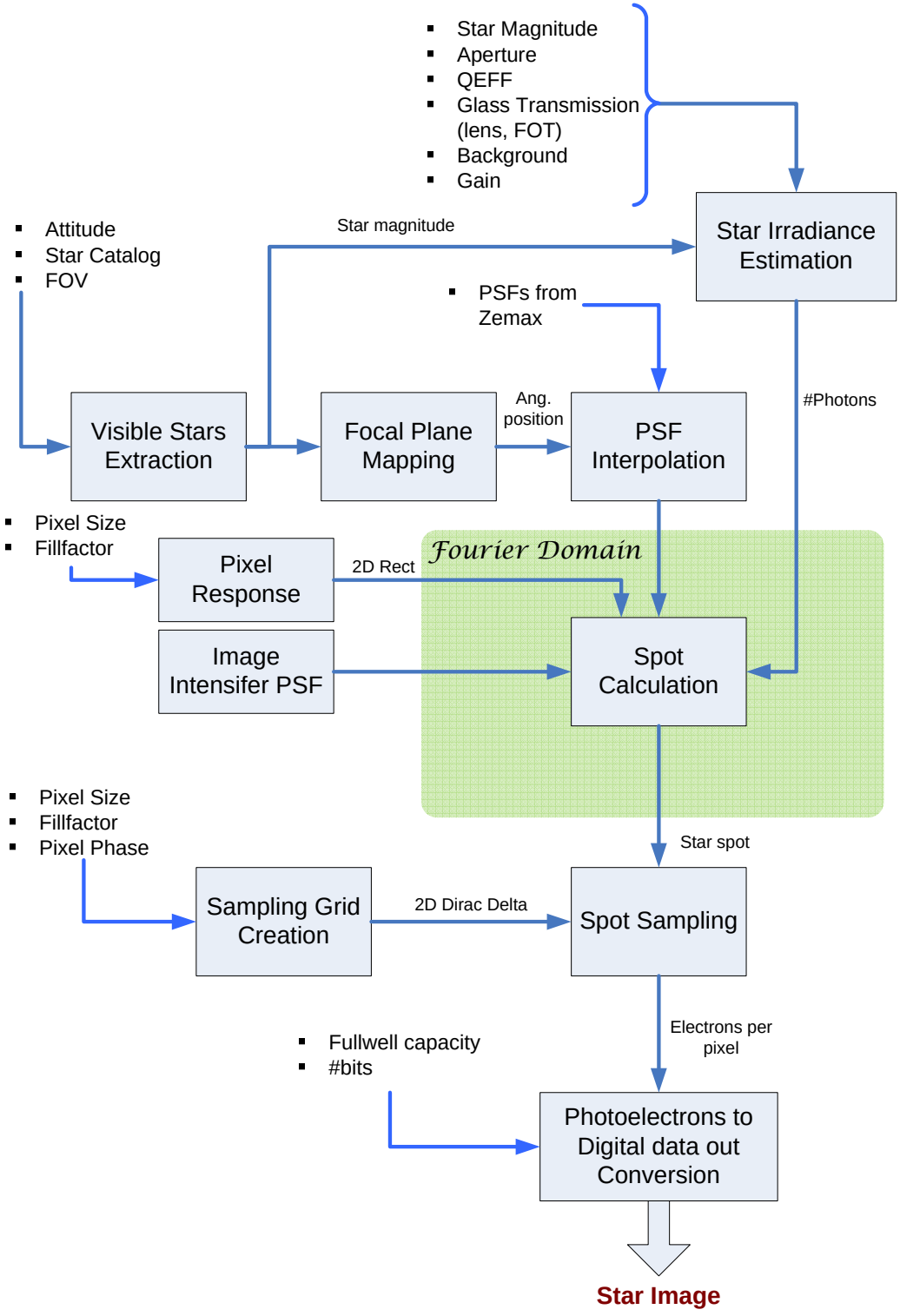

Fig. 35. Star image simulator

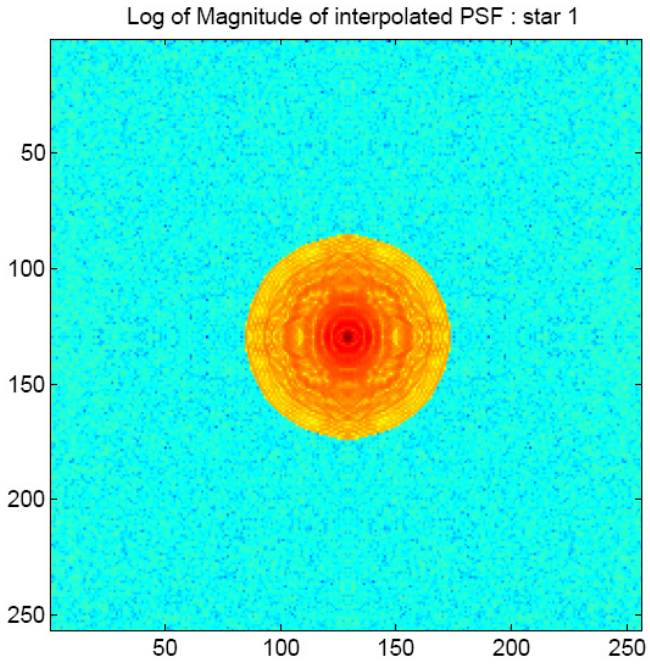

(a) Log of magnitude of the interpolated lens psf

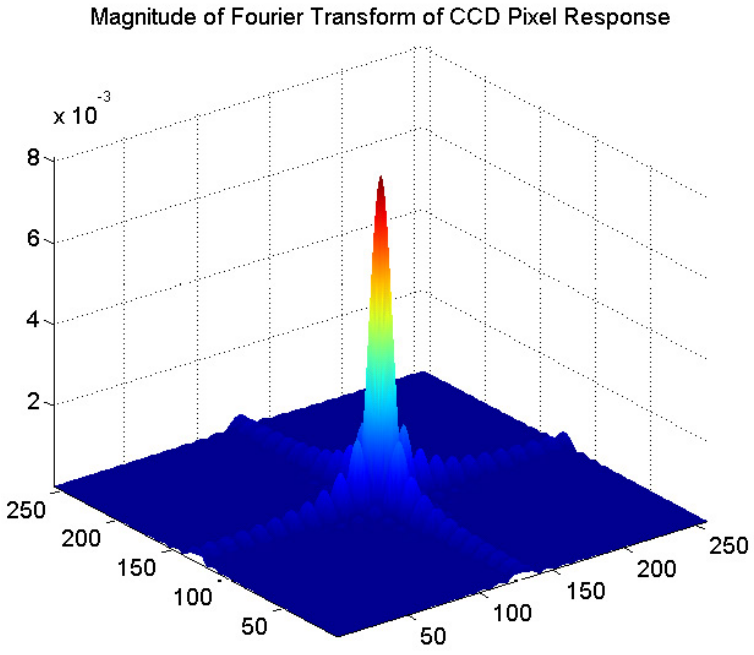

(b) Pixel response OTF

Fig. 36. Magnitude of the OTF for the interpolated star psf (star1) and the pixel response

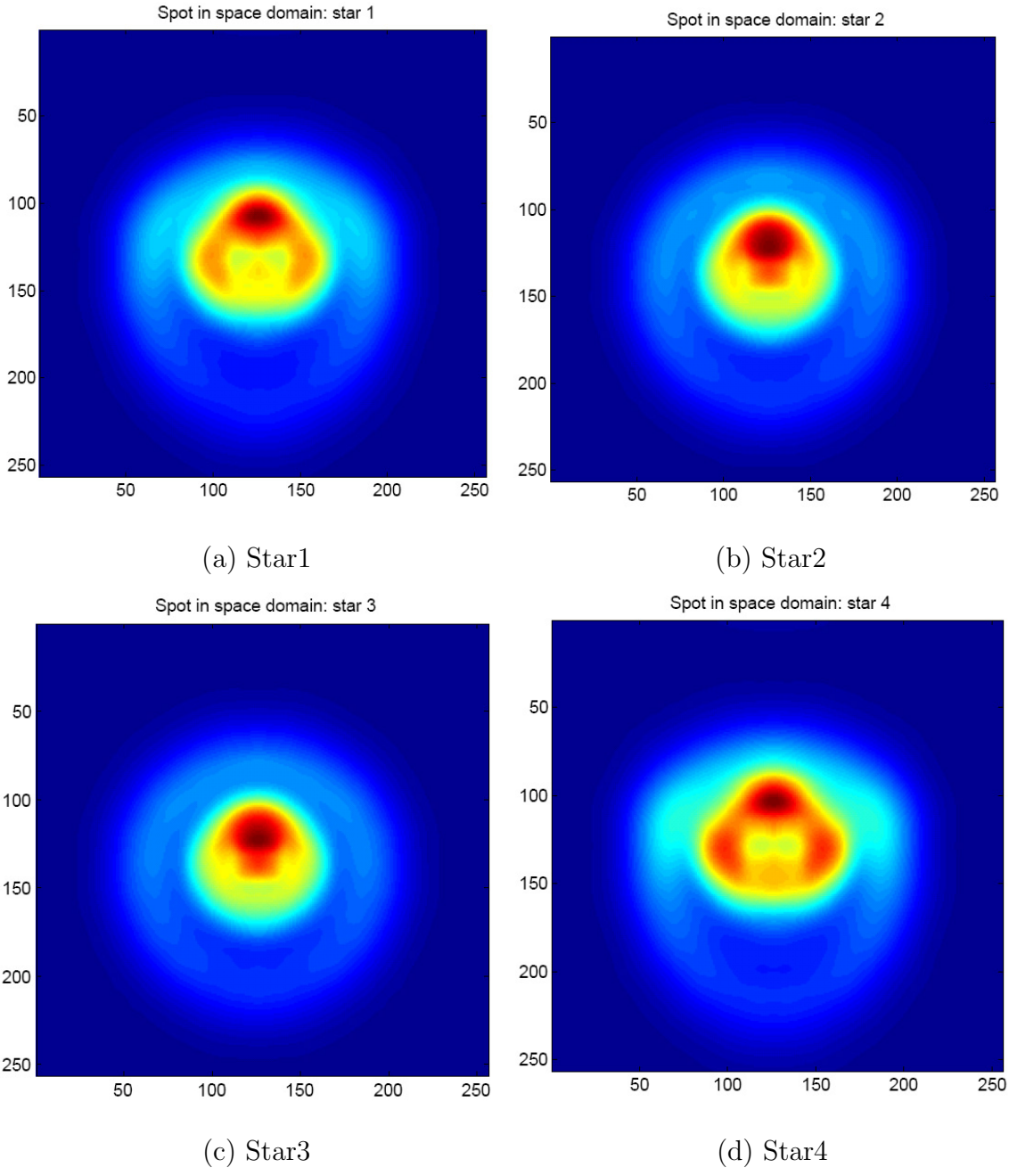

(a) Star1

(b) Star2

(c) Star3

(d) Star4

Fig. 37. Integrated continuous psfs for the stars in the image

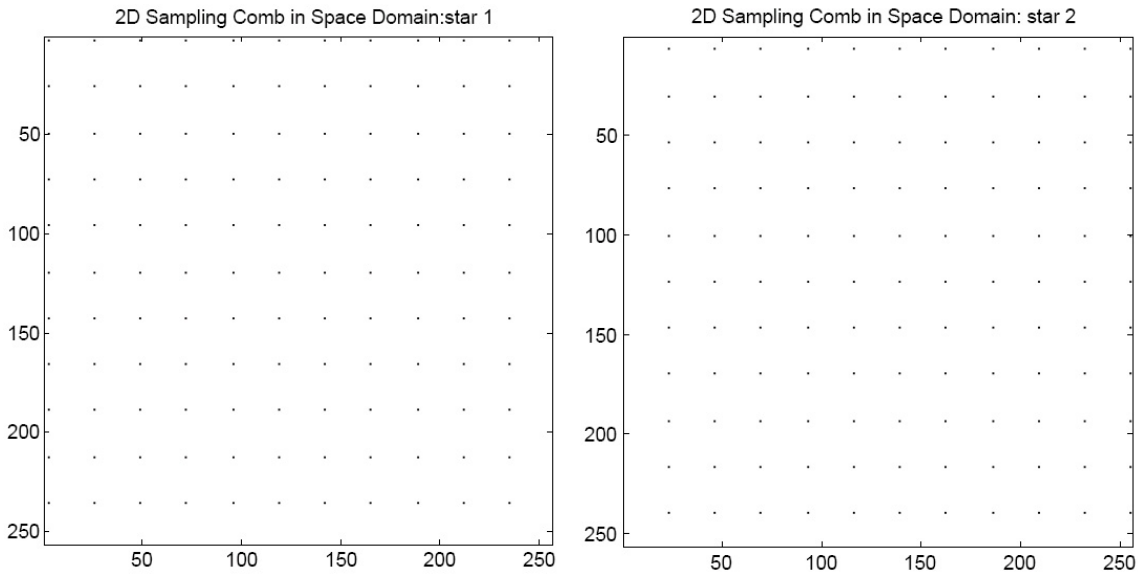

(a) Star1 (b) Star2

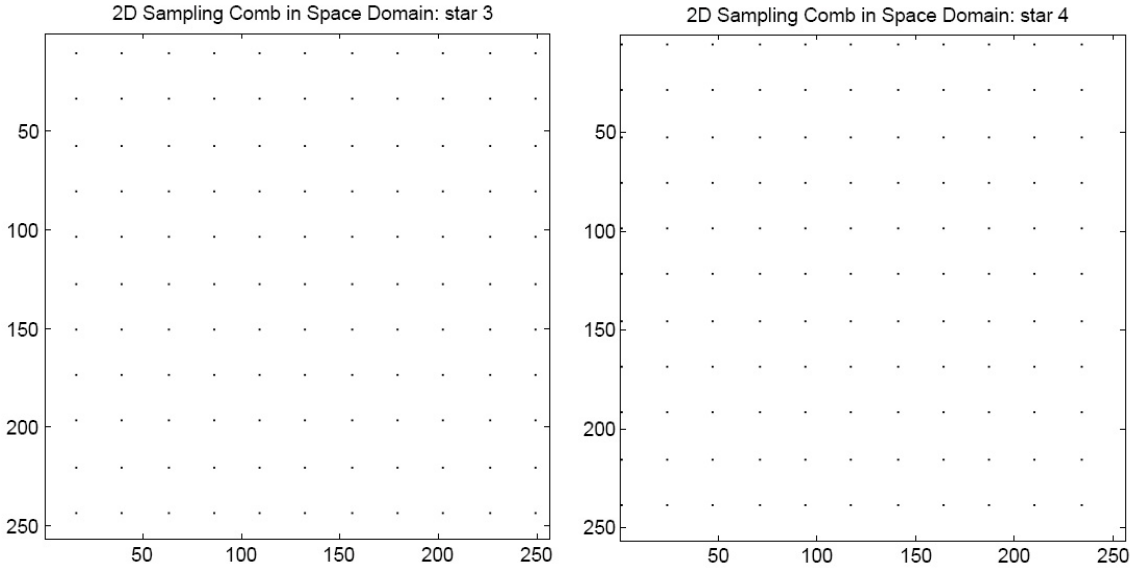

(c) Star3 (d) Star4

Fig. 38. Pixel phase corrected sampling grids for the stars in the image

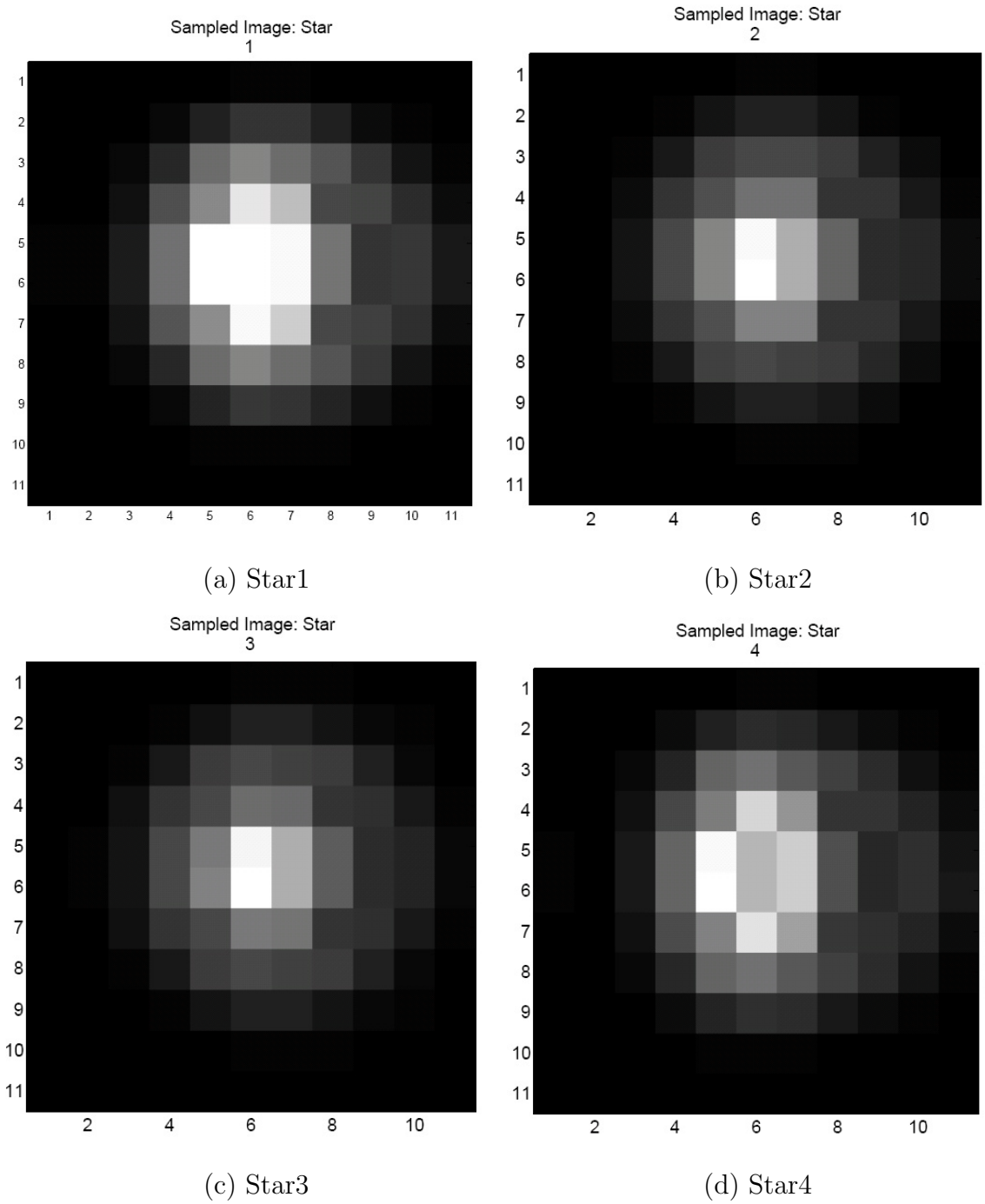

(a) Star1

(b) Star2

(c) Star3

(d) Star4

Fig. 39. Sampled stars

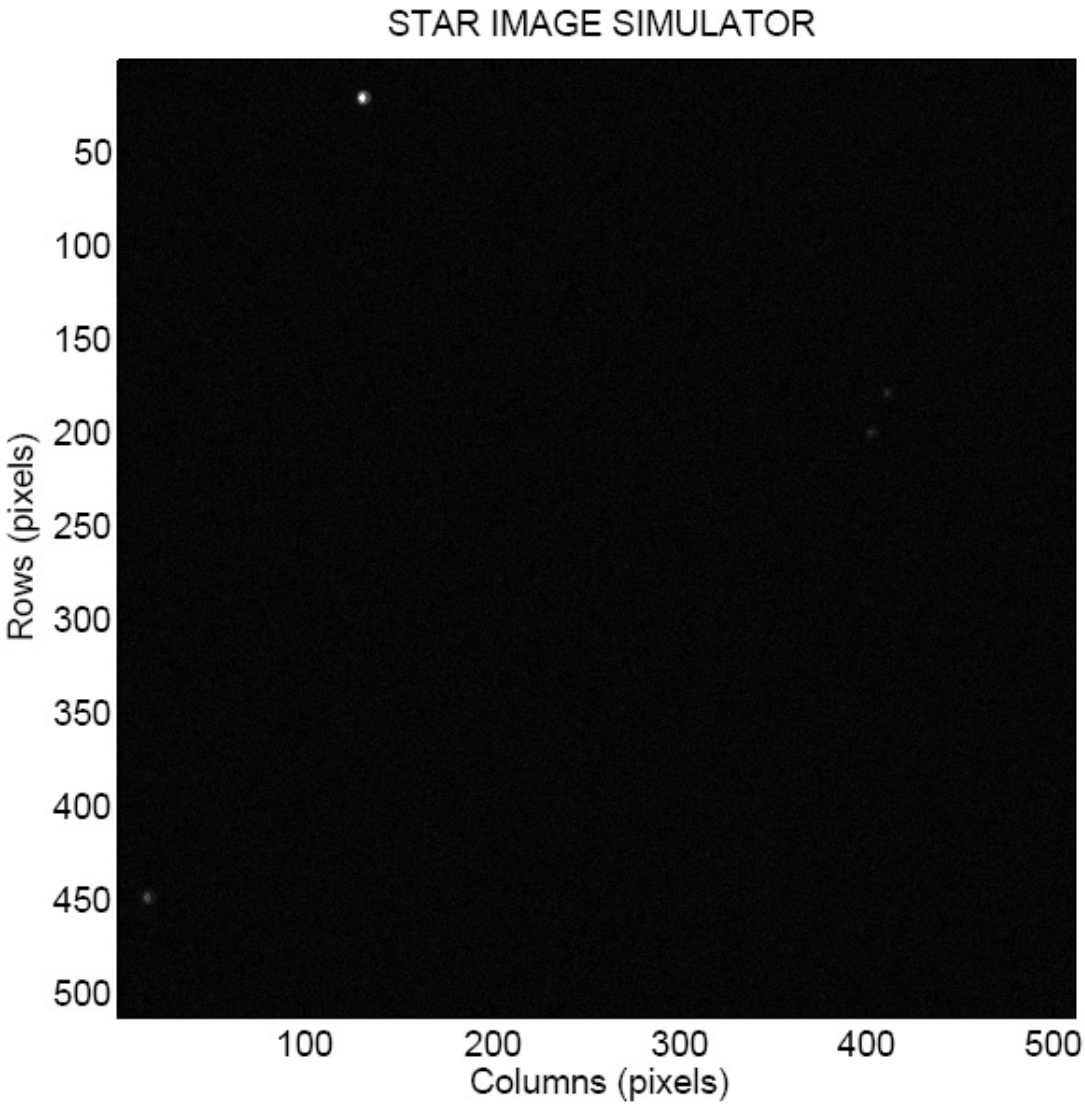

Fig. 40. Simulated night sky image for a random attitude

Table VI. Star data for one of the simulated images for a random attitude

Column (pixel)	Row (pixel)	Angular position degrees	Visual Magnitude
20.1312	130.8877	3.0567	3.3853
178.4824	411.3151	1.9883	5.9275
199.4577	401.8947	1.7924	5.7554
448.3734	15.7524	3.5224	4.7999

E. Concluding Remarks

In this chapter, we developed the electro-optical response of the image intensified camera system. A gain model of the intensifier parameterized by the operating voltages was described. Next the noise characteristics of the camera system were determined by considering various sources of noise. It was shown that under moderate gain operating conditions, the minimum gain required for the SNR of the intensified system to be comparable to the non-intensified system is around 37. Using linear system theory, the overall optical response of the system was developed. The point spread functions, OTFs, MTFs for each of the components were determined. It was seen that the system MTF is primarily limited by the MTF of the image intensifier. A high fidelity image simulator capable of accounting for lens aberrations, sensor geometries and pixel phase errors was also designed using the developed electro-optical response theory.

CHAPTER IV

STAR POSITION ESTIMATION IMPROVEMENTS

A. Introduction and Existing Centroiding Methods

The computational process that estimates the position of the star on the focal plane array is known as centroiding. It is a most crucial step since the errors in centroid estimation dictate the overall pointing accuracy of the star tracker. For a perfectly focused optical train, the image of a point source such as star will occupy only a single a pixel, thereby limiting the accuracy with which it's position can be estimated to the equivalent angle subtended by a single pixel. Thus, the optics are deliberately de-focused in order to spread the star energy over a few pixels thereby enabling sub-pixel position estimation[30]. It is well known that these defocused star centroids can be frequently be estimated to better than 1/10 of a pixel, effectively improving accuracy by an over an order of magnitude.

The accuracy with which the centroid can be determined is dependent on the angular resolution per pixel of the focal plane sensor. Star cameras with small field of view and large sensor resolution are thus being actively pursued [31]. A number of methods are available [30] for estimating the centroid locations. The center of mass or "the moment method" is one of the most commonly used techniques owing to its simplicity and robustness. The Gaussian fitting method while computationally more intensive is more accurate than the center of mass. Artificial neural network based methods [32] have also been developed that can estimate the centroid accurately to within 0.05 of a pixel. These methods however require extensive tuning for particular stars and are difficult to train.

In this chapter we develop a refinement of existing methodology for estimating

the centroid of the star intensity distribution. The procedure is based on fitting a 2D Gaussian distribution to the observed pixel profiles and using a linear least squares based algorithm to determine the best-fitting parameters of the Gaussian. We also address the issues of minimizing the effects of outlier pixels on the centroid estimate and devise a method for compensating for a variable background noise level in the image. This has been observed in real images and this variable noise background has not heretofore been compensated. We test the performance of the proposed algorithms on synthetic star profiles and images and show that the new method outperforms significantly the commonly used center of mass technique.

1. Center of Mass

The center of mass (COM) algorithm is most widely used method for determining the star centroids. In this method, pixels belonging to a star are located based upon their pixel intensity value. For this purpose a global threshold is usually computed by performing night sky experiments. A search across the entire image is performed in order to locate the maximum pixel values. A standard mask (square or rectangular) of a pre-determined size is applied about this peak intensity location and pixels lie that within the mask are extracted.

As is well known, the optical system is deliberately defocused so as to increase the accuracy with which the centroid can be estimated. The COM qualitatively treats the pixel intensities $P(x_i,\ y_j)$ as the masses attached at locations $(x_i,\ y_j)$ and estimates

the center of mass of this configuration as

$$\begin{aligned} x_c &= x_M + \frac{\sum_{i=-n/2}^{n/2}\sum_{j=-m/2}^{m/2}\left[P\left(x_M-i,\ y_M-j\right)-B\right]i}{\sum_{i=-n/2}^{n/2}\sum_{j=-m/2}^{m/2}\left[P\left(x_M-i,\ y_M-j\right)-B\right]} \\ y_c &= y_M + \frac{\sum_{i=-n/2}^{n/2}\sum_{j=-m/2}^{m/2}\left[P\left(x_M-i,\ y_M-j\right)-B\right]j}{\sum_{i=-n/2}^{n/2}\sum_{j=-m/2}^{m/2}\left[P\left(x_M-i,\ y_M-j\right)-B\right]} \end{aligned} \tag{4.1}$$

where,

$(x_M\ y_M)$: location of the peak of the intensity distribution

n, m : mask sizes along x and y directions

B : Background noise intensity (constant)

2. Non-Linear 2-D Gaussian Fitting

In this method, the pixel intensity distribution $P(x, y)$ corresponding to the star of visual magnitude m located at $[x_c\ y_c]$ is assumed to follow a 2-D Gaussian distribution given by

$$P(x,y) = \frac{t_{int}}{2\pi\sigma_x\sigma_y} e^{-\left(\frac{m_0-m}{2.5}\right)} e^{-\frac{(x-x_c)^2}{2\sigma_x^2}} e^{-\frac{(y-y_c)^2}{2\sigma_y^2}} \tag{4.2}$$

where

t_{int} : integration time for the frame

m_0 : visual magnitude of Sirius $= -1.5$

$\sigma_x\ \sigma_y$: standard deviation of the distribution along x and y directions

The process of centroiding i.e. determining $[x_c\ y_c]$ is thus equivalent to fitting a 2D Gaussian function to the star intensity distribution. Taking the natural logarithm of both sides of the above equation,

$$\ln P(x,y) = \underbrace{\ln \frac{t_{int}}{2\pi\sigma_x\sigma_y} - \frac{m_0 - m}{2.5}}_{z_c} - \frac{(x-x_c)^2}{2\sigma_x^2} - \frac{(y-y_c)^2}{2\sigma_y^2} \tag{4.3}$$

Thus, for each pixel $[x_i\ y_i]$ belonging to the star distribution, the above equation has the general form

$$z_i = z_c - -\frac{(x_i-x_c)^2}{2\sigma_x^2} - \frac{(y_i-y_c)^2}{2\sigma_y^2} = f\left(x_c,\, y_c,\, z_c\right) \tag{4.4}$$

where $z_i = \ln P(x_i, y_i)$. Let $\epsilon_i = z_i - f\left(x_c,\, y_c,\, z_c\right)$ be the error associated with the fitting process. Defining a loss function $L = \sum_{i=1}^{n} \alpha_i \epsilon_i^2 = \min$, the objective then is to minimize the loss function with respect to the unknowns $[x_c\ y_c\ z_c]$. Using the stationarity conditions we obtain

$$\begin{aligned}
\frac{\partial L}{\partial x_c} = 0 &\Rightarrow \sum_i \left[2\left(z_i - z_c\right) + \sigma_x^{-2}\left(x_i - x_c\right)^2 + \sigma_y^{-2}\left(y_i - y_c\right)^2\right]\left(x_i - x_c\right) = 0 \\
\frac{\partial L}{\partial y_c} = 0 &\Rightarrow \sum_i \left[2\left(z_i - z_c\right) + \sigma_x^{-2}\left(x_i - x_c\right)^2 + \sigma_y^{-2}\left(y_i - y_c\right)^2\right]\left(y_i - y_c\right) = 0 \\
\frac{\partial L}{\partial x_c} = 0 &\Rightarrow \sum_i \left[2\left(z_i - z_c\right) + \sigma_x^{-2}\left(x_i - x_c\right)^2 + \sigma_y^{-2}\left(y_i - y_c\right)^2\right] = 0
\end{aligned} \tag{4.5}$$

The above set of non-linear equations can be solved by using the Gaussian least squares differential correction algorithm (GLSDC) in which the system is linearized about the current estimate and a least squares update is used to obtain a correction to the estimate. Linearization leads to the following set of equations

$$x_c = \hat{x}_c + \delta x_c \quad y_c = \hat{y}_c + \delta y_c \quad z_c = \hat{z}_c + \delta z_c \tag{4.6}$$

Thus the residuals about the current estimate $[\hat{x_c}\ \hat{y_c}\ \hat{z_c}]$ are given by

$$r_i = z_i - f\left(\hat{x}_c,\ \hat{y}_c,\ \hat{z}_c\right) = \left\{ \frac{\partial f_i}{\partial x_c}\ \frac{\partial f_i}{\partial y_c}\ \frac{\partial f_i}{\partial z_c} \right\} \begin{bmatrix} \delta x_c \\ \delta y_c \\ \delta z_c \end{bmatrix} \tag{4.7}$$

For all the pixels belonging to the star, the above equation can be written in a matrix form as

$$R = \begin{bmatrix} r_1 \\ \vdots \\ r_n \end{bmatrix} = \begin{bmatrix} f_{1x} & f_{1y} & f_{1z} \\ \vdots & \vdots & \vdots \\ f_{nx} & f_{ny} & f_{nz} \end{bmatrix} = \begin{bmatrix} \delta x_c \\ \delta y_c \\ \delta z_c \end{bmatrix} = F\Delta \tag{4.8}$$

The corrections to the current estimate are found by using the iterative least squares as

$$\Delta_{k+1} = \left(F_k^T F_k\right)^{-1} F_k^T R_k \tag{4.9}$$

This procedure is found to converge with 4 iterations. The convergence, however, like all linearization and iterative schemes, is dependent on the initial guess and noise in the data set. Incorrect threshold levels and/or a bias in the background can severely degrade the computed centroid accuracy.

B. Linear Least Squares Log of Gaussian Estimation (LOG-LSQ)

The 2D Gaussian Fitting method exhibits the least error in centroiding as compared to all the other methods such COM, derivative search. As mentioned previously, the drawback of this non-linear parametrization method is the need for using a iterative estimation technique such as the GLSDC in order to solve the non-linear equations. In this section, we present an alternate centroid estimation technique that in essence performs the same 2D Gaussian fit to the star intensity data. However, in contrast to the standard Gaussian Fitting procedure, this new scheme gives rise to equations

that are rigorously linear in the transformed unknown parameters which can be solved easily by linear least squares estimators; the results can be transformed back to get the centroid locations.

1. Algorithm Development

Consider a 2D Gaussian distribution of the star intensity on the sensor given by

$$f\left(\mathbf{X}, \mathbf{X}_c\right) = \frac{1}{2\pi\sqrt{\det R}} e^{-\frac{1}{2}\left(\mathbf{X}-\mathbf{X}_c\right)^T R^{-1}\left(\mathbf{X}-\mathbf{X}_c\right)} \tag{4.10}$$

where

$$\mathbf{X} = \left[x\ y\right]^T : \text{pixel location}$$

$$\mathbf{X}_c = \left[x_c\ y_c\right]^T : \text{pixel location of the centroid} \tag{4.11}$$

$$R : 2 \times 2 \text{ symmetric covariance matrix} \tag{4.12}$$

The distribution along the the two directions x and y can be considered independent, in which case, the covariance matrix is a diagonal matrix and Eq.4.10 can be written as the product of two one-dimensional Gaussian distributions as in Eq.4.2. Taking the natural logarithm of both the sides of the above equation

$$-\ln f = -\ln \frac{1}{2\pi\sqrt{\det R}} + \frac{1}{2}\left(\mathbf{X}-\mathbf{X}_c\right)^T R^{-1}\left(\mathbf{X}-\mathbf{X}_c\right) \tag{4.13}$$

i.e.

$$-\ln f = \underbrace{-\ln \frac{1}{2\pi\sqrt{\det R}} + \frac{1}{2}\mathbf{X}_c^T D \mathbf{X}_c}_{a_0} + \frac{1}{2}\mathbf{X}^T D \mathbf{X} - \mathbf{X}_c^T D \mathbf{X} \tag{4.14}$$

where $D = R^{-1}$. The first and the second terms in the above equation are constant for a given distribution and do not depend upon the pixel locations $\mathbf{X}$. Denoting

their summation by the constant a_0 the above equation becomes

$$-\ln f = a_0 + \frac{1}{2}\mathbf{X}^T D\mathbf{X} - \mathbf{X}_c^T D\mathbf{X} \tag{4.15}$$

The product $\mathbf{X}_c^T D$ must be a 1×2 matrix since the left hand side is a scalar. Let $[a_1\ a_2]$ denote this 1×2 matrix and let $[d_{ij}]\ \ i, j = 1 \ldots 2$ denote the elements of the D matrix, then

$$-\ln f = a_0 + \begin{bmatrix} a_1 & a_2 \end{bmatrix} \begin{bmatrix} x \\ y \end{bmatrix} + \frac{1}{2} \begin{bmatrix} x & y \end{bmatrix} \begin{bmatrix} d_{11} & d_{12} \\ d_{21} & d_{22} \end{bmatrix} \begin{bmatrix} x \\ y \end{bmatrix} \tag{4.16}$$

Expanding the matrix terms in the above equation,

$$-\ln f = a_0 - a_1 x - a_2 y + \frac{1}{2}d_{11}x^2 + \frac{1}{2}d_{12}xy + \frac{1}{2}d_{21}xy + \frac{1}{2}d_{22}y^2 \tag{4.17}$$

Thus for every pixel belonging to the distribution, the above equation can be evaluated and written in a matrix form as:

$$\begin{bmatrix} -\ln f_1 \\ -\ln f_2 \\ \vdots \\ -\ln f_n \end{bmatrix} = \begin{bmatrix} 1 & -x_1 & -y_1 & \frac{1}{2}x_1^2 & \frac{1}{2}x_1y_1 & \frac{1}{2}x_1y_1 & \frac{1}{2}y_1^2 \\ 1 & -x_2 & -y_2 & \frac{1}{2}x_2^2 & \frac{1}{2}x_2y_2 & \frac{1}{2}x_2y_2 & \frac{1}{2}y_2^2 \\ \vdots & \vdots & \vdots & \vdots & \vdots & \vdots & \vdots \\ 1 & -x_n & -y_n & \frac{1}{2}x_n^2 & \frac{1}{2}x_ny_n & \frac{1}{2}x_ny_n & \frac{1}{2}y_n^2 \end{bmatrix} \begin{bmatrix} a_0 \\ a_1 \\ a_2 \\ d_{11} \\ d_{12} \\ d_{21} \\ d_{22} \end{bmatrix}$$

$$\tilde{f} = A'\mathbf{z}' \tag{4.18}$$

where $\tilde{f}$ is the vector of the measurements, n is the number of pixels in the star intensity distribution and $\mathbf{z}' = \begin{bmatrix} a_0 & a_1 & a_2 & d_{11} & d_{12} & d_{21} & d_{22} \end{bmatrix}^T$ is the 7×1 vector of unknowns. Glancing at the sensitivity matrix A' above, it is immediately evident

that the matrix is rank deficient i.e. has a rank 6. This is because the unknowns d_{12} and d_{21} have the same coefficient $1/2x_iy_i$. This problem is solved by remembering that $D = R^{-1}$ where R is the covariance matrix of the 2D Gaussian distribution. In general, the covariance matrix has the following structure

$$R = \begin{bmatrix} \sigma_x^2 & \rho\sigma_x\sigma_y \\ \rho\sigma_x\sigma_y & \sigma_y^2 \end{bmatrix} \tag{4.19}$$

where σ_x, σ_y are the standard deviations in the x and y directions, ρ is the correlation between the x and y directions. Since the covariance matrix is a real positive definite symmetric matrix, it's inverse is also a real symmetric matrix. This implies that $d_{12} = d_{21} \equiv d_2$. Consequently, the unknowns are reduced by one and Eq.4.18 becomes

$$\begin{bmatrix} -\ln f_1 \\ -\ln f_2 \\ \vdots \\ -\ln f_n \end{bmatrix} = \begin{bmatrix} 1 & -x_1 & -y_1 & \frac{1}{2}x_1^2 & x_1y_1 & \frac{1}{2}y_1^2 \\ 1 & -x_2 & -y_2 & \frac{1}{2}x_2^2 & x_2y_2 & \frac{1}{2}y_2^2 \\ \vdots & \vdots & \vdots & \vdots & \vdots & \vdots \\ 1 & -x_n & -y_n & \frac{1}{2}x_n^2 & x_ny_n & \frac{1}{2}y_n^2 \end{bmatrix} \begin{bmatrix} a_0 \\ a_1 \\ a_2 \\ d_{11} \\ d_2 \\ d_{22} \end{bmatrix} \tag{4.20}$$

$$\text{i.e.} \qquad \tilde{f} = A\mathbf{z} \tag{4.21}$$

The sensitivity matrix A is now of full rank 6 and forms a polynomial basis. Since the unknowns appear linearly, the standard least squares estimation algorithm can be readily applied to estimate $\mathbf{z}$ i.e.

$$\mathbf{z} = \left(A^T A\right)^{-1} A^T F \tag{4.22}$$

Recall that $[a_1\ a_2] = \mathbf{X}_c^T D$. Thus, the centroid of the star intensity distribution is given by the simple transformation

$$\mathbf{X}_c = \left([a_1\ a_2]\, D^{-1} \right)^T \tag{4.23}$$

2. Performance on Simulated Stars

The LOG-LSQ algorithm was implemented in MATLAB in order to compare its performance against the most commonly used COM approach. For these sets of preliminary tests, a 2D Gaussian profile with a known center and standard deviation was created over a small region. The size of this region was chosen so as to cover nearly 99% of the Gaussian distribution i.e. the $3-\sigma$ bound. Since the sensor is discrete in nature, the continuous 2D distribution was sampled at the center of the integer interval(representing the pixel center). Noise was added to the signal by treating it as a zero-mean random signal and its variance was increased to study the error in centroiding. Fig. 41 shows the 2D Gaussian distribution for one of the test cases. A noise whose amplitude was 1% of the signal amplitude was added in this case. Centroiding using LOG-LSQ and COM was performed on this distribution and 500 such runs were done in order to get statistical error data. Fig. 42 shows the errors in the centroid estimation in the x and y locations. As can be seen, the LOG-LSQ is about an order of magnitude better than the COM in estimating the centroid, for ideal low-noise star images.

Fig. 43 and Fig. 44 demonstrate the case when a noise of amplitude of 10% of the signal amplitude is added to the profile.The error in centroiding using LOG-LSQ, although have increased appreciably, are still smaller (about a factor of two), compared to the COM results.

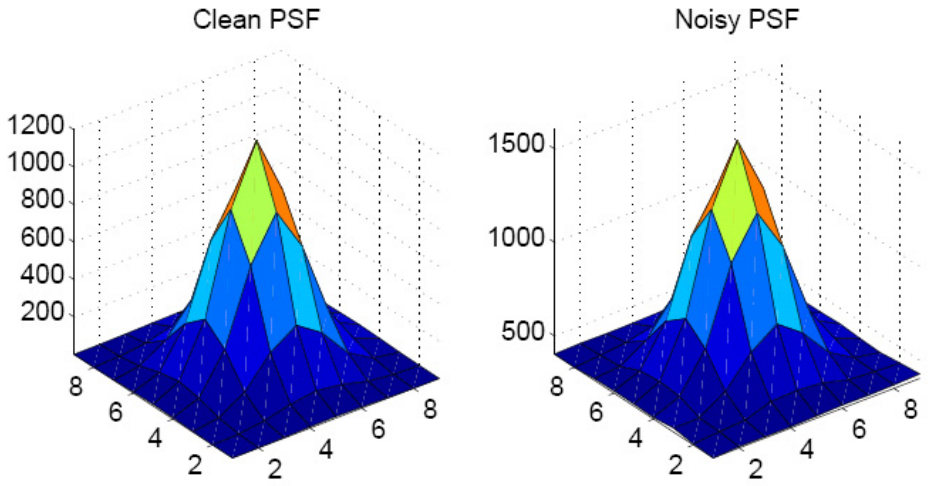

Fig. 41. 2D Gaussian distribution for noise magnitude= 1%

3. Weighted Estimation

As was seen in the previous tests, the addition of noise deteriorates the centroid estimate. Valuable insight into the effect of noise can be obtained by considering the steps involved in creating the measurement vector for the LOG-LSQ process. The first step in creating a measurement is taking the natural logarithm of the pixel intensities. Fig. 45 shows the measurements taken at different noise levels. When the noise is small, the measurement surface resembles a paraboloid as expected. However, with an increase in noise, the paraboloid shows a reduced spread and sharp variations or spikes at the periphery. At the borders of the star intensity distribution, the noise power begins to be more comparable to the signal power. Additionally in the process of centroiding, pixels that are farther away from the center, although containing very little signal, provide a significant and noisy contribution to the centroid.

In order to reduce the negative effects of outliers and peripheral pixels, a weighted scheme for centroiding can be used. The weight for each measurement can be chosen in either of the two ways - dependent on the distance of the pixel from the expected

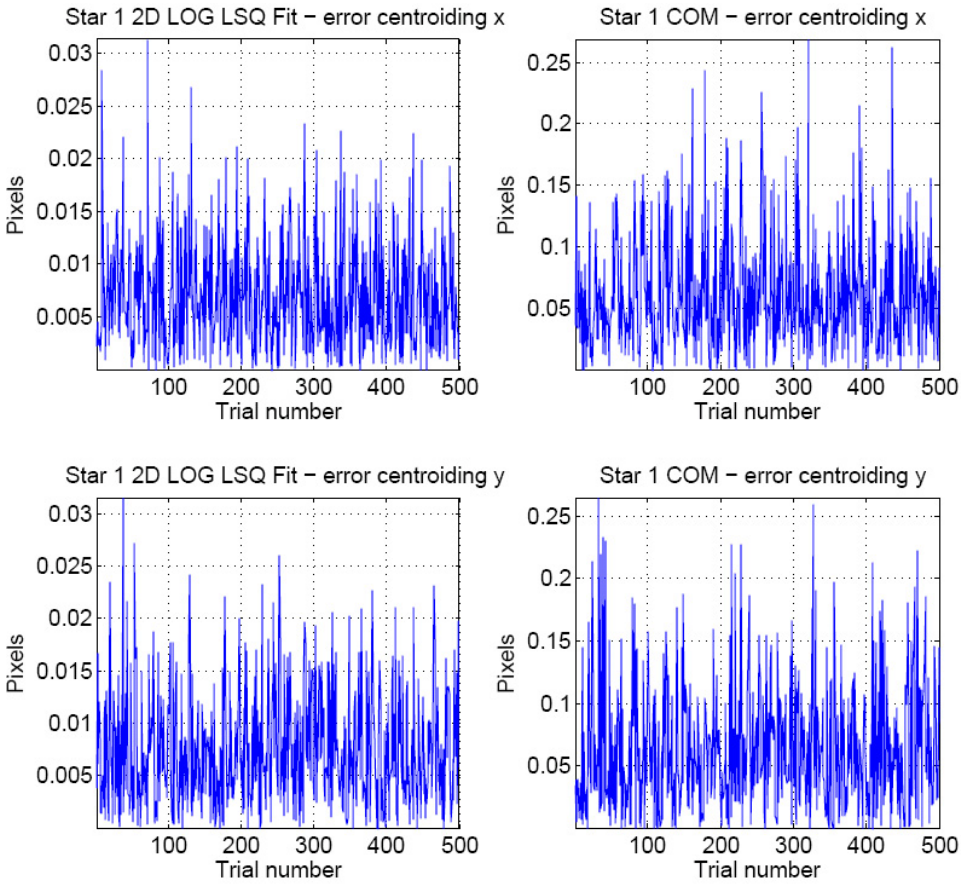

Fig. 42. Centroiding error using the LOG-LSQ and COM approaches for noise magnitude= 1%

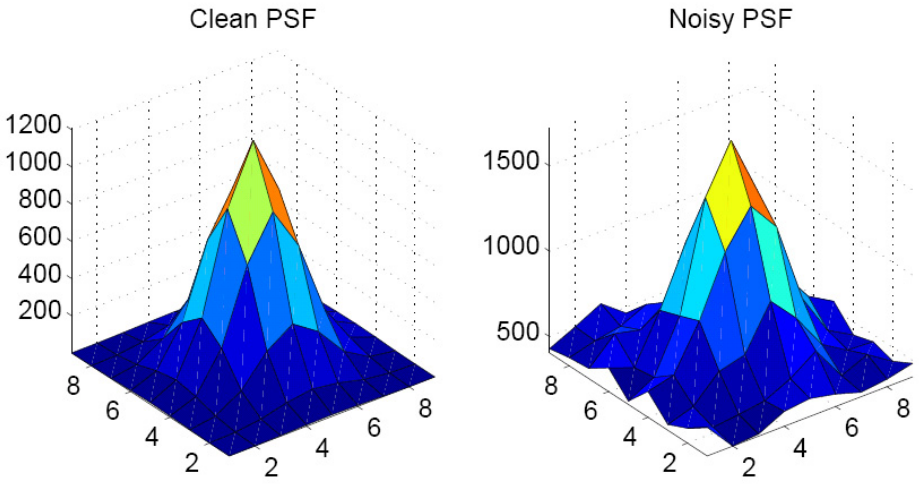

Fig. 43. 2D Gaussian distribution for noise magnitude= 10%

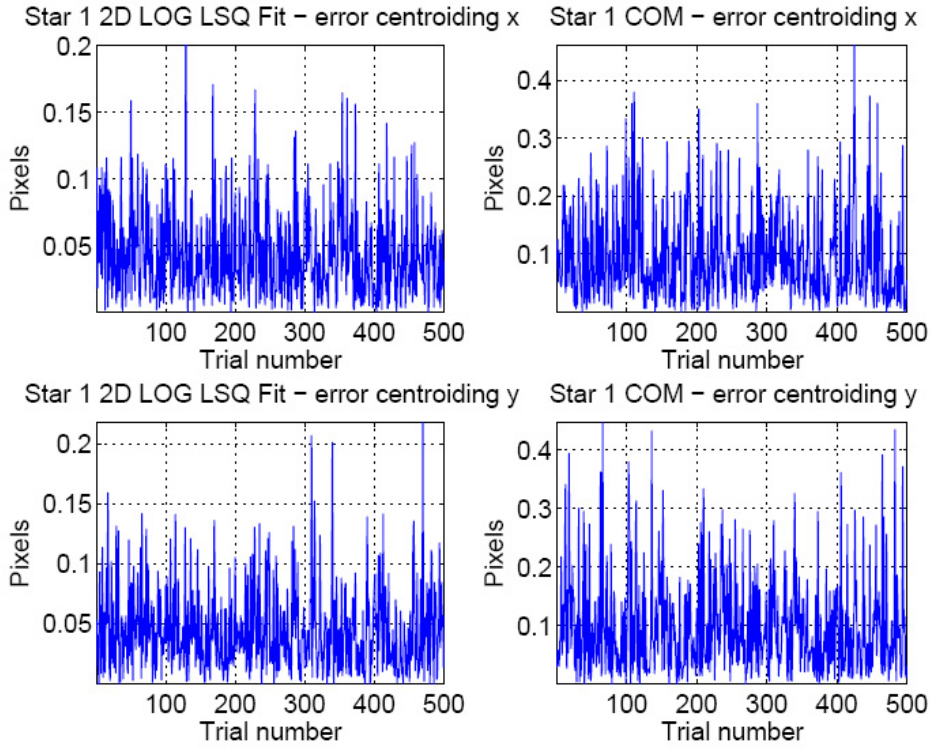

Fig. 44. Centroiding error using the LOG-LSQ and COM approaches for noise magnitude= 10% of signal amplitude

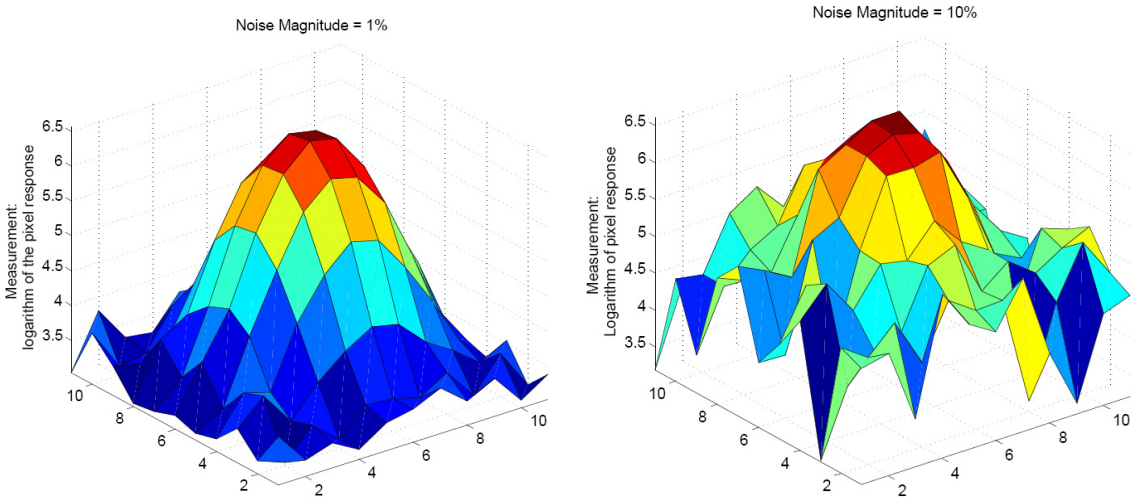

(a) Noise Magnitude= 1% (b) Noise Magnitude= 10%

Fig. 45. Effect of noise on the measurements used in the LOG-LSQ approach

center (or maximum intensity value pixel) or dependent on the measurement value itself. Several choices for the weight matrix are possible. The recently developed orthogonal polynomials[33] could be directly applied as the 2D polynomials of order 2 give rise to a similar surface as that of the measurements. These polynomials, however, require the re-scaling and shifting of origin for each star and thus increase the number of computations. Weighting by a value derived from the measurement itself provides a very easy and an efficient solution.A weight matrix in accordance with this view was heuristically chosen as:

$$W(i,j) = \begin{cases} \dfrac{\left[\tilde{f}_i - \min(\tilde{f}_m)\right]^2}{\left[\max(\tilde{f}_m) - \tilde{f}_i + \Delta\right]^2} & i = j \\ 0 & i \neq j \end{cases}$$

where $W(i,i)$ is the weight for the i^{th} measurement $\tilde{f}_i$ and Δ is a small number added so as to prevent the denominator going to zero at the location of the maximum pixel. Again, the choice of this particular weight function is arbitrary and as long

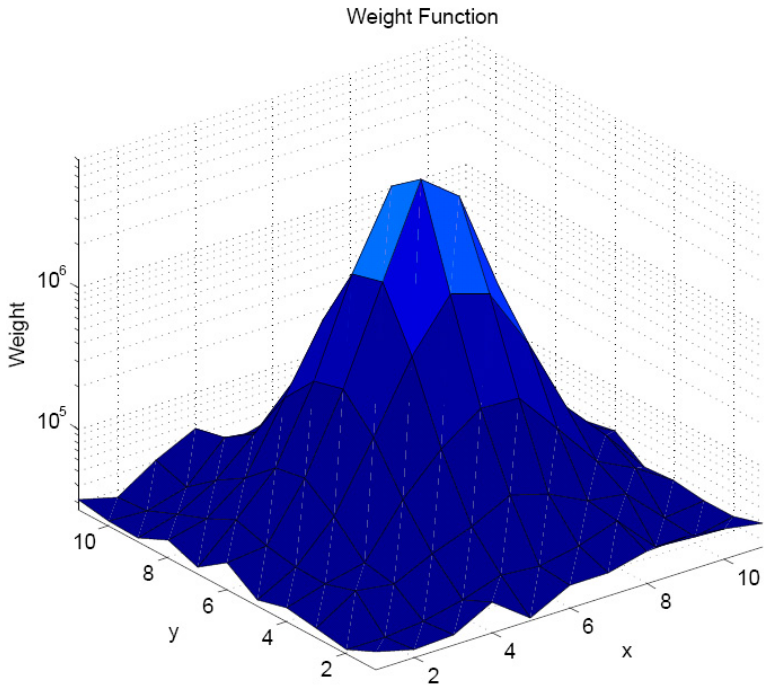

Fig. 46. Weighting function for the LOG-LSQ scheme

as the pixels lying towards the center of the distribution are weighted more than pixels along the border, the objective of minimizing the outlier contribution will be achieved. Using the weighted measurements, the least squares solution then becomes,

$$\mathbf{z} = \left(A^T W A\right)^{-1} A^T W F \tag{4.24}$$

Fig. 46 shows the weight function for one of the test cases. Table VII shows a comparison between the errors in the centroiding obtained by using the measurement weighted LOG-LSQ and without the weighting scheme. As before, 500 trial runs with random noise added to the true distribution were carried out in order to obtain the statistics. It can be seen that the error in centroiding is reduced by nearly 40% by using a weighted scheme.

Table VII. Absolute mean and standard deviations (pixels) in the error in centroiding using weighted and un-weighted measurements

Noise Magnitude	Without Weighting mean x	mean y	std.dev. x	std.dev. y	With Weighting mean x	mean y	std.dev. x	std.dev. y
1%	0.0071	0.0055	0.0054	0.0054	0.0041	0.0040	0.0031	0.0032
10%	0.0643	0.0642	0.0512	0.0491	0.0445	0.0438	0.034	0.0349

C. Background Estimation

The most critical parameter affecting the error in centroiding is the signal threshold. The threshold is used to determine which pixels belong to the star intensity distribution. The threshold is a function of two quantities - dark current of the sensor and the average signal content of the acquired image. Laboratory calibration is also essential to estimate the average dark current associated with the sensor at the nominal working temperature. Since the dark current varies exponentially with temperature, several frames of dark images are acquired and constructed by the averaging process per pixel for each temperature range. Usually $5-7$ dark frames are sufficient to estimate the average dark current per pixel. This is then followed by night sky testing in order to determine the signal to noise ratio for the nominal imaging conditions. The threshold *thr* is then constructed as the sum of the dark frame average at the working temperature T and the average of the acquired image and its standard deviation as:

$$\text{thr} = \text{DarkFrame}_{avg,T} + \text{mean}(\text{Image}_T) + 3 \times \text{std.dev}(\text{Image}_T) \tag{4.25}$$

1. Need for Automatic Thresholding

Once in-orbit the star tracker uses the pre-determined threshold that was obtained by experimentation on the ground facilities. During its operation lifetime, the star tracker experiences several adverse ageing effects such as large radiation doses and temperature cycling which cause the sensor performance to deteriorate with time. This causes the dark current to increase, thereby changing the threshold. In light intensified sensors, this problem is anticipated to be much worse. The equivalent background illumination(EBI) and the phosphor screen flux output is a function of temperature and imaging conditions. Moreover, the background noise need not be uniform across the entire field of view and there could be significant localized variations. In such a case, a single or global threshold is not an appropriate measure of the background. If a global threshold is used, an incorrect evaluation of the pixels belonging to a star may result. This will cause systematic shifts in the centroids, thereby degrading the sensor accuracy.

To demonstrate the effect on an incorrect and a global threshold, a linear tilt/bias is added across the simulated data set as shown in Fig. 47(a). A previously determined constant threshold is used to extract the pixels belonging to the star. The threshold surface is shown in Fig. 47(b). It can be seen that pixels affected by the tilt and lying above the threshold are selected thus skewing the distribution and making it asymmetric. Fig. 48 shows the impact of using on the centroid estimate. The error in centroiding using the LOG-LSQ approach has now increased beyond 0.1pixels while the increase in much more dramatic in the case of the COM approach (0.3pixels). The COM approach is thus highly sensitive to the threshold value.

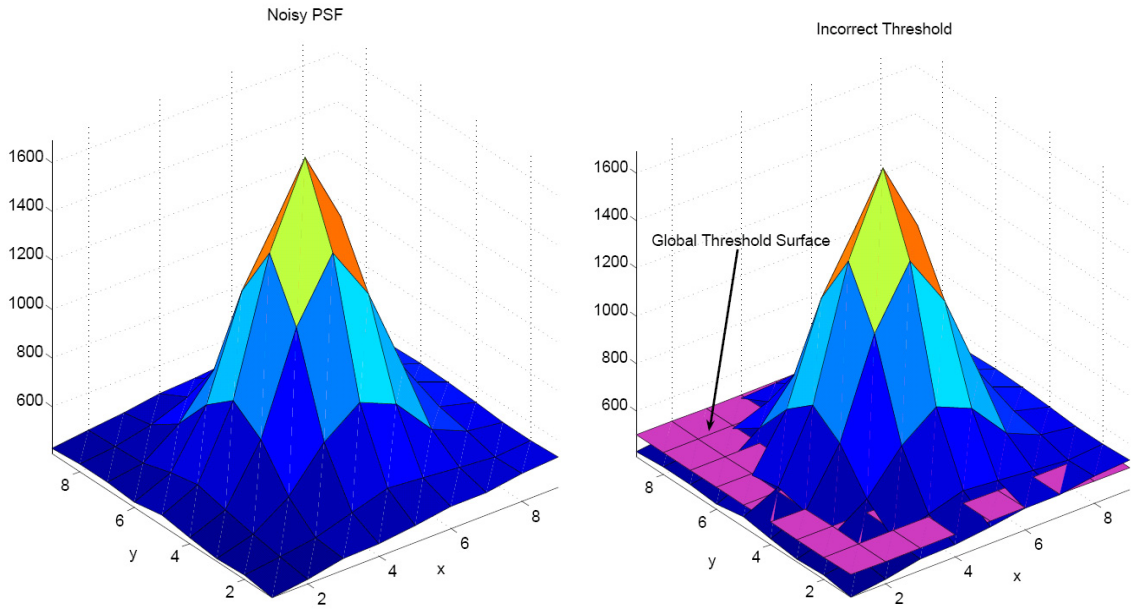

(a) Bias added Star Distribution (b) Incorrect Global Threshold

Fig. 47. A bias added star intensity distribution and incorrect extraction of pixels

2. Least Squares Bias Estimation

We make use of the observation that the background noise has an underlying low-frequency component i.e. the average background surface does not exhibit rapid variations or undulations. Thus in a local region around a star, the background level response can be represented by a plane surface. The pixels lying around the border of the star can be used to estimate the parameters defining this local plane. Doing so, results in the calculation of a local background surface for each star in the image. This can be easily subtracted from the original star mask to remove the tilt/bias in the star intensity distribution.

Consider a star mask of size $n \times m$ pixels obtained by using a global threshold Fig. 49. The noise present in the image is always going to be greater than the one for which the system was calibrated. Furthermore, the star mask will contain most of

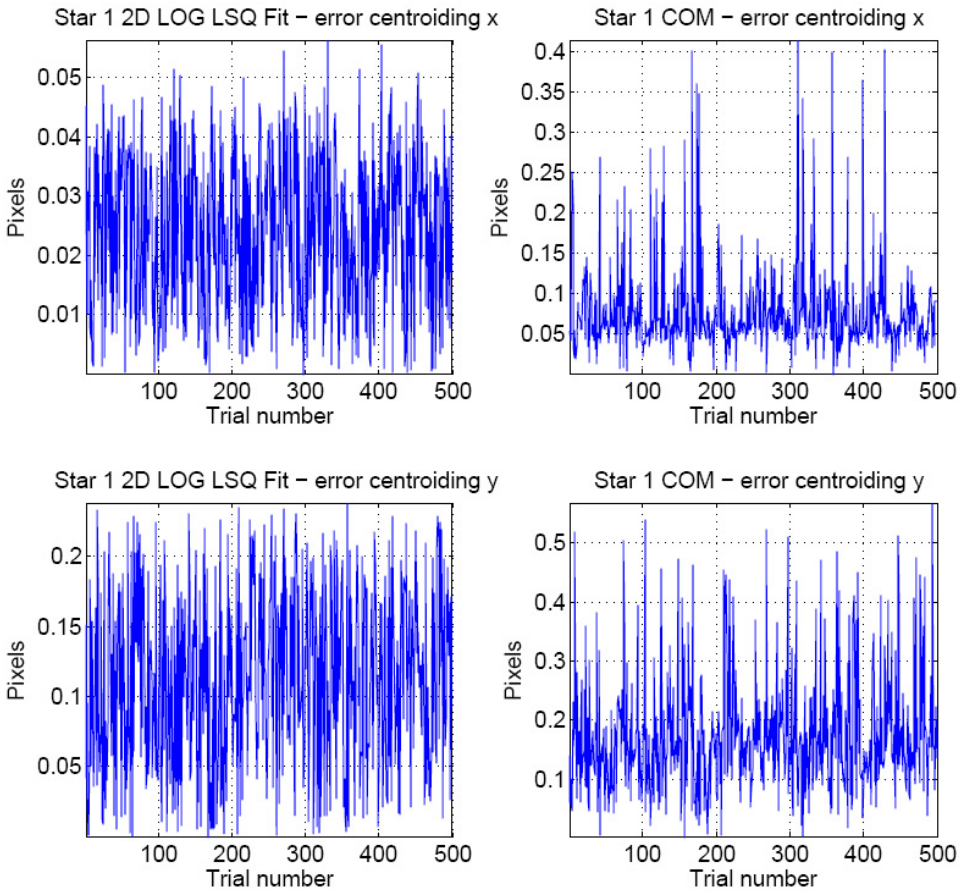

Fig. 48. Increase in the error in centroiding due to incorrect threshold

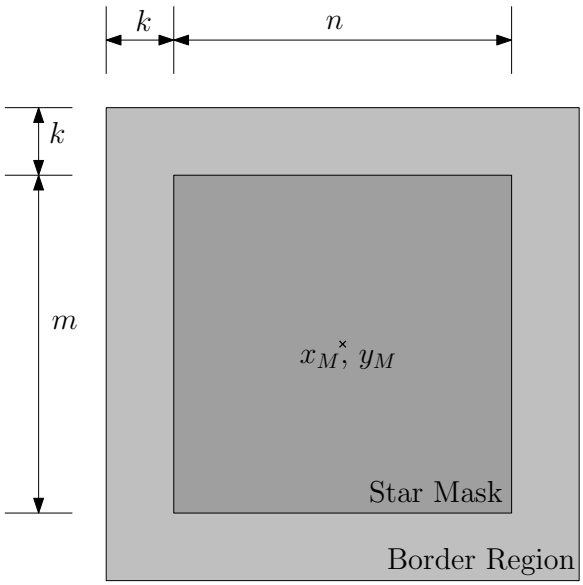

Fig. 49. Illustration of border regions used for background estimation

the star energy ($> 90\%$). Consequently, the gray-scale value of the pixels bordering the star mask can be assumed to primarily contain the underlying background noise. Let k be the number of pixel rows/columns along the border of the star mask under consideration. Thus, the total number of border pixels is $N \equiv 2k(n+2k)+2km$. We wish to fit a plane to these pixel intensities.

Through actual night-sky image analysis, we have found that rather than a plane, a biquadratic background approximation to be more useful:

$$z = a_0 + a_1 x + a_2 xy + a_3 y \tag{4.26}$$

Setting $z \equiv p(x, y)$ where $p(x, y)$ is the gray-scale value of the pixel at location $[x\, y]$, the above equation can be written in a matrix form for each pixel in the border region

as

$$\begin{bmatrix} p(x_1, y_1) \\ p(x_2, y_2) \\ \vdots \\ p(x_N, y_N) \end{bmatrix} = \begin{bmatrix} 1 & x_1 & x_1 y_1 & y_1 \\ 1 & x_2 & x_2 y_2 & y_2 \\ \vdots & \vdots & \vdots & \vdots \\ 1 & x_N & x_N y_N & y_N \end{bmatrix} \begin{bmatrix} a_0 \\ a_1 \\ a_2 \\ a_3 \end{bmatrix}$$

$$\text{i.e.} \qquad \tilde{p} = Ha \tag{4.27}$$

The above equation can be easily solved the linear least squares estimation technique to estimate the unknown parameters a. The parameters can then be readily used to determine the contribution by the background noise at each pixel location in the star mask. A point to note is that since this technique uses polynomial basis functions to estimate the background, it can be easily extended to higher order surfaces if required.

3. Performance Improvement

To confirm the increase in accuracy in centroid estimation in the presence of local noise, the algorithm was implemented in MATLAB. Random background noise was added to each trial run and a total of 500 trial runs were evaluated. Fig. 50 shows the noise-free and noise injected simulated star intensity distributions. The bias compensated/removed surface is also shown along with the weighting function applied. Fig. 51(a) shows the error in centroiding for the LOG-LSQ with weighting and COM approaches. The error in centroid estimation in this case is as high as 0.15pixels for the LOG-LSQ and about 0.175 for the COM. Fig. 51(b) shows the resultant error when the local threshold estimation is used for the LOG-LSQ estimation. The errors in centroiding have now dropped to about 0.04pixels, thus proving the effectiveness of the local background estimation.

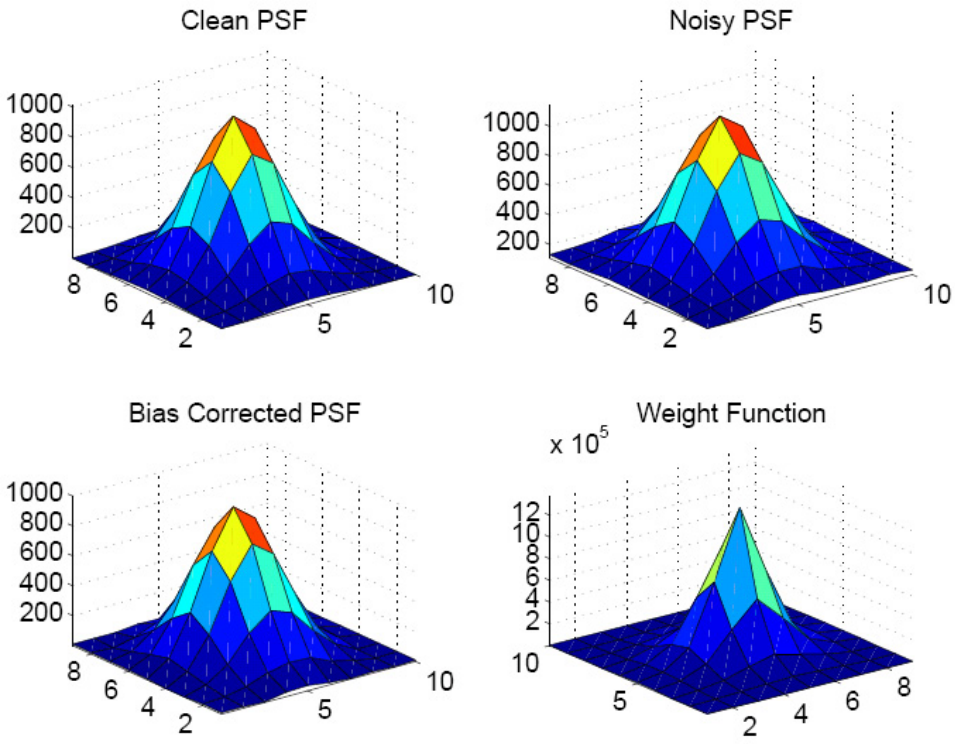

Fig. 50. Simulated star intensity distributions, recovered surface and weighting function for local background estimation

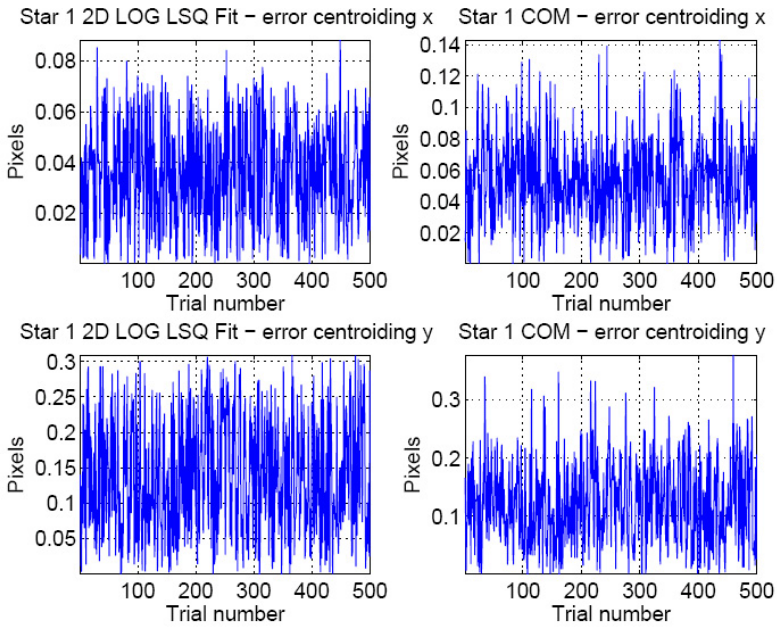

(a) Without local background estimation

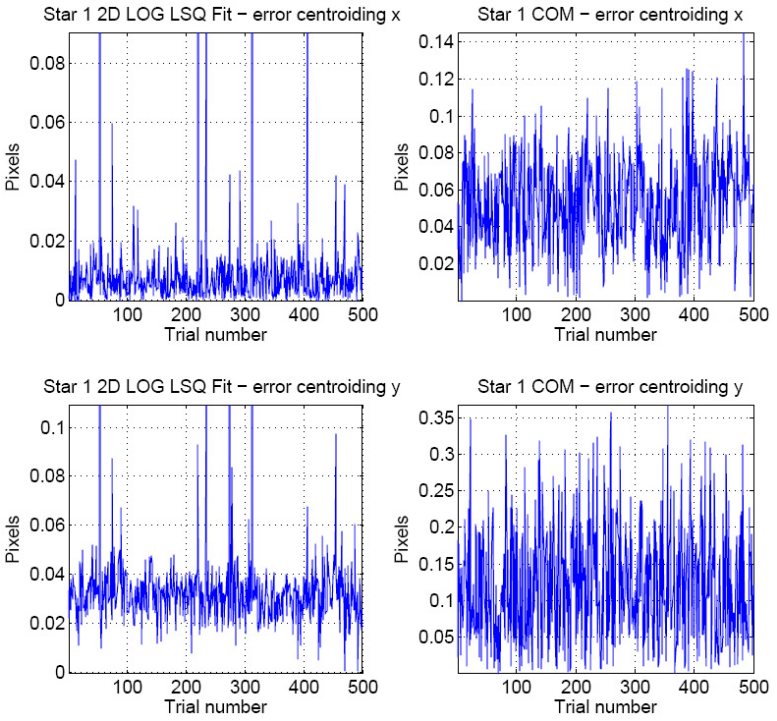

(b) With local background estimation

Fig. 51. Errors in the centroiding without using local background estimation and with background estimation

D. Centroiding Accuracy - Simulated Images

In this section our aim is to develop the end-to-end centroiding methodology based upon the techniques detailed previously and perform accuracy analysis of the centroids obtained on star images. For this purpose, the star image simulator is used to generate images of the star fields visible to the sensor. Since the true calibration parameters (focal length and optical axis offsets) and sensor geometry are user prescribed, the true centroids and consequently, the true inter-star angles are known exactly. Thus, the error in centroiding can now be characterized by a more conventional and pixel-size independent parameter - inter-star angle error.

Given the sensor geometry, the line-of-sight vectors to the centroids can be calculated as

$$\mathbf{b}^k = \frac{1}{\sqrt{(x_k - x_0)^2 + (y_k - y_0)^2 + f^2}} \begin{bmatrix} -(x_k - x_0) \\ -(y_k - y_0) \\ f \end{bmatrix} \tag{4.28}$$

where $[x_k\, y_k]$ is the centroid of the k^{th} star, $[x_0\, y_0]$ are the offsets of the optical axis from the sensor axis and f is the focal length of the sensor. The inter-star angle θ_{ij} between each star pair $i - j$ is given by

$$\cos\theta_{ij} = \mathbf{b}_i \cdot \mathbf{b}_j \tag{4.29}$$

If $\mathbf{r}_i$ is the inertial reference vector to the i^{th} star, then the error in centroiding $\sigma_{cent_{ij}}$ in terms of the inter-star angle error $\Delta\theta_{ij}$ for the $i - j$ pair can be calculated as

$$\Delta\theta_{ij} = \cos^{-1}(\mathbf{b}_i \cdot \mathbf{b}_j) - \cos^{-1}(\mathbf{r}_i \cdot \mathbf{r}_j) \tag{4.30}$$

i.e.

$$\sigma^2_{cent} = \frac{1}{N} \sum_{i=1}^{N-1} \sum_{j=i+1}^{N} \Delta\theta^2_{ij}$$

For an unbiased estimator the above equation is

$$\sigma_{cent}^2 = \frac{1}{N-1} \sum_{i=1}^{N-1} \sum_{j=i+1}^{N} \left(\Delta\theta_{ij} - \overline{\Delta\theta} \right)^2$$

where,

$$\overline{\Delta\theta} = \frac{1}{N} \sum_{i=1}^{N-1} \sum_{j=i+1}^{N} \Delta\theta_{ij} \tag{4.31}$$

Assuming that the noise in the centroiding follows a zero-mean process, the mean in the inter-star angle error given by the above equation should be near zero. Then, σ_{cent} can be computed by taking the statistical variance of an ensemble of $\Delta\theta_{ij}$ errors.

Fig. 52 shows the methodology used for the estimating the centroids of the stars in the images. The location of the maximum pixel in the image is determined by performing a search across the entire image. If the pixel intensity value lies above the pre-computed global threshold, it is considered a candidate for a star else the process terminates. Next, a local search is performed around this maximum valued pixel in order to extract the pixels belonging to a star. In our method, a variable size mask is used since stars of different visual magnitudes occupy different sized areas on the sensor. In contrast to a fixed mask size approach, this method extracts the correct number of pixels thus avoiding outlier influence in case of the star being smaller than the mask or data loss in case the star is bigger than the fixed mask size. In the next step the validity of the candidate star is verified by obtaining statistics on the mean pixel value and standard deviation of the pixels in the mask. If the mask contains a valid star, then the standard deviation in the intensity of the pixels will be large and the mean will be much greater than the global threshold. Additionally, the size of the mask must be greater than 2×2 for reliable centroids to be obtained. If all the three conditions are satisfied, the mask is accepted as a star.

Given the size and the location of the mask, a 2 pixel wide border around it is

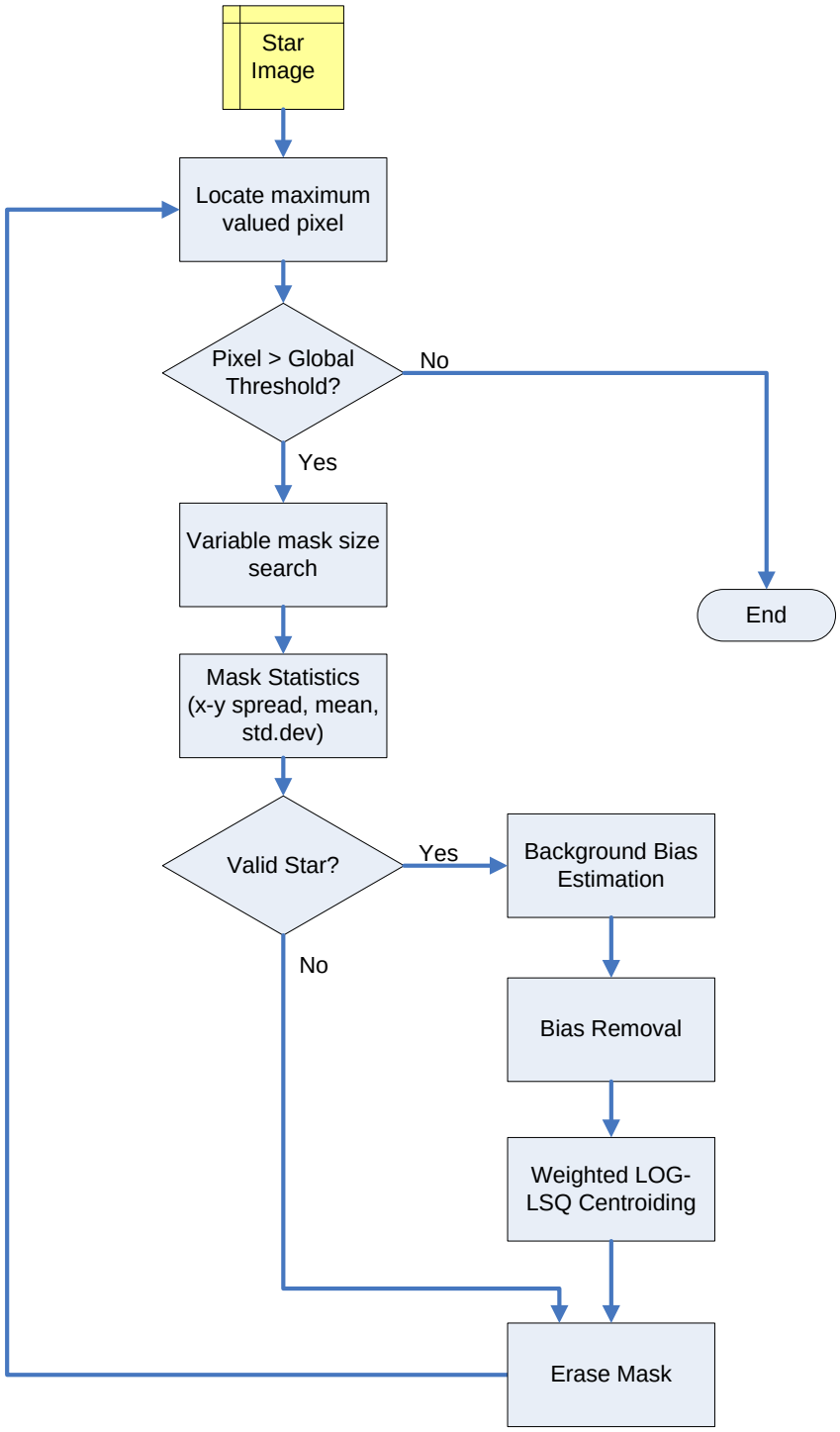

Fig. 52. Flowchart of the centroiding methodology

extracted from the image. Any pixels in this border region that are above the global threshold are rejected. Using these border pixels, the background bias is estimated and subtracted from the star mask. The bias compensated mask is then fed into the weighted LOG-LSQ algorithm where the centroid of the star intensity is estimated. The mask is then cleared from the image and the process is repeated until there are no more candidate stars in the image.

A point to note is that in the entire process, the search for the maximum pixel is the slowest step and has to be repeated n times in this implementation, where n is the total number of candidate stars in the image. Instead of searching the image n times, a single search can be performed using the method described by Mortari[25]. Furthermore, even during the single scan, knowing the size of the point spread function (PSF) of the optics and the sensor geometry, the image can be read by sub-sampling, thus reducing the scan time. For example - if the PSF size is 3×3 pixels, then every third pixel can be read, thereby cutting the scan time by a factor of nine. More complex patterns such as ray-fans and spiral scans with sub-sampling can also be adopted.

A star image containing at-least 5 stars is generated using the star simulator by prescribing a random attitude. Systematic as well as random noise is added to the image and centroiding is performed. The inter-star angle errors are determined using Eq.4.30 for each star pair. This procedure is repeated 500 times and the statistics of each inter-star pair are obtained.

Fig. 53 shows one of the images used for the centroiding analysis. The variation in the background level can be seen across the image. Fig. 54 shows the errors in the inter-star angles obtained for these tests using the LOG-LSQ method and the COM techniques. The mean error for the LOG-LSQ is around $15.6\mu rad$ which is about half as much as obtained by using the center of mass ($31.5\mu rad$). The deviation from the

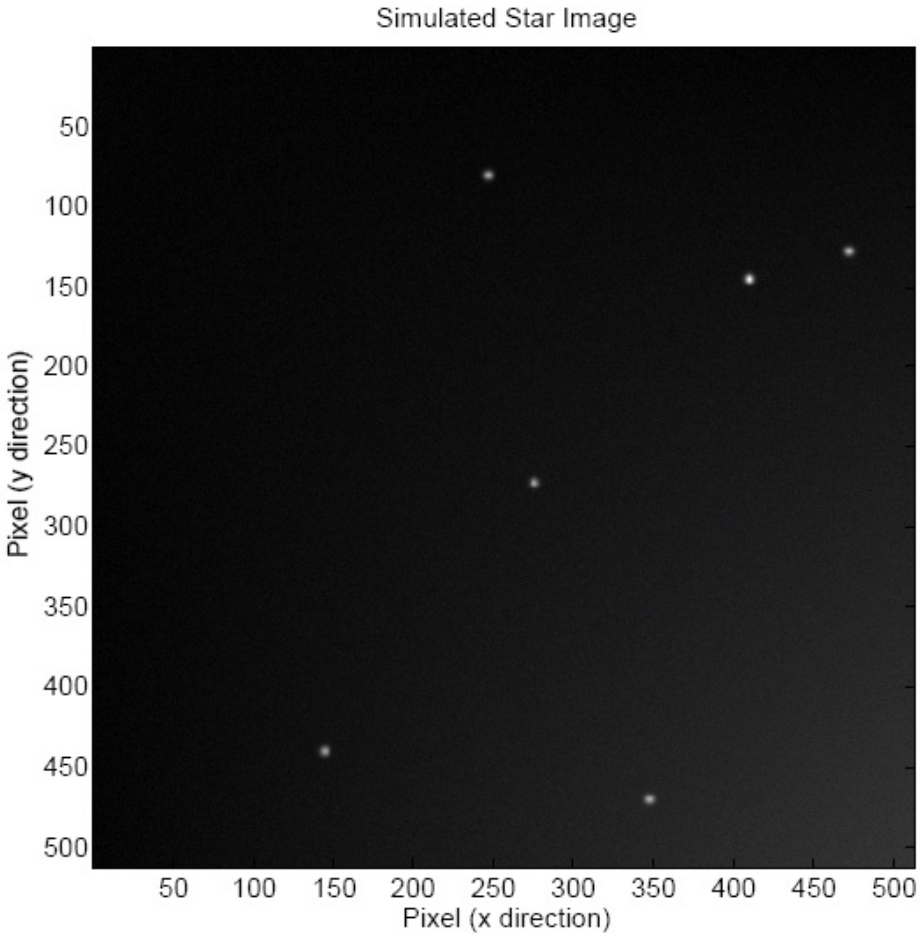

Fig. 53. Simulated star image. Note the variation in the background across the image

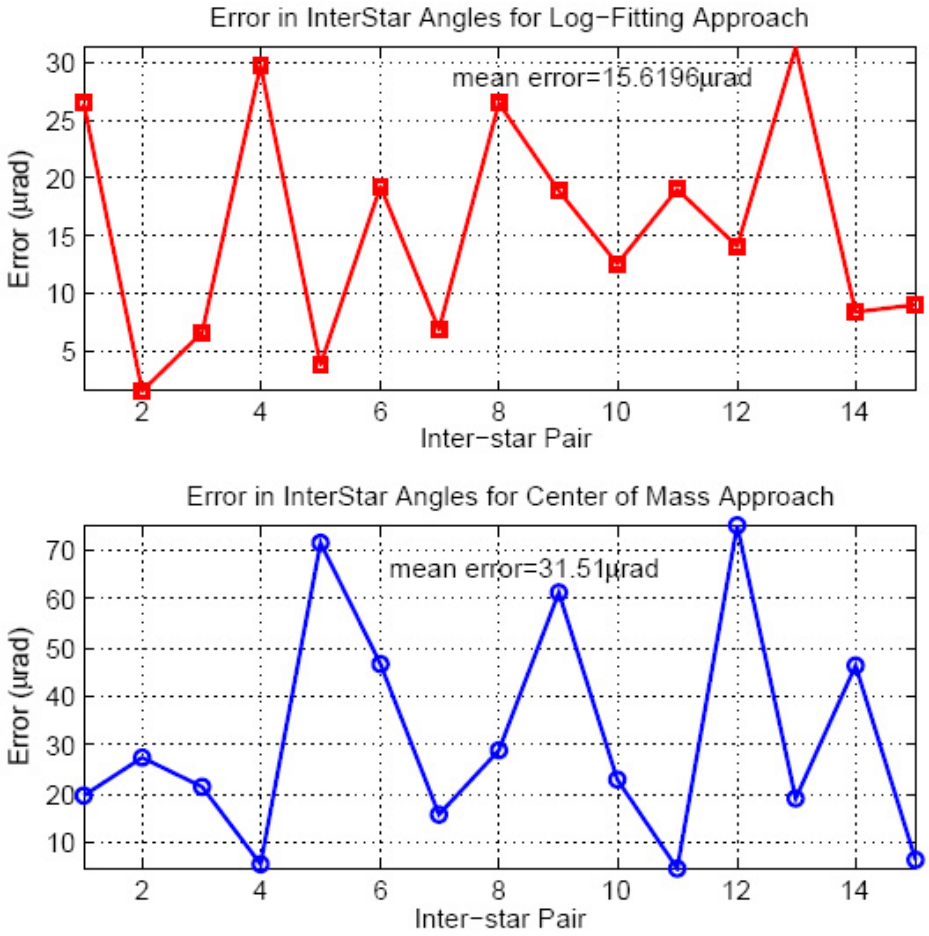

Fig. 54. Inter-star angle error for 500 tests for centroiding using LOG-LSQ and center of mass approaches

mean for the LOG-LSQ is also smaller than that of the COM.

E. Concluding Remarks

In this chapter we developed a new technique (LOG-LSQ) for centroiding of star intensity distributions on the imaging sensor. While this technique is similar to the 2D Gaussian Fitting method, it does not require a non-linear least squares to estimate the parameters of the Gaussian. By a rearrangement of the logarithm of the equation, it is possible to determine the centroid and variance of the distribution using standard linear least squares. The distribution obtained is similar in shape and spread to the original but not in pixel intensity values. However, we realize that our primary objective is astrometry and not photometry i.e. obtaining an accurate centroid location is more critical than obtaining an accurate pixel intensity profile. In order to reduce the effect of outliers on the estimate, the measurements are weighted using a weighting function derived from the intensity values. We also addressed the need to have an automatic threshold determination for each image and developed a least squares based method for the same. The accuracy of the centroids obtained by using the proposed method was compared against the center of mass techniques for a number of test cases and scenarios. It was found that in all the situations, the LOG-LSQ method outclasses the traditional and most often used center of mass technique.

In the next chapter we will address the night sky testing of the image intensified star camera prototype and use the LOG-LSQ algorithm to estimate the centroids and characterize the error performance on real intensified images.

CHAPTER V

NIGHT SKY EXPERIMENTATION

Although a multitude of simulations can be carried out in order to perform a comprehensive characterization of the light intensified star tracker, no test can simulate the actual night sky and hardware implementation, or serve as an adequate replacement for night sky experiments. The integration of several hardware components and their interaction usually gives rise to several unforeseen challenges. Additionally, the electro-optical model while being extensive, cannot be expected to predict all of the real-life noise characteristics specific to each device and setup. Thus, night sky experimentation affords an opportunity to validate and refine simulation models, as well as the hardware implementation. Furthermore, it is essential to test the capabilities and performance of the centroiding algorithms on real data-sets. The objectives of this chapter are thus twofold:

- Describe the building of a prototype image intensified star sensor
- Report results from night-sky experimentation and use them in order to -
    1. Perform a photometric analysis of the actual star sensor hardware, and
    2. Characterize the actual performance of the centroiding methodology

A. Hardware Setup

The main components required for a proof-of-concept prototype are the image intensifier, power supply with gain control, imaging sensor and the intensifier to sensor coupling mechanism. The choice of each individual component is mainly governed by performance, cost and lead time for component acquisition. Performance and cost

are highly correlated and in all but one component - image intensifier, the cost was the primary deciding factor since our budget was limited.

1. Image Intensifier

A wide variety of intensifiers are available in the market today thanks to the recent proliferation of night vision devices and security systems. Choices range from low performance inverting type Gen2 intensifiers to the latest Gen4 devices. The Gen4 devices however, are accessible only for military use. Gen3 devices with a multitude of options and configurability are available from commercial establishments such as Hammamastu Inc., ITT Industries and Proxitronic GmBH. A Gen3 Ultra-Blue image intensifier (FS9910C) made by ITT Industries was selected for the prototype design and configured as listed in Table VIII.

2. Power Supply

A compact power supply (HVPS20074000-001) made by GBS Power Systems with a maximum gating frequency of 100Hz was used to control the image intensifier. The power supply takes in as input a 5V DC signal and generates all the high voltages required by the image intensifier while drawing a maximum current of 50mA. Thus, the total power consumed by the intensifier and the power supply is less than 250mW. The power supply also has an analog input $(0-5\text{V})$ which can be used to control the gain of the MCP. Table IX lists some of the physical properties of the power unit.

3. Intensifier to Sensor Coupler

Since a fiber optic taper has a coupling efficiency of about 70% as compared to less than 5% for a relay lens mechanism, it was the easy choice for the intensifier to imager coupling. Additionally, the taper provides a compact low mass solution as compared

Table VIII. Specifications for the configured image intensifier

ITT FS9910C	
Specification	Value
Aperture effective area	18mm
Photocathode	GaAs
Photocathode sensitivity	75mA/W
Signal to Noise	21
Resolution	64lp/mm
MTF at 25lp/mm	0.4
MCP Stages	Single
MCP pore size	$6\mu m$
Phosphor screen	P43
Input window	Borosilicate glass
Output window	Fiber optic
Nominal operating voltages	
Cathode to MCP	900V
MCP input to output	$800 - 1100$V
MCP output to Phosphor screen	4000V

Table IX. Specifications of the power supply

GBS HVPS20074000-001	
Specification	Value
Input Voltage	5V
Gating frequency	100Hz
Gain Control	Analog $0 - 5$V
Maximum operating current	50mA
Size	1.5" $\times$ 1.5" $\times$ 0.40"
Weight	60gm

to a bulky relay lens system. A taper suitable for interfacing with a 1/3" imager and having an input diameter of 18mm was selected and acquired from Edmund Optics Inc. and is shown in Fig. 55. The weight of the fiber optic taper was 80gm. On the input side, the fibers were 6μm in diameter and were reduced to 3μm in diameter on the output side.

4. Imaging Sensor

A Sony ICX255AL 500×582 pixel inter-laced CCD with a pixel size of $9.8\mu m \times 6.3\mu m$ was used as the detector in the prototype. The sensor was configured to acquire CCIR video frames at 25Hz. The acquired video frames were digitized using an analog to digital converter. Automatic gain control and exposure control was turned off by modifying the video board. An important consideration during the selection of the imager was the pixel size. In order to avoid "chicken-wire" or Mòire patterns, it is essential that each pixel be illuminated by more than one fiber. Usually 4 fibers per pixel is used as a rule of thumb. Since the fibers on the output side of the taper

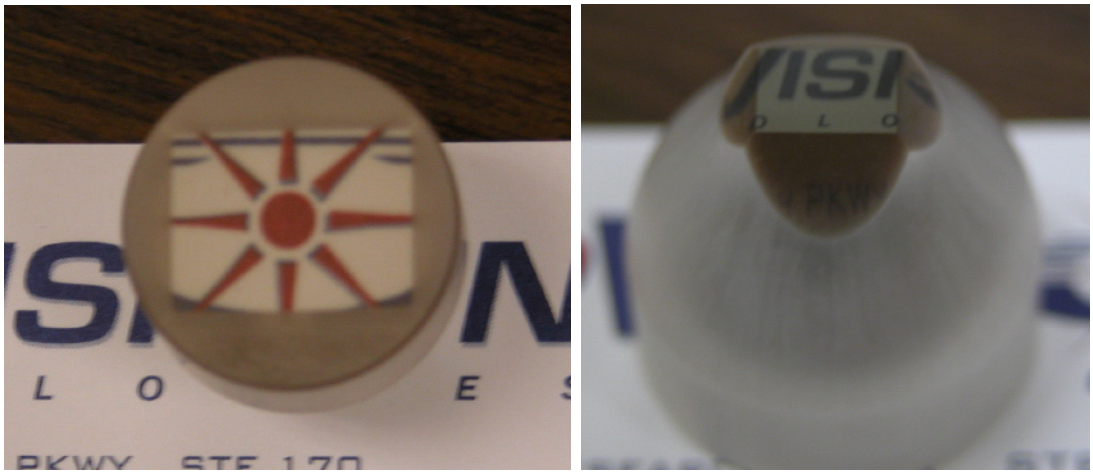

(a) Input Side (b) Output Side

Fig. 55. 18mm input and 1/3" imager compatible fiber optic taper used intensifier to CCD coupling

bundle are $3\mu m$ in diameter and the smallest pixel dimension is $6.3\mu m$, each pixel is covered by at-least 4 fibers, thereby reducing the chicken-wire patterns and creating a more uniform light distribution across the pixel.

5. Component Integration

An assembly for holding each component was designed and fabricated in the laboratory. The most challenging task was the alignment of the fiber optic taper with the output window of the intensifier on one side and the CCD on the other side. Light exiting the fiber inherently spreads in a conical fashion about the fiber axis. Thus the two surfaces - fiber taper input window and output of the intensifier have to be in perfect contact with each other. However, no surfaces can be perfect and minute variations in the surface profiles always exist. Fig. 56 shows the results of a simulation in ZEMAX when the two surfaces are not in contact with each other. The spreading of light is evident from the ray-trace. The spreading leads to a loss

in resolution and reduced coupling efficiency since reflection losses at the interfaces increase.

In order to negate the surface variations, two attachment techniques are usually employed. Both of them use an index of refraction matched chemical that acts as a filler between the two contacting surfaces. The first method uses an oil suspension on and around the interface while the second uses an optical glue. Since the oil is in a liquid phase, special packaging is required for its containment and handling is more difficult. The optical glue is the more commonly used and robust method. The viscous glue is applied in very minute quantities to both the surfaces which are then pressed against each other to give a very thin layer ($\sim 100\mathring{A}$) thick. The glue is then cured by using a UV light source. The gluing is usually permanent and in cases in which it is not so, it is extremely difficult to remove the glue. Industrial and space qualified versions of the glue are available and this method is usually the standard practice. In our case however, since this was a first attempt and it is a proof-of-concept prototype, an optical gel with an index matched to the fiber was used instead to provide reconfigurability and "learning cycles".

On the output side of the taper bundle, the toughest problem faced was the removal of the glass cover of the CCD. The die of the imager is usually located inside the chip and is protected by a glass, which is fixed to the ceramic package using a UV curable epoxy glue. No solvents are available for dissolving the glue. The cover in our case was removed by grinding and cutting the glass along the glued edges. This harsh procedure resulted in the safe removal of the glass at the cost of causing a few scratches on the surface of die. The loss in sensitivity or a few pixels at this stage was deemed tolerable for testing purposes. During the actual product manufacture, the image sensors can be procured from the sensor manufacturers with the glass removed. The integrated setup is shown in Fig. 57.

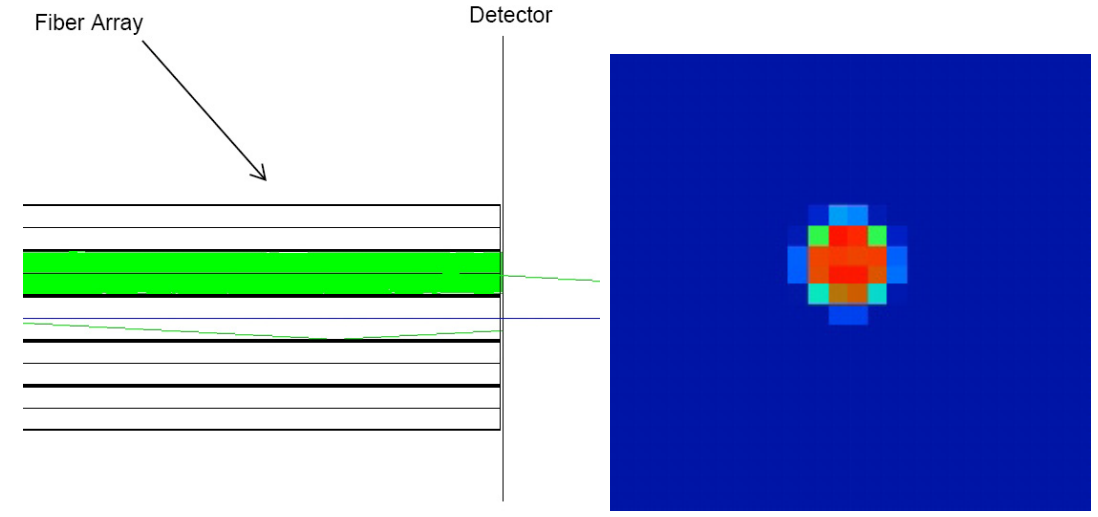

(a) No gap (b) Detector output

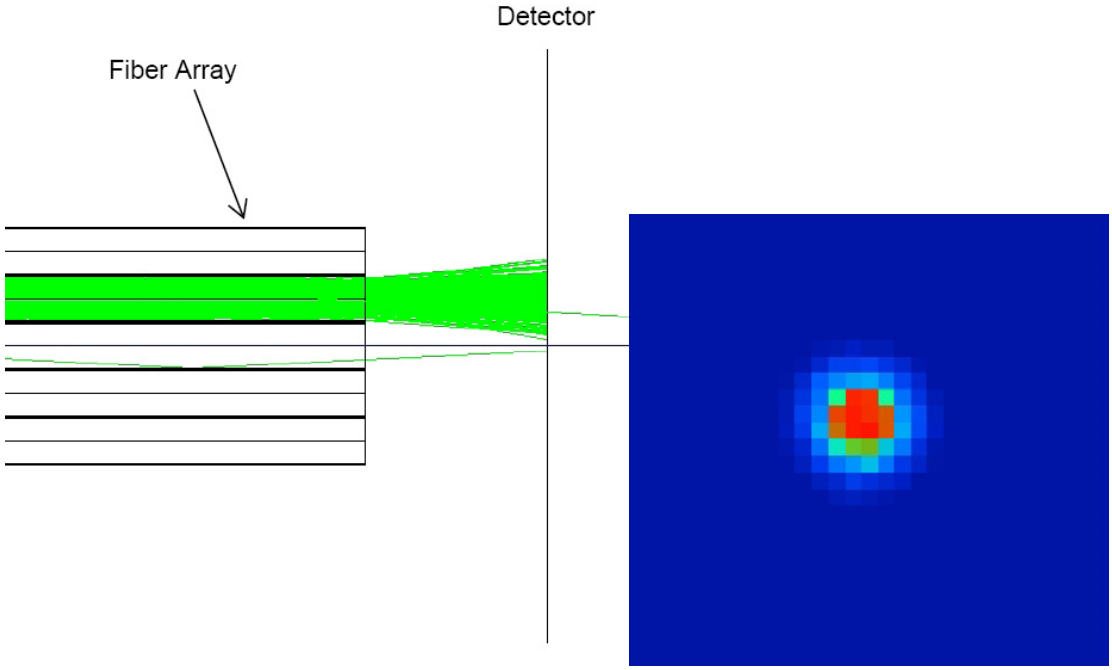

(c) $75\mu m$ gap (d) Detector output

Fig. 56. Spreading of light at the output of fiber when surfaces are not in perfect contact

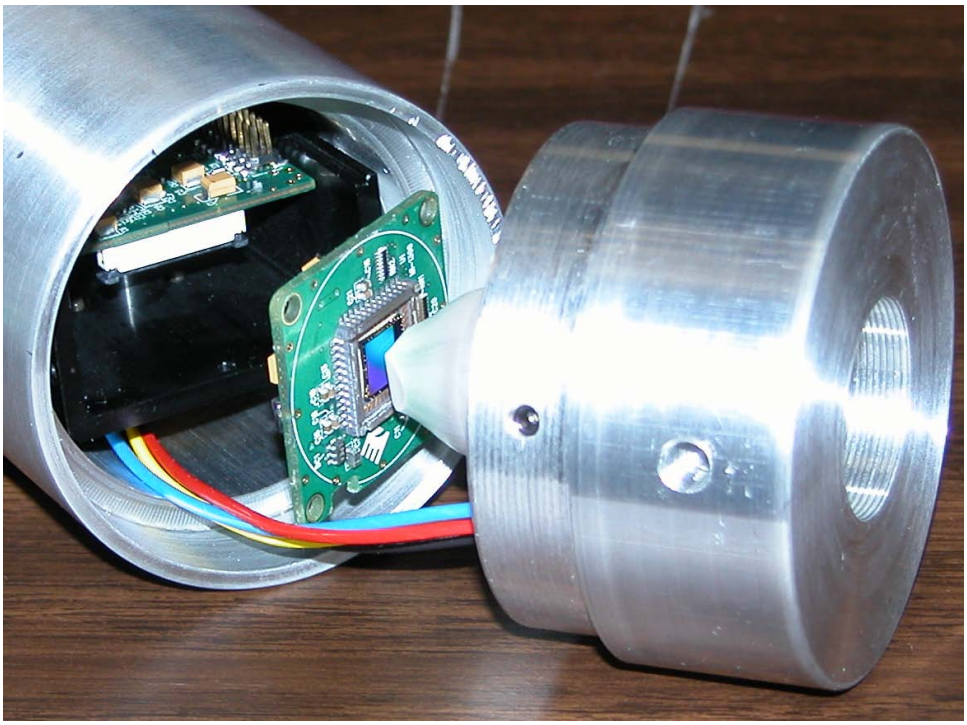

Fig. 57. An inside view of the integrated prototype

B. Night Sky Testing

A commercially available Nikon 55mm lens with variable aperture stops was used as the primary objective and was mounted to the camera housing using a C-mount adapter. The field of view of the setup was approximately $6^\circ \times 5^\circ$. The lens was focused such that the image of the night sky is formed on the photocathode. The gain control voltage and the aperture were varied to obtain a sequence of images for different parts of the sky. Fig. 58 shows some of the images acquired with the f-stop of the lens set to 4.0 i.e. an aperture of 13.75mm.

Comparing the intensified image taken of Orion's belt with the un-intensified image, the difference in the number of stars visible is striking. With the intensifier turned OFF, about 8 stars are visible and this number jumps to about 60 when the intensifier is powered and gain is applied. Note however, that the background noise

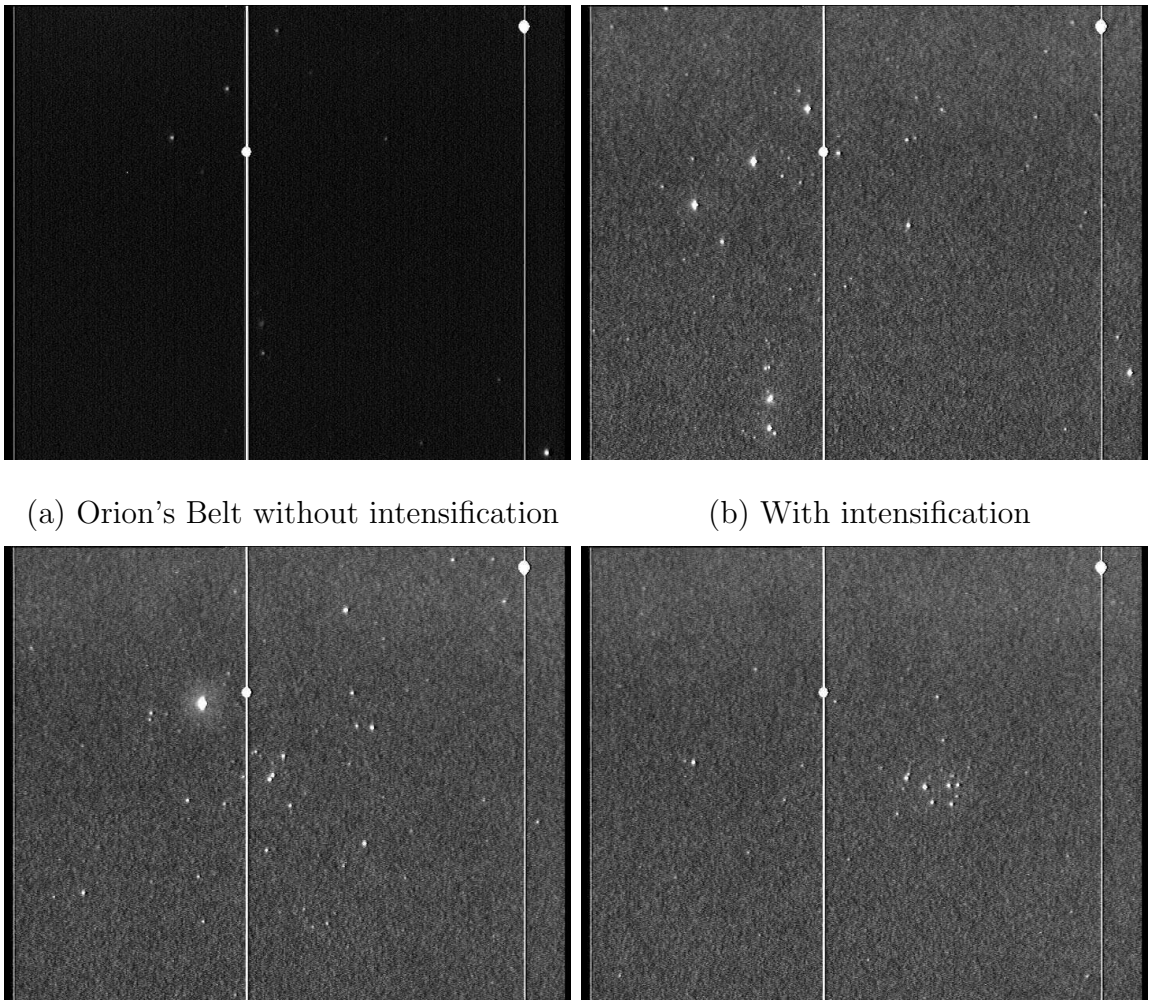

(a) Orion's Belt without intensification

(b) With intensification

(c) Aldeberan

(d) Pleadies Cluster

Fig. 58. Night sky images of various parts of the sky. Taken at f4.0 and gain control voltage of 3.7V

has increased and more importantly, it is non-uniform across the image. The two white columns are the result of the combination of irreversible CCD blooming as well as un-intentional damage to the CCD when removing the glass covering. This caused the areas to be optically inactive i.e. dead.

1. Photometric Analysis

The acquired images were analyzed using image processing software (AIPWIN) to measure image characteristics such as background noise, star spread and surface profiles. It was anticipated that since the intensifier is a non-linear amplification device and each of the MCP channels has a slightly different gain, the star point spread function could be distorted. Fig. 59 shows the pixel intensity distribution for an un-saturated star and a saturated star. It can be seen that the star profile obtained is similar to that of a non-intensified camera output but for the background noise. Even in the case of the saturated star, the saturation is pretty uniform and symmetrical about the center of the distribution. Thus, the intensifier does not add appreciable/visible distortion to the image, validating the claim in the manufacturer's data-sheets.

Although the size of the star point spread function is independent of the brightness of the star, the presence of background noise, CCD full-well capacity and resolution cause the star spread to be proportional to the brightness. In the sequence of night sky images, stars were visually identified using astronomical charts and their visual magnitudes obtained. The star spread was characterized by its half-width half-maximum (HWHM) i.e. the width at which the signal is half of that at the peak. Fig. 60 shows the plot of the HWHM against the visual magnitudes of the stars. Each datapoint was obtained by averaging the HWHM of 10 images of the same star. The HWHM shows a linear trend with respect to the star brightness. The linearity would

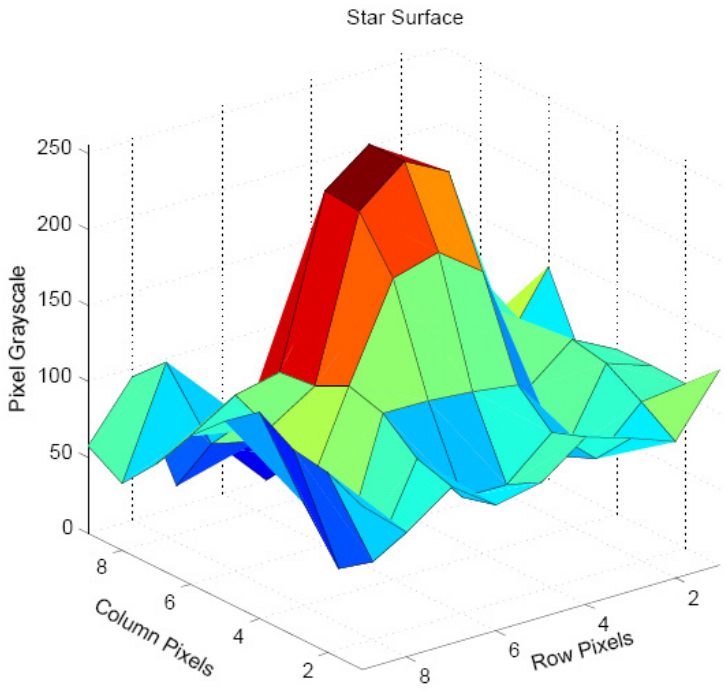

(a) Un-saturated Star

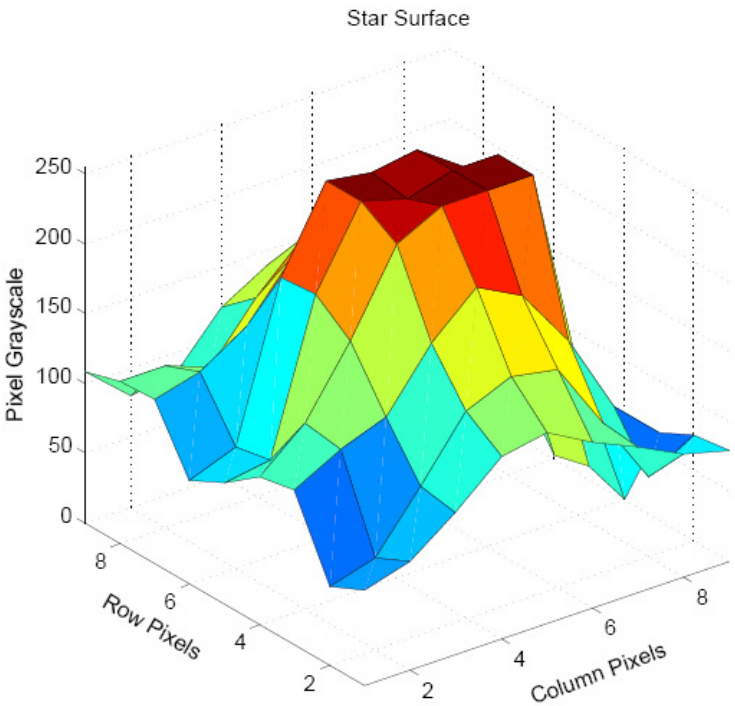

(b) Saturated Star

Fig. 59. Star intensity distribution surfaces on the imaging sensor

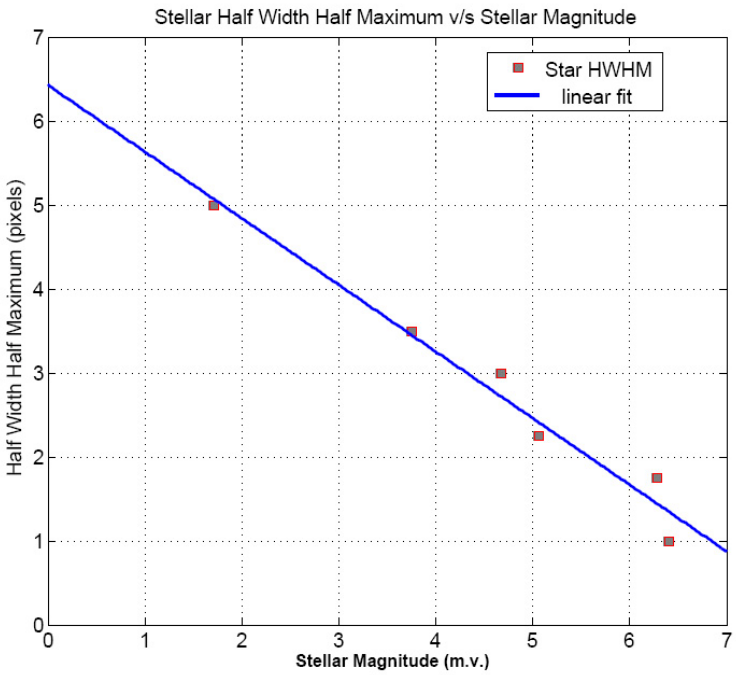

Fig. 60. Half-width half-maximum for stars of different visual magnitudes

be expected to fall off for stars that are fainter than m.v.6.0 since the background noise would contribute a large fraction of the signal i.e. the star would have poor signal to noise ratio.

a. Variable Gain at Fixed Aperture

In this set of tests, the aperture of the lens was kept constant at 27.5mm and the gain was varied. The objective of this test was to characterize the increase in the background noise with an increase in the gain. This test replicates the scenario of an actual product being used for imaging, since the aperture would be fixed by design and the only control variable would be the gain. Fig. 61 shows a sequence of images acquired of the Orion field at different gain settings. Since in a given frame the background noise is not uniform across the field of view, five background windows each of which is 21 $\times$ 21 pixels are extracted from each image. The windows are

located at the four corners and near center of the image. A set of 5 images is used at each gain setting. The mean of each of the windows across the set of the images is calculated and taken as a data point. Fig. 62(a) shows a plot of these data points against the gain control voltage applied. As was expected the background noise shows an exponential increase after a break-in or "knee" voltage of around 2.75V. This is the voltage at which the intensifier starts providing a net gain in the photoelectrons across the MCP. In addition to amplifying the starlight, beyond this gain setting the intensifier also amplifies background noise.

In addition to the internal noise of the intensified camera system, the ambient light also manifests itself in the intensified image background. The contribution due to the ambient is dependent however on the aperture of the system. Thus, rather than using the mean, the standard deviation of the pixel intensities in the background would provide a better characterization of the random noise levels in the background. Fig. 62(b) shows the standard deviation computed across the five sets of images and each of the five windows in the images. As can be seen from the plot, the random component of the noise also shows an exponential rise with increasing gain voltage. The "knee" is clearly evident as well. An interesting observation is that the variation in the standard deviations within each image also increases with increasing gain. This shows that the noise characteristics vary spatially and temporally. This further reinforces the need to perform on-line autonomous local background estimation for each star location.

2. Centroiding Performance

The objective of this test is to estimate the error in centroiding of the intensified images. The addition of the fiber optic taper, imperfect surface contacts and limited resolution of the intensifier cause a spread in the star point spread function, thereby

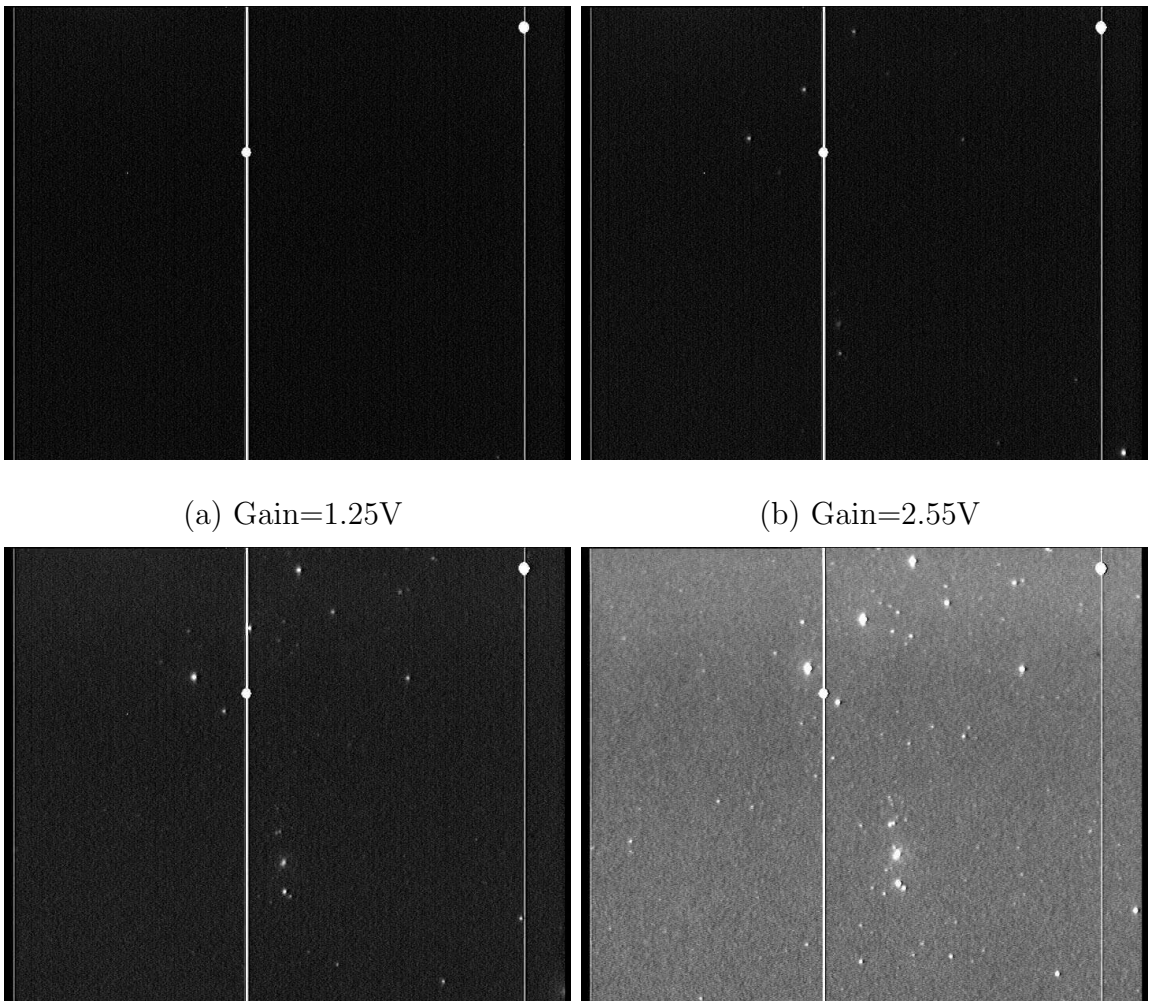

(a) Gain=1.25V

(b) Gain=2.55V

(c) Gain=3.0V

(d) Gain=3.5V

Fig. 61. Acquired images at various gain voltages at f2.0

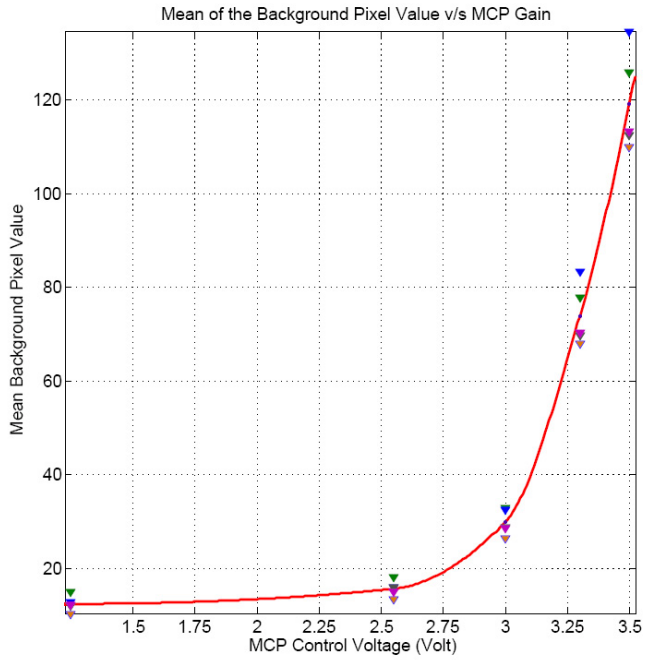

(a) Mean background levels

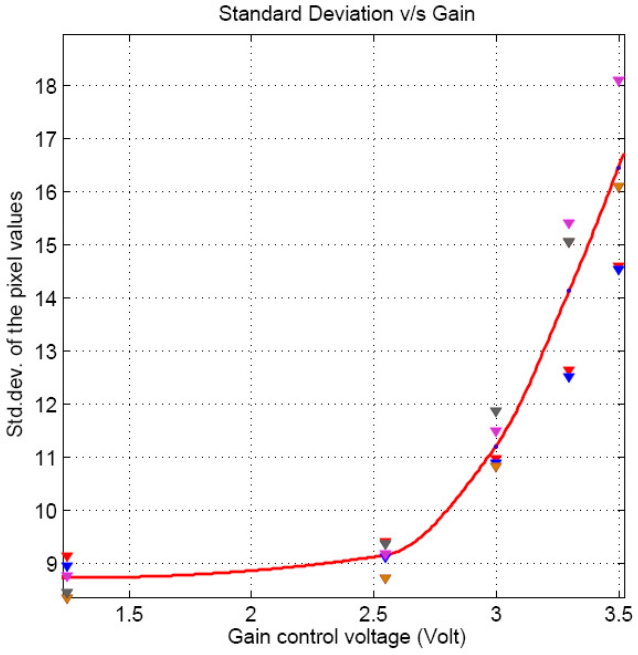

(b) Standard deviation of the background level

Fig. 62. Statistics of the background noise levels for different gain settings

possibly corrupting the centroids. The error in centroiding can be characterized by two metrics - pixel errors and inter-star angle errors. The inter-star angle error was chosen as the metric for comparison since it provides a pixel size independent measure. A sequence of 200 frames of the same star field were acquired and centroided using the center of mass and the LOG-LSQ techniques. The global threshold for both the methods was identical and was calculated using the mean and standard deviation of all the pixels in the image and for each image as

$$\text{Global threshold} = \text{mean(image)} + 8 \times \text{std.dev(image)} \tag{5.1}$$

Using the threshold given by the above equation the centroiding methodology outlined in the previous chapter was used for determining the LOG-LSQ centroids. In order to correctly characterize the inter-star angles, it is essential to have the exact intrinsic calibration parameters i.e. optical axis offsets and focal length in addition to the inertial reference vectors to the stars in the field of view. However, at this stage, the calibration parameters are not available. It can be shown however [34] that under the assumption of the noise being described by a Gaussian random process, the mean and the variance of the sample set are equivalent to the mean and variance of the process. Thus, using the nominal focal length and nominal offsets, the body measured vectors can be easily determined and inter-star angles estimated. The deviation from the mean then characterizes the error in the inter-star angles. Fig. 63 shows the centroids obtained for the Orion star field. Even though a very high threshold was used, centroids to about 37 stars were still obtained. Since many of the stars are relatively faint or of approximately the equal brightness, it was difficult to correlate and track the stars across the entire set of images. If a star was not detected in the consecutive image frame it was dropped from the analysis. Thus, at the end of the run, about 18 of the total 37 stars were used in the error computations. For each star

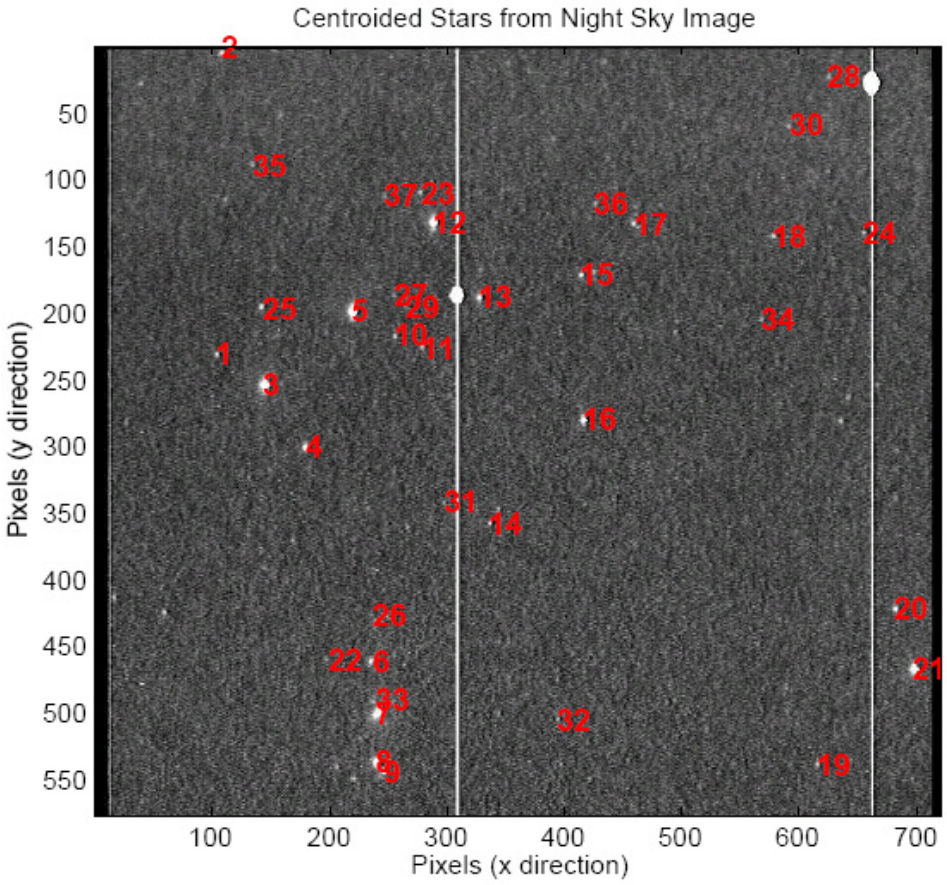

Fig. 63. Detected star centroids in the night sky image of the Orion's belt

Table X. Performance comparison in the inter-star angle errors obtained by using center of mass and LOG-LSQ methods on the night-sky images

Method	Without Background Estimation	With Background Estimation
COM	7.95 arcsec	7.91 arcsec
LOG-LSQ	5.86 arcsec	4.68 arcsec

pair in the image, the inter-star angle was determined and tracked across the set. The mean and deviation from the mean for each star pair data set was calculated. Fig. 64 shows the deviation from the mean in the inter-star angles between star number and some its associated star pairs as it was tracked across all the valid images.

In the above test, the local background was not estimated for each star and only the global threshold was used to extract the star windows. It was seen that the inter-star angle errors in the centroids obtained by using the LOG-LSQ method are smaller than those of COM technique. Comparing these results to the outcome predicted based on the simulations in Chapter IV, we see that we approach the factor of 2 improvement anticipated for the 10% noise case. This experimental result is very gratifying. Fig. 65(a) shows the mean of the deviations across all the star pairs for all the images in the dataset. As can be seen from Table X, the LOG-LSQ algorithm performed better than the COM on an average.

The test was repeated with the local background estimation being performed for each star during the LOG-LSQ process and the mean of the deviations was recomputed as shown in Fig. 65(b). The error in inter-star angles was reduced by a non-negligible amount of about 1.2arcsec or 21%. Note that the inter-star angle centroiding error is theoretically equal to $\sqrt{2}$ times the centroid location error expressed

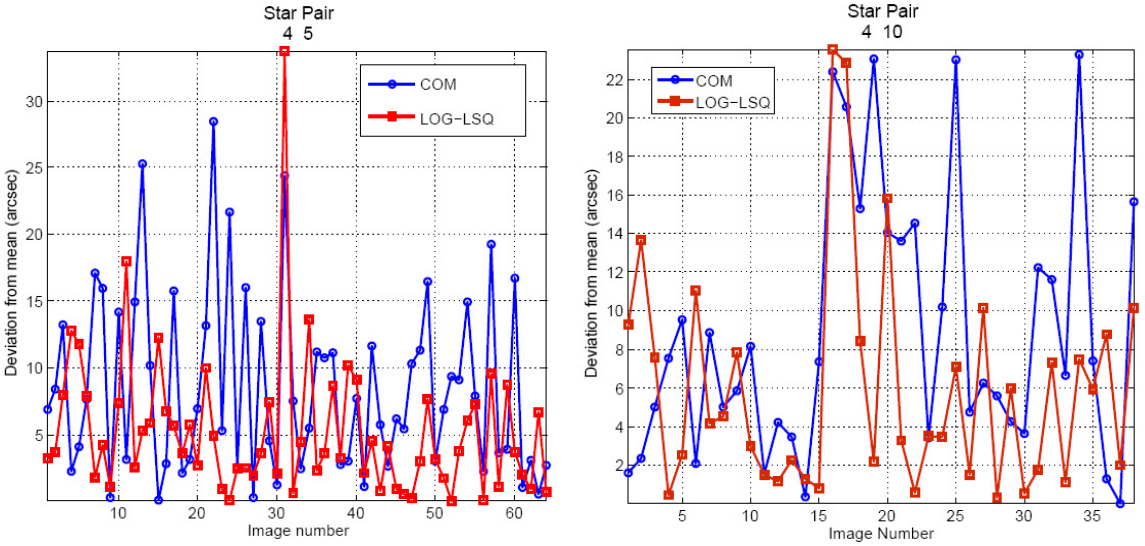

(a) Star pair 4 5

(b) Star pair 4 10

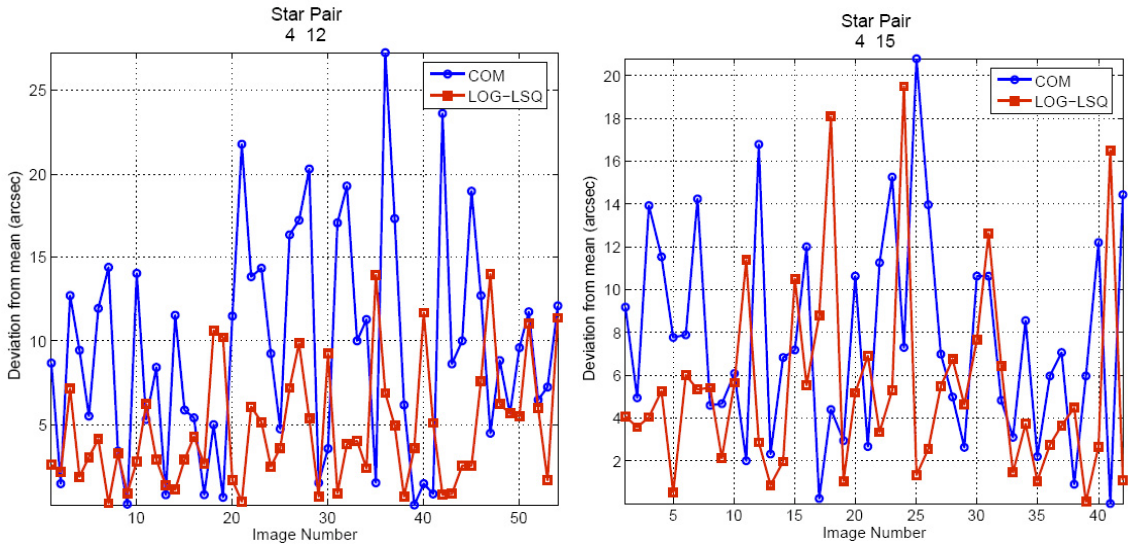

(c) Star pair 4 12

(d) Star pair 4 15

Fig. 64. Inter-star angle statistics for star number 4 using COM and LOG-LSQ methods

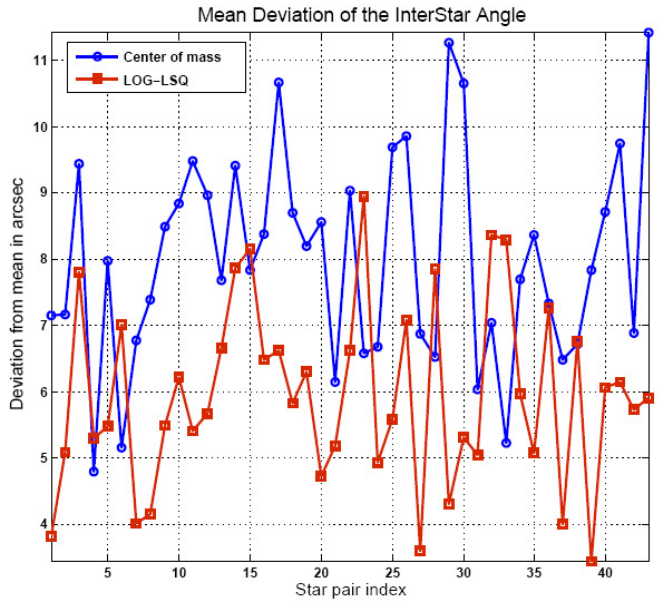

(a) Without background estimation

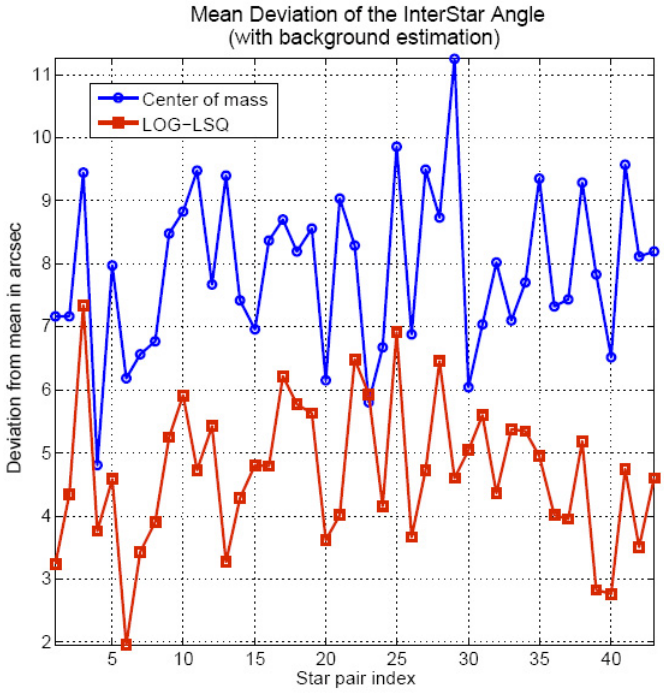

(b) With background estimation

Fig. 65. Mean of the deviations in the inter-star angles for all star pairs across all image sets

as equivalent angle.

C. Concluding Remarks

In this chapter, we described the component selection and their integration to create a proof-of-concept image intensified camera prototype that can be used for night-sky testing. A 18mm Gen3 Ultrablue image intensifier from ITT Industries along with a power supply from GS Electronics was procured and attached to a fiber optic taper and CCD imaging sensor. The attachment of the taper proved to be the most difficult task as it involved removal of the protective glass cover of the CCD. Surface contact imperfections not only cause an unwanted spreading of the star PSF but also a reduction in coupling efficiency due to interface reflections.

Night-sky testing of the prototype was performed and sequence of images from various parts of the sky were obtained. A photometric analysis was performed to study the background noise levels and the star intensity distributions. The image sequences were also centroided using the COM and LOG-LSQ approaches. It was seen that the LOG-LSQ method performs better than the COM i.e. the errors in the inter-star angles are reduced by about 40% when the LOG-LSQ with background estimation is used. In the previous chapter, we had claimed the superiority of the LOG-LSQ over COM based upon simulated images and data. The night-sky testing provides an experimental validation of our claims.

CHAPTER VI

CONSTRAINED STAR RE-CENTROIDING AND ATTITUDE ESTIMATION

A. Introduction and Wahba's Problem

The most critical step in the attitude determination process is the estimation of the centers of the star intensity distribution (centroids) on the sensor. The centroiding process effectively derives a composite "measurement" of the star position from the pixel response. Knowing the camera calibration parameters, the effective measurement of the line-of-sight vectors to the centroids can be calculated as

$$\mathbf{b}^k = \frac{1}{\sqrt{(x_k - x_0)^2 + (y_k - y_0)^2 + f^2}} \begin{bmatrix} -(x_k - x_0) \\ -(y_k - y_0) \\ f \end{bmatrix} \tag{6.1}$$

where $[x_k\, y_k]$ is the centroid of the k^{th} star, $[x_0\, y_0]$ are the offsets of the optical axis from the sensor axis and f is the focal length of the sensor. Without loss of generality, the optical offsets can be assumed to be zero for the purpose of discussion here. We discuss elsewhere (Chapter V), the traditional as well as significant enhancements of the methods used to estimate the star centroids from the pixel response data.

The stars are identified using the inter-star angles or any suitable star pattern matching methods to give a set of inertial reference vectors. In the ideal case of perfect observations, the problem of estimating the attitude of the sensor boils down to simply calculating the attitude transformation matrix A such that

$$\mathbf{b}_i = A\mathbf{r}_i \tag{6.2}$$

where $\mathbf{b}_i$ and $\mathbf{r}_i$ are the body measured and the corresponding inertial unit vectors respectively. If the body vectors are known perfectly and they are not nearly co-linear;

i.e. they are of 2 or more stars and do not contain any measurement error, then the attitude matrix can be easily derived from the above equation. However, since no sensor is perfect and noise is omnipresent, errors between the measured inter-star angles and the matching inertial inter-star angles arise. Under the assumption that the error in the sensor's output is governed by white noise, the attitude estimation problem is posed as an "optimal" estimation problem by Wahba. The optimal rotation matrix A is obtained by minimizing the Wahba cost function

$$W = \frac{1}{2}\sum_i \alpha_i ||\mathbf{b}_i - A\mathbf{r}_i||^2 \tag{6.3}$$

where α_i's are the weights representing the sensor's relative precision. Assuming the errors in the measurement follow a Gaussian distribution with standard deviation σ, choosing $\alpha_i = 1/\sigma_i^2$ transforms the above cost minimization problem into a maximum likelihood estimation problem as shown by Shuster[35].

Eqn.6.3 can be re-written as

$$\begin{aligned} W &= \frac{1}{2}\sum_i \alpha_i ||\mathbf{b}_i - A\mathbf{r}_i||^2 \\ &= \frac{1}{2}\sum_i \alpha_i \left(\mathbf{b}_i - A\mathbf{r}_i\right)^T \left(\mathbf{b}_i - A\mathbf{r}_i\right) \\ &= c - \sum_i \alpha_i \mathbf{b}_i^T A\mathbf{r}_i = \text{minimum} \end{aligned} \tag{6.4}$$

where $c = \sum_i \alpha_i$.

B. Classical Solution to the Wahba Problem

Although Farrell and Stuelpnagel[36] were the first to provide a solution to the Wahba's problem, Davenport's q-method[37] was the first robust solution. In the

q-method, the attitude matrix A is parameterized by the quaternion as

$$q = \begin{bmatrix} \mathbf{q} \\ q_4 \end{bmatrix} = \begin{bmatrix} \mathbf{e}\sin(\phi/2) \\ \cos(\phi/2) \end{bmatrix} \tag{6.5}$$

and

$$A(q) = \left(q_4^2 - |\mathbf{q}|^2\right) I + 2\mathbf{q}\mathbf{q}^T - 2q_4 \left[\mathbf{q}\times\right] \tag{6.6}$$

where $[\mathbf{q}\times]$ is the cross product matrix

$$[\mathbf{q}\times] = \begin{bmatrix} 0 & -\phi_3 & \phi_2 \\ \phi_3 & 0 & -\phi_1 \\ -\phi_2 & \phi_1 & 0 \end{bmatrix} \tag{6.7}$$

In the above equation, ϕ is the Euler principal angle of rotation about the Euler axis $\mathbf{e}$. Since $A(q)$ is a homogenous quadratic function of q, we can write

$$\mathrm{tr}(AB^T) = q^T K q \tag{6.8}$$

where K is the symmetric traceless matrix

$$\begin{bmatrix} S - I\mathrm{tr}B & \mathbf{z} \\ \mathbf{z}^T & \mathrm{tr}B \end{bmatrix} \tag{6.9}$$

with

$$S \equiv B + B^T \qquad \mathbf{z} \equiv \begin{bmatrix} B_{23} - B_{32} \\ B_{31} - B_{13} \\ B_{12} - B_{21} \end{bmatrix} = \sum_i \alpha_i \mathbf{b}_i \times \mathbf{r}_i \tag{6.10}$$

Thus, the optimal attitude is obtained by minimizing the right hand side of Eq.6.8 subject to the unity quaternion constraint $|q| = 1$. This has been shown to be equivalent to an eigenvalue problem with the optimal quaternion being equal to the

normalized eigenvector corresponding to the largest eigenvalue of K i.e.

$$Kq_{opt} = \lambda_{max} q_{opt} \tag{6.11}$$

Several methods such as FOAM[38], QUEST[39, 40], ESOQ2[41] have been developed to efficiently calculate the eigenvalue and the associated attitude matrix. The attitude matrix obtained from all these methods is optimal and hence identical. The only source of attitude error (departure from the true attitude) is the small angular mismatch due to the image processing (centroiding, calibration) processes. The centroiding procedures are able to estimate centroids routinely to within a $1/10^{th}$ of a pixel or about $3.2 arcsec$ for a 8° field-of-view 1Mpixel sensor. Given a well calibrated sensor, the final error in attitude estimation in directions orthogonal to the boresight is approximately $\sigma = \sigma_{cent}/\sqrt{n}$ where σ_{cent} is the error in single star centroiding and n are the total number of identified stars in the image frame. Thus, the only approaches to increase the attitude estimation accuracy are (i)to increase the number of imaged stars and (ii) to decrease the centroiding error. It can be learned experimentally that for $n > 6$, the actual advantage of increasing the number of stars does not follow the $1/\sqrt{n}$ rule because systematic errors limit the ultimate accuracy. Typically $n > 5$ results in small improvements and $n > 10$ is seldom advantageous. In traditional approaches, the centroids and subsequently the body measurements are used directly in their original form in the Wahba problem. However, we note that once the star identification is performed the cataloged high precision angular separation between the stars is readily available. Knowing this truth, if somehow the centroid positions can be corrected, even approximately, to account for the sensor measurement and algorithm deficiencies, a very significant gain in precision attitude estimation becomes available.

C. Constrained Centroiding - A Mechanical Equilibrium of a Rigid Body Analogy

In the Energy Approach Algorithm(EAA) by Mortari[42], a mechanical analogy to the Wahba optimality criterion was presented. The body measured vectors to the star centroids can be considered to be attached to a rigid body. The presence of errors in the image processing causes them to be displaced from the ideal projected reference vectors. The angular displacement between them is governed by a spherical spring whose stiffness is given by the measurement weights α. Thus, the cost function minimization problem of Wahba was shown to be equivalent to the minimization of the mechanical energy stored in the springs and the optimal attitude was the rigid rotation required to align the body measured vectors and projected vectors as close as possible. The method, while being a nice mechanical analogy for the Wahba problem and providing a good mathematical exercise, does not improve the attitude estimate.

Now, consider a scenario in which the stars have been centroided, using one of the previously discussed methods, with sufficient precision to allow the stars to be identified to yield inertial reference vectors. Now, the true inter-star angles are available with near-negligible catalog errors. Needless to say the true angles will differ from the body measured inter-star angles due to measurement noise and calibration errors. The extra knowledge of the ideal inter-star angles can now be readily exploited as constraints. The image can be re-centroided with the ideal inter-star angles acting as constraints that need to be satisfied. Thus, the previously estimated centroids can be corrected and their relative positions altered to minimize the inter-star angle error. In this case it can be said that that these inertially fixed vectors are attached "flexibly" to the rigid body (which is the bundle of vectors whose inter-star angles are known) and we seek the minimum energy equilibrium orientation.

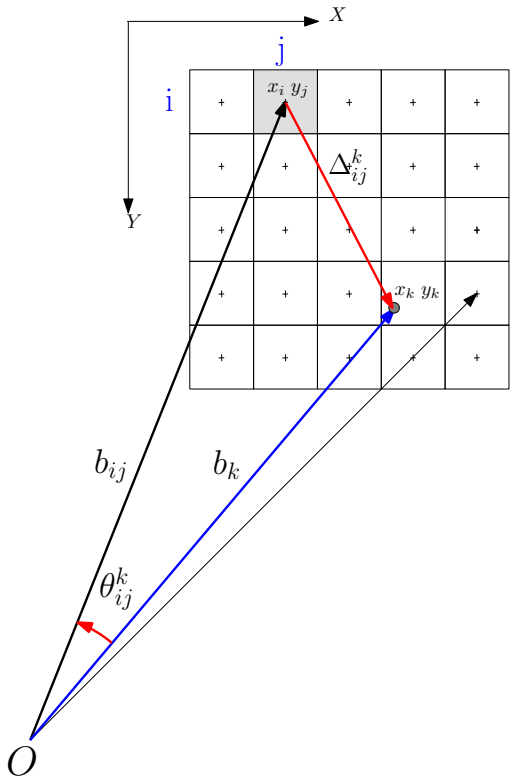

Fig. 66. Body measured vectors to the pixel centers and centroid

1. Development of the Algorithm

Consider the case of a single star energy intensity distribution obtained from the imaging sensor. The star energy can be assumed to be spread over $n \times m$ pixels which gives rise to a rectangular mask. In reality, the energy distribution more closely resembles a Gaussian-like distribution, so that the contours of equal-intensity are approximately circular or elliptical in shape. Thus, a more appropriate mask shape would be elliptical. Nonetheless, irrespective of the mask shape, it can be assumed that a list of the pixels (location and intensity value) belonging to a star is available.

Let T_{ij} be the gray-tone (intensity) of a pixel located at $[x_i\ y_j]$ as shown in Fig. 66. Also, let $[x_k\ y_k]$ be the location of the true centroid of the energy distribution.

The body measured vectors from the optical center to a pixel are given by

$$\mathbf{b}_{ij} = \frac{1}{\sqrt{(x_{ij} - x_0)^2 + (y_{ij} - y_0)^2 + f^2}} \begin{bmatrix} -(x_{ij} - x_0) \\ -(y_{ij} - y_0) \\ f \end{bmatrix} \tag{6.12}$$

Again without the loss of generality, it can be assumed that the optical center offsets are zero. The line-of-sight vector to the true centroid location is given by Eq.6.1. The angle θ_{ij}^k between the vectors $\mathbf{b}_{ij}$ and $\mathbf{b}^k$ is given by the dot product of the two vectors

$$\theta_{ij}^k = \cos^{-1}\left(\mathbf{b}_{ij} \cdot \mathbf{b}^k\right) \tag{6.13}$$

The gray-tone of the pixel is an indicator of the contribution of the pixel to the centroid. A pixel with a large gray-tone value causes the centroid to shift towards it. Thus, it can be envisioned that a "torque" acts on the pixel and this torque rotates the body vector of a pixel towards the body vector of the centroid. The gray-tone can be considered equivalent to the stiffness of a spherical spring that is located between the vector to the centroid and the vector to a pixel in the intensity distribution. The angular displacement is then the angle between these two vectors. Hence, the torque due to this angular displacement is given by

$$L_{ij}^k = T_{ij}\, \theta_{ij}^k\, \hat{\mathbf{d}} \tag{6.14}$$

where $\hat{\mathbf{d}}$ is the direction along which the torque is applied. This direction is perpendicular to both $\mathbf{b}^k$ and $\mathbf{b}_{ij}$

$$\hat{\mathbf{d}} = \frac{\mathbf{b}_{ij} \times \mathbf{b}^k}{\|\mathbf{b}_{ij} \times \mathbf{b}^k\|} \tag{6.15}$$

Since the pixels and the centroids are located in proximity and the pixel dimensions are in the order of microns, the inter-vector angles are very small. Thus

$\sin(\theta) \approx \theta$. Consequently, the above equation becomes

$$\hat{\mathbf{d}} = \frac{\mathbf{b}_{ij} \times \mathbf{b}^k}{\theta_{ij}^k} \tag{6.16}$$

Using this in Eq.6.14

$$\begin{aligned} L_{ij}^k &\approx T_{ij}\, \theta_{ij}^k \left(\frac{\mathbf{b}_{ij} \times \mathbf{b}^k}{\theta_{ij}^k} \right) \\ &= T_{ij} \left(\mathbf{b}_{ij} \times \mathbf{b}^k \right) \end{aligned} \tag{6.17}$$

2. Coplanarity of Torques

Each of the pixels contributing to the centroid is acted upon by a torque given by Eq.6.17. It can be shown that the torques lie in a plane i.e. they are coplanar. Let $L_{ij_1}^k$, $L_{ij_2}^k$, $L_{ij_3}^k$ be the torques acting on three pixels belonging to the intensity distribution for the k^{th} star. Then, the directions of these torques are given by

$$\hat{\mathbf{d}}_1 = \frac{\mathbf{b}_{ij_1} \times \mathbf{b}^k}{\|\mathbf{b}_{ij_1} \times \mathbf{b}^k\|} \qquad \hat{\mathbf{d}}_2 = \frac{\mathbf{b}_{ij_2} \times \mathbf{b}^k}{\|\mathbf{b}_{ij_2} \times \mathbf{b}^k\|} \qquad \hat{\mathbf{d}}_3 = \frac{\mathbf{b}_{ij_3} \times \mathbf{b}^k}{\|\mathbf{b}_{ij_3} \times \mathbf{b}^k\|} \tag{6.18}$$

Three vectors are coplanar if their scalar triple product is zero i.e.

$$\hat{\mathbf{d}}_1 \cdot \left(\hat{\mathbf{d}}_2 \times \hat{\mathbf{d}}_3 \right) = 0$$

Using the expression for the directions given above and ignoring the normalizing terms

$$\left(\mathbf{b}_{ij_1} \times \mathbf{b}^k \right) \cdot \left\{ \left(\mathbf{b}_{ij_2} \times \mathbf{b}^k \right) \times \left(\mathbf{b}_{ij_3} \times \mathbf{b}^k \right) \right\} = 0 \tag{6.19}$$

The vector quadruple product can be rewritten using the identity

$$(\mathbf{a} \times \mathbf{b}) \times (\mathbf{c} \times \mathbf{d}) = [\mathbf{a}, \mathbf{b}, \mathbf{d}]\, \mathbf{c} - [\mathbf{a}, \mathbf{b}, \mathbf{c}]\, \mathbf{d} \tag{6.20}$$

where $[\mathbf{a}, \mathbf{b}, \mathbf{c}]$ denotes the scalar triple product. Eq.6.19 then becomes

$$\begin{aligned}
& \left(\mathbf{b}_{ij_1} \times \mathbf{b}^k\right) \cdot \left\{ \left[\mathbf{b}_{ij_2}, \mathbf{b}^k, \mathbf{b}^k\right] \mathbf{b}_{ij_2} - \left[\mathbf{b}_{ij_2}, \mathbf{b}^k, \mathbf{b}_{ij_3}\right] \mathbf{b}^k \right\} \\
= & \left(\mathbf{b}_{ij_1} \times \mathbf{b}^k\right) \cdot \left\{ 0 - \underbrace{\left\{\mathbf{b}_{ij_2} \cdot \left(\mathbf{b}^k \times \mathbf{b}_{ij_3}\right)\right\}}_{\beta} \mathbf{b}^k \right\} \\
= & -\left(\mathbf{b}_{ij_1} \times \mathbf{b}^k\right) \cdot \beta \mathbf{b}^k \\
= & \ 0
\end{aligned}$$

since the second scalar triple product yields a scalar (β) which is then multiplied by vector $\mathbf{b}^k$. This vector is orthogonal to the cross product $\left(\mathbf{b}_{ij_1} \times \mathbf{b}^k\right)$ and the dot product is hence zero, thus proving the coplanarity of the torques acting on the pixels of the intensity distribution.

3. Energy Approach Using Forces

The centroid of the star energy distribution can be thought of being connected by a "spring" to each of the pixels that contribute to its position. The "force" with which the centroid attracts the pixel is dependent on the displacement between the centroid and the pixel, and the gray-tone of the pixel i.e.

$$\mathbf{F}_{ij}^k = T_{ij}\, \Delta_{ij}^k = T_{ij}\, \left(\mathbf{b}^k - \mathbf{b}_{ij}\right) \tag{6.21}$$

The energy stored in the spring due to this force is given by

$$\mathcal{E}_{ij}^k = \frac{1}{2} T_{ij} \left(\mathbf{b}^k - \mathbf{b}_{ij}\right)^T \left(\mathbf{b}^k - \mathbf{b}_{ij}\right) \tag{6.22}$$

For an optimal attitude and centroid location, the net energy stored in all springs

for all stars should be a minimum i.e.

$$\begin{aligned}\mathcal{E} &= \sum_k \sum_{ij} \mathcal{E}_{ij}^k \\ &= \sum_k \sum_{ij}^k \frac{1}{2} T_{ij} \left(\mathbf{b}^k - \mathbf{b}_{ij}\right)^T \left(\mathbf{b}^k - \mathbf{b}_{ij}\right) \\ &= \text{minimum} \end{aligned} \tag{6.23}$$

The dot product in the above equation can be expanded and terms can be re-combined to give

$$\sum_k \sum_{ij}^k \left(T_{ij} - T_{ij} \mathbf{b}^{k^T} \mathbf{b}_{ij}\right) = \text{minimum} \tag{6.24}$$

i.e.

$$\sum_k \sum_{ij}^k \left(T_{ij} \mathbf{b}^{k^T} \mathbf{b}_{ij}\right) = \text{maximum} \tag{6.25}$$

Substituting Eq.6.2 in the above for the centroid vector $\mathbf{b}^k$ we get

$$\sum_k \sum_{ij}^k \left(T_{ij} \mathbf{r}^{k^T} A^T \mathbf{b}_{ij}\right) = \text{maximum} \tag{6.26}$$

Note that in the above expression the result is a scalar quantity, and thus using the trace properties of a matrix the above equation can be written as

$$\begin{aligned}\sum_k \sum_{ij}^k \left(T_{ij} \mathbf{r}^{k^T} A^T \mathbf{b}_{ij}\right) &= \sum_k \sum_{ij}^k T_{ij} \text{Tr}\left[\mathbf{r}^{k^T} A^T \mathbf{b}_{ij}\right] \\ &= \sum_k \sum_{ij}^k T_{ij} \text{Tr}\left[A^T \mathbf{b}_{ij} \mathbf{r}^{k^T}\right] \\ &= \sum_k \text{Tr}\left[\sum_{ij}^k T_{ij} A^T \mathbf{b}_{ij} \mathbf{r}^{k^T}\right] \\ &= \sum_k \text{Tr}\left[A^T \sum_{ij}^k T_{ij} \mathbf{b}_{ij} \mathbf{r}^{k^T}\right] \\ &= \text{Tr}\left[\sum_k A^T \sum_{ij}^k T_{ij} \mathbf{b}_{ij} \mathbf{r}^{k^T}\right] \\ &= \text{Tr}\left[A^T F\right] \end{aligned} \tag{6.27}$$

where Tr is the trace operator and the matrix F is

$$F = \sum_{k} \sum_{ij} T_{ij} \mathbf{b}_{ij} \mathbf{r}^{k^T} \tag{6.28}$$

Eq.6.27 is identical to the matrix version of the Wahba optimality condition with the attitude profile matrix replaced by F. Several methods exist to solve the above equation for A.

In the above formulation, it can be seen that the stars are implicitly re-centroided using the true inter-star angles available from the star identification process. Thus, the attitude is estimated using this method is likely to be in closer agreement with the truth. Because the cataloged inter-star angles are enforced as constraints, we are using important information not present in the traditional approach. The upper bound on the attitude accuracy is obviously determined by the error in the knowledge of the inertial reference vectors. The star tracker carries a star catalog derived from the Tycho2 star database which is complete for stars up to visual magnitude 10. The errors in the reference vectors are less than $0.2 arcsec$, assuming all aberrations such as starlight and relativistic, parallax errors and proper motion errors have been accounted for. Thus, the theoretical upper bound for the attitude error should be a fraction of the $0.2 arcsec$ error. Assuming a sufficiently precise star tracker and that the signs of the catalog errors are random, we can anticipate that filtering will allow us to approach perhaps $0.02 arcsec$ attitude error without enhancing the Tycho-2 data.

4. Torque Balance Approach

Each of the pixels contributing to a star, is acted upon a torque given by Eq.6.17. At equilibrium, the net torque acting on the body must be zero. Equivalently at equilibrium, the centroids are located at the optimal position so as to minimize the

inter-star angular error. In a mathematical form

$$\mathbf{L} = \sum_k \sum_{ij} L_{ij}^k = \sum_k \sum_{ij} T_{ij} \left(\mathbf{b}_{ij} \times \mathbf{b}^k \right) = 0 \tag{6.29}$$

Since $\mathbf{L} = 0$, the cross-product of any vector $\mathbf{k}$ with $\mathbf{L}$ will be zero as well, i.e.

$$\begin{aligned} \mathbf{k} \times \mathbf{L} = 0 &= \mathbf{k} \times \sum_k \sum_{ij} T_{ij} \left(\mathbf{b}_{ij} \times \mathbf{b}^k \right) \\ &= \sum_k \sum_{ij} T_{ij} \, \mathbf{k} \times \left(\mathbf{b}_{ij} \times \mathbf{b}^k \right) \end{aligned} \tag{6.30}$$

Using the vector triple product identity $\mathbf{a} \times (\mathbf{b} \times \mathbf{c}) = \mathbf{b}(\mathbf{c}^T\mathbf{a}) - \mathbf{c}(\mathbf{b}^T\mathbf{a})$ the above equation becomes

$$\sum_k \sum_{ij} T_{ij} \left(\mathbf{b}_{ij} {\mathbf{b}^k}^T - \mathbf{b}^k \mathbf{b}_{ij}^T \right) \mathbf{k} = 0 \tag{6.31}$$

Since $\mathbf{k}$ is any general vector

$$\sum_k \sum_{ij} T_{ij} \left(\mathbf{b}_{ij} {\mathbf{b}^k}^T - \mathbf{b}^k \mathbf{b}_{ij}^T \right) = 0 \tag{6.32}$$

It was assumed that the star identification has been performed using the initial centroid vectors and hence the inertial vector $\mathbf{r}$ to each of the centroided star is available. The above equation can then be re-written in terms of the inertial vectors as

$$\sum_k \sum_{ij} T_{ij} \left(\mathbf{b}_{ij} {\mathbf{r}^k}^T A^T - A \mathbf{r}^k \mathbf{b}_{ij}^T \right) = 0 \tag{6.33}$$

or,

$$FA^T - AF^T = 0 \tag{6.34}$$

where

$$F = \sum_k \sum_{ij} T_{ij} \, \mathbf{b}_{ij} {\mathbf{r}^k}^T \tag{6.35}$$

Post-multiplying Eq.6.34 by A and noting that $A^T = A^{-1}$ we obtain

$$F = AF^TA \tag{6.36}$$

which is henceforth referred to the as the F-equation. Notice that the balancing of torques leads to a set of equations that is similar to the Wahba optimality conditions with the difference being that the attitude profile matrix is replaced by the F matrix. The classical solution to the Wahba problem tries to minimize the error between the body measured vectors and the reference vectors by estimating an optimal rotation matrix. The mechanical analogy as described above, not only tries to find an optimal rotation matrix but also implicitly updates the body measurement vectors. The inter-star angles obtained from the inertial reference vectors act as constraints to the positions of the body vectors to force them to have inter-star angles equivalent to their known cataloged values.

5. Solution to the Flexible Body System

Mortari[42] has demonstrated that the algebraic matrix equation (R-equation) obtained for the energy approach to Wahba's problem can be solved by eigenanalysis of the modified attitude profile matrix. For this purpose a 6×6 symmetric matrix can be constructed as

$$H = \begin{bmatrix} 0 & B \\ B^T & 0 \end{bmatrix} \tag{6.37}$$

Let $\mathbf{u}_i$ and $\mathbf{v}_i$ be the upper and the lower three elements of the i^{th} eigenvector of the H matrix. It was shown that $A = UD^{-1}$ is a form of the solution for the R-equation, where the matrices $U = [\mathbf{u}_1\ \mathbf{u}_2\ \mathbf{u}_3]$ and $D = [\mathbf{v}_1\ \mathbf{v}_2\ \mathbf{v}_3]$ are obtained by an arrangement of the vectors $\mathbf{u}_i$ and $\mathbf{v}_i$ associated with the three distinct positive eigenvalues of the matrix H. Several alternative solution forms were described to

reduce the number of computations and lead to the same optimal attitude estimate.

a. Solution by Singular Value Decomposition

It was shown by Markley[43] that the attitude can be estimated by performing a singular value decomposition (SVD) of the B-matrix in the classical Wahba problem. The same methodology can be readily applied in this case since the F-equation exhibits a similar structure. The SVD of the F matrix is given by

$$F = USV^T \tag{6.38}$$

where both U and V are orthonormal matrices; i.e $UU^T = I$ and $VV^T = I$, and $S = \text{diag}\,(\sigma_1, \sigma_2, \sigma_3)$ is a diagonal matrix containing the singular values of F. Substituting Eq.6.38 into the F-equation (Eq.6.36) gives

$$A\left(VSU^T\right)A = USV^T \tag{6.39}$$

Pre-multiplying by U^{-1} $(= U^T)$ and post-multiplying by ${V^T}^{-1}$ $(=V)$, the above equation becomes

$$\left(U^TAV\right)S\left(U^TAV\right) = S \tag{6.40}$$

Let $Z = \left(U^TAV\right)$. If the number of body vector measurements is greater than two, it can be verified that $\det(U) = \det(V) = \pm 1$. Moreover, since U and V are orthonormal, their product Z is also orthonormal. Then, it follows that $\det(Z) = +1$ and thus Z is a rotation matrix. The F-equation re-written in terms of Z is

$$ZSZ = S \tag{6.41}$$

Let $\mathbf{e}$ be the Euler axis corresponding to the rotation matrix Z. Then,

$$Z\mathbf{e} = \mathbf{e} \tag{6.42}$$

Post-multiplying Eq.6.41 by $\mathbf{e}$

$$ZSZ\mathbf{e} = ZS\mathbf{e} = S\mathbf{e} \tag{6.43}$$

The above equation implies that the Z matrix has two distinct Euler axis of rotations, $\mathbf{e}$ and $S\mathbf{e}$. This is not possible until and unless Z is an identity matrix; i.e.

$$Z = U^T AV = I \tag{6.44}$$

This leads to the elegant SVD solution of the F-equation,

$$A_{SVD} = UV^T \tag{6.45}$$

b. Singularity Avoidance for the Case of Two Body Observations

When only two body measurements are available, the singular values of the F matrix are not all non-zero and thus the condition $\det(U) = \det(V) = \pm 1$ is violated. The singularity can be easily overcome by using the technique proposed by Mortari[42]. In the case of the classical Wahba problem, Mortari[44] showed that the Wahba cost function implies a coplanarity condition among the body measured vectors ($\mathbf{b}_1,\ \mathbf{b}_2$) and the projected inertial reference vectors ($A\mathbf{r}_1,\ A\mathbf{r}_2$) where A is Wahba's optimal attitude matrix. The attitude matrix represents a rigid rotation about the Euler axis by the Euler angle. The coplanarity condition is thus satisfied for any vector in the inertial frame that is rotated by the attitude matrix.

Consider a vector $\mathbf{r}_1 \times \mathbf{r}_2$ acted upon by the rotation described by A. Then, $A(\mathbf{r}_1 \times \mathbf{r}_2) = A\mathbf{r}_1 \times A\mathbf{r}_2$. This projected vector must be parallel to $\mathbf{b}_1 \times \mathbf{b}_2$. The coplanarity condition implies that the following equation holds:

$$\frac{A(\mathbf{r}_1 \times \mathbf{r}_2)}{\sin(\theta_r)} = \frac{\mathbf{b}_1 \times \mathbf{b}_2}{\sin(\theta_b)} \tag{6.46}$$

where $\mathbf{b}_1^T\mathbf{b}_2 = \cos(\theta_b)$ and $\mathbf{r}_1^T\mathbf{r}_2 = \cos(\theta_r)$ are the inter-star angles. Thus, adding third vector $\mathbf{b}_3 = (\mathbf{b}_1 \times \mathbf{b}_2)/\sin(\theta_b)$ and the corresponding inertial reference vector to the data set does not alter the estimated optimal attitude matrix. This approach can be readily applied for any algorithm or set of sensors when only two observations are available. This causes the algorithm to degenerate to Black's classical TRIAD algorithm[45].

D. Numerical Tests and Results

The rigid body equilibrium approach for constrained centroiding and attitude determination was implemented in the MATLAB environment in order to characterize its attitude error performance as compared to the classical Wahba problem solution. ESOQ2 was the algorithm of choice for the classical Wahba problem owing to its computational efficiency and reliability.

1. Input Conditions

The star simulator developed in the previous chapters was used to generate images for the visible portion of the sky. The star catalog was derived from the Tycho2 catalog and contained stars upto visual magnitude 7.0. The specifics of the simulator parameters are given in Table XI.

2. Measurement of Attitude Error

If T is the true attitude matrix and C is the estimated attitude, then the error in the attitude estimation Δ is given by

$$\Delta = TC^T \tag{6.47}$$

Table XI. Parameters of the star simulator

Parameter	Value
Focal length	50mm
Imager Size	512×512 pixels
Pixel Size	$15\mu m$
Star Catalog	Tycho-II
Star Magnitude Threshold	5.5

Since Δ is a rotation matrix, it has an associated Euler axis and principal angle of rotation Φ. The angle Φ is the amount by which the constrained set of estimated body measured vectors must be rotated about the Euler axis so as to coincide with the corresponding ideal, noise-free measurement vectors and thus represents the error associated with a given attitude. The maximum orientation error can be shown to be given by [46]

$$\cos\Phi = \frac{\mathrm{tr}(\Delta) - 1}{2} \tag{6.48}$$

In terms of the more frequently used attitude parameterizations, the Euler-Rodrigues parameters, the maximum direction error can be written as

$$\cos\Phi = 2\left(q_c^T q_{true}\right)^2 - 1 \tag{6.49}$$

where q_c and q_{true} are the 4×1 quaternions representing the estimated and the true attitude respectively. It is a well known fact that for a single narrow field-of-view star tracker, the rotation about the boresight is known less accurately than the directions orthogonal to the boresight. Let ϕ_x denote the error along the boresight, ϕ_{yz} denote the error in a direction orthogonal to the boresight and $q_{err} = [\mathbf{q}_{err}\ q_{err4}]^T$ be the quaternion associated with the error matrix Δ. If $\mathbf{e}_x = [1\ 0\ 0]$ be the unit vector

along the $\mathbf{x}$ direction and $\mathbf{e}_{yz}$ the unit vector orthogonal to $\mathbf{e}_x$, then

$$\begin{aligned} q_{err} &= \begin{bmatrix} \mathbf{q}_{err} \\ q_{err4} \end{bmatrix} = \begin{bmatrix} \mathbf{e}_x \sin(\phi_x/2) \\ \cos(\phi_x/2) \end{bmatrix} \otimes \begin{bmatrix} \mathbf{e}_{yz} \sin(\phi_{yz}/2) \\ \cos(\phi_{yz}/2) \end{bmatrix} \\ &= \begin{bmatrix} \mathbf{e}_x \sin(\phi_x/2)\cos(\phi_{yz}/2) + \mathbf{e}_{yz} \sin(\phi_{yz}/2)\cos(\phi_x/2) + \\ -(\mathbf{e}_x \times \mathbf{e}_{yz}) \sin(\phi_x/2)\sin(\phi_{yz}/2) \\ \hline \cos(\phi_x/2)\cos(\phi_{yz}/2) \end{bmatrix} \end{aligned} \tag{6.50}$$

Since ϕ_x always lies between $[-\pi, \pi]$, by selecting $\mathbf{e}_{yz}$ appropriately, ϕ_{yz} can be found to lie in the interval $[0, \pi]$. Also, $\mathbf{e}_{yz}$ and $\mathbf{e}_x \times \mathbf{e}_{yz}$ form an orthogonal basis for the $y-z$ plane. The error angles are then given by

$$\begin{aligned} \phi_x &= 2\tan^{-1}(q_{err1}/q_{err4}) \\ \phi_{yz} &= 2\sin^{-1}\left(\sqrt{q_{err2}^2 + q_{err3}^2}\right) \end{aligned} \tag{6.51}$$

where q_{erri} is the i^{th} component of the error quaternion. The maximum direction error Φ can be written in terms of the errors along the boresight and orthogonal to the boresight as

$$\cos(\Phi/2) = q_{err4} = \cos(\phi_x/2)\cos(\phi_{yz}/2) \tag{6.52}$$

$\Phi/2$ is the hypotenuse of a right spherical triangle with sides $\phi_x/2$ and $\phi_{yz}/2$. The angles ϕ_x and ϕ_{yz} can be thought of as the spherical trigonometry equivalents of the two orthogonal components of the error vector.

3. Attitude Error v/s Number of Observations

The objective of these tests was to characterize the attitude error for different number of visible stars in the field-of-view. The number of stars was varied from 3 to 6. A random attitude was prescribed for each case. For each attitude, when the number

of stars were exactly equal to the desired number, centroiding was performed on the acquired image using the Linear Least Squares LOG algorithm developed in the previous chapters (Chapter.5) and the most commonly used Center of Mass (COM) algorithm. The threshold for the center of mass was calculated for each image based on the mean and the standard deviation of the entire image. A fixed size mask of 9×9 pixels was used for the center of mass, while a variable size rectangular mask was employed for the LOG centroiding. Furthermore, only the pixels with response values greater than the threshold were selected for calculating the centroid. The mean centroiding error for both COM and LOG was found to be less than 0.1 pixels.

Since the LOG centroids have been found to be more accurate than their COM counterparts, the LOG centroids were used to create the body measurement vectors. The optical axis offsets in these test cases were assumed to zero and the focal length exactly known. The attitude was estimated using the classical ESOQ2 algorithm and was compared against the rigid body equilibrium algorithm developed in the previous sections. Since the true attitude is known, the error in the attitude was computed using Eq.6.51 for each method. Statistics on the root-mean-square and standard deviations of the attitude errors along the boresight and orthogonal to the boresight were calculated and are shown in Table XII

Fig. 67-Fig. 70 show the plots of the net attitude errors, error along the boresight and orthogonal to the boresight for all the cases. As can be seen from the statistics of the attitude error, the constrained recentroiding using the rigid body equilibrium approach outperforms the classical approach to attitude estimate. This is because the classical approach methods such as ESOQ2 or EAA try to estimate a rigid rotation between the inertial reference vectors and the body measured vectors using the computed centroid information only. However, the rigid body equilibrium approach poses additional constraints of inter-star angle matches between the measured vectors

Table XII. Statistics - root mean square error(rmse) and standard deviation(std) in the attitude estimate error using the classical ESOQ2 and flexible body constrained recentroiding approaches

	Classical ESOQ2		**Recentroiding COM**		**Recentroiding LOG**	
Number of stars	Around boresight rmse[std] (arcsec)	Cross boresight rmse[std] (arcsec)	Around boresight rmse[std] (arcsec)	Cross boresight rmse[std] (arcsec)	Around boresight rmse[std] (arcsec)	Cross boresight rmse[std] (arcsec)
3	3.668[26.19]	0.164[1.65]	1.381[9.65]	0.064[0.65]	1.132[7.83]	0.041[0.41]
4	1.982[12.73]	0.119[1.17]	1.113[7.14]	0.051[0.51]	0.632[4.23]	0.034[0.33]
5	1.366[7.99]	0.084[0.85]	0.719[4.31]	0.041[0.41]	0.546[3.25]	0.028[0.28]
6	1.213[7.67]	0.069[0.69]	0.616[3.95]	0.035[0.35]	0.437[2.67]	0.026[0.26]

and implicity computes the *optimal* centroid locations. Thus, the computed attitude is a lot closer to the true attitude. Theoretically, the upper limit to the error in inter-star angle computation is set by the star catalog error, which is usually very low ($\ll$ 1arcsec). As expected the error in the attitude estimate decreases with increasing number of measurements (stars) per image frame.

E. Concluding Remarks

A new algorithm for accurate attitude estimation was presented. This method takes advantage of the known inter-star geometry to implicitly alter the locations of the centroids to be compatible with known inter-star angles. This gives us an inertial set of star position vectors, and the corresponding set of vectors in the body axes are rotated as a rigid body to be best consistent with the measured star vectors. A mechanical analogy of the problem using spherical springs was developed. A modified Wahba's optimality criterion was obtained by energy minimization and balance of torques. An algebraic matrix equation similar in structure to the classical matrix version of the Wahba problem was obtained and solved using singular value decomposition. In essence, optimal re-centroiding of identified stars (subject to known inter-star angle constraints) is accomplished simultaneously with final attitude estimation. The algorithm was programmed in MATLAB and was tested using the star image simulator. It was seen that the new constrained centroiding attitude estimation approach gave a very significant reduction (a factor of 2 to 3) in the attitude error as compared to the classical ESOQ2 solution. Although the proposed algorithm involves additional computations and processing time, the computational cost is easily offset by a gain in the accuracy of the attitude estimate. A factor of 2 to 3 increase in the attitude accuracy on this now-classical problem is believed to be a remarkable contribution.

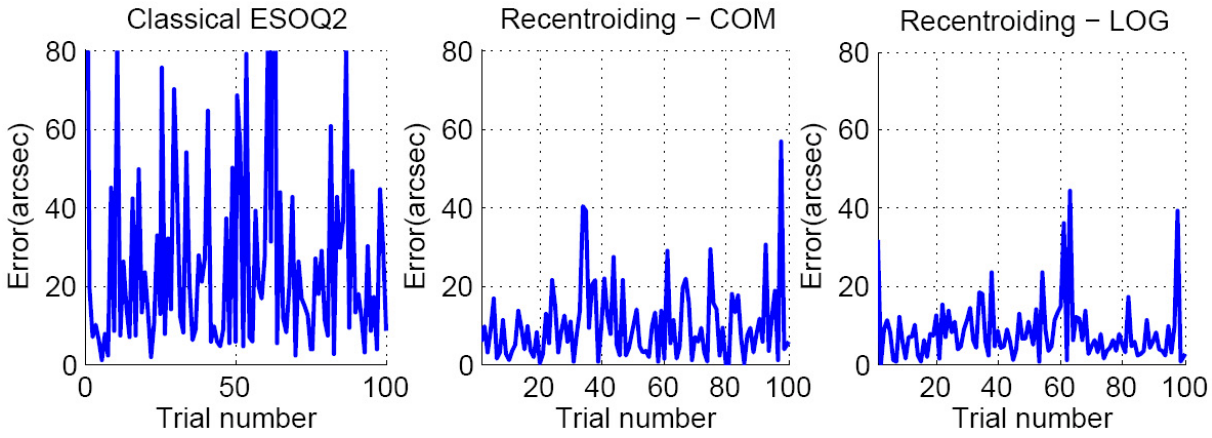

(a) Around Boresight

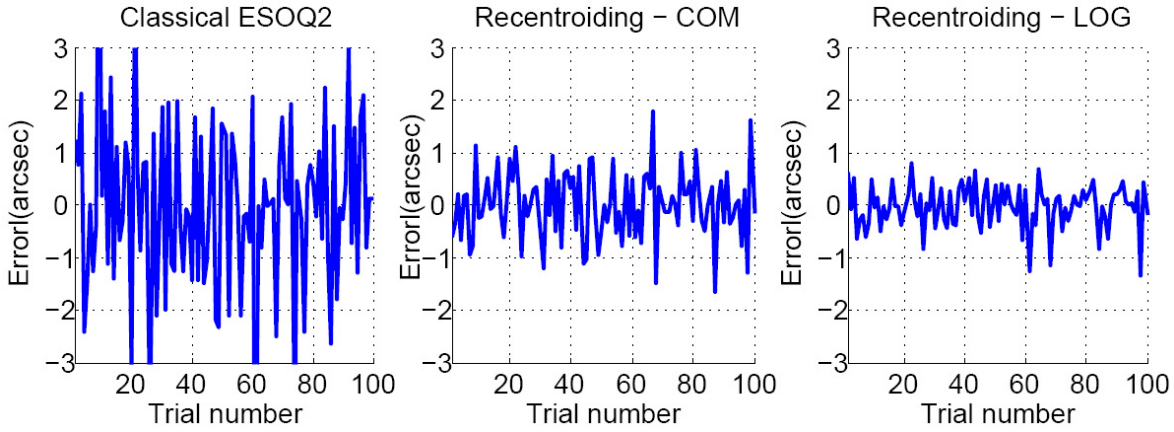

(b) Cross Boresight

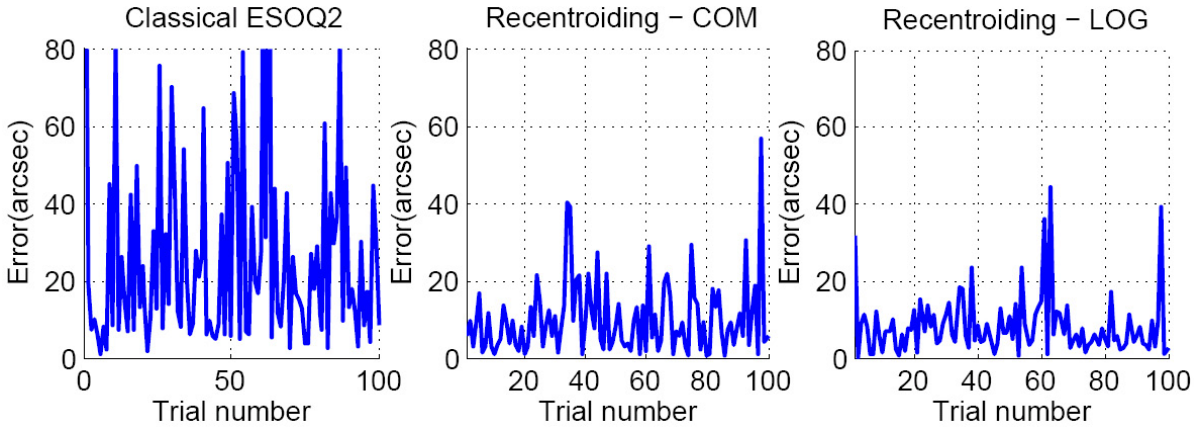

(c) Net Attitude Error

Fig. 67. Attitude errors: around boresight, orthogonal to boresight and net error for 3 stars in the field of view

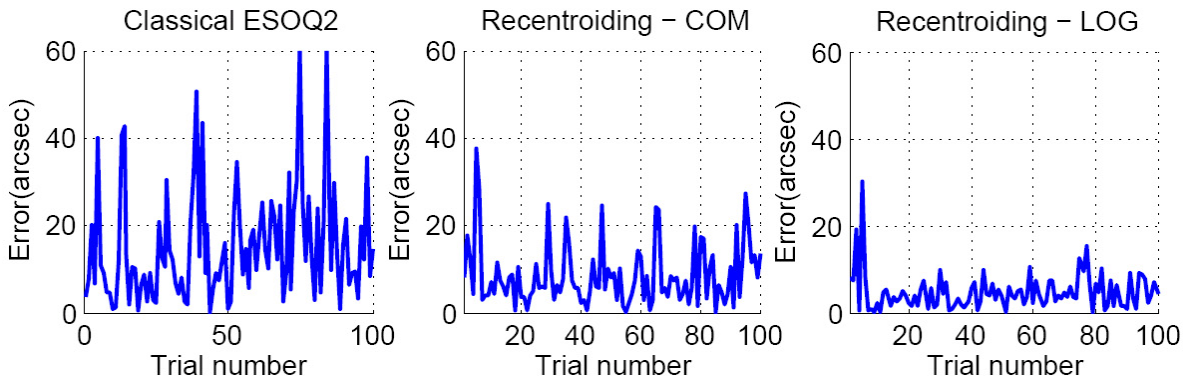

(a) Around Boresight

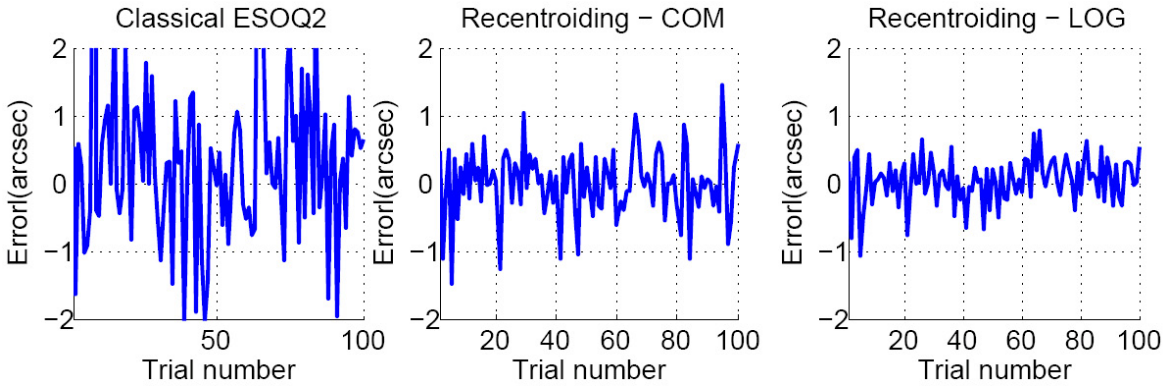

(b) Cross Boresight

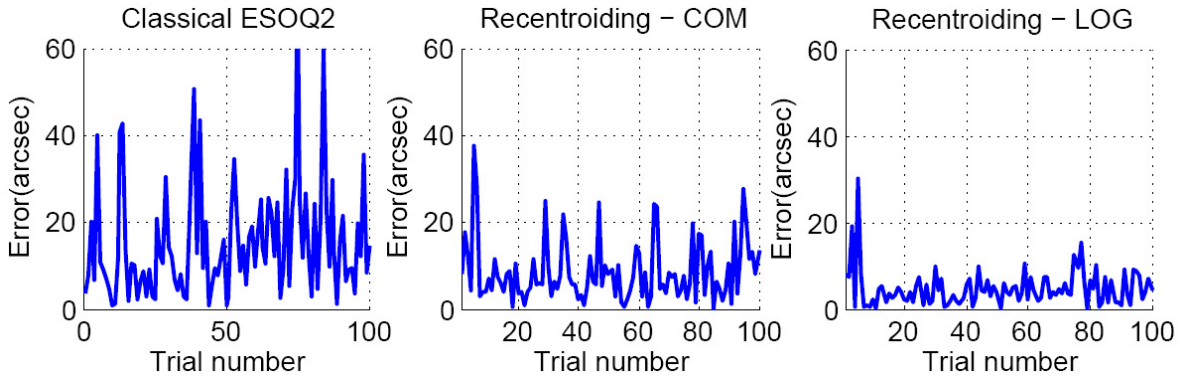

(c) Net Attitude Error

Fig. 68. Attitude errors: around boresight, orthogonal to boresight and net error for 4 stars in the field of view

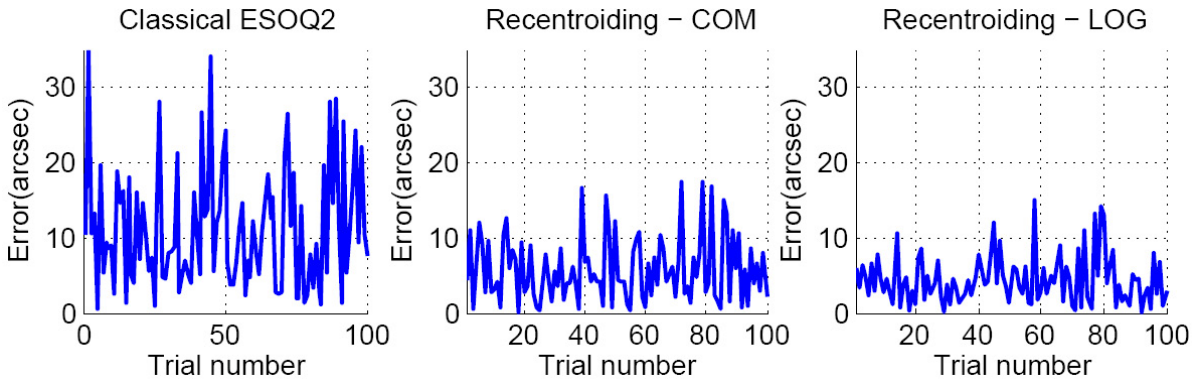

(a) Around Boresight

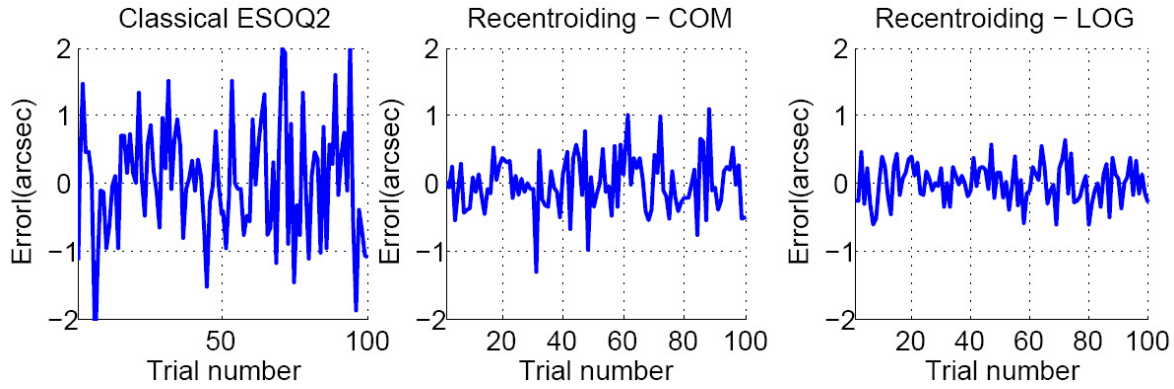

(b) Cross Boresight

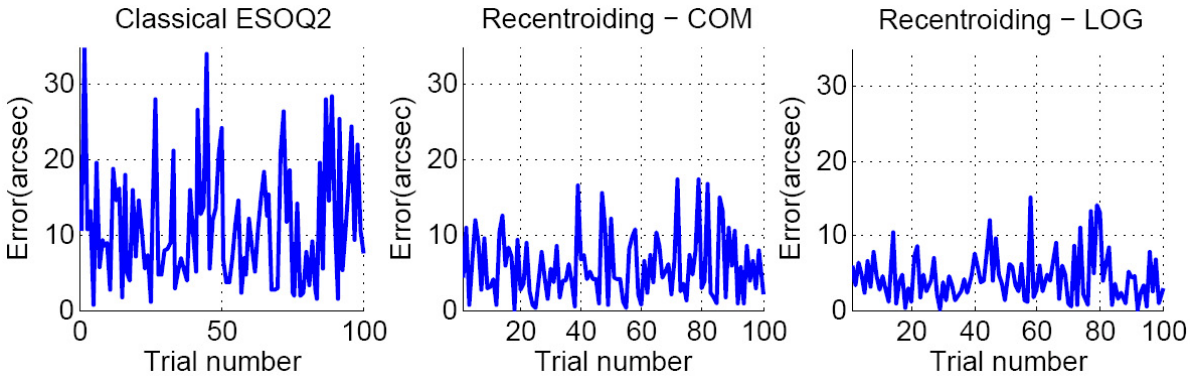

(c) Net Attitude Error

Fig. 69. Attitude errors: around boresight, orthogonal to boresight and net error for 5 stars in the field of view

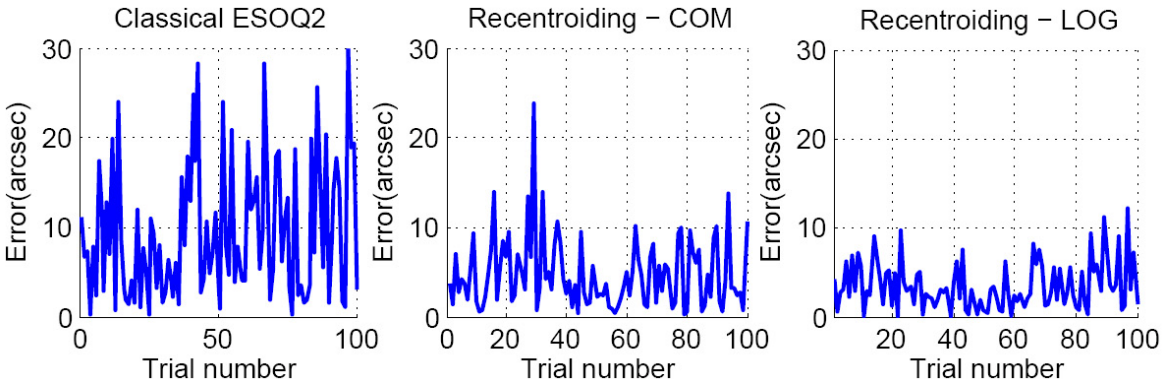

(a) Around Boresight

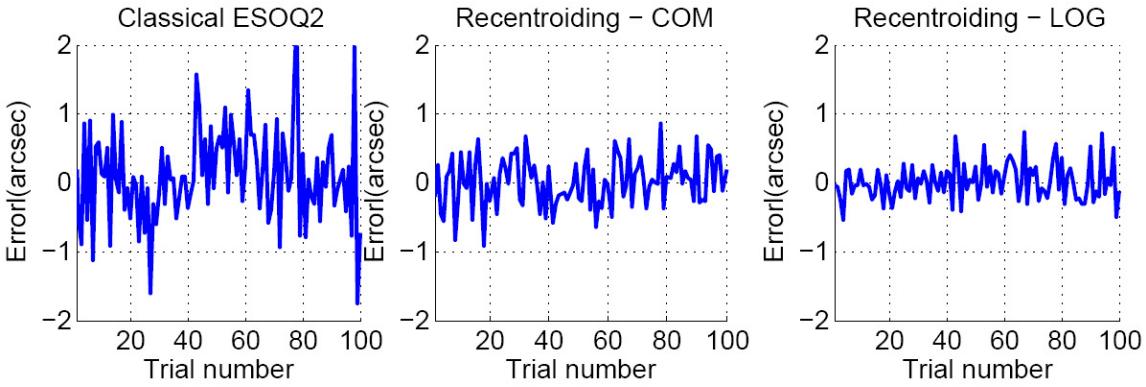

(b) Cross Boresight

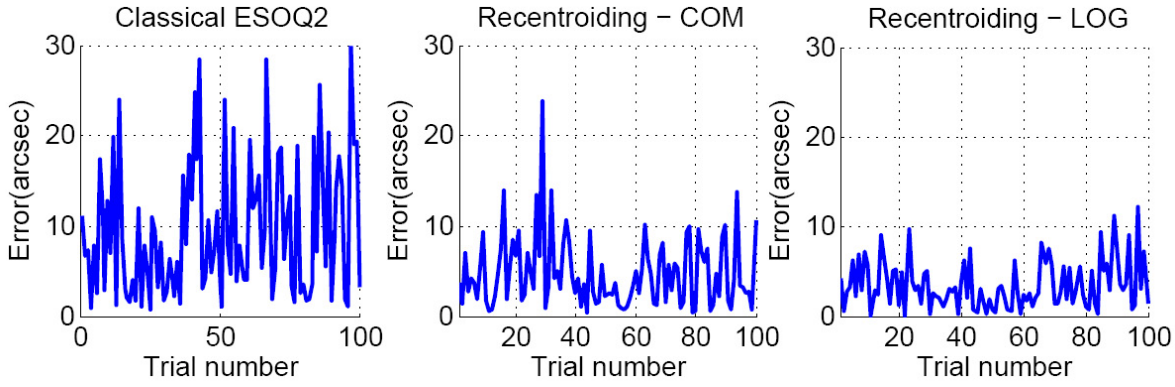

(c) Net Attitude Error

Fig. 70. Attitude errors: around boresight, orthogonal to boresight and net error for 6 stars in the field of view

CHAPTER VII

SPECTRAL MATCHING OF STAR CATALOGS

A. Introduction

Star trackers, until very recently, were capable of performing only centroiding and line-of-sight estimation using their limited computing hardware resources and transferring this information to the spacecraft computer for further processing. Since memory has historically been at a premium, the large star catalog was usually stored on the spacecraft computer which performed the star identification and attitude estimation processes. Furthermore, until recently, algorithms for reliably performing star identification required extensive processing. As technology breakthroughs on algorithms, computers, focal plane sensors and fabrication innovations have occurred, the star trackers have been transformed into a self-contained "smart-sensor" with embedded processing system which can output not only the attitude estimates but also enable real-time interface with external sensors such as rate measurements gyroscopes to provide high accuracy filtered pointing information [31].

Although commercial memory is now cheap, radiation hardened memory is still expensive and occupies a substantial portion of the printed circuit board real-estate. Thus, optimization of resources and minimization of hardware volume for spacecraft is not only practical but also essential. The bulk of the non-volatile storage space is taken up by the star catalogs and the derived star angle pattern databases (such as the k-vector[47]). Moreover, to account for radiation effects and failures, a TMR (Triple Modular Redundancy) approach is usually employed in which the data is stored in triplicate. Any reduction in the size of the catalog during its creation hence remains extremely beneficial.

Another factor adding to the size of the star catalog is the recent trend in the design of star sensors. In order to increase the angular resolution per pixel without compromising image acquisition/processing time, the field-of-view is made smaller ($< 10^{\circ}$). This leads to a higher precision line-of-sight estimation and consequently more precise attitude estimates. Star trackers using this feature have been able to achieve pointing accuracies of less than $10\mu rad$ [31, 48, 49]. Unfortunately, a smaller field-of-view implies a smaller sky coverage per frame and larger dropouts of stars. In order to have at least 4 stars to perform reliable star identification, fainter stars have to be sensed and included in the catalog. The number of faint stars in the catalog however, increases in a dramatic fashion with an increase in magnitudes. Fig. 71 shows the number of stars in the sky at various visual magnitudes obtained by analyzing the Hipparcos catalog containing a total of $118,218$ stars. At magnitude 5.0 and below, only 1624 visible stars were extracted from the catalog. Increasing the magnitude from 5.0 to 6.0, however, causes the number of stars extracted to more than triple to 5030. The increase is much more drastic in going to magnitude 7 where the number triples again to about $15,486$ stars are visible.

The most commonly used method for generating a star catalog is based on a fixed visual magnitude cutoff approach wherein, stars brighter than a given magnitude are extracted from a master catalog. This technique however, assumes that all the stars of equal magnitudes appear equally bright when imaged through an optical train. Unfortunately, this assumption is false. As is well known, the photospheric temperatures of the stars dictate the radiated energy distribution. In addition to this, the spectral response of the electro-optical system is a function of the wavelength of the incident light. Thus, a loss in brightness is observed for stars of the same visual magnitude but different emission spectra. This implies that the visual magnitude cutoff for the catalog extraction should be tuned to the spectral response of the entire

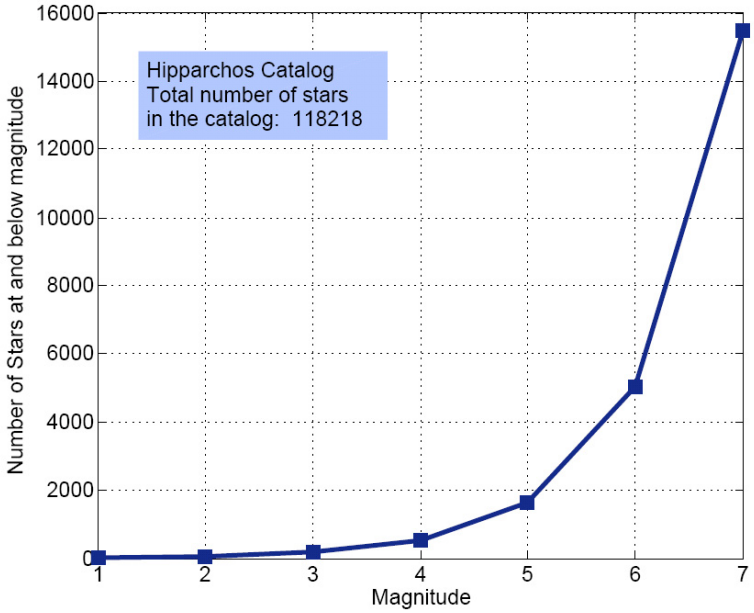

Fig. 71. Number of stars at and below a given magnitude extracted from the Hipparcos catalog

system. Moreover, in terrestrial applications, the atmosphere filtering effects cause an additional loss in the energy from the starlight. The attenuation is a function of the location of the sensor on the Earth, the wavelength of the light being imaged and angular position of the star in the sky.

As a result, a star catalog obtained by the traditional method will virtually certainly contain stars that can never be observed by the sensor. This has direct implications on the memory requirements for the embedded system. Each of the stars is stored as a three component unit vector which is by default a fixed point entity. At least 4 bytes of data are required to represent each component along with a two byte star identifier. Thus each star adds, at a minimum, 14 bytes to the size of the star catalog. In addition to the catalog, the star sensor also carries a database of patterns which could be polygons or search-less vector tables such as the k-vector for

identifying stars. During the star identification process, these "extra" stars broaden the search space for the solution, thereby increasing not only the probability of a mismatch but also the computational time.

In this chapter, we develop a procedure to characterize the spectral response of the star sensor system and modify the existing catalog extraction procedure to account for the loss in the brightness as observed by the sensor. The case of terrestrial applications of the star sensing technology are also addressed. The loss in the transmittance due to the atmosphere is quantified and integrated into the spectral response of the entire system. The magnitude cutoffs for each spectral class are obtained using this method and are used for extracting stars from a master star catalog. We show that by using such an approach, a significant reduction in the number of stars extracted is obtained. The savings in the star catalog storage are thus significant. These optimized catalogs have also been found to contain many fewer unobservable stars and yet ensure that at least (4, for example) measurable stars are present in all feasible pointing directions of the sensor.

B. Background on Stellar Photometry and Radiometry

1. Stellar Magnitudes

The oldest known classification of the stars visible to the naked eye was performed in 120B.C. by Hipparcos. He divided the stars based on their brightness into six classes or magnitudes, with the first class containing the brightest and the sixth class the faintest star visible. The six classes formed a uniform scale where each magnitude difference represented an equal step in visual perception. This classification was further modified by Ptolemy and he assigned integer values to the six magnitudes. It was discovered in the mid 1800's, however, that the response of the human eye to

illuminance is not linear. Moreover, the eye does not sense the absolute illuminance level of the stars but rather approximately perceives the relative differences. Based on this observation, a logarithmic scale was defined ed by Pogson in 1856 as

$$\frac{E_1}{E_2} = 2.512^{(m_2 - m_1)} \tag{7.1}$$

where E_1, E_2 represent the recorded illuminance and m_1, m_2 represent the corresponding magnitudes. The number 2.512 is the fifth root of 100 and thus a change of five magnitudes ($m_1 = 1$ and $m_2 = 6$) indicates that the magnitude six star is 100 times fainter than the magnitude one star. Eq.7.1 leads to the famous Pogson's formula

$$m = -2.5 \log E + C \tag{7.2}$$

The coefficient -2.5 is called the Pogson scale and the term C is an arbitrarily chosen constant called the zeropoint.

a. Visual and Apparent Magnitudes

Historically, the magnitude of a star was calculated based upon the brightness as perceived by the human eye and hence called *visual magnitude*. Given that the eye is most sensitive in the green wavelengths ($550nm$), the visual magnitude reflects, approximately, the brightness of the star at this wavelength. Unfortunately, however, the illuminance from the stars is not monochromatic and contains components at various wavelengths ranging from deep ultraviolet to far infra-red. With the advent of photographic recording plates, the calculation of the stellar magnitudes at once became more precise and much more diverse since different people used plates and filters of varying spectral responses. In order to standardize the magnitude estimation, a photometric system called UBV system was introduced. In the UBV system the

magnitude is measured at three different wavelengths: U(centered at about 350nm in the ultra-violet), B(435nm in the blue) and V(555nm in the visible green). The V band was chosen since it closely matches the eye response.

The *apparent magnitude* is a combination of the measured magnitudes at the UBV wavelengths and is officially defined as the brightness of the star observed above the Earth's atmosphere. In the absence of any information regarding the wavelength of measurement, the apparent magnitude is assumed to be equivalent to the visual magnitude.

2. Spectral Classification of Stars

As the use of photographic plates for magnitude estimation became popular, the study of the color of the stars gained more attention. The photographic plates were sensitive only to the blue part of the spectrum. It was observed that two stars of the same visual magnitude but different colors appeared to differ in brightness when imaged. Pickering (1888) pointed out that as long as the spectral distributions of the two objects are the same, the relative intensity will appear to be the same irrespective of the measurement detector technique (eye or plate).

The Harvard system was the earliest classification system that divided the stars into various spectral types based upon on the strength of the hydrogen absorption lines in the star spectrum. The classes were labeled alphabetically by letters A,B,C... from the strongest to the weakest. Unfortunately, this proved to be an unreliable technique. Cannon and Pickering altered this system such that the stars were divided into seven spectral classes based on the temperature of the stars. They arrived at a spectral sequence of O, B, A, F, G, K, M with O being the hottest and M the coolest. Morgan and Keenan modified this system to include the luminosity of the star. This system, called the Yerkes system, is now the most commonly used classification system. Table

Table XIII. Spectral classes of the Yerkes System, luminosity compared with Sun

Class	**Temperature**	**Star Color (visible)**	**Luminosity**
O	$30,000 - 60,000$K	Blue	$1,400,000$
B	$10,000 - 30,000$K	Blue	$20,000$
A	$7,500 - 10,000$K	White-blue	80
F	$6,000 - 7,500$K	White	6
G	$5,000 - 6,000$K	Yellow-white	1.2
K	$3,500 - 5,000$K	Yellow-orange	0.4
M	$2,000 - 3,500$K	Orange-red	0.004

XIII lists the spectral classes along with some of their characteristics.

3. Stars as Blackbody Radiators

A continuous spectrum can be produced by thermal emission from a black body. The spectrum characteristics are completely specified by the effective temperature of the body. The spectral radiance of a blackbody at a temperature T is given by Planck's equation

$$L(\lambda, T) = \frac{2hc^2}{\lambda^5}\left[\exp\left(\frac{hc}{\lambda kT}\right) - 1\right]^{-1} \tag{7.3}$$

where h is the Planck's constant, $k = 1.38062 \times 10^{-23} JK^{-1}$ is Boltzman's constant, c is the speed of light in vacuum and λ is the wavelength. Fig. 72 illustrates the spectral distribution of blackbody radiation. It can be observed that the curves have the following characteristics:

- The spectral radiance at all wavelengths increases with increasing temperatures

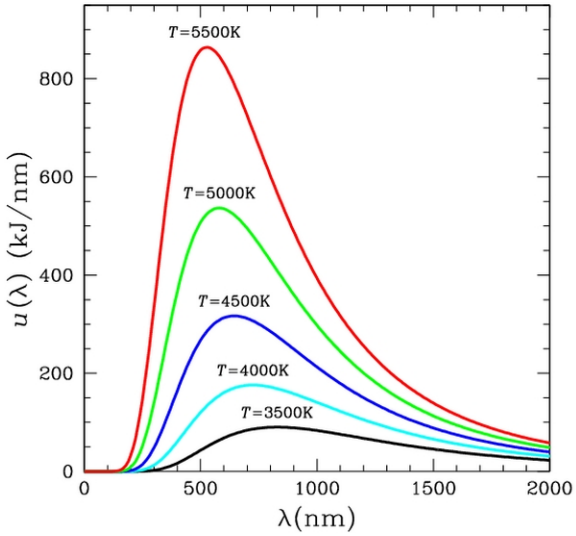

Fig. 72. Blackbody radiation for different temperatures

- The higher the temperature of the blackbody, the smaller is the wavelength at which the peak of the emission occurs. This is known as *Wein's displacement law*

A dense hot object such as the core of a star, acts like a blackbody radiator emitting radiation at all wavelengths. Although the gases present at the surface of the star or the gases in the interstellar space cause absorption of some of the wavelengths, the overall shape of the spectrum approximates a black body curve with a peak wavelength. Fig. 73 shows the normalized spectral radiance curves obtained for each of the spectral class of the stars classified according to their photospheric temperatures. As can be observed from the curves, the relative brightness increases with an increase in the temperature.

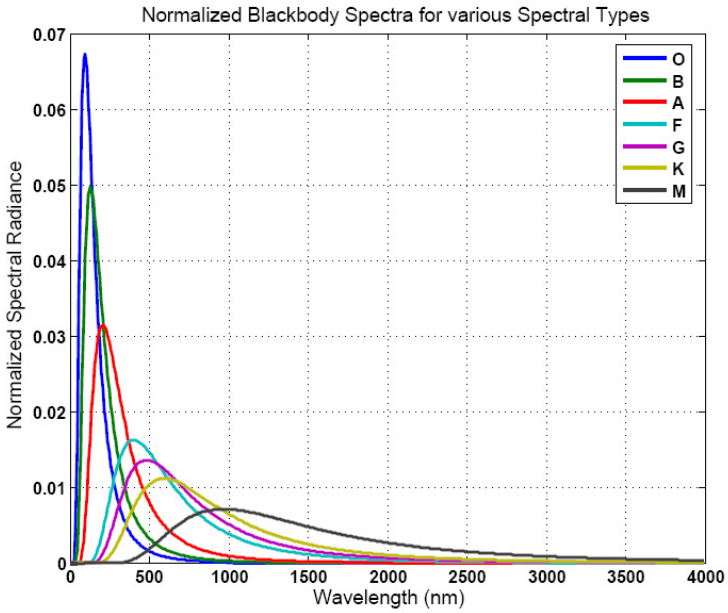

Fig. 73. Spectral radiance curves for spectral classes of the stars

C. Generation of On-board Star Catalogs

In order to identify the observed stars, every modern star sensor carries onboard a star catalog. The star catalog is a repository of the location of the stars (line-of-sight vectors or angles) in an inertial frame such as the J2000. For star trackers that rely on photometric estimations to identify stars, the star magnitude is also included in the catalog. The number of stars present in the catalog is dependent on the operation regime of the star tracker and the instrument sensitivity. For a spacecraft with small attitude excursions, the star catalog could contain only the potentially observable stars in its orbit. On the other hand, for a satellite that needs to acquire its initial attitude knowledge from any state without prior information (the lost-in-space case), a richer catalog is required. The sensitivity of the imaging optics and sensor dictates the faintest star that can be visible to the instrument.

The on-board star catalog can be extracted from a wide database of publicly available catalogs such as the Hipparcos catalog, Tycho-2 catalog, HST Guide Star Catalog etc. The Tycho-2 catalog [26] is a refined version of the Hipparcos catalog [27] and presently is considered the most reliable and accurate of all the catalogs. It contains star data for over one-million stars and is nearly complete for star magnitudes $m \leq 10.5$. We briefly discuss two methodologies of generating a mission star catalog: (1)fixed magnitude cutoff and (2)quasi-uniform distribution.

1. Fixed Magnitude Cutoff Star Catalog

The traditional method of building a catalog for a star tracker is outlined in Fig. 74. Given a star tracker field-of-view, the magnitude of stars required in order to perform identification can be deduced. This information is fed into a catalog parsing algorithm that reads a standard database such as Hipparcos or Tycho-2. The algorithm extracts all stars that are at and below the specified magnitude. All other data fields such as spectral class, luminosity etc. are ignored and a subset of the original catalog is obtained.

Post processing of the extracted data is usually done in order to remove multiple and or unreliable entries. If 3σ is taken as an estimate of the maximum centroiding error for a star, then in order for two neighboring stars to be distinctly visible, the minimum angular separation between them should theoretically be $4 \times 3\sigma$. Stars that violate this condition are thus eliminated from the catalog. Proper motion of a star causes its position vector on the celestial sphere to shift with time. Thus, stars with large proper motions do not form good inertial reference vectors. With the knowledge of the mission launch time, the positions of these stars can be updated. In most cases, however, these are simply removed from the catalog. The final step is to validate the generated star catalog. For this purpose, the reference vectors to a subset of stars are

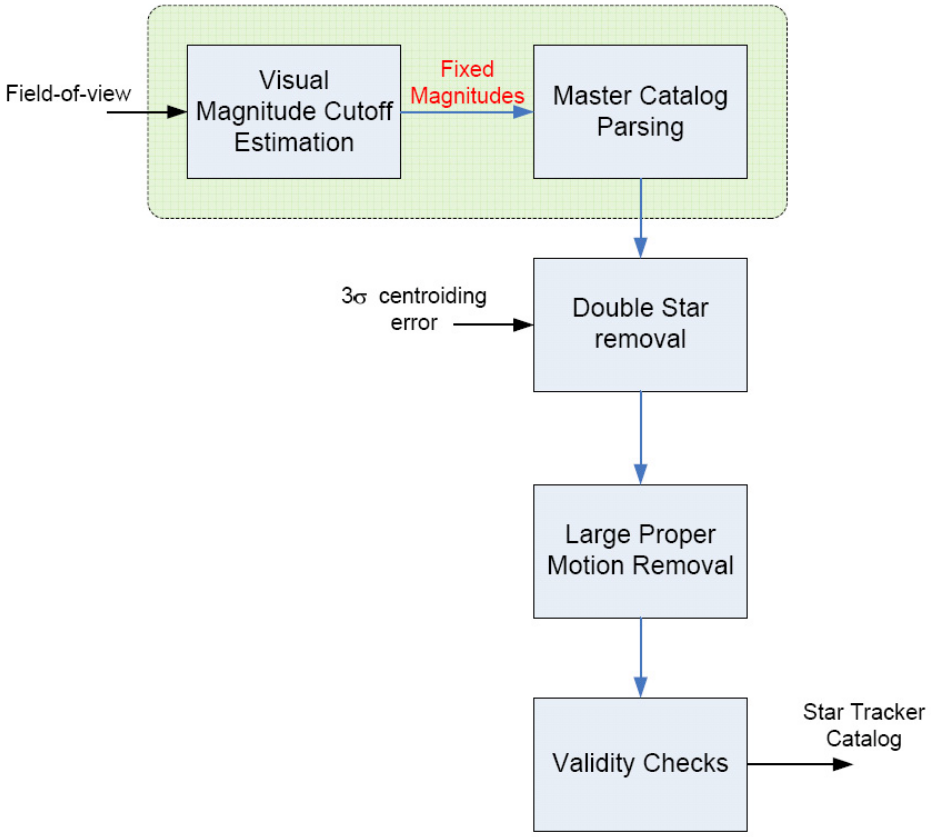

Fig. 74. Steps involved in creating a mission star catalog based on a fixed magnitude cutoff approach

obtained from the generated star catalog. These are compared against their values from the master catalog and if they match, the catalog is approved.

2. Quasi-uniform Star Catalog

The distribution of the stars over the celestial sphere is non-uniform in nature. Regions in the Milky Way are heavily populated with stars while the polar regions are very sparse. In order for the star tracker to produce a reliable identification, and consequently an attitude estimate, it is mandatory to have at least 4 stars in the

field-of-view at any attitude for the lost-in-space case. In a fixed magnitude cutoff star catalog, there exist holes in the sky where this requirement of 4 visible stars is not met. On the other hand, having more than 5 or 6 stars in the field-of-view leads to the phenomenon of diminished returns, wherein the costs of including more than the required number of stars in the field-of-view begin to outweigh the benefits. Thus, a need exists for a star catalog that has a uniform distribution of stars in the field-of-view at any given attitude.

Kim[50] has proposed a method based on thinning to generate a star catalog in which every single boresight direction contains at least two guide stars. Mortari et.al in [51] have developed the Quasi-Uniform Star Catalog (QUSC) to guarantee an average of 5 stars in the star tracker field-of-view no matter what the attitude. In the dense regions of the sky, the cutoff magnitude is adaptively decreased to reduce the number of extracted stars while in the sparse regions the cutoff magnitude is raised to extract fainter stars to satisfy the minimality criterion. However, note that the inclusion of faint stars calls for an increase in the sensitivity of the imaging device to gather sufficient starlight for accurate centroiding. Ideally, the integration time or light amplification technology can be used to gather more light in regions having a small number of faint stars. In the event that the sensitivity of the sensor cannot be increased, the method assumes that the faint stars are still visible, although at a non-optimal pixel intensity distribution. This reduces the accuracy of the centroid estimate, but nevertheless provides an attitude solution in the sparse region.

Several techniques have been used to create the quasi-uniform distribution. In the method of spherical squares, the unit sphere, representing the celestial sphere, is divided into a number of squares with equal areas. Stars with unit vectors that lie close to the center of the squares are chosen to create the on-board QUSC catalog. In the Fixed Slope Spiral procedure, a spiral of constant slope is overlaid on the

unit sphere and is uniformly divided. As before, stars with unit vectors given by the right ascension and declination at points along the spiral are extracted from a master catalog. The Spherical Triangles method divides the unit sphere into non-overlapping spherical triangles and the stars lying inside each triangle are derived. The most successful method, Repulsive Charged Particles, tries to assign a fixed number of "charged particles" uniformly on a sphere. Equilibrium between these charged particles is obtained when the forces of repulsion are balanced. For a large number of points, it is shown that the particle distribution approaches a uniform distribution. To establish the near uniform catalog, the large catalog can be searched to place the brightest cataloged stars nearest to the quasi-uniform distribution that corresponds to a desired near-uniform inter-star separation angle.

D. A Methodology for Building a Spectrally Matched Catalog

The objective of this method is to estimate the cutoff magnitudes for each spectral class of stars based upon the loss incurred due to the non-uniform sensitivity of the system. Fig. 75 gives an outline of this process. As before, the field-of-view information is used to determine the cutoff magnitude required in order to have a minimum of 4 stars in the frame. This cutoff magnitude is assigned to the stars of the spectral class M. The decision to select class M as the reference point is based upon the qualitative study of the spectral profiles of the components of the system. A class M star being coolest emits most of its radiation in the IR region and very little in the UV. Since each of the components appear to have a higher sensitivity to the red wavelengths, it is expected that a class M star would suffer the least loss in magnitude when imaged through the system.

To obtain the relative loss in magnitudes, it is first necessary to characterize the

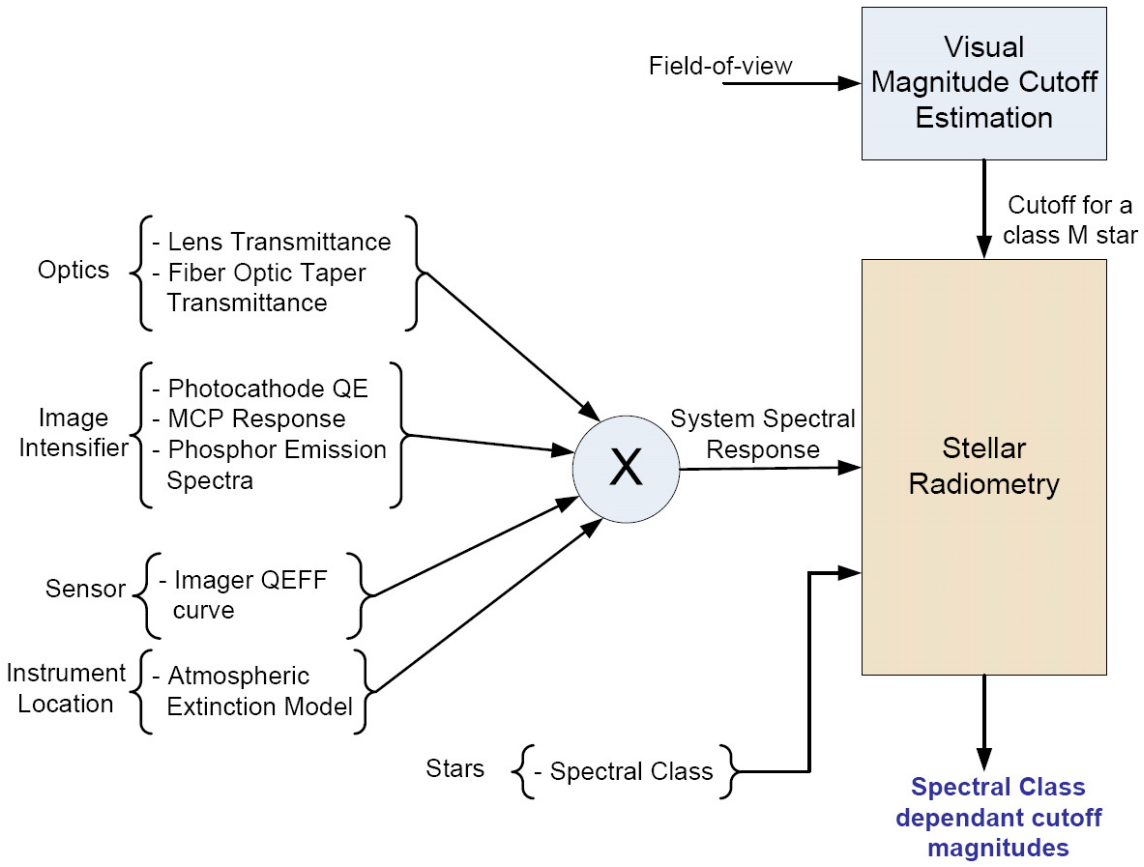

Fig. 75. Outline of the steps involved in obtaining spectral response dependant cutoff magnitudes

spectral response of the intensified star sensor. For an imaging sensor system this can be simply defined as the sensitivity of the system with respect to wavelength of incident radiation. If the sensitivity curve is uniform/constant across all wavelengths of interest, then the all the signals will be detected with equal relative brightness. On the other hand, a non-uniform spread of the spectral curve indicates a preferential treatment of wavelengths. To determine the overall response, the system is broken down into its constituent elements - lens assembly, image intensifier, fiber optic taper and imaging sensor and the response of each component is estimated separately. The transmittance of a lens assembly is an indicator of how much optical power is transferred from input to output at each wavelength. Knowing the material and the thickness of each of the elements making up the lens, the overall transmittance can be obtained. The image intensifier is characterized by the quantum efficiency of its photocathode and the emission characteristics of the phosphor screen. To account for terrestrial applications, the attenuation due to the atmosphere is modeled using extinction coefficients. The extinction coefficients along with the angular position of the stars in the sky give rise to the transparency of the sky for a observer located on Earth. Finally, the imaging sensor QEFF curve is used to model the sensitivity of the imager in use.

Once the system response i.e. sensitivity as a function of wavelength, is determined, the loss in the apparent magnitudes can be estimated by performing stellar radiometry. The energy distributions of each of the spectral classes of stars are calculated assuming the star to be a black body radiator. Regions of interest in the spectrum are extracted and normalized so that they correspond to equal apparent magnitudes. The normalized curves are then propagated through each of the system components. At each stage, they get modified by the response curves of the component that were obtained in the previous step. After the last stage, the area under the

curves is calculated to give the effective brightness per spectral class. The relative loss in the magnitude for a spectral class is then readily obtained by comparing the brightness of the class of interest against a class M star.

Having obtained the relative magnitude loss, the cutoff per spectral class is simply determined by subtracting this loss from the reference magnitude. The magnitudes for each class can then be fed into a catalog parsing algorithm to extract relevant stars. Post-processing steps such as proper motion removal, double star removal and validity checks can be performed as before. The end product of the exercise is a mission star catalog that is tuned to the spectral sensitivity of the instrument i.e. it is "spectrally matched" and nominally does not contain stars that are "invisible" to the sensor. Of course, this ideal goal can never be realized exactly. In the following sections, we describe in detail each of the steps discussed above.

1. Optical Train Spectral Response

The lens system is a complex assembly of several glass elements placed at precise locations in order to minimize aberrations and thus maximize resolution. Different types of glass materials are used in conjunction with each other so as to overcome the wavefront distortions induced by modifying the optical path. For example, a combination of a flint (high dispersion,negative element) and a crown (low dispersion, positive element) is commonly used to overcome the primary axial color aberration that occurs because of the dependence of the refractive index on the wavelength of the light.

Each of elements in the optical train, while performing a necessary function, is also responsible for a loss in the transmittance. The loss in the optical energy is proportional to the thickness of the element and is also wavelength dependant. Fig. 76 shows the transmittance of a commonly used crown glass - BK7 [52]. The glass

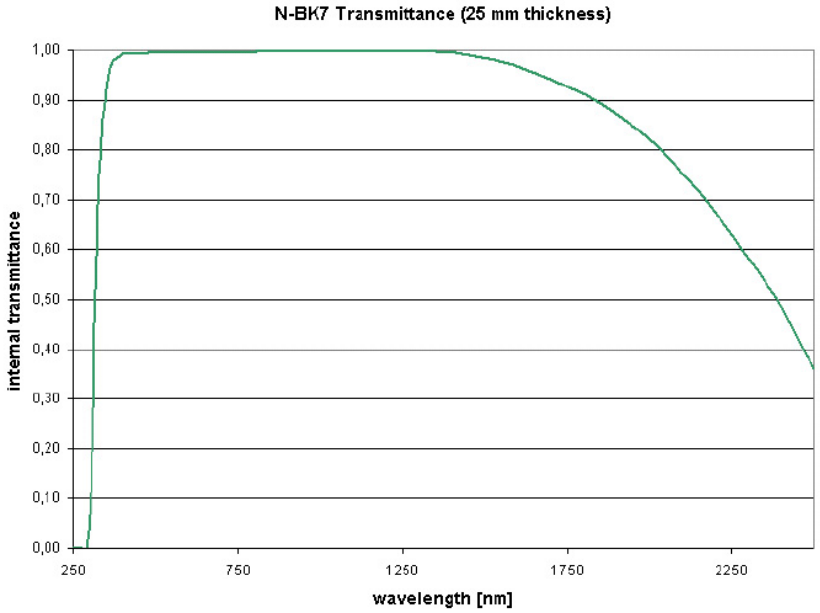

Fig. 76. Transmissivity of a commonly used glass material - Schott N-BK7

performs very poorly in the deep UV region but has greater than 95% transmittance in the visible range. Since the application sought lies in the visible range, this poses no problems. However, space is a very harsh energy environment and the spacecraft is constantly bombarded with high energy radiation such as γ-rays, protons, heavy ions, etc. The electronics are usually well protected from these harmful rays by a heavy duty metallic shielding which stops the propagation of most of the radiation. The lens, on the other hand, forms an optical window and thus cannot be shielded. When the high energy rays strike the glass, the atoms are dislodged from their lattices leaving a void. This causes the glass to blacken locally and leads to a drop in the transmittance. Fig. 77 shows the transmission curves for a BK7 glass before and after irradiation with high energy rays, the drop in transmittance is clearly visible.

The blackening of the glass is usually prevented by selective doping of the glass by materials such CeO_2. Although the doping shifts the UV transmission cutoff farther

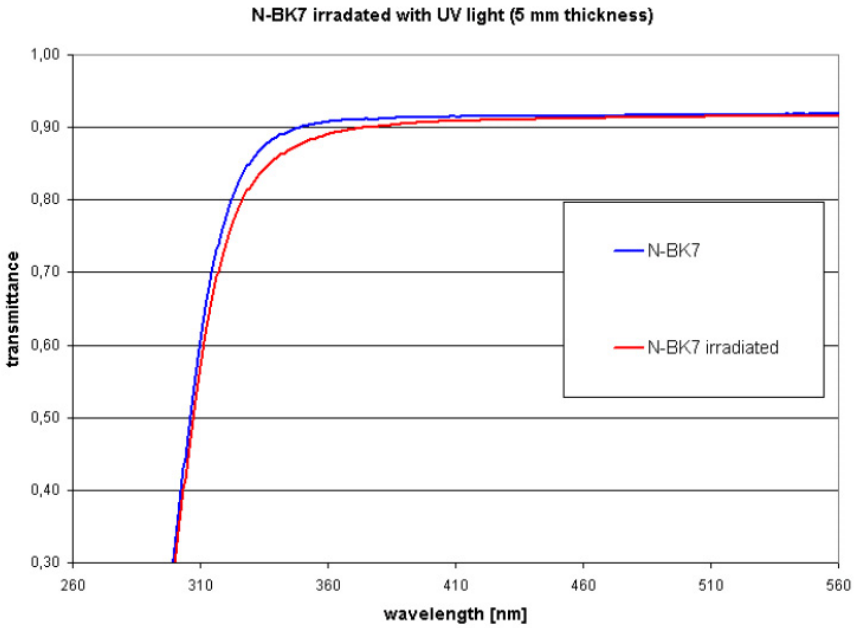

Fig. 77. Transmittance of BK7 before and after exposure to radiation

towards the visible (towards the right), the glass transmittance remains stable even in the presence of radiation. Such glasses are termed as radiation-hardened glasses and are suitable for operation in space. The drawback of using these glasses however, is that the transmittance is reduced.

a. Transmittance of a Radiation Hardened Lens

Fig. 78 shows the layout of a 5 element lens made up of radiation hardened glass for a 8° field-of-view star tracker [53]. The design consists of three crown elements constructed of glasses BK7G18 and K5G20, and two flints made of SF8G07 and F2G12 glasses. The system was designed and optimized for performance in the ZEMAX optical design environment.

The transmittance as a function of wavelength for each of the glass types was obtained from ZEMAX database (Fig. 79). No data was available for the SF8G07

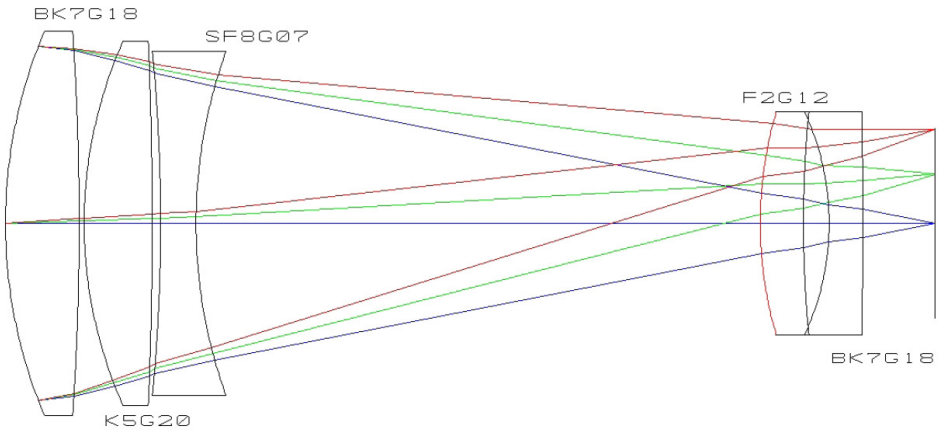

Fig. 78. Layout of a possible radiation hardened lens design for a star tracker

glass and thus the transmittance was assumed to be equal to the F2G12. The net transmittance can be derived as the product of the individual transmittances:

$$T_{lens}(\lambda) = T_{BK7G18}(\lambda) \times T_{K5G20}(\lambda) \times T_{SF8G07}(\lambda) \times T_{F2G12}(\lambda) \tag{7.4}$$

Fig. 79(d) shows the net transmittance of the rad-hard lens system. Notice that the transmittance in the near UV and blue regions is very small (0.4).

2. Image Intensified Sensor Spectral Response

The image intensified sensor spectral response can be decomposed into the spectral response of its constituent elements - photocathode, MCP, P43 phosphor screen, fiber optic taper and imaging sensor.

$$T_{IIsensor}(\lambda) = T_{photocath}(\lambda) \times T_{MCP} \times T_{P43}(\lambda) \times T_{taper}(\lambda) \times QEFF_{sensor}(\lambda) \tag{7.5}$$

Since the photocathode converts the incident photons into electrons (much like an imager) it is mainly characterized by it's quantum efficiency or QE. The higher the QE, the better the photo-electric conversion. The QE however, is not constant at

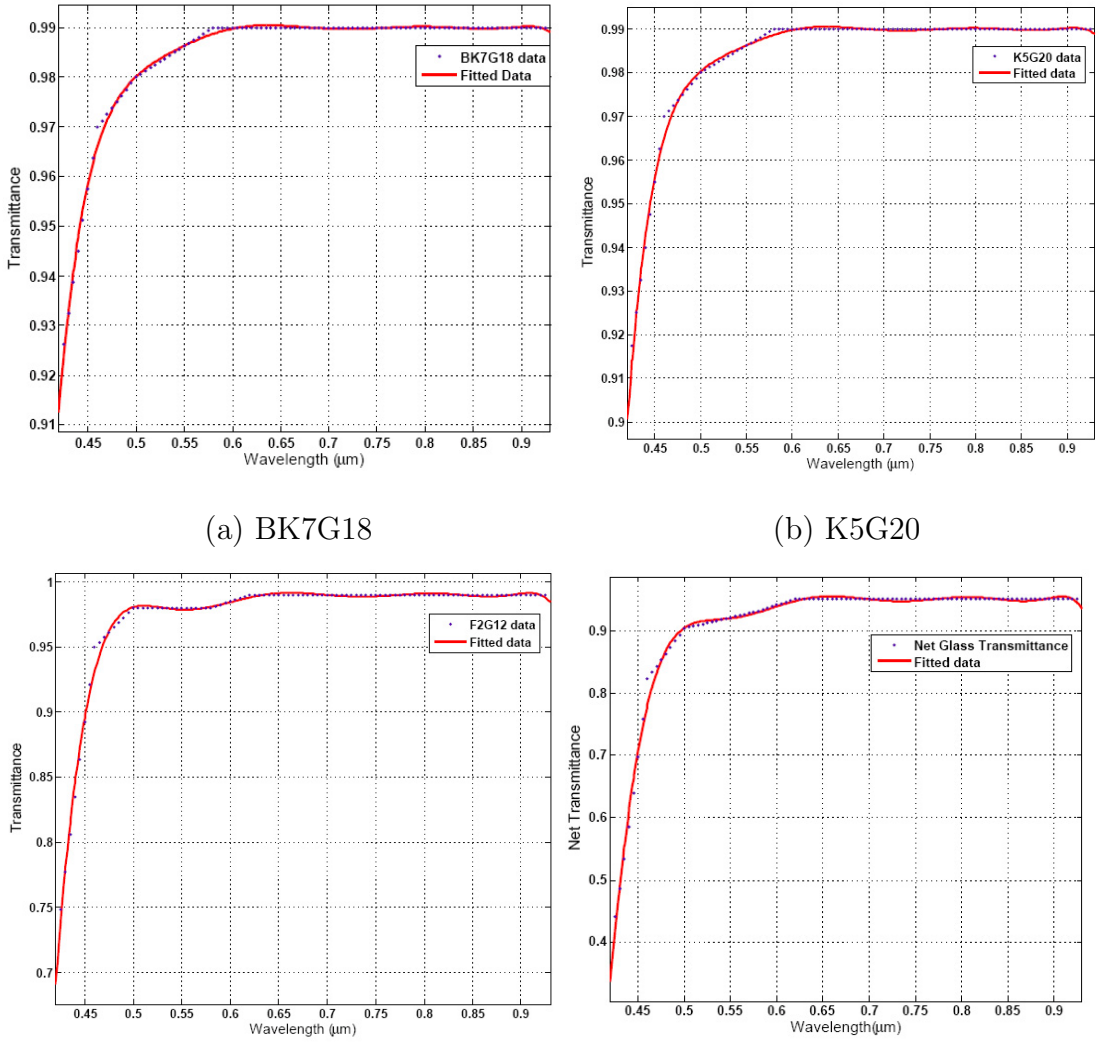

(a) BK7G18

(b) K5G20

(c) F2G12

(d) Net Glass Transmittance

Fig. 79. Transmittance versus wavelength curves for the glass types used in the rad-hard lens design

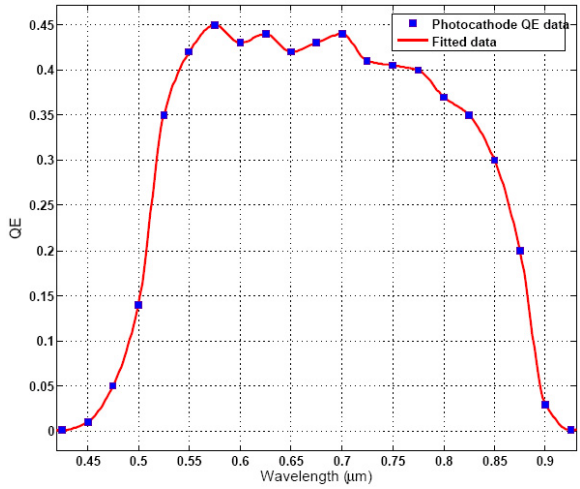

Fig. 80. QE of the GenIII image intesifier GaAsP photocathode

all wavelengths and its spectral distribution depends on the materials that are used to make up the photocathode. For intensifiers operating in the visible regime, the most commonly used photocathodes are GaAsP and GaAs.

Fig. 80 shows the quantum efficiency as a function of the wavelength for the GaAsP photocathode of a GenIII image intensifier from ITT Industries [28] that was used in the Speedstar system. The data was obtained from the specifications of the device and was fit using a shape-preserving spine interpolating function. The maximum QE is about 45% at $575nm$ i.e. green wavelength. The spectral response extends well into the IR region, indicating that the same photocathode can be used for multi-spectral i.e. visible and near IR imaging.

The photo-generated electrons are then multiplied by the MCP. Since the MCP is an electronic device, a spectral response cannot be appropriately defined for it and only an expression for an electronic gain can be obtained. This gain depends only on the acceleration potential across the device and is thus independent of the spectral characteristics of the radiation incident on the photocathode. For the purpose of

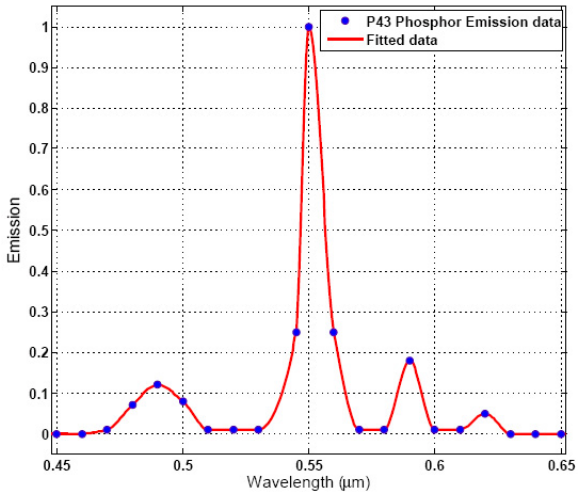

Fig. 81. Emission characteristics of the P43 phosphor

calculations, this element is assumed to provide a unity contribution to the spectral response of the intensifier.

The multiplied electrons are converted back to photons by a phosphor screen. The emission characteristics of the phosphor completely dictate the spectral distribution of the photons. As in the case of the MCP, the phosphor has no "memory" of the wavelength of radiation that led to the creation of photo-electrons. In the Speedstar system a P43 phosphor is used and its emission is shown in Fig. 81 [28].

The phosphor emits almost 90% of all its photons in a very narrow band ($\sim$ 20nm) centered at 550nm i.e. green wavelength. The emitted radiation is captured by the fiber optic taper which has a non-uniform transmittance with a maximum of about 70%. The propagated radiation is then incident on the imaging sensor which converts the photons back to electrons and transfers them for a readout. Depending on the technology used (CMOS or CCD) the imaging sensor has a characteristic QEFF curve which varies with the wavelength of the incident light. The opacity of the poly-silicon gate on the pixel to UV leads to a reduced sensitivity in the blue

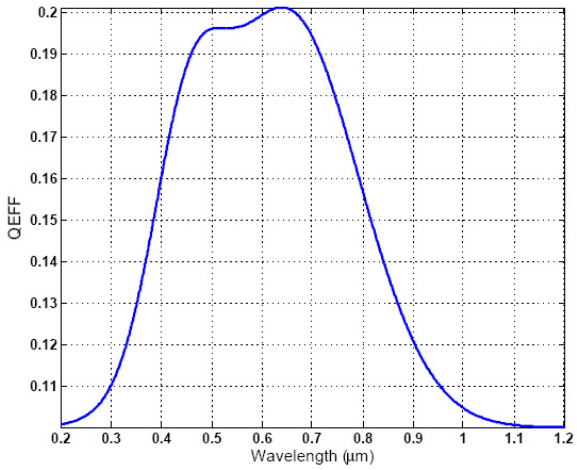

Fig. 82. QEFF of a typical CMOS image sensor

region, thus shifting the peak towards the red part of the spectrum. Fig. 82 shows the QEFF of a CMOS imager. As compared to a CCD imager the CMOS sensors have a very small QEFF. However, in our application, the reduced sensitivity can be easily gained back by using the intensifier.

Since the emission from the phosphor is limited to a very narrow band, this is the only region of interest for the imager and fiber taper response. Over this small region, the transmittance of the taper and the QEFF of the sensor can be assumed to be constant. The transmittance of the intensified sensor is then given by

$$T_{IIsensor}(\lambda) = T_{photocath}(\lambda) \times T_{MCP} \times T_{P43} \times QEFF_{sensor} \tag{7.6}$$

The net end-to-end transmittance between the star sensor aperture and the sensor is

$$T_{system}(\lambda) = T_{glass}(\lambda) \times T_{IIsensor}(\lambda) \tag{7.7}$$

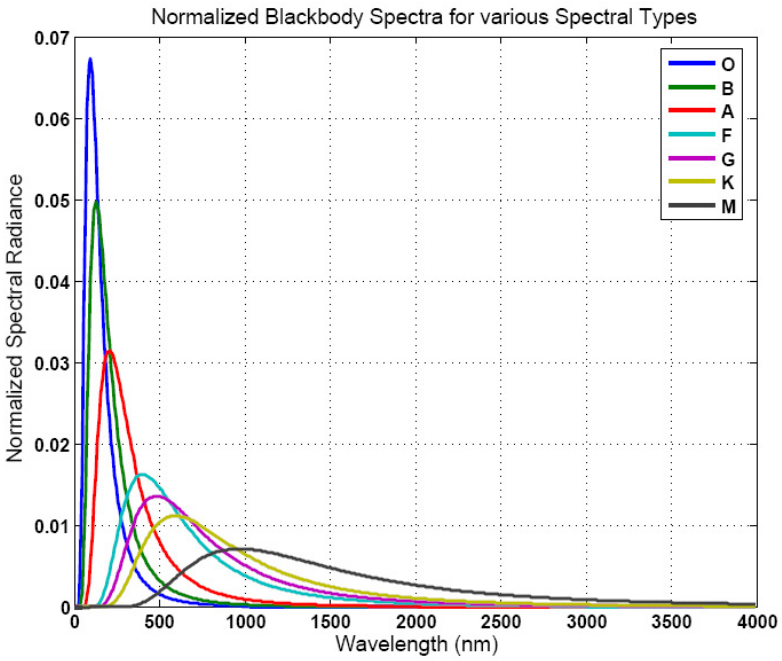

Fig. 83. Spectral radiance curves for spectral classes of the stars

3. Loss in Apparent Magnitudes

The non-uniform spectral response of the imaging train leads to a lossy transfer of the faint star signals. Moreover, since stars of different classes possess different energy spectra, the relative apparent magnitudes sensed by the detector are different from those entering the aperture of the star sensor. In this section we shall derive a methodology for quantifying the relative loss.

The blackbody radiation spectra for each of the spectral classes as defined by their photospheric temperatures is given by Eq.7.3 and shown in Fig. 83. Each of the curves are normalized so that the area under the curve is equal to unity i.e. if $L_j(\lambda)$ is the spectral radiance of a star belonging to class j then

$$Ln_j(\lambda) = \frac{L_j(\lambda)}{\int_\lambda L_j(\lambda) d\lambda} \tag{7.8}$$

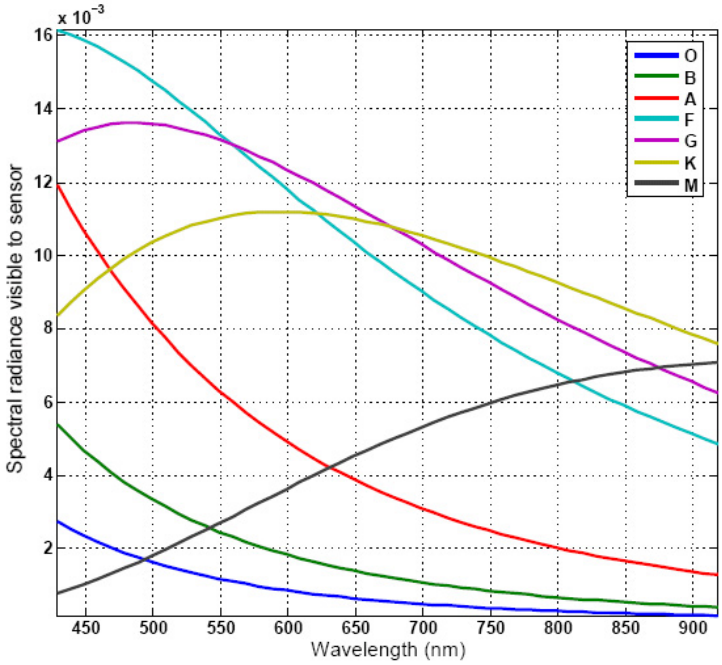

Fig. 84. Spectral Profiles of the region of interest

where $Ln_j(\lambda)$ is the normalized spectral radiance. For implementation purposes, the wavelength is varied from $0.01\mu m$ to $4\mu m$ and is discretized into 400 intervals. The discrete version of the above equation then becomes

$$Ln_{j,k} = \frac{L_j(k\Delta\lambda)}{\sum_{k\Delta\lambda=0.01\mu m}^{4\mu m} L_j(k\Delta\lambda)\Delta\lambda} \tag{7.9}$$

The curves of Fig. 83 represent stars of equal magnitudes but with different temperatures. The imaging train however is sensitive only to wavelengths ranging from $425nm$ to $925nm$, so the appropriate sections of the curves are extracted and shown in Fig. 84. The indices corresponding to the wavelengths of interest are calculated as

$$\begin{aligned} \text{iL} &= \text{floor}\left(\frac{0.4\times10^{-6}-\lambda_{min}}{\Delta\lambda}\right) \\ \text{iU} &= \text{ceil}\left(\frac{0.9\times10^{-6}-\lambda_{min}}{\Delta\lambda}\right) \\ Ev_{j,k} &= Ln_j(k=iL\ldots iU) \end{aligned} \tag{7.10}$$

The area under the curves in the portion of the spectrum visible to the instrument gives the amount of the energy captured by a detector of constant sensitivity with respect to the wavelength and has the following expression

$$Es_j = \sum_k Ev_{j,k} = \begin{pmatrix} 0.042 \\ 0.087 \\ 0.225 \\ 0.505 \\ 0.528 \\ 0.494 \\ 0.226 \end{pmatrix} \tag{7.11}$$

Thus the detector is able to gather only 4.2% of the net energy from a class O star in the region of interest of the spectrum and about 52.8% of the energy of a class G star. Normalizing the energy profiles by the area under the curves gives the apparent brightness of the stars above the Earth's atmosphere $En_{j,k}$ as shown in Fig. 85,

$$En_{j,k} = \frac{Ev_{j,k}}{Es_j} \tag{7.12}$$

The light energy given by Eq.7.12 is incident on the intensified star sensor system and suffers a loss in transmittance given by Eq.7.7. The resulting magnitude profiles $Esys_{j,k}$ are thus given by

$$Esys_{j,k} = En_{j,k}T_{system}(k\Delta\lambda) \tag{7.13}$$

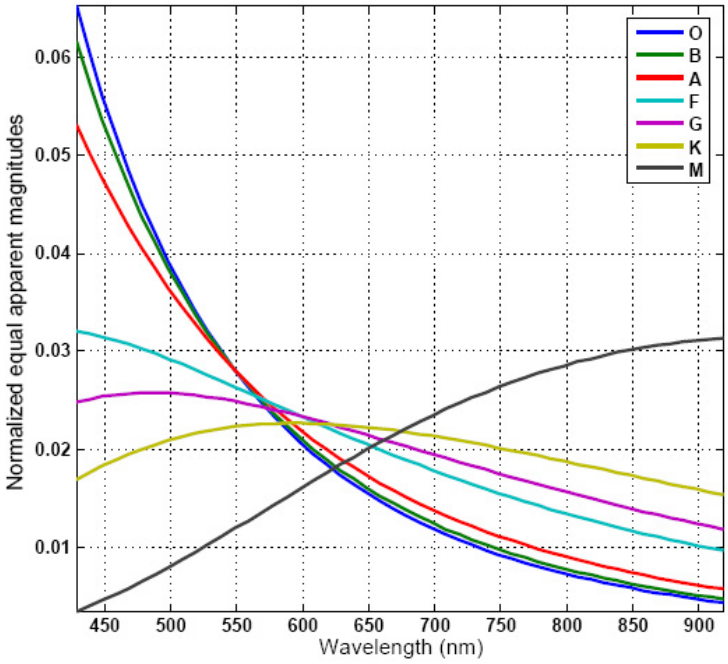

Fig. 85. Normalized equal apparent brightness in space

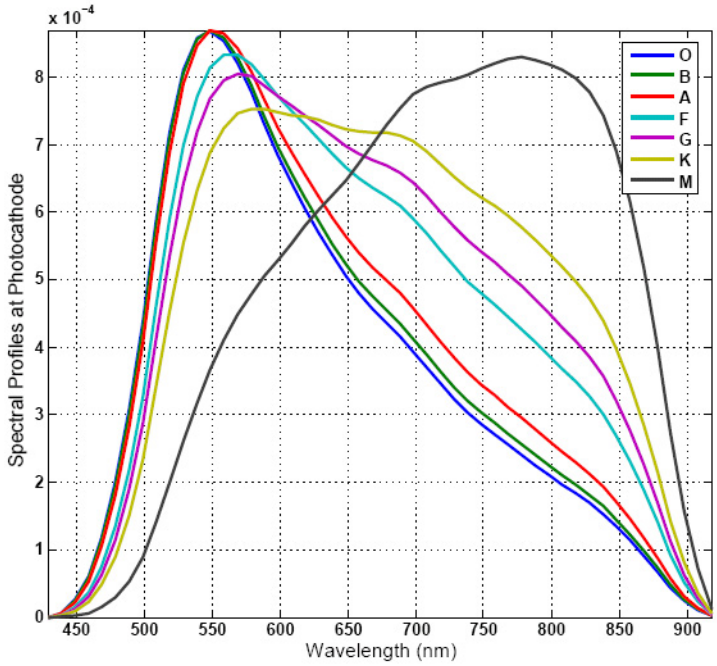

Fig. 86. Apparent brightness profiles at the output of the image intensified star sensor system

where $T_{system}(k\Delta\lambda)$ is the discrete version of Eq.7.7. Fig. 86 shows the apparent brightness profiles at the output of the image intensified system. The shape of the curves can be seen to be primarily affected by the response of the photocathode. In the absence of the image intensifier, the QEFF curve of the imaging sensor will dictate the shape of the profiles. Notice from the curves that the area under the curve of a class M star seems to be larger than any other classes implying that this class is "spectrally best matched" to the response of the sensor system.

Normalizing the area under each of these curves with the maximum area gives a

measure of the relative loss in brightness between the spectral classes,

$$Eac_j = \sum_{k=iL}^{iU} Esys_{j,k} \tag{7.14}$$

$$Ea = \frac{Eac_j}{\max\left(Eac_j\right)} = \begin{pmatrix} 0.732 \\ 0.749 \\ 0.790 \\ 0.891 \\ 0.933 \\ 0.979 \\ 1.000 \end{pmatrix}$$

where Eac_j is the area under the curve for each spectral class and Ea is the normalized loss in brightness. Thus a class O stars loses about 27% of its brightness as compared to a class M star when imaged through the system. In terms of apparent magnitude, the loss is given by

$$\text{Magloss} = 2.5 \log \frac{1}{Ea} \tag{7.15}$$

Fig. 87 shows the loss in the apparent magnitudes as sensed by the star sensor for all the spectral classes. A class O star thus appears to be 0.34 in magnitude dimmer than a class M star of the equal magnitude.

4. Accounting for Atmospheric Transmission

The starlight reaching the surface of the Earth is dimmed by the atmosphere in an effect called *atmospheric extinction*. Although this is inconsequential to the star sensors aboard spacecraft in orbit around the Earth, it is of importance in terrestrial applications that rely on imaging of stars. A few such applications would be night sky testing, star gazing and the stellar compass. The atmospheric extinction compounds

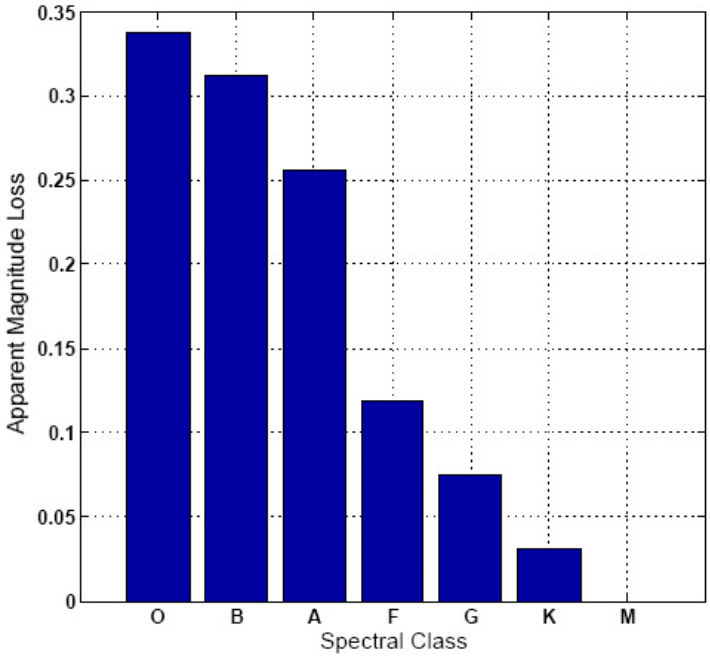

Fig. 87. Apparent magnitude loss in space with respect to Class M star for various spectral classes

the loss in the magnitude experienced by the detector and can lead to non-optimal detection and incorrect photometry of stars.

As the light passes through the atmosphere, it undergoes absorption and scattering by the air molecules, aerosols and dust particles and thus gets attenuated. The attenuation is dependant on the wavelength of the light. Gamma rays, X-rays, radio waves of long wavelengths are completely absorbed by the atmosphere while wavelengths around the visible spectrum and short radio-waves have relatively higher transparency. Additionally, the longer the path length the starlight traverses through the atmosphere, the higher is the extinction. Thus, a star close to the horizon will be dimmed more than one close to the zenith. The path length through the air is known as *air mass*. Fig. 88 shows a beam of radiation from a star at a zenith angle z entering the Earth's atmosphere and observed on the surface at O. At any particular wavelength, the magnitude observed at the Earth's surface $m(\lambda)$ can be related to the extra-terrestrial magnitude $m_0(\lambda)$ measured just outside the Earth's atmosphere by an expression called *Bouguer's law*:

$$m(\lambda) = m_0(\lambda) + \kappa(\lambda)X(z) \tag{7.16}$$

where $X(z)$ is the airmass, $\kappa(\lambda)$ is the extinction coefficient at wavelength λ and z is the zenith distance at the time of observation. The airmass $X(z)$ is defined as the number of times the quantity of air seen along the line of sight is greater than the quantity of air in the direction of the zenith and will vary as the observed line of sight moves away from the zenith, that is, as z increases. The airmass is a normalized quantity and has the unity value at zenith.

For small zenith angles $X = \sec z$ is a reasonable assumption, but as the zenith angle increases various effects such as curvature of the atmosphere, refraction and variations of air density with height become important. To account for these effects,

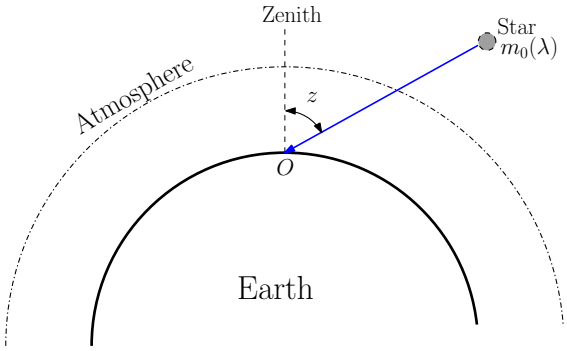

Fig. 88. Path traversed by stellar radiation at zenith angle z

Young and Irvine [54, 55] give a more refined relationship

$$X = \sec z \left(1 - 0.0012 \left(\sec^2 z - 1\right)\right) \tag{7.17}$$

The extinction coefficients are estimated by performing night sky experiments using a very well calibrated setup. We use the results obtained by Vargas [56] in our discussion. The authors performed observations using a set of photometric filters at ($B : 440nm$, $V : 550nm$, $R : 650nm$, $I : 800nm$) wavelengths using a $0.4m$ reflector telescope. The atmospheric transparencies at zenith angles of $0°, 20°, 40°$ and $60°$ over the set of wavelengths was obtained and is shown in Fig. 89. The data points were fit using a cubic polynomial. Note that the extinction coefficients obtained are local to the place and the elevation of the location above the sea level. The transparency of the atmosphere is greater at higher altitudes owing to lesser pollution and reduced air mass. For this reason, most of the observatories are located atop mountains. Nonetheless, the methodology presented here can be applied to any location as the coefficients can be obtained via experimentation or by using online databases if available.

The magnitude loss analysis performed in the previous section can now be ex-

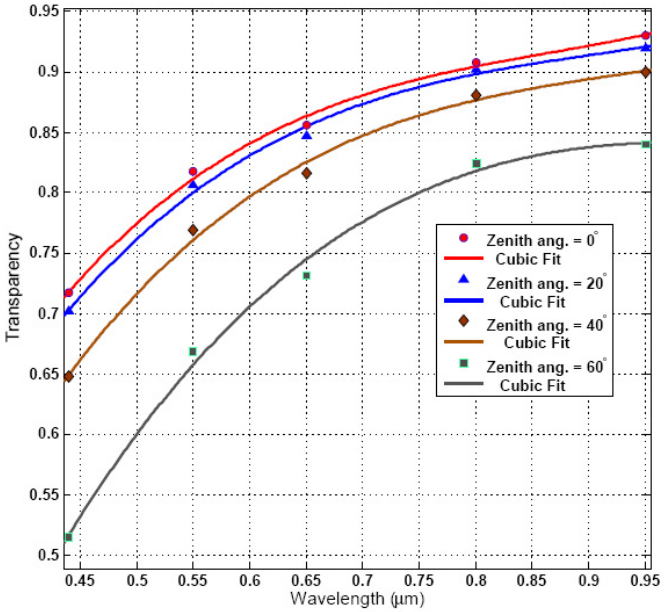

Fig. 89. Atmospheric transparency v/s wavelength for various zenith angles

tended to include the effects of the atmosphere. The net system transmittance on the Earth's surface $T_{Earth}(\lambda, z)$ at sea level and zenith angle z is thus given by

$$T_{Earth}(\lambda, z) = T_{atm}(\lambda, z) \times T_{system}(\lambda) \tag{7.18}$$

where $T_{atm}(\lambda, z)$ is the atmospheric transparency model obtained above. Using this in Eq.7.13, the series of calculations can be repeated yield the loss in the apparent magnitudes. Figs.90(a) and 90(b) show the results of the calculations for observation at zenith and zenith angle 60° respectively for an observer at sea level.

Comparing against the data in Fig. 87 it can be seen that an additional loss of 0.1 in magnitude is incurred while viewing from the surface of the Earth. Although this may not seem significant at first sight, we will show in the next section that for embedded systems such as star trackers and image intensified sensors especially, this number has a large impact on the size of the star database.

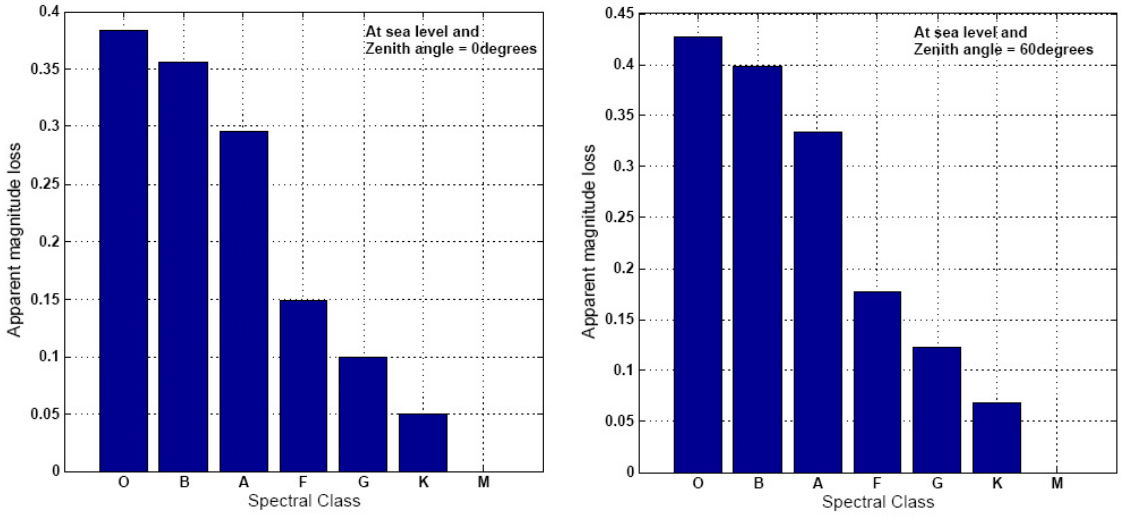

(a) At zenith (b) At zenith angle = 60°

Fig. 90. Loss in apparent magnitudes with observer at sea level and zenith angles 0° and 60°

E. Catalog Extraction Results

In our experimentation, the Hipparchos catalog was used. Although, the Tycho2 catalog is more recent and accurate than the Hipparchos, it does not contain information pertaining to the spectral class of the star. It does include for each star, however, a cross-reference to the Hipparchos star index. Thus, once the stars are extracted from the Hipparchos, their celestial information can be obtained from the Tyhco2 catalog using these unique identifiers.

The procedure outlined in the above section was used to obtain the relative magnitude cutoffs for each spectral class. A class M star is taken as the reference point for all magnitude calculations since it is best matched to the response of the system. These were used as input to a script written in Python programming language which is optimal for string processing. The Hipparchos catalog was parsed and the stars

meeting the magnitude criteria were extracted. The spectral subfields for luminosity etc were ignored in the parsing.

Night sky experiments on the intensified camera system revealed that capturing a magnitude 7.0 star is easily achievable and thus this was chosen as the reference magnitude for class M stars. Fig. 91 shows the stars extracted per spectral class using the traditional fixed cutoff method and the spectral matching based method for the instrument located in space. The difference in the number of stars between the two approaches is also indicated. The total number of stars extracted using the fixed cutoff method was $15,486$ while that using spectral matching was $13,067$ corresponding to a reduction by 2419 stars or 16.6%. As can be noticed, the relative difference is very high for classes B and A. This is as expected since these classes are "spectrally farthest" from the peak star sensor spectral transmittance.

The procedure was repeated for the condition where the star sensor is located on the Earth's surface at sea level and at zenith angles of $0°$ and $60°$. Fig. 92 illustrates the differences in the number of stars per spectral class between the stars extracted using fixed cutoff and spectral matching at these imaging conditions. The number of stars extracted for imaging at zenith were 2945 or 21% lower in number than the fixed magnitude and 3545 or about 25% lower for zenith angle of $60°$.

For a star sensor with limited hardware resources, this represents a significant savings in the memory requirement for on-board storage. Moreover since the number of star pairs are reduced, the computation time required for star identification is smaller. The probability of a false match is also reduced.

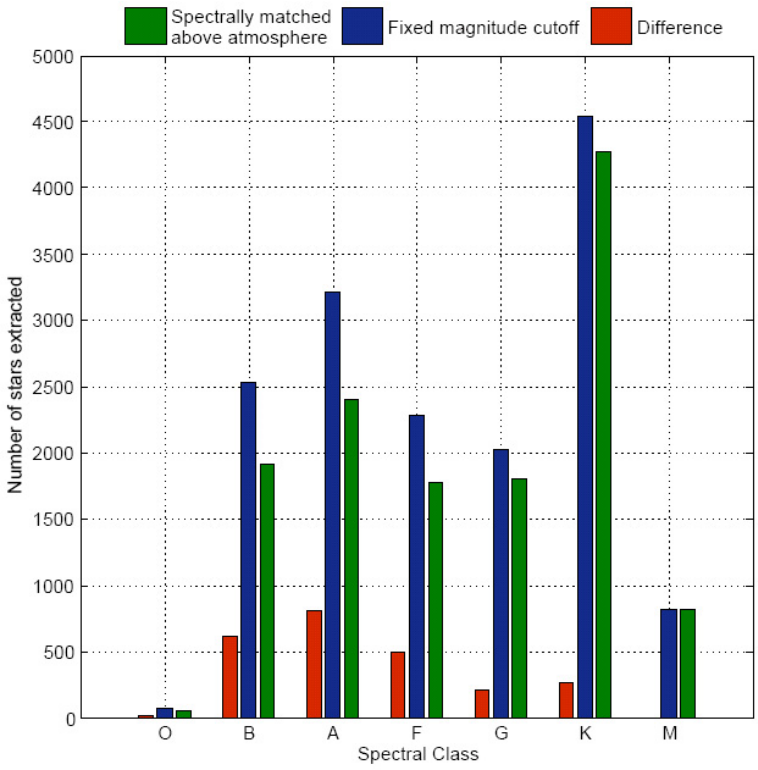

Fig. 91. Number of stars extracted per spectral class from the Hipparchos catalog using fixed cutoff and spectral matching for a instrument located above the Earth's atmosphere

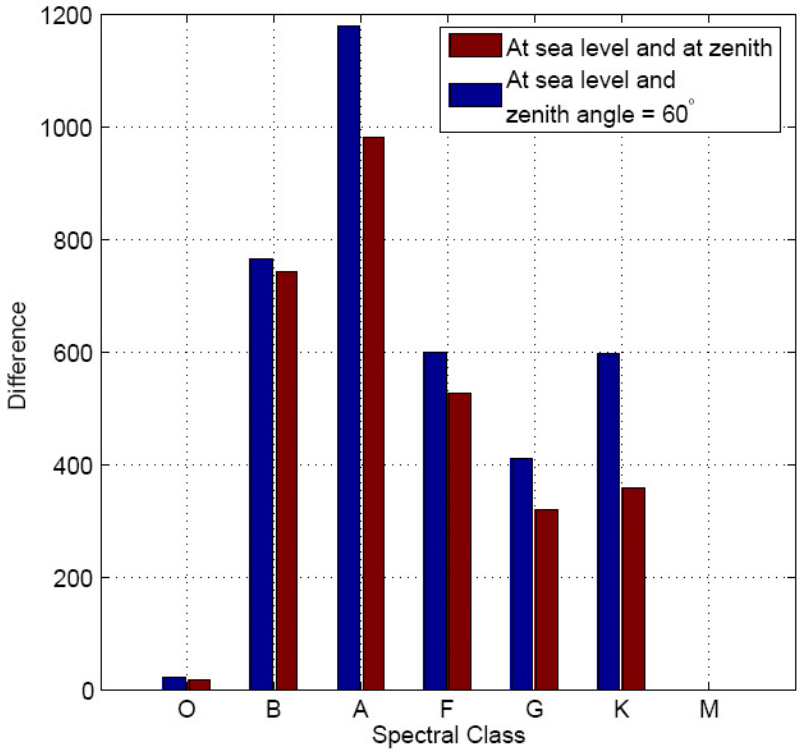

Fig. 92. Difference in the number of stars extracted per spectral class between the fixed cutoff and spectral matching approaches

F. Concluding Remarks

In this chapter, we developed a methodology for creating a mission star catalog that is spectrally tuned to the response of the imaging system. As compared to a method based on a fixed magnitude cutoff, the spectral matching approach calculates a cutoff magnitude for each spectral class depending upon the imaging system and imaging conditions. This leads to a more efficient, reliable and a compact star catalog optimized for embedded systems.

It was demonstrated that stars undergo a loss in apparent magnitude when imaged through an optical system. The loss was attributed to the difference between the spectral response of the imaging system and the spectral signature of the star. More importantly, the loss was shown to be relative i.e. stars with equal brightness but belonging to different spectral classes have different magnitude losses.

The response of the imaging system was calculated using a divide and conquer strategy, wherein, the spectral response of each component of the system was calculated. These were combined to give a net system response. For the lens design adopted, the transmittance as a function of wavelength was obtained by analyzing the design in optical ray-tracing software ZEMAX. It was shown that radiation hardened glass materials exhibit a reduced transmittance in the UV. Knowing the materials used and the thickness of each element making up the lens, the overall transmittance of the lens was calculated. As was expected, the radiation-hardened lens was found to perform very poorly in the UV and the blue part of the spectrum.

Quantum Efficiency curves of the photocathode of the image intensifier were obtained from the data sheets of the product used in the design. Since the MCP is an electron multiplication device, it does not contribute to the non-uniformity of the spectral response and the transmittance was thus assumed unity. The Phosphor

screen has a very narrow bandwidth emission spectra, within which the transmittance of the fiber optic taper and the QEFF of the imaging sensor can be assumed to constant.

Having calculated the spectral response of the system, the loss in apparent magnitude was estimated by performing stellar radiometry. The star was assumed to be a black body radiator and the radiation profiles were derived using Planck's Law. A class M star was chosen as the reference point for magnitude comparisons, since its spectral profile was closest to the sensor spectral response. It was shown that for an image intensified system, the loss in magnitude is about 0.34. For terrestrial applications, it was shown that the atmosphere of the Earth causes an additional loss that is dependent on the zenith angle and location of observer on Earth. Extinction coefficients were obtained by experimental analysis done by Vargas [56] and were used to calculate the transparency (transmittance) of the atmosphere at various zenith angles. It was shown that the loss in the stellar magnitude is as high as 0.45 for a class O star when compared against a class M star.

Star catalog parsing was performed using the relative magnitudes derived above for various operating scenarios. It was observed that using a spectrally matched catalog leads to a reduction in the number of stars extracted by about 17% for a space application and about 21% in the best case for a terrestrial application.

CHAPTER VIII

STRAY LIGHT MITIGATION

A. Origins of Stray Light

Stray light is defined as any unwanted light entering into the optical system of the imaging device. Light rays from a bright object not in the field-of-view of the sensor can enter the optical path either due to reflections or scattering at the optical/mechanical surfaces and interfaces. Some of the ways in which stray light arises are:

- Unblocked or "straight shots" seen mainly in reflective systems or systems with poor light shade design
- Ghosting in refractive optics due multiple reflections between the lens surfaces and consequently a formation of the "ghost image" at the detector. To cause a ghost image, light must reflect an even number of times from the lens surfaces
- Single and multiple scattered light due to non-optimal baffle design or a highly reflective detector. Single scatter occurs when a stray light source such as the sun directly illuminates the optics and causes scattered light to reach the detector. Multiple scatter occurs when the optics are illuminated indirectly by the light source by scatter from the light shade surfaces.

1. Effect on Imaging Performance

For a low-light level imaging system such as the star tracker, stray light can create a havoc in image processing. Stray light incident on the imager can cause an increase in the background noise level, thereby decreasing the signal-to-noise ratio and obscuring

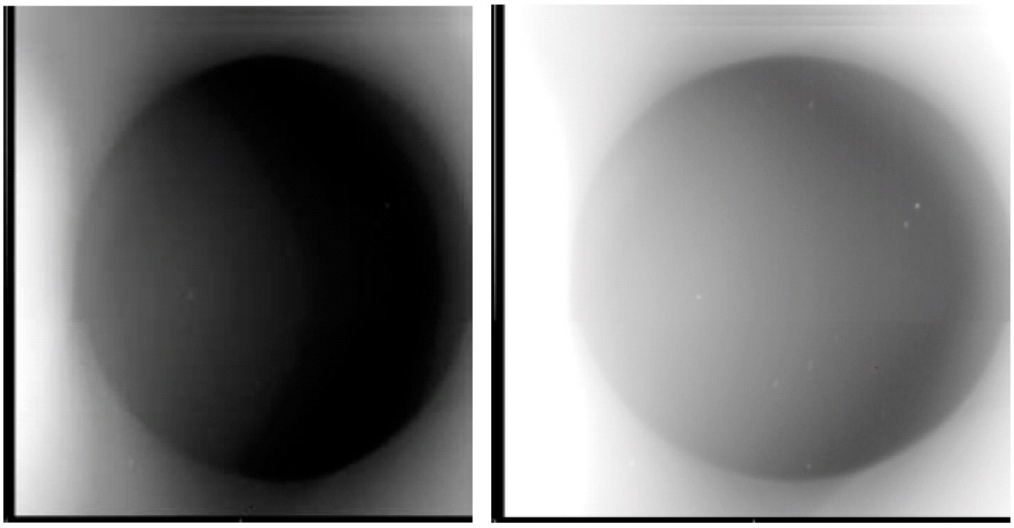

(a) Unprocessed Image (b) Processed Image

Fig. 93. Stray light decreases signal-to-noise ratio and post processing of the image reveals the presence of faint stars

the faint stars. Fig. 93 shows the images obtained from the StarNav1 experimental star tracker on the STS-107 mission [57]. In this experiment, the star tracker was mounted on the rooftop of the SPACEHAB module which was blanketed by a diffusely reflective material. This provided the sunlight or Earth light an easy path for entering the optical train. This particular raw image is thus severely affected by stray light captured by the sensitive imager and thus there seem to be no stars visible in the field-of-view of the star tracker. Post-processing of the image on ground facilities reveals the presence of many stars. Such processing, however, is infeasible in real-time using the limited computational resources on-board. We mention that the STS-107 images with the SPACEHAB roof in the shadow were not affected by stray light.

Unwanted light can also manifest itself as bright streaks or patterns, see Fig. 94, which may fool the sensor in associating the pattern with a plausible star or body [58].

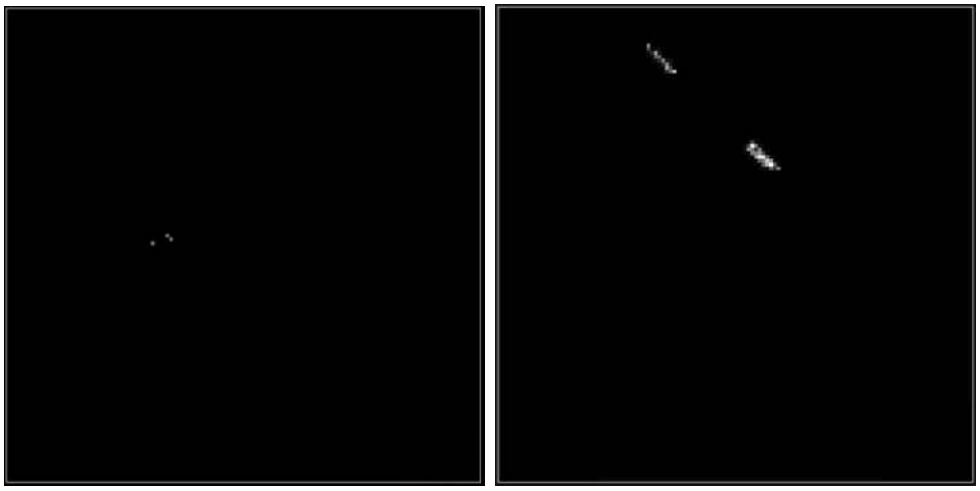

Fig. 94. Stray light rays hitting the detectors as patterns and streaks.

2. Mitigation Techniques - Light Shades

The main source for stray light is the light from the Sun, the Earth and the Moon. The solar irradiance on the Earth's atmosphere is about $1371 W/m^2$ and the Earth has an average albedo of 0.39 leading to an Earth reflected irradiance of around $534 W/m^2$. As compared to this, a star of visual magnitude 5.0 has an irradiance of only $2.5 \times 10^{-10} W/m^2$. Thus, for a star tracker on-board a spacecraft orbiting the Earth, the sunshine and the earthshine are the major sources of stray radiation and care must be taken to avoid "swamping" starlight with these sources of stray light.

Although stray light can never be completely eliminated, by judicious design, it can be reduced to a level at which it is insignificant for most pointing directions. Light shades or baffles are mechanical enclosures that surround the optical train and are most commonly used to mitigate stray light. In its simplest form, the baffle is a conical section with an entrance window and an exit window which is aligned with the optical axis. The baffle is usually made up of aluminum or a light weight material and is coated with optically black paint. Ridges or vanes are also placed on the inner

Table XIV. Example of stray light specifications for a star tracker

System Parameters	Requirements
Earth Rejection Angle	15°
Sun Rejection Angle	30°
Field of View	8°
Stray Light Attenuation	90dB

wall of the baffle to provide higher stray light attenuation by diffraction and multiple reflections. The rejection angle of the baffle; i.e. the angle beyond which no direct rays of light can enter the baffle, is primarily decided by the length of the baffle. The longer the length, the smaller the rejection angle can be. Table XIV lists the stray light rejection requirements of a star tracker.

Keeping track of these rejection angles is critical during mission planning of the spacecraft. Excursion of the sun or the Earth in the rejection angle zone of the star tracker can lead not only to unavailability of attitude estimate but also pose a serious threat to the health of the sensitive detector. This in turn places constraints on the maneuver design and instrument placement for the systems engineer. Consequently, the systems engineer will desire for the sensor rejection angles to be as small as possible. Fig. 95 shows a sketch of a double baffle. The sun and the Earth rejection angles are given by ϕ_S and ϕ_E respectively. The double baffle is designed as two sections - front and rear. The front section is dimensioned so as to block the Sun illumination while the rear baffle blocks the Earth illumination. The length of the baffle L can be determined geometrically [59] by

$$L = \frac{(2a + \epsilon)(\tan\phi_S + \tan\alpha)}{(\tan\phi_E - \tan\alpha)(\tan\phi_S - \tan\phi_E)} \tag{8.1}$$

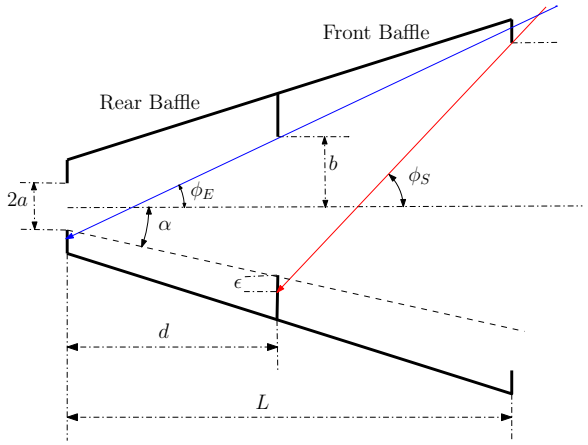

Fig. 95. Schematic of the double baffle

where a is the semi-aperture of the optical train, ϵ is the additional safety margin to the entrance aperture, α = FOV + FOV safety margin, is the field-of-view plus a safety margin. Fig. 96 shows the baffle length calculated using the above relation for a narrow FOV (8°) star tracker with a safety margin of 1°, semi-aperture of 17.5mm with a safety margin of 1mm.

Thus, in order to meet the requirements on the stray light rejection given in Table XIV, a double baffle of length 780mm will be required. Increasing the baffle length for a star sensor to such proportions is generally not acceptable since it adds mass and volume to the instrument. Moreover, the large length, depending on the mass/stiffness of the baffle, causes the principal vibration modes to shift to lower frequencies, thereby making the system more prone to mechanical vibrations and instabilities. Significant effort has been made towards the reduction in the baffle length by complete re-design, optimal vane placement and absorption material development [60, 59, 61]. In [61], the authors replace the standard knife-edge vanes by surfaces arranged using a corner-reflector inspired design. The surfaces are inter-leaved with reflecting and absorbing coatings. Light that is not reflected back towards the incident direction strikes the

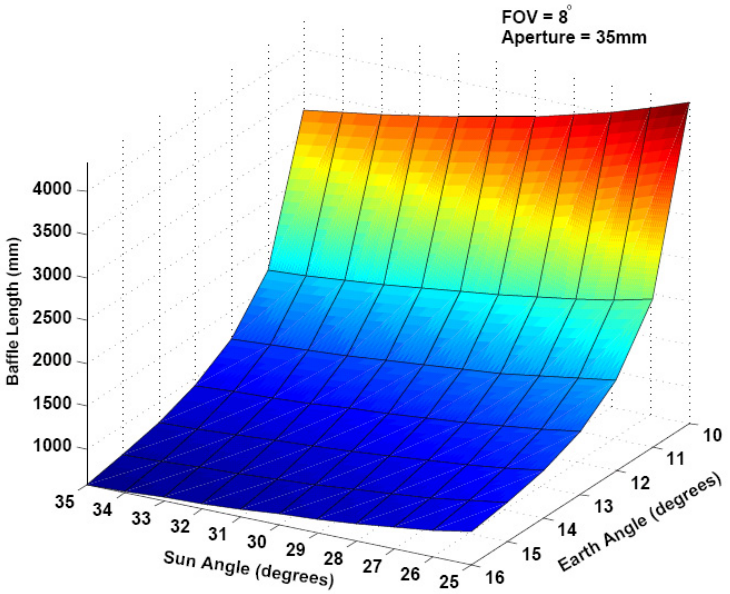

Fig. 96. Baffle length v/s Sun rejection angle and Earth rejection angle

absorbing surface and is rapidly attenuated. In [62] a new light shielding technique based on total internal reflection (TIR) is presented which reduces the baffle length by 25%. For this purpose, a half-sphere convex lens is used as the first focussing element. The bottom surface of this lens reflects any incident radiation greater than 50° by TIR. Additionally, gloss paint is used instead of a frosted or matte paint for the baffle surface. This technique, however, poses limitations in the case where a much smaller rejection angle is desired. For small rejection angles, the hemi-spherical lens will shrink in size thus limiting its light gathering capacity and will have a very small curvature which will increase the optical distortions.

B. Fiber Optics Technology

Inspired by the idea of total internal reflection, we seek to provide an additional means of stray light mitigation in order to reduce the length and consequently the mass of the standard double baffle. An optical device that works on the principle of TIR is

the optical fiber. The basic optical fiber can be thought of as a waveguide for the electro-magnetic radiation. Light that is incident on one end of the fiber at angles within its acceptance cone is captured by the fiber and transmitted down its length by TIR. Recent advances in the fabrication technology have enabled the creation of fused optical fibers in which millions of fibers are arranged in a matrix along their length to create a light conduit or bundle. This process has given rise to fiber optic tapers and faceplates that can be used to relay image information without distortion.

1. Theory of Ray Propagation

Light undergoes the phenomenon of refraction at the interface of materials having different indices of refraction. The amount of refraction is given by Snell's law and is dependent on the refractive index and the angle of incidence

$$n_1 \sin \phi_1 = n_2 \sin \phi_2 \tag{8.2}$$

where n_1 and n_2 are the refractive indices of the incident and refracted mediums, ϕ_1 and ϕ_2 are the angles of incidence and refraction respectively. If $n_1 > n_2$, at a particular incidence angle, called *critical angle*, the refracted ray will remain in the incident medium leading to total internal reflection (Fig. 97). In this situation, the angle ϕ_2 is equal to 90° and the critical angle is given by

$$\theta_c = \sin^{-1}\left(\frac{n_2}{n_1}\right) \tag{8.3}$$

An optical fiber consists of a high refractive index material that forms the "core" surrounded by a "cladding" which is made up of a comparatively smaller refractive index material. In the case where individual fibers are used, the cladding may be further covered with a buffer and a jacket that form a protective coating.

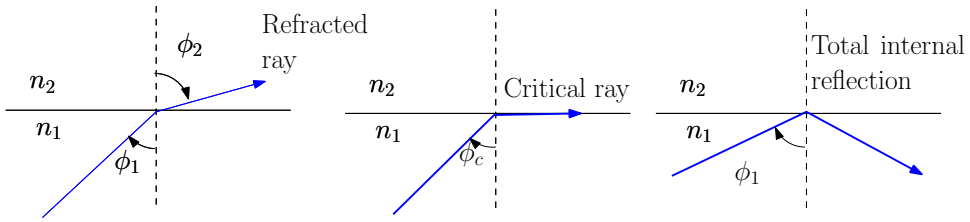

Fig. 97. Ray incident at a plane interface with $n_1 > n_2$. Ray is refracted into n_2 if $\phi_1 < \phi_c$

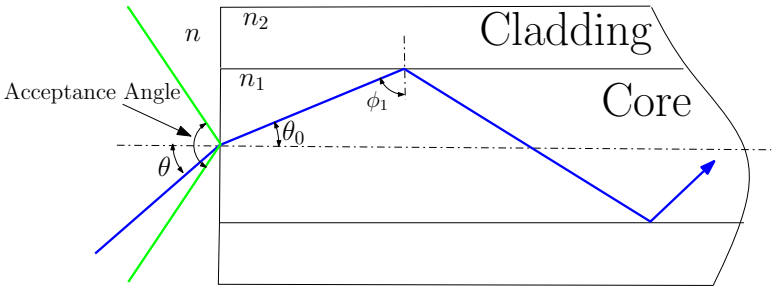

Fig. 98. Illustration of meridional ray propagation along the fiber

2. Meridional Model

Fig. 98 illustrates a cross-section of a flat ended optical fiber. A ray incident at angle θ is refracted at the entrance end to an angle θ_0 to the cylinder axis and strikes the wall of the cylinder at angle $\phi_1 = (\pi/2 - \theta_0)$. As long as the angle ϕ_1 is equal to or greater than the critical angle, this ray will be totally reflected and strike the other side of the cylinder and continue to undergo multiple internal reflections, propagating towards the end of the fiber. Rays which pass through the optical axis while propagating along the cylinder are called *meridional rays* [63].

The critical angle for the TIR is dependent on the relative refractive indices of the device and thus poses a limit to the acceptance angle of the fiber. Snell's law

states that

$$n \sin\theta = n_1 \sin\theta_0 \tag{8.4}$$

$$= n_1 \sin\left[(\pi/2) - \phi_c\right] \tag{8.5}$$

$$= n_1 \left[1 - (n_2/n_1)^2\right]^{1/2} \tag{8.6}$$

Therefore,

$$\mathrm{NA} = n \sin\theta = (n_1^2 - n_2^2)^{1/2} \tag{8.7}$$

where, NA is the numerical aperture of the system and serves to indicate the overall acceptance angle of the fiber. Obviously, the larger the difference between the refractive indices, greater the acceptance angle is and the more is the light gathered by the fiber. Commercially available fiber optic products use the NA obtained by the above developed meridional model to indicate the acceptance angles. Fig. 99 shows a plot of the acceptance angle for various NAs. For an NA of 1.0 the fiber accepts light over 180°. An arrangement of such high NA fibers is routinely used in fiber optic tapers to couple the radiation emitted by the phosphor screen to the imaging sensor.

3. Skew Rays

The meridional analysis assumes that the rays pass through the axes of the fibers. In practice however, the number of rays that propagate in this fashion are highly limited. The conduction of the light through the fiber occurs predominantly via *skew rays*. Skew rays as the name suggests are rays that are skewed relative to the fiber axis. For a fiber whose diameter is many times the wavelength of the light ray, the ray travels along the the length of the fiber in a helical fashion, never intersecting the fiber axis as illustrated in Fig. 100. Consequently, the path length, number of reflections and effective numerical aperture of the skew rays is much different than

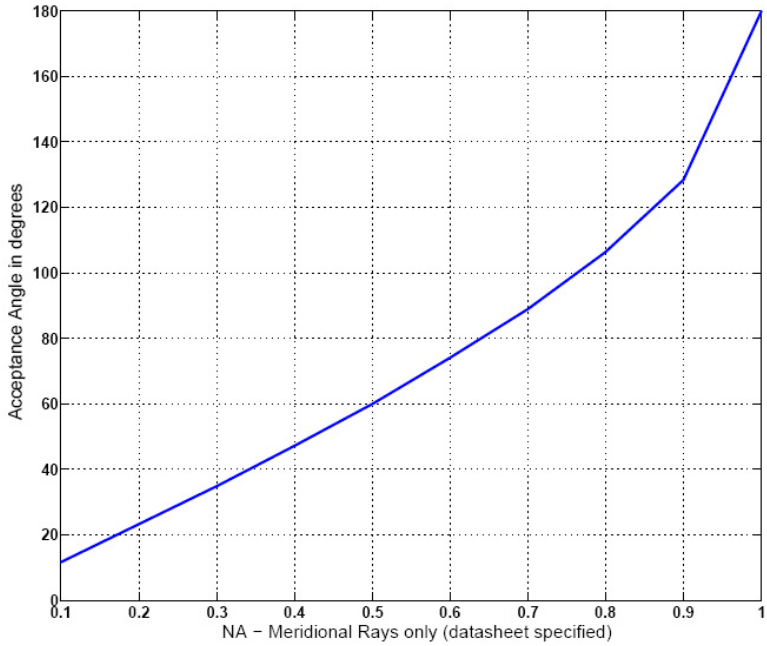

Fig. 99. Acceptance angle for varying NA using the meridional model

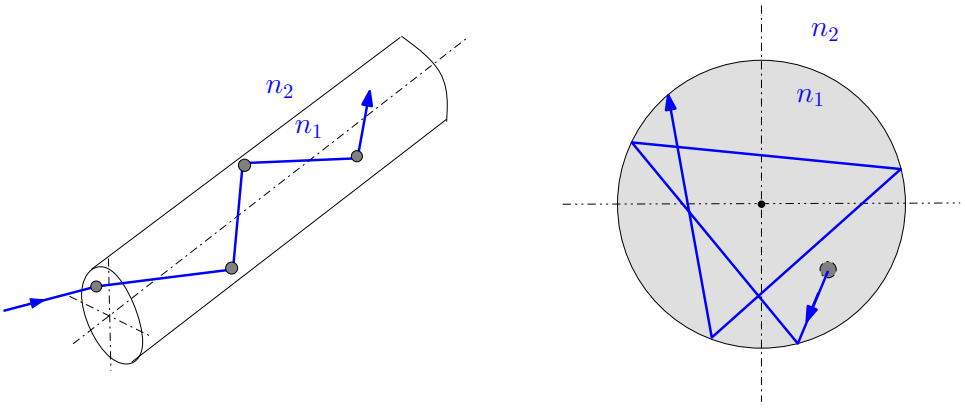

Fig. 100. Propagation of a skew ray along the fiber in a helical path

that of the meridional rays. In fact, the meridional rays are a special subset of the skew rays. The functional expression for the numerical aperture in the presence of skew rays can be written as

$$n \sin\theta = (n_1/n)\left[1 - (n_2/n_1)^2\right]^{1/2} f(a, \Psi, \beta) \tag{8.8}$$

where (a, Ψ) are the polar co-ordinates of the ray intersection at the entrance end of the cylinder, β is the angle of incidence of ray at the cylinder wall. The theory of skew ray propagation is much more complex than that of the meridional rays and thus it is not possible to obtain a closed form expression for the numerical aperture. In [64], Porter derived a generalized expression for the effective numerical aperture as a function of the refractive indices and the incident cone of light. In the absence of Fresnel reflections at the faces, losses due to absorption, reflection and scattering, the expression for the effective numerical aperture, NA_{skew} is given by

$$\begin{aligned} \mathrm{NA}_{skew}^2 &= n^2 - (2/\pi)\left\{\left[(n_1^2 - n_2^2)(n^2 - n_1^2 + n_2^2)\right]^{1/2}\right\} \\ &\quad -(2/\pi)\left\{\left[n^2 - 2\left(n_1^2 - n_2^2\right)\right]\cos^{-1}\frac{\left(n_1^2 - n_2^2\right)^{1/2}}{n}\right\} \end{aligned}$$

If the initial ray propagation medium is air, then $n = 1$, and using the meridional numerical aperture NA_m expression given by Eq.8.7, the above expression becomes

$$\mathrm{NA}_{skew}^2 = 1 - \frac{2}{\pi}\left\{\left[\mathrm{NA}_m^2\left(1 - \mathrm{NA}_m^2\right)\right]^{1/2} + \left(1 - 2\mathrm{NA}_m^2\right)\cos^{-1}\left(\mathrm{NA}_m^2\right)\right\} \tag{8.9}$$

The primary affect of the inclusion of the skew rays is the increase in the effective numerical aperture; i.e. the acceptance angle of the fiber as shown in Fig. 101. Since the manufacturer stated NA is the meridional NA, care must be taken while designing the optics to this specification. The meridional NA should be used as a starting point for preliminary design but as the design matures, the skew ray model should be used

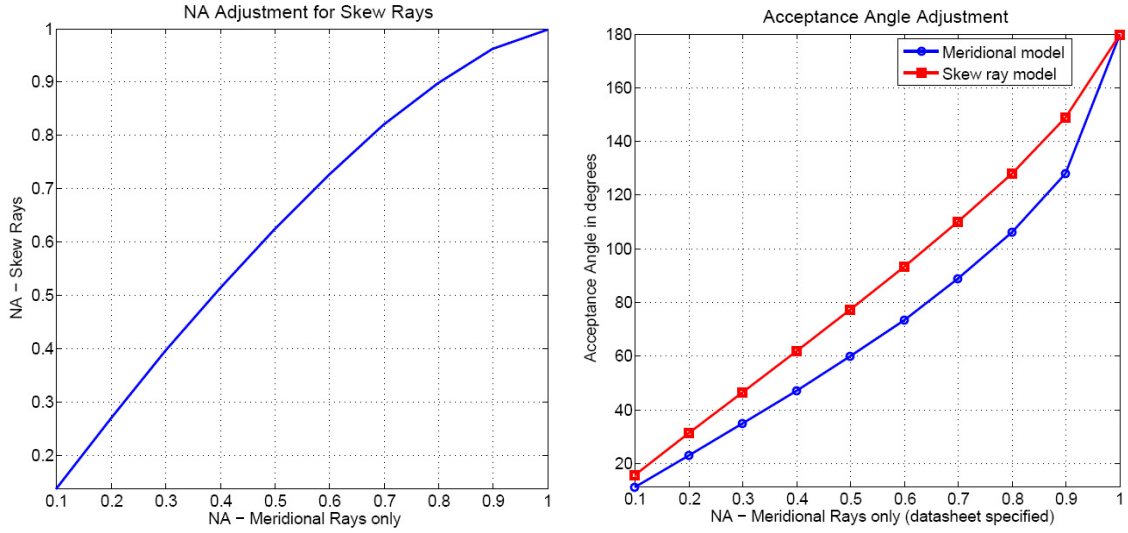

(a) NA Adjustment (b) Acceptance Angle Adjustments

Fig. 101. Increase in the effective numerical aperture due to the presence of skew rays instead.

4. Fiber Optic Faceplate

A fiber optic faceplate (FOP) is made up of millions of optical fibers fused together along their length to create a glass plate. Two types of fused bundles are available- coherent and incoherent. In the coherent bundles, the fibers have the same orientation and arrangement at both the input and output ends while in the incoherent case, the orientation is not preserved. The coherent bundles or image bundles, thus can be used to transport image data over distances. Because of this the FOPs are routinely used as a replacement for ordinary glass viewing areas. They also find applications as field flatteners, distortion correctors and angular light distribution controllers.

a. Construction

The fiber optic faceplates can be constructed into any desired surface profiles including aspheric configurations. FOPs can be fabricated in a variety of sizes with diameters up to 12inches and the mechanical dimensions are usually controllable to a very high tolerance. The fibers in the faceplate range from 3μm to 75μm and the numerical apertures commonly available are 1.0 and 0.66, with smaller NAs available by custom design.

Each fiber in the FOP is surrounded by a transparent cladding and a second opaque coating called *extra-mural absorption* or EMA glass. In the absence of EMA, light rays that escape the transparent cladding can enter the adjacent fibers and continue to propagate towards the output. This leads to a phenomenon of cross-talk between the fibers, causing signal corruption and increase in noise. The opaque EMA cladding is thus placed so as to absorb this "stray" radiation and attenuate it rapidly. The fibers in the FOP are arranged in a hexagonal grid so as to maximize the packing density and the EMA can be placed in three configurations around the fibers:

- **Circumferential EMA**: In this configuration every single glass fiber is surrounded by an EMA cladding. Although, this is the best configuration for cross-talk prevention, the pitch between the light conducting fibers increases, thereby causing a loss in resolution.

- **Statistical EMA**: The EMA is added to the FOP as glass rods that are statistically placed in the FOP matrix.

- **Interstitial EMA**: This is the most commonly available configuration. The opaque glass rods are much smaller in diameter than the fibers and are placed in the interstitial spaces between the fibers. The interstitial arrangement is a

compromise between resolution and cross-talk prevention performances.

5. FOP as a Stray Light Mitigation Device

The ability of the FOP to accept light that lies within its cone of acceptance and block light that escapes the fibers makes us realize that it might be possible to use the FOP to suppress stray light. This can be done by a judicious selection of a FOP whose acceptance angle is matched to the field-of-view of the star tracker or to the minimum rejection angle according to the stray light specifications. The FOP can be placed in the optical train before the image intensifier stage, with its actual position depending upon the lens design. In order to validate this idea, an optical model of the FOP was made in the optical ray tracing software package and a simplified stray light analysis was performed. Post simulation, a hardware setup was made in the laboratory and a commercially available FOP was tested.

C. Modeling Using Non-sequential Ray Tracing

Various software packages such as ZEMAX, CodeV, ASAP offer a combination of geometrical optics simulation along with physical optics calculations that allow the user to model a wide variety of phenomena and processes including stray light. The most common computational technique for stray light analysis is ray tracing. Ray tracing simulates the propagation of light in an optical system with a ray, which is a vector representation of light normal to the wavefront. As compared to geometrical optics, the ray tracing for stray light analysis is non-sequential in nature. Usually, computer aided design models of the lens elements, mechanical housing, baffles and mounts are made and are imported into the ray tracing software. Sources of known power are placed in the vicinity of the model and the rays from the sources are traced

as they propagate towards detectors placed at regions of interest. By observing the output of this detector, the performance of the system can be analyzed and the system components can be tuned/re-optimized to meet the requirements.

1. Setup

A sectional model of the FOP was created in ZEMAX. Each of the optical fiber elements was modeled as three cylindrical volume elements - core, cladding and EMA sheath located concentrically. The materials of the core and cladding determine the numerical aperture (NA) of the fiber and thus were chosen based upon the NA requirements and the materials used by commercial manufacturers. The fibers were arranged in a cubical packing structure. A three element aspheric lens system with an aperture of 34mm and a focal length of 25mm was designed to act as the primary optic. The input surface of the fiber array was placed at the focus of the lens. Table XV lists the specifications of the fibers and the designed lens system. Fig. 102-Fig. 103 show the layout of the modeled components. A 64×64 pixel detector was placed at the output of the fiber bundle.

Stray light was modeled as a collimated source of light located in the space between the lens and the fiber optic plate. This serves to model stray reflections off of the mechanical housing of the optical assembly. Radiometric analysis was done in order to determine the radiant power of a m.v.0 star and solar flux incident on the optical assembly. It was also assumed that this stray light had undergone a prior reflection off of the optical black surface of the housing which had resulted in a decrease in its radiant power. The radiant power of the star was 60.7pW and that of the stray light was 61nW.

Table XV. Parameters of the modeled FOP and lens system

Fibers	
Core Diameter	19μm
Core Material	K7 ($n = 1.51120$)
Length	5mm
Cladding Diameter	19.5μm
Cladding Material	K10 ($n = 1.50137$)
EMA Type	Circumferential
EMA Diameter	20μm
EMA Material	Absorb
NA (meridional)	0.17
Lens System	
No. of elements	3
Type	Aspheric
Aperture	34mm
Focal length	25mm
Field of View	8°
Material	PMMA, Polycarbonate plastic

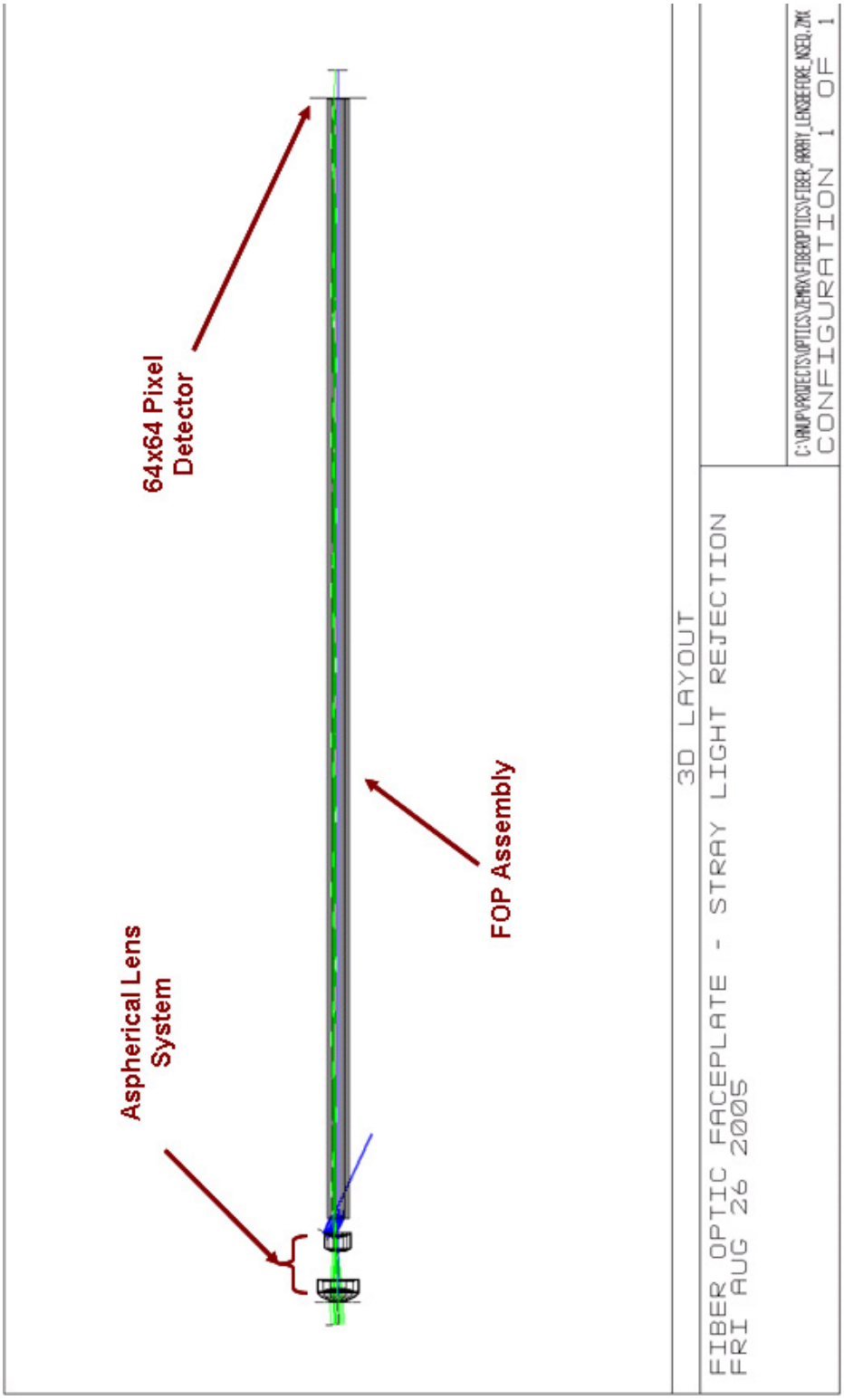

Fig. 102. The modeled fiber optic bundle in ZEMAX. Complete system layout - side view

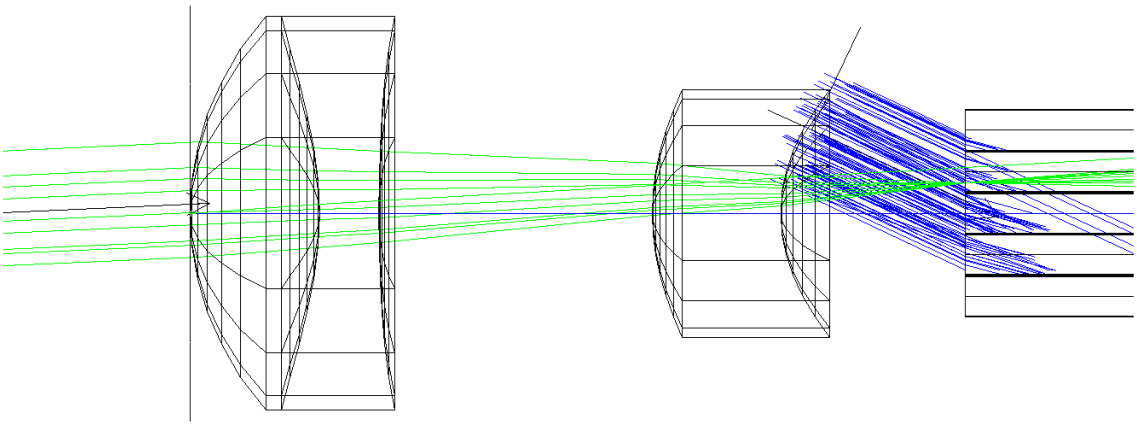

(a) Close-up of the aspherical lens system

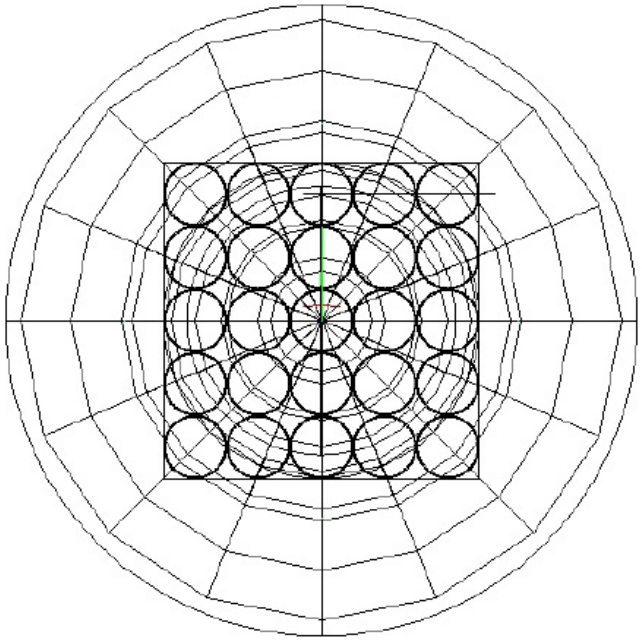

(b) Front view of the fiber arrangement - cubical packing

Fig. 103. Close-up and side view of the setup in ZEMAX. Blue rays are stray light and green rays are star light

2. Simulation Results

A Monte-Carlo ray trace was performed using the non-sequential analysis toolbox. The number of rays launched for each source - stray light and star light was 10^4 each. The angle of incidence of the stray light was varied from 0° to 45° and the output of the detector was observed. Fig. 104 shows the resulting irradiance at the detector surface. Note that in the absence of stray light, the detector response is Gaussian in shape as expected. When the stray light is launched on-axis to the fibers i.e. zero angle of incidence, the stray radiation overwhelms the star light. As the angle of incidence is increased more and more rays are blocked from reaching the detector. At 45° of incidence angle only 36 out of the total 10^4 stray light rays are able to reach the detector.

The designed numerical aperture of the FOP is 0.17 which corresponds to a half-acceptance angle of about 20°. This is however, for the meridional ray model. If the skew rays are taken into consideration and a correction to the meridional NA is applied using Eq.8.9, the NA becomes 0.28 i.e. a half-acceptance angle of 42° which is observed in the simulation results. Also note that the adjusted NA is still an approximation to the actual skew ray propagation theory. Thus, the 36 rays that reach the detector are rays that were not accounted for by this approximate skew ray model. Indeed, a closer inspection of the ray paths (see Fig. 105) reveals that they are skew rays propagating in a helical path and are incident at very oblique angles to the fiber walls.

The simulation results validate the hypothesis that it is possible to use the FOP as an additional means to mitigate stray light and thus provide a basis of optimism for laboratory testing.

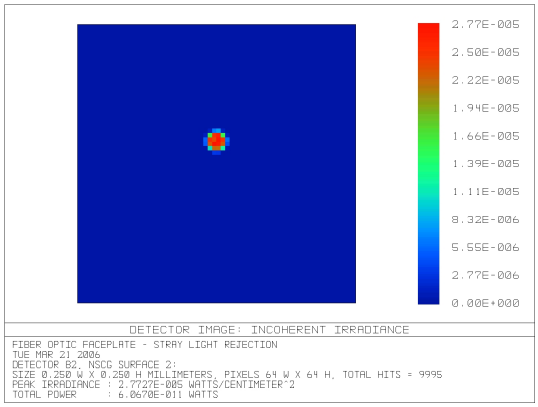

(a) No stray light

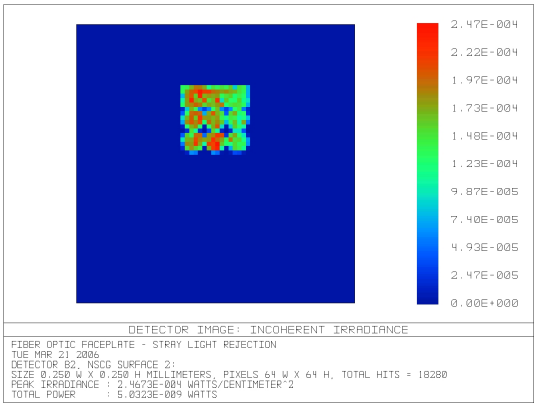

(b) On-axis stray light

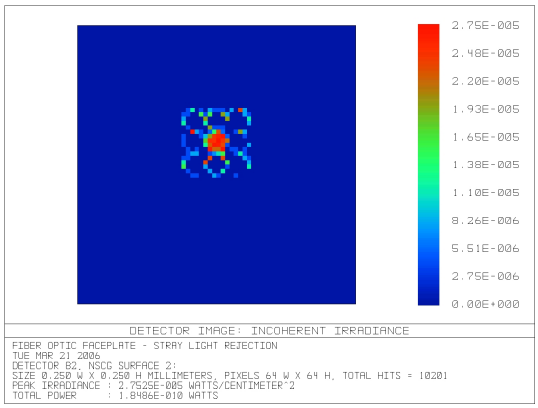

(c) Stray light at 25°

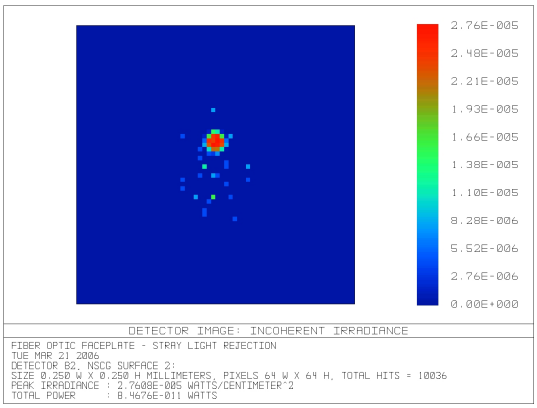

(d) Stray light at 45°

Fig. 104. Detector output after non-sequential ray trace for stray light incident at various angles

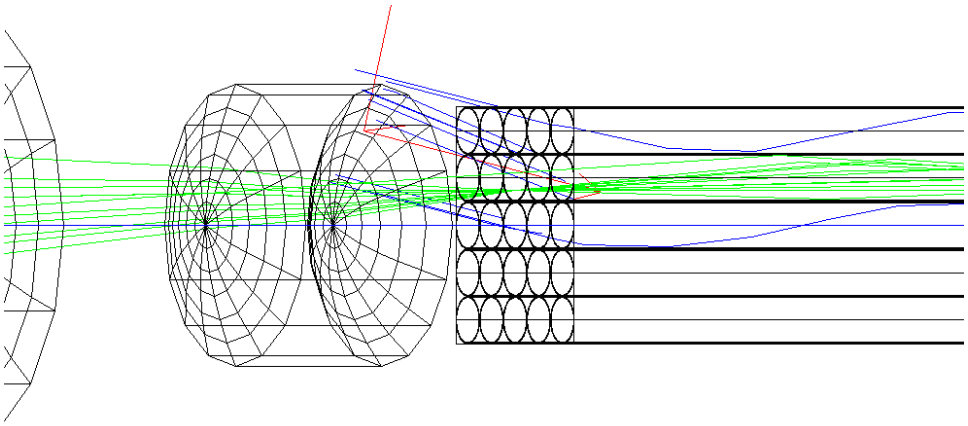

(a) Side view of the skew rays

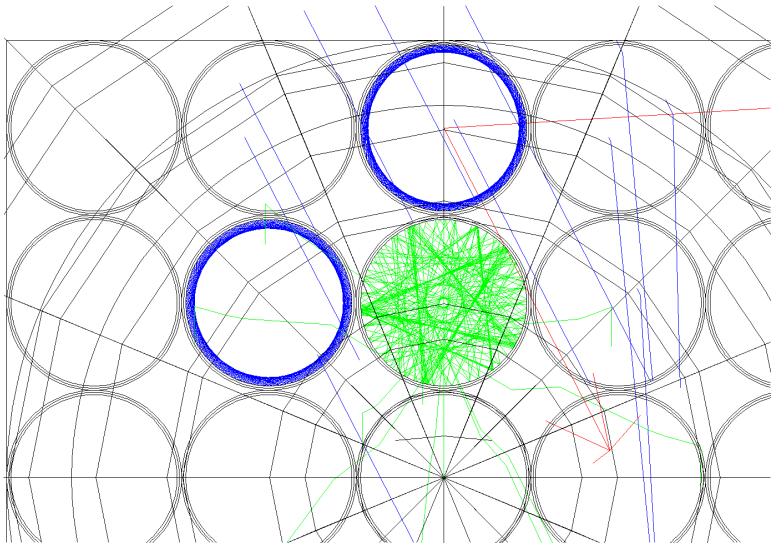

(b) Front view of the skew rays

Fig. 105. Helical paths taken by highly oblique angle of incidence skew rays (shown in blue). Notice how the rays never intersect the fiber axis

(a) FOP viewed from inside acceptance cone

(b) FOP viewed outside acceptance cone

Fig. 106. The procured FOP as viewed in different angles. The black appearance is due to the EMA

D. Experimental Testing

Encouraged by the simulation results, a fiber optic faceplate was acquired from Collimated Holes Inc. The FOP was 45mm in diameter, 15mm in thickness and was made of fibers 6μm in diameter. The NA of the plate was 0.66 and contained EMA in an interstitial configuration. Fig. 106 shows the procured FOP. The ability to block light at angles of incidence greater than the acceptance angle is immediately evident while viewing the FOP from different angles.

The FOP was interfaced to a Micron MT9M001 1.3Mpixel (1280×1024 pixels) imager by placing it flush against the glass window of the imager. An air gap still exists between the sensor die and the glass. This causes light exiting the FOP to spread in a conical fashion before hitting the optically sensitive die. Although this is a serious problem for high resolution image acquisition, in the current test scenario, the loss in resolution is not of a great consequence. The correct and the proper way to do interface the FOP with the imager requires the removal of the glass window from the detector which is a very challenging task. Additionally, image sensors can

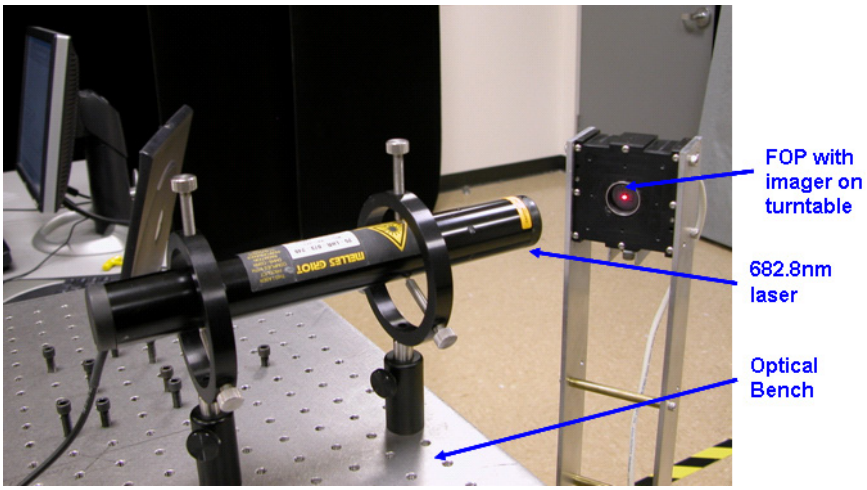

Fig. 107. The experimental setup for the stray light measurements

be procured from vendors without the glass window, however, this is expensive and a long lead time purchase item and thus the research proceeded with the less expensive detector. The imager/FOP setup was securely mounted on a computer controlled turn-table which had a minimum step size of 0.22°. A FPGA based controller was used for image acquisition and interface control.

A 682.8nm wavelength laser with adjustable power (maximum power of 20mW) was used as the stray light source. The laser was mounted on an optical bench and the geometrical axis of the imager was aligned to the laser in order to minimize laser walk during rotation. The experimental setup is shown in Fig. 107. The imager setup was rotated in known increments and images were acquired at integration times of 1ms, 2ms and 5ms. A set of ambient light frames were acquired with the laser turned off to provide "dark" frames in the image processing.

1. Results

The acquired images were processed in the Matlab environment. Dark frame subtraction was performed on each of the images and the laser spot was located in the

subtracted frame. The intensity of each pixel directly corresponds to the amount of energy that was incident on the pixel. Thus, the summation of all pixels with intensity levels above the noise floor was taken as a measure of the total energy transmitted by the FOP onto the sensor.

Fig. 108 shows a montage of the acquired images for increasing angles of incidence of the laser. As can be seen from the images, the pixels making up the laser spot on the imager appear to saturated when the laser beam is aligned with the optical axis of the FOP and imager. As the angle of incidence is increased, the central region of the spot decreases in intensity, creating a donut like shape. The donut hole increases in size with increasing angle of incidence. This is because at these oblique angles the skew rays are the dominant mode of propagation and they travel in a tight helical path around the fiber axis. At a particular angle, negligible energy is noticed on the sensor. This angle is the half-acceptance angle corresponding to the skew ray model of the plate NA. For this FOP, the half-acceptance angle is around 48°.

Fig. 109 shows a logarithmic plot of the attenuation of the stray light energy versus incidence angle for three different integration times. The curves for 1ms and 2ms integration times show that the attenuation is rapid around 40°, which corresponds to the half-acceptance angle using the meridional assumption. However, as the integration time is increased to 5ms, the weak skew rays are integrated for a longer time and cause an increase in the total energy captured by the imager. Thus, the attenuation angle shifts towards the real skew ray model half-acceptance angle of 48° as expected.

The total attenuation in the stray light energy is on the order of 10^5 or about 50dB in energy. A point to note is that, although this method of measuring the stray light attenuation is sufficient for proving the mitigation capabilities of the FOP, it is not very accurate for characterizing it's performance. The attenuation is calculated

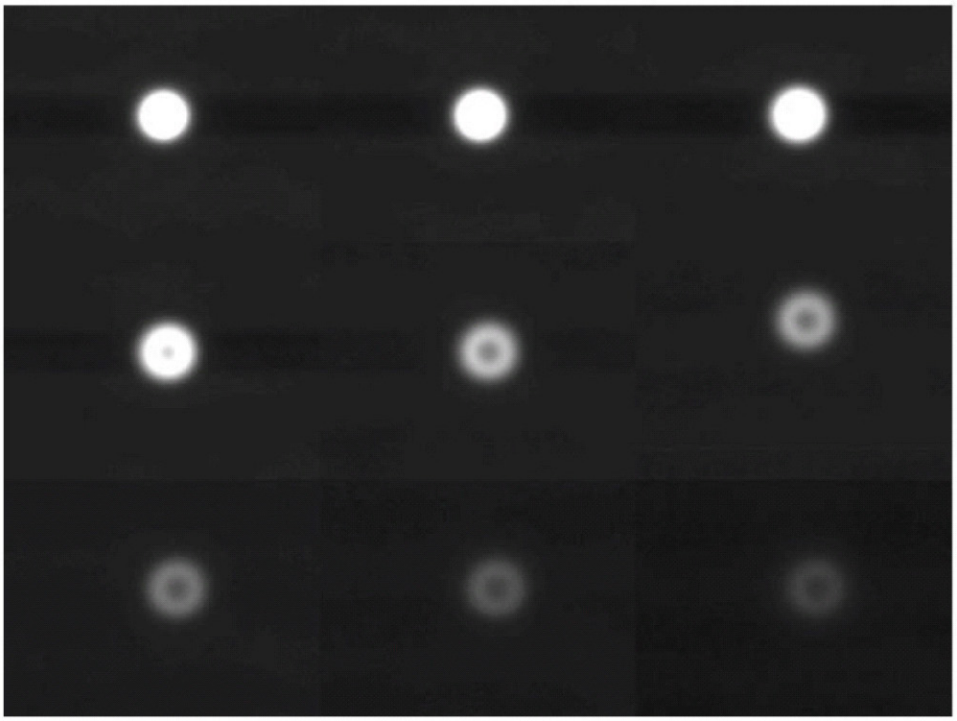

Fig. 108. A montage of the acquired images at increasing angles of incidence of the laser

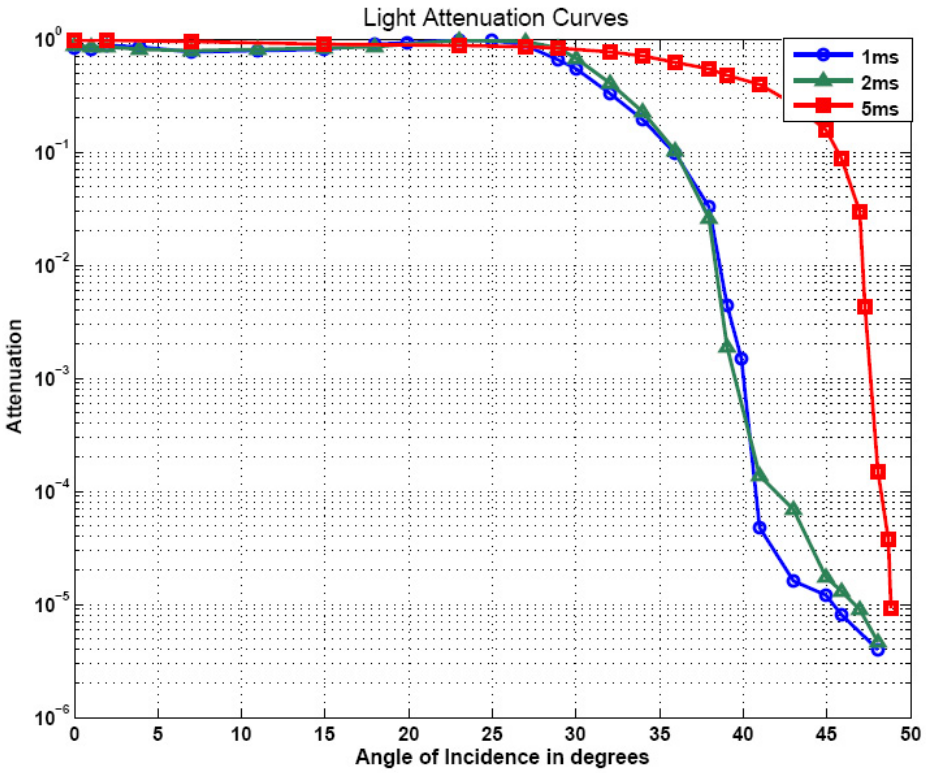

Fig. 109. Stray light energy attenuation curves obtained for various integration times

as the ratio of the sum of all the pixel energies at zero angle of incidence to the sum of pixel energies at the particular angle of incidence. Given that the spot size is constant, the dynamic range (68dB) of the imager itself poses an upper limit to the measurable variation in the light energy. Moreover, at zero angle of incidence the pixels are already saturated and their intensities do no reflect the true integrated energies. Thus, the attenuation estimate obtained is extremely conservative.

E. Concluding Remarks

In this chapter we proposed an alternative means of reducing stray light in the star tracker system using fiber optic faceplate. The theory for ray propagation - meridional and skew rays was developed and it was shown that the skew rays increase the effective numerical aperture of the fiber optic faceplate. A model of the FOP was made in the ray tracing software ZEMAX. A simplified stray light analysis was performed and irradiance on the detector was measured. It was observed that the FOP is able to block all but 36 rays out of the 10^4 rays that were launched.

Experimental testing of the fiber optic faceplate was performed in a laboratory environment by procuring a FOP and interfacing with an imager. A red laser was used as the stray light source. The acquired images were analyzed and the attenuation in the stray light energy was calculated to be around 10^5 or 50dB in energy.

We have demonstrated the effectiveness of the FOP by theory, simulation and experimentation. Although fiber optic faceplates have been around for quite a while, their application in star sensors has not been envisioned. This is mainly because the fiber optics have a transmissivity of about 60% in the visible band. In a low-light level application, this loss in transmission would be huge and would drown faint stars. In our application however, since an image intensifier was used, this loss can be easily

overcome by a slight increase in the gain of the MCP and consequently,the advantages of a FOP can be fully exploited.

CHAPTER IX

CONCLUSIONS

In this dissertation, a novel star sensor was designed and developed. This "stellar gyroscope" design seeks to replace existing separate star tracker and gyroscope subsystems with a single sensor system that can estimate angular velocities of the spacecraft using the measured star locations at high update rates. In order to overcome the limitations of mass, power, integration time of conventional imaging systems, the proposed sensor employs state-of-the-art image intensification technologies coupled with high efficiency fiber optics. The main contributions of this dissertation are the conceptual design/validation of the light intensified star sensor and novel algorithms for star position estimation and attitude determination that lead to a remarkable improvement in the knowledge of the spacecraft attitude. This also translates to an increase in the accuracy of the estimated angular rates as well as fidelity of the sensor calibration.

Another contribution of this dissertation is the development of the electro-optical model of the sensor system. An analysis of the signal strengths and sources of noise leads to the estimation of the signal-to-noise ratio of the sensor in various operating conditions. Using linear systems theory, the optical response of the system is calculated and found to be primarily limited by the resolution of the image intensifier. These models are then used to design a high fidelity image simulator for generating night sky images as seen by the sensor. Since this simulator accounts for various non-ideal behaviors such as lens aberrations, intensifier distortions, image sensor geometries and responses, the images obtained are near realistic and are used as inputs for testing of the algorithm developed in the subsequent chapters.

In order to perform precision attitude determination and angular velocity deter-

mination, it is critical to have good estimates of the star positions on the focal plane. Algorithms based on fitting a two-dimensional Gaussian profile to the measured pixel intensities and estimating the local background surfaces are developed. These algorithm differ from previously developed fitting techniques as they result in equations that contain the unknowns linearly and thus do not require iterative non-linear parameter estimation schemes. An important contribution of this dissertation is the development of a novel attitude determination algorithm that uses the knowledge of the true inter-star angles of the identified stars as constraints and recomputes the measured body vectors. This leads to a dramatic improvement in the estimation of the pointing direction as compared to other classical solutions such as ESOQ2, FOAM, QUEST to name a few. It is envisioned that with the development of higher resolution focal plane arrays and computing technologies, the error in the attitude determination will be bounded by the errors in the knowledge of the star vectors in the databases such as TychoII. Furthermore, with intelligent filtering it will be possible to reduce this error to a fraction of the database errors.

Additionally, a technique for generating compact and efficient on-board star catalogs based on the spectral response of the imaging system is also developed. The extracted star catalog is "spectrally matched" to the system and does not contain any stars that are invisible to the sensor. This leads to a reduction in the memory requirements on the flight unit, a reduction in the computational time for star search and pattern identification as well as a decrease in the probability of identification mismatch. A novel concept for stray light mitigation is also discussed. A fiber optic faceplate with extra-mural absorption around the fibers and a numerical aperture consistent with the field-of-view of the sensor placed in the optical path leads to an attenuation in the stray light rays. This concept was shown to be viable by ray tracing and by simplified experimental testing in the laboratory.

The results presented in this work open up several avenues for further research and development. Although the image simulator produces night sky images that are photo-realistic, no comparisons to the images obtained from the real star camera system have been made. In order to perform such a comparison, however, it is required to build and integrate the exact components used in the simulator design. Having done this, the results from the night sky imaging through the actual camera system can then be used to provide a feedback to the simulator design and fine-tune its operating parameters. Similarly, although the results from the spectral matching based star catalog creation algorithms seem promising, it is essential to validate the "visibility" or "invisibility" of the stars through night-sky experimentation of the corresponding camera system. In the near future, the entire star sensor system will be rebuilt using components whose designs are known very well. The models of the hardware components used in image simulator and the star catalog creation algorithms will be modified to correspond to the actual hardware used and night sky testing will be performed to validate and tune the algorithms.

A critical concern that needs to be answered is the susceptibility of the image intensified sensor to damage from high energy radiation in space. For this purpose, experimental testing will be performed by bombarding the device with radiation in a test chamber. Another important concern that will be rigorously investigated, is the ability to perform all the computations on space qualified platforms in the short processing times allotted. Although, the stellar gyroscope aims to replace the conventional gyroscopes, as compared to the conventional systems it has a limited range of operation with respect to the maximum angular rates the spacecraft will experience. This range is dictated by the signal-to-noise ratio between the star signal and the background and also by the smear induced due to motion. At very high angular rates, these problems will likely lead to a drop in the accuracy of the estimated

angular velocities. Nonetheless, the intensified star sensor presents an attractive all-in-one low mass, low power package for satellites, especially small satellites and non-spinning satellites, as their primary guidance, navigation and control sensor.

REFERENCES

[1] C. C. Liebe, E. W. Dennison, B. Hancock, R. C. Stirbl, and B. Pain, "Active pixel sensor (APS) based star tracker," in *Proc. IEEE Aerospace Conference*, 1998, vol. 1, pp. 119–127.

[2] W. M. Johnson and R. E. Phillips, "Stellar/inertial (EBCCD/MEMS) attitude measurement and control of small satellite," presented at the AIAA Space 2001 - Conference and Exposition, Albuquerque, NM, August 2001.

[3] J. L. Crassidis, "Angular velocity determination directly from star tracker measurements," *AIAA Journal of Guidance, Control, and Dynamics*, vol. 25, pp. 1165–1168, 2002.

[4] G. N. Rao, T. K. Alex, and M. S. Bhat, "Incremental-angle and angular velocity estimation using a star sensor," *AIAA Journal of Guidance, Control, and Dynamics*, vol. 25, pp. 433–441, 2002.

[5] C. C. Liebe, K. Gromov, and D. M. Meller, "Toward a stellar gyroscope for spacecraft attitude determination," *AIAA Journal of Guidance, Control, and Dynamics*, vol. 27, pp. 91–99, 2004.

[6] Olympus Resource Center, "Image intensified camera systems," World wide web: http://www.olympusfluoview.com/theory/detectorsintro.html, Accessed January 2005.

[7] R. Waynant and M. Ediger, *Electro-optics Handbook*, New York: McGraw-Hill, 1994.

[8] Proxitronic, "Fiber optic couplings," World wide web: http://www.proxitronic.de/, Accessed March 2005.

[9] R. A. Sturz, "Advances in low light-level video imaging," in *Proc. of* SPIE *Airborne Reconnaissance XIX*, 1995, vol. 2555, pp. 196–206.

[10] Hamamatsu Inc., "Hamamatsu image intensifiers," World wide web: http://sales.hamamatsu.com/en/products/electron-tube-division/detectors/image-intensifiers.php, Accessed January 2005.

[11] Photek Inc., "Phosphor screens: Photek limited," World wide web: http://www.photek.com/phoprodf3.htm, Accessed March 2005.

[12] L. A. Bosch, "Dynamic uses of image intensifiers," in *Proc. of* SPIE, 1995, vol. 2551, pp. 159–172.

[13] Sony Global, "Sony superhad technology," World wide web: http://www.sony.net/SonyInfo/IR/info/sonyf/kumatec/index.html, Accessed May 2006.

[14] D. Litwiller, "CCD vs. CMOS: Facts and fiction," *Photonics Spectra*, pp. 10–15, January 2002.

[15] J. Janesick, "Dueling detectors: CCD or CMOS?," *Optical Engineering Magazine*, pp. 30–33, February 2002.

[16] A. D. A. Maidment and M. J. Yaffe, "Analysis of signal propagation in optically coupled detectors for digital mammography: II. Lens and fibre optics," *Physics in Medicine and Biology*, vol. 41, pp. 475–493, March 1996.

[17] G. C. Holst, *CCD Arrays, Cameras, and Displays*, Bellingham, WA: SPIE-International Society for Optical Engineering, 1998.

[18] E. H. Eberhardt, "Gain model for microchannel plates," *Applied Optics*, vol. 18, pp. 1418–1426, 1979.

[19] E. Hecht, *Optics*, San Francisco, CA: Addison Wesley, 2001.

[20] G. C. Holst, *Electro-optical Imaging System Performance*, Bellingham, WA: SPIE-International Society for Optical Engineering, 2000.

[21] M. Born and E. Wolf, *Principles of Optics: Electromagnetic Theory of Propagation, Interference and Diffraction of Light*, Cambridge, NY: Cambridge University Press, 1999.

[22] R. R. Shannon, "Aberrations and their effects on images," in *Proc. of the* SPIE - *Geometric optics, Critical Review of Technology*, 1985, vol. 531, pp. 1230–1240.

[23] I. P. Csorba, "Analytical approach to the modulation transfer function of the generation II wafer tube," in *Proc. of SPIE Electro-optical Systems Design Conference and International Laser Exposition*, September 1976, pp. 646–653.

[24] C. B. Johnson, "MTF's: a simplified approach," *Electro-optical Systems Design*, vol. 4, pp. 22–26, 1972.

[25] D. Mortari, C. Bruccoleri, S. LaRosa, and J. L. Junkins, "CCD data processing improvements," presented at the International Conference on Dynamics and Control of Systems and Structures in Space, July 2002.

[26] E. Hg, C. Fabricius, V. V. Makarov, S. Urban, T. Corbin, G. Wyco, U. Bastian, P. Schwekendiek, and A. Wicenec, "The Tycho-2 catalogue of the 2.5 million brightest stars," *Astronomy and Astrophysics*, vol. 10, pp. L27–L30, 2000.

[27] European Space Agency, "The Hipparcos and Tycho catalogs," World wide web: http://www.rssd.esa.int/Hipparcos/catalog.html, Accessed July 2005.

[28] ITT Night Vision, "ITT Industries: Speciality products ITT9910," World wide web: http://www.nightvision.com, Accessed February 2005.

[29] J. Anderson and I. R. King, "Toward high-precision astrometry with WFPC2. I. deriving an accurate point-spread function," *Publications of the Astronomical Society of the Pacific*, vol. 112, pp. 1360–1382, 2000.

[30] R. C. Stone, "A comparision of digital centering algorithms," *The Astronomical Journal*, vol. 97, pp. 1227–1237, 1989.

[31] P. Singla, D. T. Griffith, J. L. Crassidis, and J. L. Junkins, "Attitude determination and autonomous on-orbit calibration of star tracker for the GIFTS mission," in *AAS/ AIAA Space Flight Mechanics Meeting, San Antonio, TX*, January 2002, vol. 112, pp. 19–38.

[32] G. Rufino and D. Accardo, "Enhancement of the centroiding algorithm for star tracker measure refinement," *Acta Astronautica*, vol. 53, pp. 135–147, 2003.

[33] P. Singla, "Multi-resolution methods for high fidelity modeling and control allocation in large-scale dynamical systems," Ph.D. dissertation, Department of Aerospace Engineering, Texas A&M University, 2006.

[34] J. L. Crassidis and J. L. Junkins, *Optimal Estimation of Dynamical Systems*, Applied Mathematics and Nonlinear Science Series. Boca Raton, FL: Chapman and Hall/CRC, 2004.

[35] M. D. Shuster, "Maximum likelihood estimate of spacecraft attitude," *Journal of the Astronautical Sciences*, vol. 37, pp. 79–88, 1989.

[36] J. L. Farrell and J. C. Steulpnagel, "A least squares estimate of spacecraft attitude," *Siam Review*, vol. 8, pp. 384–386, 1966.

[37] G. M. Lerner, *Spacecraft Attitude Determination and Control*, Boston, MA: Reidel, 1978.

[38] F. L. Markley, "Attitude determination using vector observations: a fast optimal matrix algorithm (FOAM)," *Journal of the Astronautical Sciences*, vol. 41, pp. 261–280, 1993.

[39] M. D. Shuster and S. D. Oh, "Three axis attitude determination from vector observations," *Journal of the Guidance and Control*, vol. 4, pp. 70–77, 1981.

[40] M. D. Shuster, "Approximate algorithms for fast optimal attitude computation," in *AIAA Guidance and Control Conference, Palo Alto, CA*, August 1978, pp. 89–95.

[41] D. Mortari, "Second esimator of the optimal quaternion," *Journal of the Guidance, Control and Dynamics*, vol. 23, pp. 885–888, 2000.

[42] D. Mortari, "Energy approach algorithm for attitude determination from vector observations," *Journal of the Astronautical Sciences*, vol. 45, pp. 41–55, 1997.

[43] F. L. Markley, "Attitude determination using vector observations and the singular value decomposition," *Journal of the Astronautical Sciences*, vol. 36, pp. 245–258, 1988.

[44] D. Mortari, "EULER-2 and EULER-n algorithms for attitude determination from vector observations," *Space Technology*, vol. 16, pp. 317–321, 1996.

[45] H. D. Black, "A passive system for determining the attitude of a satellite," *AIAA Journal*, vol. 2, pp. 1350–1351, 1964.

[46] F. L. Markley and D. Mortari, "Quaternion attitude determination using vector observations," *Journal of the Astronautical Sciences*, vol. 48, pp. 359–380, 2000.

[47] D. Mortari, "Search-less algorithm for star pattern recognition," *Journal of the Astronautical Sciences*, vol. 45, pp. 179–194, 1997.

[48] StarVision Technologies Inc., "Star tracker products," World wide web: http://www.starvisiontech.com, Accessed March 2006.

[49] Goodrich Corporation, "HD1003 star tracker," World wide web: http://www.oss.goodrich.com/datasheets/oss, Accessed March 2006.

[50] H. Y. Kim, "Novel methods for spacecraft attitude estimation," Ph.D. dissertation, Department of Aerospace Engineering, Texas A&M University, College Station, 2002.

[51] M. Samaan, C. Bruccoleri, D. Mortari, and J. L. Junkins, "Novel techniques for the creation of a uniform star catalog," *Advances in Astronautical Sciences*, vol. 116, pp. 1691–1703, August 2004.

[52] Schott Optics, "Transmittance of optical glass," World wide web: http://www.schott.com, Accessed March 2006.

[53] T. Pollock, "Star tracker radiation hardened lens design," Personal communications, Texas A&M University, College Station, TX, August, 2006.

[54] A. T. Young and W. M. Irvine, "Multicolor photoelectric photometry of the brighter planets. i. program and procedure," *Astronomical Journal*, vol. 72, pp. 945–955, 1967.

[55] A. T. Young, "Air mass and refraction," *Applied Optics*, vol. 33, pp. 1108–1110, 1994.

[56] M. J. Vargas, P. M. Bentez, and F. S. Bajo, "Atmospheric extinction of stellar radiation in the optical domain," *European Journal of Physics*, vol. 21, pp. 245–252, 2000.

[57] M. Samaan, A. Katake, T. C. Pollock, and J. L. Junkins, "STARNAV1:Star tracker experiment on the space shuttle mission STS-107," *Advances in Astronautical Sciences*, vol. 116, pp. 2471–2481, 2004.

[58] T. Pollock, "Khalstar optical system design," Tech. Rep., Texas A&M University, College Station, 2003.

[59] J. Arnoux, "Star sensor baffle optimization: some helpful practical design rules," in *Proc. of SPIE: Optical System Contamination V, and Stray Light and System Optimization*, November 1996, vol. 2864, pp. 333–338.

[60] R. P. Heinish and C. L. Jolliffe, "Light baffle attenuation measurements in the visible," *Applied Optics*, vol. 10, pp. 2016–2022, 1971.

[61] W. Lu and Z. Li, "Optimum baffle design of star sensor," in *Proc. of SPIE: Optical Design and Testing*, September 2002, vol. 4927, pp. 374–380.

[62] H. Kawano, Y. Sato, K. Mitani, H. Kanai, and K. Hama, "New light shielding technique for shortening the baffle length of a star sensor," in *Proc. of SPIE: Current Developments in Lens Design and Optical Engineering III*, October 2002, vol. 4767, pp. 62–69.

[63] N. S. Kapany, *Fiber Optics: Principles and Applications*, New York, NY: Academic Press, 1967.

[64] R. J. Potter, "A theoretical and experimental study of optical fibers," Ph.D. dissertation, University of Rochester, Rochester, NY, 1960.

VITA

Anup Bharat Katake was born in Tarapur, India in 1977. He received his baccalaureate (B.Tech.) degree in electrical engineering from Indian Institute of Technology, Bombay, India in May, 1999. In August, 1999, he joined the Aerospace Engineering Department of Texas A&M University for his graduate studies and received his master's degree (M.S.) in Aerospace Engineering in May 2002. During this time period he has worked on sensors for precision relative navigation and an experimental star tracker that flew on STS-107 . His research for the Ph.D. program is concentrated on the design of star sensors with high update rates. All graduate level work was performed under the supervision of Dr. John L. Junkins.

He can reached at anup.katake@gmail.com or by contacting Dr. John L. Junkins, Department of Aerospace Engineering, Texas A&M University, College Station, TX 77843.